

**BIOPHYSICAL AND PHARMACOLOGICAL CHARACTERIZATION OF
CYTOPLASMIC DYNEIN HEAVY CHAIN 1**

by

Hikmat N. Daghestani

B.S., Allegheny College, 2006

Submitted to the Graduate Faculty of
School of Medicine in partial fulfillment
of the requirements for the degree of
Doctor of Philosophy

University of Pittsburgh

2010

UNIVERSITY OF PITTSBURGH

SCHOOL OF MEDICINE

This dissertation was presented

by

Hikmat N. Daghestani

It was defended on

December 10, 2010

and approved by

Ronald Wetzel, Ph.D., Department of Structural Biology

James F. Conway, Ph.D., Department of Structural Biology

Guillermo Romero, Ph.D., Department of Pharmacology & Chemical Biology

Michael Cascio, Ph.D., Department of Chemistry & Biochemistry, Duquesne University

Dissertation Advisor: Billy W. Day, Ph.D., Departments of Pharmaceutical Sciences and
Chemistry

Copyright © by Hikmat N. Daghestani

2010

BIOPHYSICAL AND PHARMACOLOGICAL CHARACTERIZATION OF CYTOPLASMIC DYNEIN HEAVY CHAIN 1

Hikmat N. Daghestani, Ph.D.

University of Pittsburgh, 2010

The cytoplasmic dynein motor protein complex transports a number of different important cargos along microtubules (MTs) in a retrograde manner. Cytoplasmic dynein plays an important role in many cellular processes and a number of diseases have been associated with defects in its activity. Despite its importance, there are no small molecules that selectively modulate cytoplasmic dynein activity, nor is its atomic structure elucidated. In an effort to identify compounds that target cytoplasmic dynein, hits from a high information content cell-based nuclear translocation assay were further evaluated biochemically. High throughput assays were developed to screen for glucocorticoid ligand competition, MT perturbation, and the ATPase activities of Hsp 70 and 90, cytoplasmic dynein heavy chain 1, and myosin. Several compounds from screening the Library of Pharmacologically Active Compounds (LOPAC1280) were identified to inhibit cytoplasmic dynein, though they had several unattractive pharmacological properties and were generally non-specific. Additional screening of the Molecular Libraries Screening Center Network >220,000-member library showed a number of compounds that specifically inhibited the ATPase activity of cytoplasmic dynein heavy chain 1 with little or no interaction with other proteins involved in cargo complex formation. A novel approach to screen for MT perturbing agents was also developed using biosensors. Thickness, mass, and density measurements from dual polarization interferometry suggested the growth process of MTs on

surfaces. Resonant mirror biosensors were used to distinguish MT stabilizers from destabilizers based on rates of MT assembly on the surfaces.

In addition, the structure of the cytoplasmic dynein heavy chain motor domain was characterized by computational and experimental methods. Comparative homology structural modeling was used to predict 15 surface accessible cysteines, which were then correlated experimentally by mass spectrometry. Five cysteines were matched computationally and experimentally to be surface-accessible, suggesting some inadequacy of the proposed model. Finally, attempts to reconstruct a model of cytoplasmic dynein heavy chain 1 by electron microscopy were hindered by the purification of the protein from both a Hi5/baculovirus expression system and bovine brain, although the latter appeared to provide better quality micrographs. Ultimately, structural characterization will assist with the discovery of cytoplasmic dynein heavy chain 1 modulators.

TABLE OF CONTENTS

ACKNOWLEDGEMENTS	xvi
ABBREVIATIONS.....	xviii
1.0 INTRODUCTION.....	1
1.1 EUKARYOTIC CYTOSKELETAL STRUCTURE & INTRACELLULAR TRANSPORT	1
1.1.1 Cytoskeleton	1
1.1.1.1 Microtubules.....	1
1.1.1.2 Microfilaments	4
1.1.1.3 Intermediate Filaments.....	5
1.1.2 Cytoskeletal Motor Proteins	6
1.1.2.1 Cytoplasmic Dynein	6
1.1.2.2 Kinesin.....	9
1.1.2.3 Myosin	11
1.2 SIGNIFICANCE.....	12
1.2.1 Microtubule Perturbing Agents as Cancer Therapeutics	12
1.2.2 Potential use of Dynein Activators/Inhibitors	13
1.3 BIOPHYSICAL TOOLS.....	16
1.3.1 Computational Modeling	17

1.3.2	Mass Spectrometry	18
1.3.3	Electron Microscopy	21
1.3.4	Optical Biosensors.....	22
1.3.4.1	Surface Plasmon Resonance.....	23
1.3.4.2	Resonant Mirror Biosensor.....	29
1.3.4.3	Resonant Waveguide Grating Biosensor	31
1.3.4.4	Dual Polarization Interferometry Biosensor	33
2.0	MATERIALS & METHODS.....	40
2.1	MATERIALS	40
2.2	METHODS.....	41
2.2.1	Protein Purification	41
2.2.1.1	Tubulin Isolation and Purification from Bovine Brain	41
2.2.1.2	Cytoplasmic Dynein Isolation and Purification from Bovine Brain 43	
2.2.1.3	Rat Cytoplasmic Dynein Heavy Chain 1 Expression and Purification.....	44
2.2.2	DEX-induced Glucocorticoid Receptor Translocation HCS Assay	45
2.2.2.1	Cell Culture	45
2.2.2.2	Image Acquisition	46
2.2.2.3	Image Analysis.....	47
2.2.2.4	Indirect Immuno-fluorescent staining of 3617.4 cell MTs	48
2.2.3	Glucocorticoid Receptor Competition Binding Assay.....	49
2.2.4	ATPase Activity Inhibition Assays	49

2.2.4.1	Cytoplasmic Dynein	49
2.2.4.2	Hsp70.....	50
2.2.4.3	Hsp90.....	51
2.2.4.4	Myosin	51
2.2.5	Microtubule Polymerization Assay	51
2.2.6	Optical Biosensors.....	52
2.2.6.1	Tubulin Biotinylation.....	52
2.2.6.2	Biosensor Surface Functionalization.....	52
2.2.6.3	Microtubule Polymerization on Biosensor Surfaces.....	53
2.2.7	Computational Modeling	54
2.2.7.1	Secondary Structure Prediction	54
2.2.7.2	Three-Dimensional Comparative/Homology Modeling	55
2.2.8	Cysteine Labeling.....	55
2.2.9	Protein Digestion.....	56
2.2.9.1	In-gel Trypsin Digestion	56
2.2.9.2	In-solution CNBr Digestion.....	57
2.2.10	Mass Spectrometry	57
2.2.10.1	MALDI-TOF-MS and -MS/MS.....	57
2.2.10.2	LC-ESI-MS	58
2.2.10.3	LC-ESI-FTMS.....	59
2.2.10.4	LC-ESI-MS/MS.....	59
2.2.11	Electron Microscopy	61

3.0	IDENTIFICATION OF SMALL MOLECULES THAT TARGET RETROGRADE TRANSPORT	62
3.1	INTRODUCTION	62
3.2	RESULTS & DISCUSSION	65
3.2.1	High Information Content Cell-Based Screen	65
3.2.2	Biochemical Characterization of GR-GFP Translocation Inhibitors	70
3.2.2.1	Glucocorticoid Receptor Competitive Binding	70
3.2.2.2	Targeting the Cellular Tracks	73
3.2.2.3	Targeting Hsp Chaperones	74
3.2.2.4	Targeting Cytoplasmic Dynein	79
3.2.2.5	Eliminating Non-Specific Motor Protein Inhibitors	83
3.3	CONCLUSIONS	86
4.0	DEVELOPMENT OF BIOSENSOR APPLICATIONS TO EVALUATE MICROTUBULE PERTURBING AGENTS.....	90
4.1	INTRODUCTION	90
4.2	RESULTS & DISCUSSION	91
4.2.1	Microtubule Polymerization on Biosensor Surfaces.....	91
4.2.2	Temperature Dependent Microtubule Polymerization using Biosensors..	98
4.2.3	Comparison of Microtubule-Perturbing Agents Using RM Biosensors	101
4.3	CONCLUSIONS	103
5.0	BIOPHYSICAL CHARACTERIZATION OF CYTOPLASMIC DYNEIN	104

5.1	INTRODUCTION	104
5.2	RESULTS & DISCUSSION	105
5.2.1	Computational Modeling of Cytoplasmic Dynein Heavy Chain 1 Motor Domain	105
5.2.1.1	Secondary Structure Prediction	105
5.2.1.2	Three Dimensional Modeling of Cytoplasmic Dynein Motor Domain	109
5.2.2	Cysteine Mapping	111
5.2.3	Electron Microscopy	120
5.3	CONCLUSIONS	127
6.0	OVERALL CONCLUSIONS & FUTURE DIRECTIONS	129
	APPENDIX A	133
	APPENDIX B	139
	APPENDIX C	141
	BIBLIOGRAPHY	151

LIST OF TABLES

Table 1. Inhibition of GTP-induced assembly and hypernucleation/polymer stabilization of bovine brain tubulin by hits from the HCS analysis of the LOPAC1280 collection.....	74
Table 2. Biochemical IC ₅₀ values of test agents against both basal and MT-stimulated cytoplasmic dynein.	83
Table 3. Summary of the potential target(s) of molecules that inhibited GR translocation.	87
Table 4. Comparison of Surface-Accessible Cysteines Detected by Mass Spectrometry and Computational Prediction	120
Table 5. Protein Identification of Gel Bands by MALDI-TOF-MS and -MS/MS	125

LIST OF FIGURES

Figure 1. Structure of Tubulin/Microtubules	2
Figure 2. Microtubule Dynamics	4
Figure 3. Structure of Actin/Microfilaments	5
Figure 4. Structure of Intermediate Filaments	6
Figure 5. Structural Model of Cytoplasmic Dynein.....	8
Figure 6. Computational Models of Cytoplasmic Dynein Motor Domain	9
Figure 7. Structural Model of Kinesin	10
Figure 8. Structural Model of Myosin	11
Figure 9. Chemical Structures of Microtubule Perturbing Agents	13
Figure 10. Chemical Structures of Cytoplasmic Dynein Inhibitors.....	16
Figure 11. Schematic of a Surface Plasmon Resonance Biosensor	25
Figure 12. Detection of Binding Events with an SPR Biosensor	26
Figure 13. Schematic of a Resonant Mirror Biosensor.....	31
Figure 14. Schematic of a Resonant Grating Waveguide Biosensor	33
Figure 15. Schematic of a Dual Polarization Interferometer Biosensor	34
Figure 16. Cell-Based Concentration Dependence of LOPAC Collection on GR-GFP Translocation.....	66

Figure 17. Multi-Parameter Immunofluorescence Visualization of Treated Cells.....	68
Figure 18. Quantitation of Multi-Parameter Immunofluorescence in Cells Treated with LOPAC 1280 Hits.....	69
Figure 19. Four of the Potential Target(s) of Retrograde Transport Inhibitors	70
Figure 20. Fluorescence Polarization GR Competitive Binding Assay.....	71
Figure 21. GR Competitive Binding Assay with MLSCN Collection.....	72
Figure 22. DMSO Tolerance of Hsp70 ATPase Activity	76
Figure 23. Evidence of Precipitation of Ssa1p Samples in the Presence of LOPAC Collection..	77
Figure 24. Hsp ATPase Inhibition Assays with LOPAC Collection	78
Figure 25. Hsp70 ATPase Inhibition Assay with MLSCN Collection.....	79
Figure 26. DMSO Tolerance of Cytoplasmic Dynein ATPase Activity	80
Figure 27. Comparison of Basal and MT-Stimulated ATPase Activity of Cytoplasmic Dynein.	81
Figure 28. Cytoplasmic Dynein ATPase Inhibition Assay with LOPAC Collection.....	82
Figure 29. Cytoplasmic Dynein ATPase Inhibition Assay with MLSCN Collection	83
Figure 30. DMSO Tolerance of Myosin ATPase Activity	84
Figure 31. Myosin ATPase Inhibition Assay with LOPAC Collection.....	85
Figure 32. Myosin ATPase Inhibition Assay with MLSCN Collection	86
Figure 33. Functionality of Biotinylated Tubulin.....	92
Figure 34. Resolved Mass, Thickness, and Density of Tubulin Assembly as Assessed with DPI93	
Figure 35. Schematic Representation of the Microtubule Polymerization Process on Biosensor Surfaces.....	95
Figure 36. Microtubule Assembly Process as Assessed with RM.....	96
Figure 37. Microtubule Polymerization on a RM Biosensor	97

Figure 38. Binding of Preformed Microtubules to a Biotinylated Tubulin Surface as Assessed with RM	98
Figure 39. Temperature Dependent Microtubule Polymerization assessed with RM	100
Figure 40. Effect of Microtubule Perturbing Agents on the Temperature-Dependent Polymerization as Assessed with RM.....	101
Figure 41. Comparison of the Slopes of Initial Rates of Microtubule Assembly with Various Microtubule-Perturbing Agents	102
Figure 42. Secondary Structure Prediction of Cytoplasmic Dynein Motor Domain.....	106
Figure 43. Histogram of Secondary Structure Probabilities for Cytoplasmic Dynein Motor Domain.....	107
Figure 44. Ramachandran Plot of Predicted Dihedral Angles of Cytoplasmic Dynein Motor Domain.....	108
Figure 45. Surface Representation of Comparative/Homology Structural Models of Cytoplasmic Dynein Motor Domain.....	110
Figure 46. Surface Representation of a Modified Comparative Homology Structural Model of Cytoplasmic Dynein Motor Domain.....	111
Figure 47. Quantitation of Reactive Cysteines by Fluorescence Spectroscopy.....	112
Figure 48. Time Dependence of GSH-TG1 Fluorescence Signal.....	113
Figure 49. Base Peak Chromatogram of CNBr Digests of Cytoplasmic Dynein from LC-ESI-TOF-MS with Positive Ion Detection	114
Figure 50. Positive Ion Mass Spectra of Cytoplasmic Dynein CNBr Digests from LC-ESI-TOF-MS Analysis.....	114

Figure 51. Base Peak Chromatogram of CNBr Digests of Cytoplasmic Dynein from nanoLC-ESI-FTMS with Positive Ion Detection	115
Figure 52. Mass Spectra of Cytoplasmic Dynein CNBr Digests from ESI-FTMS	116
Figure 53. Base Peak Chromatogram of CNBr Digests of Cytoplasmic Dynein from nanoLC-ESI-LIT-Orbitrap with Positive Ion Detection	117
Figure 54. LIT-Orbitrap-MS/MS Spectrum of a Dynein-Derived Peptide Found to be Labeled with TG1	118
Figure 55. ThioGlo1 Adducts Detected by MS/MS	119
Figure 56. SDS-PAGE Gel Electrophoresis of Hi5/Baculovirus Expression of 380 kDa Cytoplasmic Dynein.....	121
Figure 57. SDS-PAGE Gel of Cytoplasmic Dynein After Additional Purification	122
Figure 58. Negative Stain Electron Micrographs of 380 kDa Rat Cytoplasmic Dynein Fragment	123
Figure 59. SDS-PAGE Gel from Tubulin Isolation Protocol	124
Figure 60. SDS-PAGE Gel of ATP-Released Cytoplasmic Dynein Fraction Purified by Size Exclusion Chromatography	126
Figure 61. Negative Stain Electron Micrographs of Bovine Cytoplasmic Dynein.....	127

ACKNOWLEDGEMENTS

I would first like to thank my advisor, Dr. Billy W. Day, for his continuing encouragement, guidance, and support over the past several years. He has truly helped me become an independent and interdisciplinary researcher. Additionally, I acknowledge all the members of the Day lab for their support over the years, especially Brianne Raccor, Miranda Sarachine, and Dan Brody. I thank Dr. Dave Fernig from the University of Liverpool and Drs. Neville Freeman, Mark Gostock, Jon Popplewell, Marcus Swann, Gerry Ronan, and Mrs. Cam Hick for their tremendous support receiving the Marie Curie fellowship and their assistance while I was abroad, which helped me achieve my first publication. I would like to thank Dr. James Conway for his guidance and introduction to electron microscopy. I also thank the Proteomics Core Lab for their technical assistance, especially Dr. Guy Uechi, John Cardamone, and Chris Bolcato for their helpful discussions and advice, both scientific and nonscientific. I would also like to thank Drs. Brian Hood and Thomas Conrads for their patience and assistance with MS/MS work. I thank Berquin Feese for his assistance with computational modeling. I would like to acknowledge my thesis committee for all of their valuable feedback throughout my dissertation work and writing.

A special thanks to Dr. Gronenborn and the entire MBSB faculty and staff for their support and guidance throughout my graduate studies. I sincerely would like to thank the

Molecular Pharmacology Program for their financial support along with Dr. John Horn, Sandi Honick, and Jen Walker for their help working out a solution to support my final year of graduate studies. I would also like to thank Jen and Cindy from the Grad Office, along with staff members from the School of Pharmacy for their assistance with administrative forms and documents throughout the years.

I have to thank all my friends both MBSB and the BGSA (Wazo, Kalyan, Rakesh, Liz, Cody, Harshad, Grant, Jerry, Addy, Matt, Naima, Adri, Carolyn, Robb, Michelle, Christi, Sarah, Jake, Meghan, Nisa, Callie, Miranda, and Neil) along with friends from outside of school (Safi, Ahmad, Simon, Brandon, Vahid, Aarish, Soubhi, Eiyass, the guys from WM2 FD, the Bannas, Sarachines, and Dratlers). I also thank my past mentors and friends Drs. Doros Petasis and Shafiq Rahman for their constant encouragement and advice throughout grad school. I would like to thank my entire family for their support and patience with me during my busy schedule throughout grad school. Finally, I would like to thank my fiancé Sarah for brightening my days while I was confined in the library working on my dissertation.

ABBREVIATIONS

17-AAG – 17-(allylamino)-17-demethoxygeldanamycin
AAA – ATPases associated with diverse activities
ADP – adenosine diphosphate
ALS – amyotrophic lateral sclerosis
AMP – adenosine monophosphate
ATP – adenosine triphosphate
ATR – attenuated total reflection
BCA – bicinchoninic acid
BSA – bovine serum albumin
CCD – charge-coupled detector
Ch – channel
CHC – colchicine
CHCA – γ -cyano-4-hydroxycinnamic acid
CID – collision induced dissociation
DCD – discodermolide
DEX – dexamethasone
DMEM – dulbecco's modified eagle medium
DMSO – dimethylsulfoxide
DNA – Deoxyribonucleic acid
DOPE – discrete optimized protein energy
DPI – dual polarization interferometry
DTT – dithiothreitol
EDTA – ethylenediaminetetraacetic acid
EGTA – ethylene glycol tetraacetic acid
EHNA – *erythro*-9-(2-hydroxy-3-nonyl)adenine
EM – electron microscopy
EPR – electron paramagnetic resonance
ER – estrogen receptor
ESI – electrospray ionization
FBS – fetal bovine serum
FITC – fluorescein isothiocyanate
FP – fluorescence polarization
FT-ICR – Fourier transform-ion cyclotron resonance
FTMS – Fourier transform mass spectrometry
GDP – guanosine diphosphate
GFP – green fluorescent protein

GR – glucocorticoid receptor
GTP – guanosine triphosphate
H/D – hydrogen/deuterium
HCS – high content screen
HEPES – 4-(2-hydroxyethyl)-1-piperazineethanesulfonic acid
HPLC – high performance liquid chromatography
HSC – heat shock cognate
Hsp – heat shock protein
IAC – iodoacetamide
IC₅₀ – half maximal inhibitory concentration
IF – intermediate filament
IgG – immunoglobulin G
LC – liquid chromatography
LIT – linear ion trap
LM – light microscopy
LOPAC – library of pharmacologically active compounds
m/z – mass-to-charge
MALDI – matrix assisted laser desorption ionization
MAP – microtubule associated protein
MCRAID – mean circ-ring average intensity difference
MES – 2-(*N*-morpholino)ethanesulfonic acid
MF – microfilament
MLSCN – molecular library screenings center network
MS – mass spectrometry/spectrometer
MSG – monosodium glutamate
MT – microtubule
MTBD – microtubule binding domain
NEM – *N*-ethylmaleimide
NF- κ B – nuclear factor kappa-light-chain-enhancer of activated B cells
NHS – *N*-hydroxysuccinimide
Ni-NTA – nickel nitrilotriacetic acid
NMR – nuclear magnetic resonance
OV – orthovanadate
P-loop – phosphate binding loop
PAGE – polyacrylamide gel electrophoresis
PBS – phosphate buffered saline
PDB – protein data bank
PIPES – piperazine-*N,N'*-bis(2-ethanesulfonic acid)
PTX – paclitaxel
RM – resonant mirror
RP – reverse phase
RWG – resonant waveguide grating
SCC – selected cell count
SD – standard deviation
SDS – sodium dodecyl sulfate
SPP – surface plasmon polaritons

SPR – surface plasmon resonance
TCEP – *tris*(2-carboxyethyl)phosphine
TE – transverse electric
Tet – tetracycline
TG1 – methyl-10-(2,5-dioxo-2,5-dihydro-1*H*-pyrrol-1-yl)-9-methoxy-3-oxo-3*H*-benzo[*f*]chromene-2-carboxylate (ThioGlo1[®])
TM – transverse magnetic
TOF – time-of-flight
Tris-HCl – tris(hydroxymethyl)aminomethane hydrochloric acid
TRITC – Tetramethylrhodamine-5-(and 6)-isothiocyanate
VCN – vincristine

1.0 INTRODUCTION

1.1 EUKARYOTIC CYTOSKELETAL STRUCTURE & INTRACELLULAR TRANSPORT

1.1.1 Cytoskeleton

The cell is a highly organized system consisting of multiple components that serve different roles in cell development and function. The component that provides the cell its mechanical strength and mobility is called the cytoskeleton – a system of protein filaments that interacts with other proteins in the cytoplasm. The cytoskeleton plays several other important roles such as pulling apart the chromosomes during mitosis (Tolic-Norrelykke, 2008), providing pathways for cargos to shuttle across the cell (Vale, 2003), and providing the mechanical force of flagellar systems to propel through the cytoplasm (Misamore and Lynn, 2000). These functions depend on the organization of three main types of filaments: microtubules, microfilaments, and intermediate filaments.

1.1.1.1 Microtubules

Microtubules (MTs) are formed from the assembly of tubulin protein. Tubulin in its soluble form is a heterodimer of tightly bound α and β isotypes (Burns, 1991). Both isotypes are

globular proteins with molecular weight of ca. 50 kDa that share approximately 40% sequence identity and are almost identical in structure (Downing and Nogales, 1998). Each monomer has a nucleotide binding site, which lies at the interface between the two monomers. As a result, guanosine triphosphate (GTP) bound to the α subunit is shielded in a non-exchangeable manner, while GTP bound to the β subunit is partially exposed and can hydrolyze to guanosine diphosphate (GDP) (MacNeil and Purich, 1978; Downing and Nogales, 1998). Tubulin heterodimers assemble vertically to form protofilaments. Protofilaments have directionality, with the α subunit pointing towards the minus (-) end and the β subunit pointing towards the plus (+) end. Approximately 13 protofilaments join laterally in a three-start left-handed helix to form a hollow tube that is ~25 nm in diameter, the MT (Wade and Chretien, 1993; Chretien and Fuller, 2000) depicted in Figure 1.

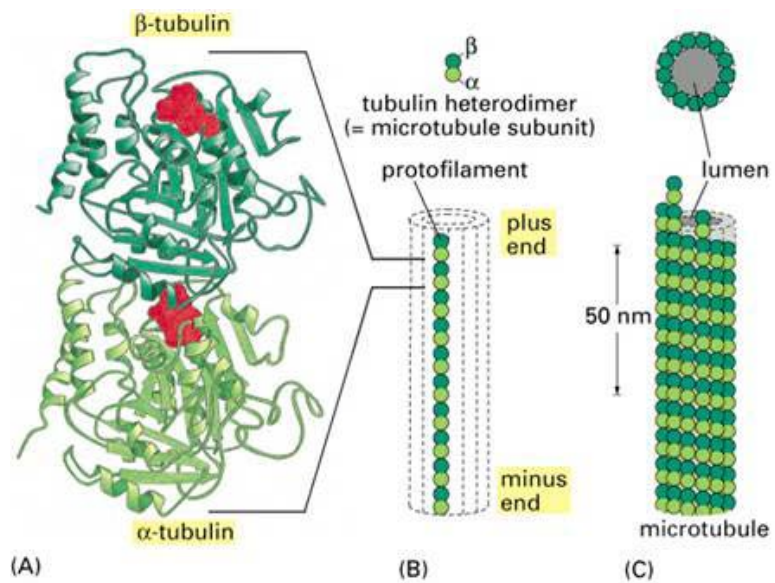


Figure 1. Structure of Tubulin/Microtubules

(A) Crystal structure cartoon of a tubulin heterodimer consisting of α and β subunits, each possessing a GTP binding site. (B) Heterodimers stack vertically to form the protofilament with the α subunit towards the minus end and the β subunit towards the plus end. (C) Approximately 13 protofilaments join laterally in a three-start left handed helix to form a hollow tube called the microtubule. Figure ©2008 from Molecular Biology of the Cell 5E by Alberts *et al.* Reproduced by permission of Garland Science/Taylor and Francis.

The process of MT formation begins with the slow association of soluble heterodimers to begin the nucleation process (Figure 2). Following this phase, protofilament elongation and subsequent formation of the MT will occur at a greater rate until the MT reaches a steady state assembly and disassembly rate (Voter and Erickson, 1984). The presence of GTP plays an important role in the stability of the MT; heterodimers GDP bound to heterodimers tends to make MTs unstable and, therefore, prone to disassembly (MacNeil and Purich, 1978). MTs are an important component of the cell, providing cells with a scaffold for signaling proteins, as well as a railway for molecular motor proteins to perform their trafficking duties. MTs are also an essential component of the mitotic spindle, the apparatus that segregates sister chromatid pairs during cell division (Jordan and Wilson, 1998). These roles are a function of microtubule dynamics (Saxton *et al.*, 1984), the relative rates of assembly (growth or rescue) and disassembly (shrinkage or catastrophe) at both the plus and minus ends of the MTs. These dynamics are also regulated by the interaction of a number of different microtubule associated proteins (MAPs), which can either stabilize (e.g., MAP2) (Gamblin *et al.*, 1996) or destabilize (e.g., stathmin) (Cassimeris, 2002) the MT.

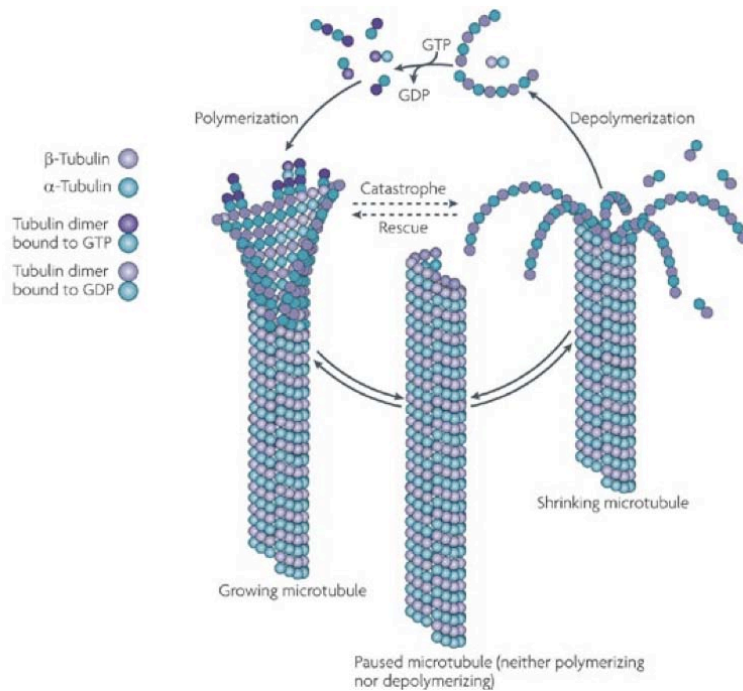


Figure 2. Microtubule Dynamics

The association of GTP-bound tubulin to MTs will cause the MT to polymerize or grow. Upon hydrolysis of GTP on the β subunit to GDP, protofilaments and tubulin heterodimers will dissociate from the MT causing MT depolymerization or shrinkage. The transition between MT depolymerization to polymerization is called rescue and the reverse transition is termed catastrophe [adapted from Conde and Caceres, 2009 with permission from publisher].

1.1.1.2 Microfilaments

Actin, like tubulin, exists as a globular protein termed G-actin, which assembles linearly to form a helical filamentous polymer called F-actin or microfilaments (MF) that are approximately 9 nm in diameter (Figure 3) (Dos Remedios *et al.*, 2003). Actin polymerization takes place in the presence of ATP, Mg^{2+} and K^+ and similarly to MTs, the hydrolysis of ATP to its respective diphosphate and subsequent release of ADP will cause the MF to depolymerize (Korn *et al.*, 1987). Also similarly to MTs, MFs possess polarity, causing the MF to increase in length in a specific direction (Kirschner, 1980). This property allows the MF to treadmill in a particular direction and is therefore responsible for cell movement (Theriot and Mitchison, 1991; Pollard and Borisy, 2003). An actin associated protein called filamin will crosslink MFs with each other

to increase the strength and rigidity of MFs (Goldman *et al.*, 1997). Filamin also links the actin cytoskeleton to the cell membrane by binding to transmembrane proteins (Calderwood *et al.*, 2001). In order for cells to avoid overstretching during cell movement, actin filaments are depolymerized via severing proteins such as gelsolin (McGough *et al.*, 2003) and cofilin (Pavlov *et al.*, 2007).

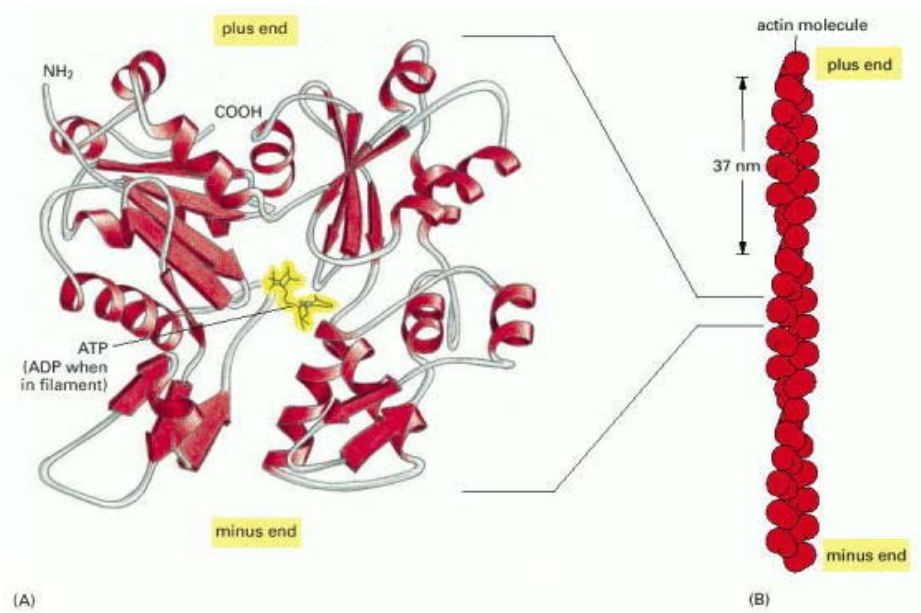


Figure 3. Structure of Actin/Microfilaments

(A) Crystal structure cartoon of an actin protein. (B) Actin molecules will form linear filaments that intertwine into a helical filament polymer known as the microfilament. Figure ©2008 from Molecular Biology of the Cell 5E by Alberts *et al.* Reproduced by permission of Garland Science/Taylor and Francis.

1.1.1.3 Intermediate Filaments

Intermediate filaments (IFs) are formed from the non-covalent assembly of a large family of rod like-proteins, giving rise to a wide variety of IFs such as keratins and lamins to name a few (Herrmann *et al.*, 2007). The term IF stems from the intermediate size of filaments in comparison to MTs and MFs, averaging around 10 nm in diameter (Fuchs and Weber, 1994). The alpha-helical rod domains from two proteins intertwined like a rope, forming either a homodimer or heterodimer, which then line up head-to-tail in a staggered confirmation to form the filaments

(Figure 4) (Fuchs and Weber, 1994). Unlike MTs or MFs, IFs do not require binding and subsequent hydrolysis of a nucleotide (Angelides *et al.*, 1989). These filaments do not exhibit the same nucleotide-dependent dynamic properties as the other two cytoskeletal structures nor do they possess a polarity. IFs are very tensile and are primarily responsible for providing the cell with a great amount of strength (Goldman *et al.*, 2008).

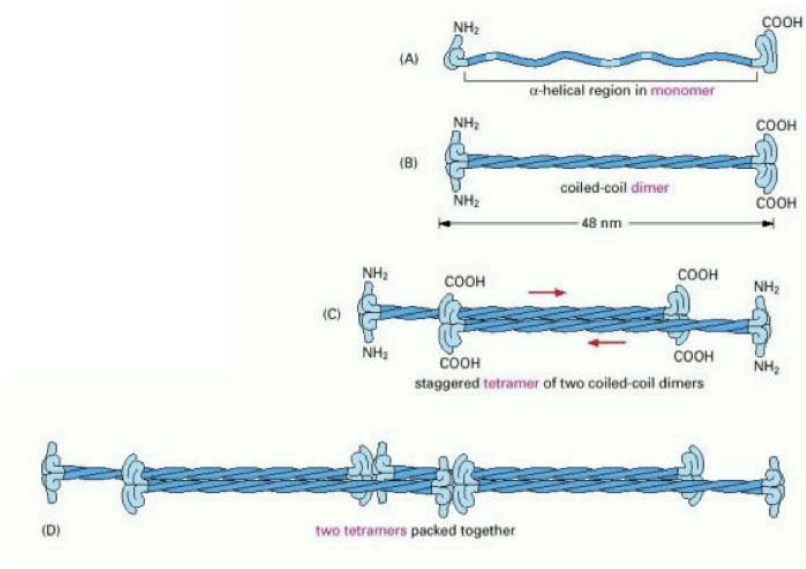


Figure 4. Structure of Intermediate Filaments

(A) A monomeric cartoon of a rod-like protein that forms the basis of intermediate filaments. (B) A coiled-coil dimer is formed between two monomers. (C) Dimers will non-covalently bind with each other forming tetramers. (D) Tetramers continue to associate with each other forming intermediate filaments. Figure ©2008 from Molecular Biology of the Cell 5E by Alberts *et al.* Reproduced by permission of Garland Science/Taylor and Francis.

1.1.2 Cytoskeletal Motor Proteins

1.1.2.1 Cytoplasmic Dynein

Cytoplasmic dynein is a large multi-protein complex amassing to ~ 1.2 MDa that translocates along MTs retrogradely (i.e., towards the minus end of MTs) (Paschal *et al.*, 1987; Vale, 2003; Vallee *et al.*, 2004). The dynein complex consists of a heterodimer of large (~ 530 kDa), globular heavy chains that contain the motor domain, and pairs of intermediate, light

intermediate and light chains that are associated with subcellular localization, MT recognition, and cargo binding as depicted in Figure 5 (Vale, 2003). The dynein motor is a ring-like structure, consistent with proteins from the AAA (ATPases *associated with diverse cellular activities*) family, consisting of six AAA domains and a seventh domain, protruding between AAA modules 4 and 5 (King, 2000). This latter domain leads to the ~10-15 nm coiled-coil stalk, which recognizes and binds MTs through a MT-binding domain (MTBD) (Mizuno *et al.*, 2007). The first four AAA domains possess phosphate binding loop (P-loop) motifs necessary for nucleotide binding, which provides the AAA domains the ability to hydrolyze ATP (Asai and Koonce, 2001). Conformational changes due to the ATP hydrolysis from the first AAA domain is responsible for motor function while the other three domains are believed to have regulatory roles (e.g., increasing the rate of MT movement driven by dynein) (Reck-Peterson and Vale, 2004; Cho *et al.*, 2008). Conformational changes have also been observed with other AAA proteins upon nucleotide binding, hydrolysis and release (Mocz and Gibbons, 2001; Burgess *et al.*, 2003).

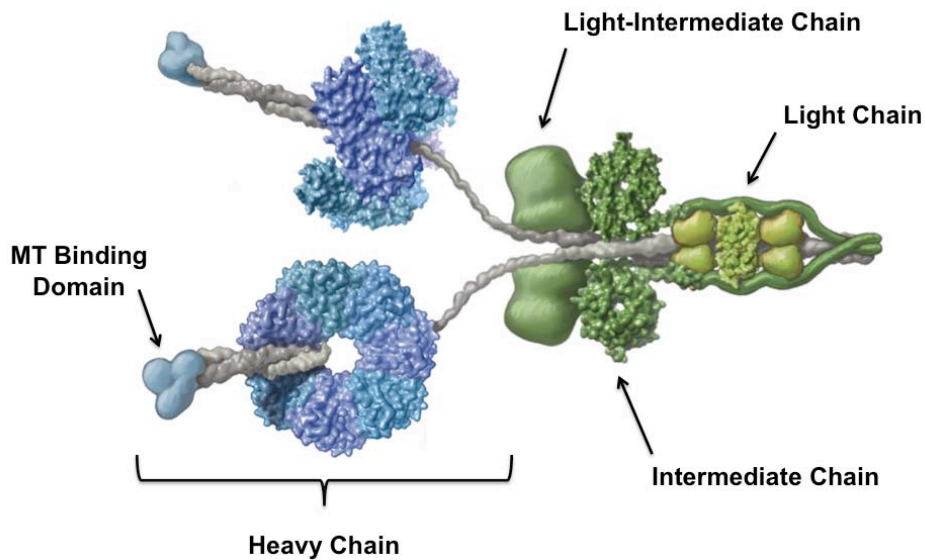


Figure 5. Structural Model of Cytoplasmic Dynein

A proposed cartoon model of cytoplasmic dynein showing a pair of heavy, light-intermediate, intermediate, and light chains. The heavy chain consists of a central ring motor domain with a protruding coiled-coil stalk that leads to a MT binding domain. The heavy chain also possesses a stalk domain that interacts with the other chains of cytoplasmic domain [adapted from Vale, 2003 with permission from publisher].

The intermediate chains connect the motor domain to a complex of proteins that is deemed the cargo. Proteins transported by cytoplasmic dynein are linked through dynactin (Gill *et al.*, 1991; Holleran *et al.*, 1998) and immunophilin-heat shock protein complexes (Galigniana *et al.*, 2004). Such cargos can vary from large Golgi vesicles (Corthesy-Theulaz *et al.*, 1992) and viruses (Dohner *et al.*, 2002; McDonald *et al.*, 2002) to smaller proteins such as the tumor suppressor p53 (Galigniana *et al.*, 2004) or even nuclear hormone receptors such GR (Harrell *et al.*, 2004).

Electron micrograph images of cytoplasmic dynein in different ATP-transition states have provided insights into the mechanism of cytoplasmic dynein translocation along MTs (Burgess *et al.*, 2003). The only structural information about cytoplasmic dynein, however, is based on low-resolution (~ 25 Å) negative stain electron microscopy images (Samso and Koonce,

2004) and a recent cryoelectron microscopy structure of cytoplasmic dynein bound to MTs (Mizuno *et al.*, 2007). Other research groups have added green-fluorescent protein (GFP) tags to cytoplasmic dynein's motor domain in order to assist with mapping the domains from negative stain electron micrographs (Roberts *et al.*, 2009). In addition, a number of groups have attempted to build models of cytoplasmic dynein based on homology with other AAA proteins (Figure 6) (Mocz and Gibbons, 2001; Serohijus *et al.*, 2006), yet these models do not necessarily correspond well to electron microscopy images. Despite all these attempts, a clear atomic resolution structure of cytoplasmic dynein is yet to be achieved.

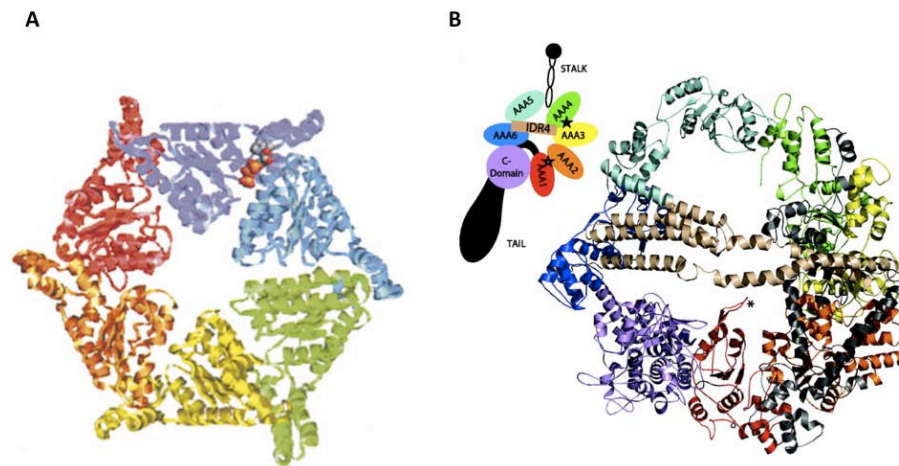


Figure 6. Computational Models of Cytoplasmic Dynein Motor Domain

(A) Structural model of cytoplasmic dynein motor domain based on sequence homology of hexameric AAA proteins proposed by Mocz and Gibbons, 2001. (B) Comparative structural homology model of cytoplasmic dynein motor domain based on crystal structures of proteins with sequence homologies of domains within motor domain proposed by Serohijus *et al.*, 2006.

1.1.2.2 Kinesin

Kinesin is another molecular motor that utilizes the energy harvested from ATP to transport cargo along MTs, but predominantly in an anterograde manner (Hirokawa *et al.*, 1991) with the exception of the Kinesin-14 family (Ambrose *et al.*, 2005). Kinesin is smaller (~ 100-200 kDa) than dynein and has very little similarity in structure, consisting of a dimer of heavy and light

chain dimers (Figure 7). The heavy chain motor domain has been previously crystallized (Kull *et al.*, 1996) whose structure is depicted as a globular protein with a P-loop motif that is capable of MT binding. A long (~ 70 nm) coiled-coil stalk facilitates dimerization and links the heavy chains to the light chains where cargos bind to kinesin (Gennerich and Vale, 2009). The kinesins consist of a relatively large family of motor proteins that vary in length and size that can be found in monomeric, dimeric, tetrameric, and heterotrimeric forms (Hirokawa, 1998), with conventional kinesin being the most abundant in the nervous system (Wagner *et al.*, 1991).

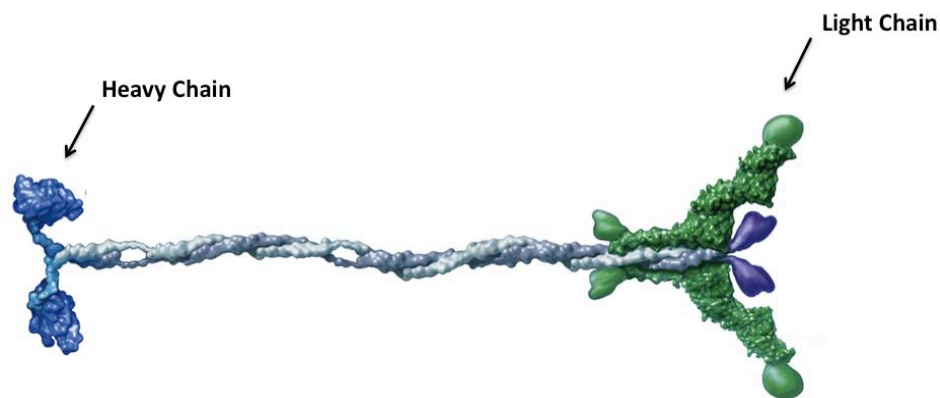


Figure 7. Structural Model of Kinesin

A cartoon model of conventional kinesin showing a pair of heavy and light chains. The heavy chain consists of a globular motor domain that binds and hydrolyzes ATP to produce the energy needed to translocate along MTs. The heavy chain also directly binds to MTs. A long (~70 nm) coiled-coil filament connects the heavy chains to the light chains, where cargo binding takes place [adapted from Vale, 2003 with permission from publisher].

Kinesin has been shown to mediate MT-MT interactions and MT bundling (Straube *et al.*, 2006). As with dynein, kinesin transports a number of different cargos including organelles (Hirokawa, 1998), scaffolding proteins (Verhey *et al.*, 2001), the amyloid precursor protein involved in Alzheimer's disease (Kamal *et al.*, 2000), and is involved in chromosome segregation (Barton and Goldstein, 1996).

1.1.2.3 Myosin

Myosin is a large family of motor proteins that uses ATPase activity to translocate along MFs rather than MTs. Although myosin and kinesin do not share any sequence homology, their structures are very similar (Kull *et al.*, 1996) based on crystal structures of the motor or head domain. Similar to kinesin, ATP binding and hydrolysis occur at the motor domain and the motor domain directly interacts with microfilaments. In addition, myosin has a coiled-coil filament, termed the light chain, which mainly dimerizes two heavy chains and also directly binds to various cellular targets (Figure 8). Myosin translocation is generally directed towards the plus (+) end of actin filaments with the exception of myosin VI, which uniquely translocates towards the minus (-) end of actin filaments (Rodriguez and Cheney, 2000).

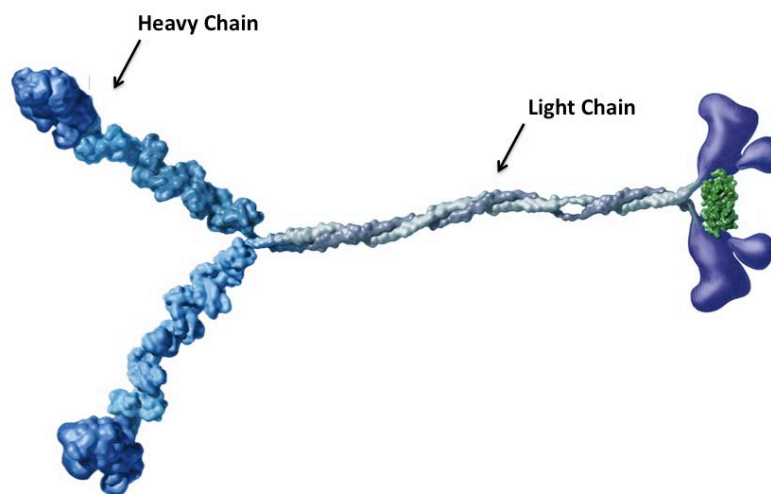


Figure 8. Structural Model of Myosin

A cartoon model of myosin showing a pair of heavy, light-intermediate, intermediate, and light chains. The heavy chain consists of a central ring motor domain with a protruding coiled-coil stalk that leads to a MT binding domain. The heavy chain also possesses a stalk domain that interacts with the other chains of cytoplasmic domain [adapted from Vale, 2003 with permission from publisher].

Myosin, along with MFs, is responsible for important processes involved at the leading edge of migrating cells (Chibalina *et al.*, 2009). Myosin is also responsible for vesicle transport and signal transduction (Mermall *et al.*, 1998), golgi transport (Ikonen *et al.*, 1997), and is

believed to play a role in cytokinesis following mitotic spindle signaling events (Matsumura, 2005). Myosin also transports mitochondria in axons, but there is evidence that mitochondria are also transported bidirectionally along MTs through interactions with both kinesin and dynein (Hollenbeck and Saxton, 2005).

1.2 SIGNIFICANCE

1.2.1 Microtubule Perturbing Agents as Cancer Therapeutics

With MTs playing an important role in cell structure and function, it is not surprising that defects in MT organization are associated with diseases such as the increased MT dynamics observed in cancer cells (Jordan and Wilson, 2004). There are many MT-stabilizing and -destabilizing drugs that have been demonstrated to suppress cancer growth and cause cell death (Jordan and Wilson, 2004). For example, paclitaxel (PTX; Taxol[®]) (Figure 9), a known natural product derived from the bark of Pacific yew (*Taxus brevifolia*) trees, is commonly used in the clinic to treat solid tumors (Rowinsky and Donehower, 1995) and has been demonstrated to stabilize MTs (Kumar, 1981), even in the absence of GTP (Howard and Timasheff, 1998). Other drugs used to treat cancer include the MT stabilizer epothilone B (Hamel, 2003), while other products such as dolastatin 10 (Hamel, 1992) and colchicine (Bhattacharyya, 2008) have a negative effect on MTs by destabilizing their formation. As many of the current anticancer drugs have undesired toxicities, and/or cancer cells may become resistant to such drugs by increasing expression of multidrug resistance-associated proteins (Drukman and Kavallaris, 2002; Kavallaris, 2010), it is, therefore, critical to screen for other agents and mixtures of agents that perturb MTs, but with

fewer undesired toxicities. The structural changes that take place upon binding of MT-perturbing agents to tubulin vary with the type and location of tubulin binding (Sackett, 1995). An important step towards understanding the mechanism of such compounds depends on detecting the structural changes that take place upon binding.

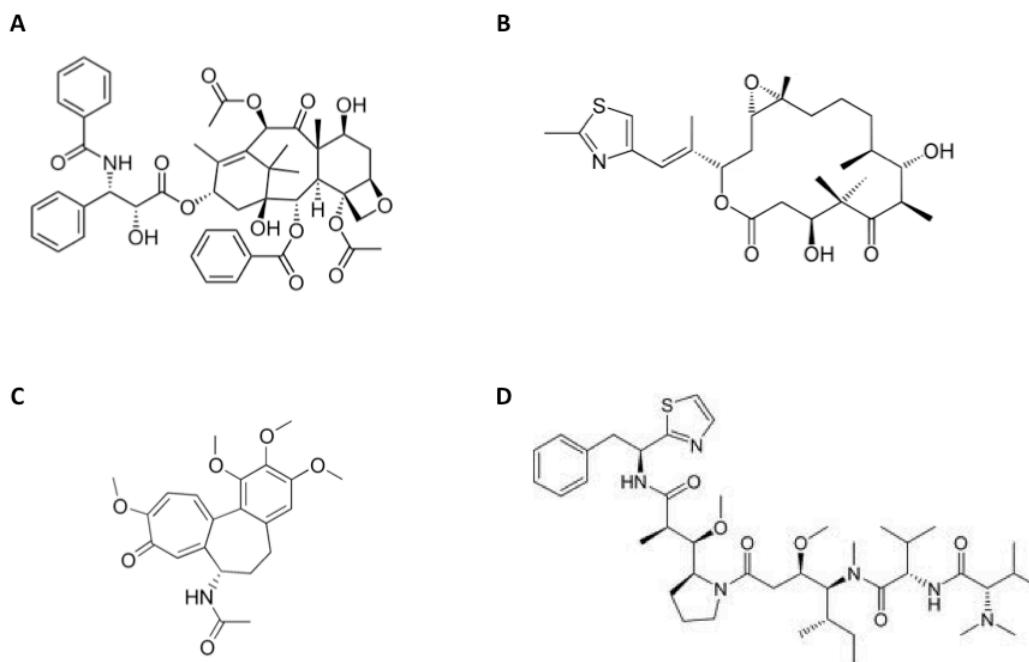


Figure 9. Chemical Structures of Microtubule Perturbing Agents

(A) Paclitaxel, a MT stabilizer. (B) Epothilone B, a MT stabilizer. (C) Colchicine, a MT destabilizer. (D) Dolastatin 10, a MT destabilizer.

1.2.2 Potential use of Dynein Activators/Inhibitors

Through interactions with the intermediate chains, immunophilins link important cargo, such as the tumor suppressor p53, to the Hsp90 chaperone complex and bind to cytoplasmic dynein (Galigniana *et al.*, 2004). Dynein then translocates the attached cargo to the nucleus where the tumor suppressor p53 transcriptional factor can activate genes in response to DNA damage (Liu and Kulesz-Martin, 2001). Cytoplasmic dynein also contributes to many important cellular

functions such as providing the force needed in nuclear envelope breakdown (Salina *et al.*, 2002), chromosome segregation (Sharp *et al.*, 2000), mitotic spindle formation (Vaisberg *et al.*, 1993), and cytokinesis (Yeh *et al.*, 1995).

Increased expression of cytoplasmic dynein light chain 1 has been associated with the acceleration of the G1/S transition and breast tumorigenesis (den Hollander and Kumar, 2006; Vadlamudi *et al.*, 2004). Additional information suggests that the cytoplasmic dynein light chain is a co-activator for estrogen receptor (ER) transactivation in breast cancer cells (Rayala *et al.*, 2005). Since cytoplasmic dynein's light chain 1 associates with the heavy chain 1 motor domain along with the apparent role of the light chain in breast cancer, inhibiting the motor domain can be a potential target for anti-cancer drugs. Similarly, there have been implications in the literature that motor protein inhibitors such as monastrol, which inhibits kinesin motor activity, can be used to target and kill cancer cells (Wacker and Kapoor, 2010).

Moreover, defects in cytoplasmic dynein have implications in neurodegenerative diseases. Lissencephaly, a devastating neurological disorder characterized by decreased brain folds and the development of smaller than usual brain sizes (Wynshaw-Boris and Gambello, 2001), like several other neuronal disorders, is associated with malfunctions in neuronal migration (Mesngon *et al.*, 2009). A number of genetic studies have pointed to the *LIS1* gene as the cause for lissencephaly as well as other neuronal migration disorders (Smith *et al.*, 2000). LIS1 is believed to associate with and regulate the function of cytoplasmic dynein in neuronal movement (Smith *et al.*, 2000). Other disorders such as amyotrophic lateral sclerosis (ALS) and spinal muscle atrophy are also associated with deterioration of motor neurons, which disrupts axonal retrograde transport mediated by dynein, while mutations in dynein or dynactin exhibit similar phenotypic characteristics as the abovementioned disorders (Bartlett *et al.*, 1998;

LaMonte *et al.*, 2002; Ateh *et al.*, 2008; Banks and Fisher, 2008). This highlights the importance of targeting cytoplasmic dynein with chemical biology tools (inhibitors and activators) to study the mechanism of neurodegenerative diseases associated with neuronal motor function. With cytoplasmic dynein's apparent role in neuronal migration and neurological disorders, it is important to understand the structure of cytoplasmic dynein and how conformational changes effect its mechanism of action.

To date, there are only a handful of small molecules that target cytoplasmic dynein, most of which are either ATP/transition state mimics (e.g., EHNA, AMP-PNP, orthovanadate) (Bouchard *et al.*, 1981; Vallee and Shpetner, 1990) or sulfhydryl-reactive agents (e.g., thiourea and *N*-ethylmaleimide (NEM)) (Blum *et al.*, 1979; Vallee and Shpetner, 1990) (Figure 10). The Day lab previously examined purealin, a natural product derived from the sea sponge *Psammaphysilla purea*, that has been shown enhance the ATPase activity of myosin (Takito *et al.*, 1986) while also inhibiting the ATPase activity of axonemal dynein (Fang *et al.*, 1997). Synthetic analogues of purealin inhibited the ATPase activity of rat cytoplasmic dynein heavy chain 1 (Zhu *et al.*, 2006). Although purealin itself was a potent inhibitor of cytoplasmic dynein heavy chain *in vitro*, the compound was unable to do so in cells. Purealin as well as other compounds that have been recently screened in the Day lab are of specific interest because they are not ATP mimics and do not compete with ATP binding to the dynein motor. This is important because such uncompetitive inhibitors (Nelson and Cox, 2005) can potentially increase the specificity of targeting only cytoplasmic dynein rather than inhibiting other important ATP-dependent proteins such as those from the Hsp family (Rowlands *et al.*, 2004). Understanding how purealin and other agents inhibit cytoplasmic dynein's motor activity is an important step towards identifying other more selective inhibitors. Because of the many important roles in

which cytoplasmic dynein participates, small molecule inhibitors of dynein could be useful as chemical and cell biology tools.

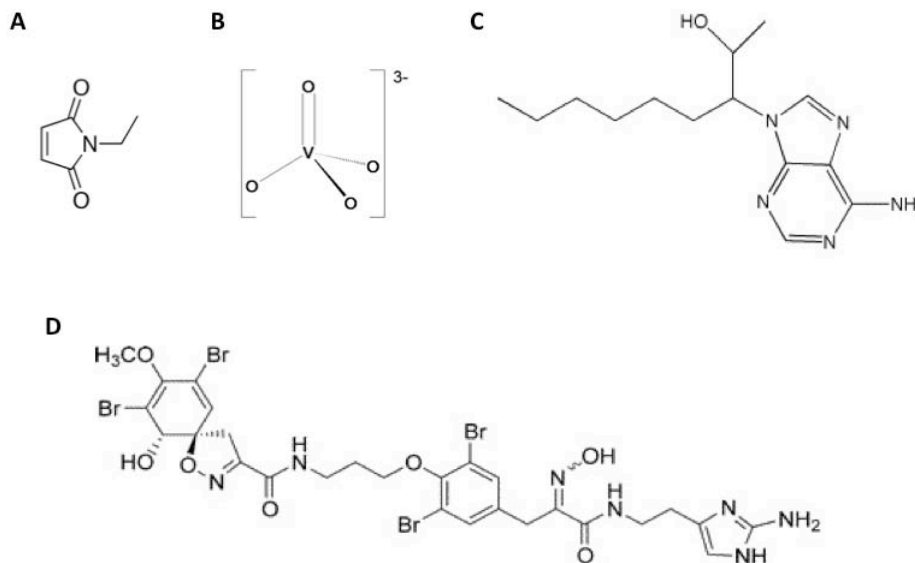


Figure 10. Chemical Structures of Cytoplasmic Dynein Inhibitors

(A) *N*-Ethylmaleimide (NEM), a sulfhydryl reactive reagent. (B) Orthovanadate, a phosphate analog. (C) *erythro*-9-(2-Hydroxy-3-nonyl)adenine (EHNA), an ATP mimetic. (D) Purealin, a natural product derived from the sea sponge *Psammaphysilla porea* known to enhance the ATPase activity of myosin, while also inhibiting both axonemal and cytoplasmic dynein *in vitro*.

1.3 BIOPHYSICAL TOOLS

Understanding the particular role of a given protein and how it relates to disease is an important step in treating the disease. Identifying the structure of a protein is one of the most important steps at understanding the function, followed by a number of biochemical assays. Many biophysical techniques have been used extensively to elucidate the structures of macromolecules. Here I will discuss the basic principles behind some of the techniques used to shed light towards the structure and function of cytoplasmic dynein heavy chain 1.

1.3.1 Computational Modeling

A large part of understanding the roles and functions of biological systems involves visualizing the molecular interactions that take place between proteins. More recently, advances in biophysical techniques has allowed for greater resolution of data collected, along with the assistance and supplementation of computational modeling and data fitting. Since experimental techniques often have limitations, most commonly due to size constraints, computational modeling can assist with the prediction of three-dimensional protein structures. Computational prediction is particularly useful in generating comparative homology models of a protein with unknown experimental structure by comparison with known structures of proteins of shared sequence homology. There are several computer programs and web servers that use different algorithms to generate such data. For example, MODELLER is a program used for comparative homology modeling that, like many other programs, follows four main steps: fold assignment, target-template alignment, model building, and model evaluation (Marti-Renom, 2000). Comparative homology modeling begins by searching protein data bank (PDB) structures of proteins with high sequence homology (template) to the protein sequence of interest (target). Model building is based on dissecting template PDB structures into smaller conserved core regions followed by aligning and superimposing portions of the target sequence into these core structures (Blundell *et al.*, 1987) and using distance and dihedral angle restraints (Sali and Overington, 1994). Loops to connect the core domains with each other are generated by scanning a broader subset of PDB structures that connect similar core structures to each other (Topham *et al.*, 1993). Amino acid side chains are then modeled to fit their intrinsic conformation properties and based on the orientation of side chains from the template structure (Sutcliffe *et al.*, 1987). Finally, the 3D model is evaluated by the stereochemistry (bond length,

bond angle, chirality, side chain torsion angles, clashes between nonbonded pairs of atoms, etc.) based on statistical potentials of mean force profiles (Sipl, 1990). Performing a number of iterative model building and evaluation steps generally optimizes final 3D models and experimental data is often used to supplement model constraints (Eswar *et al.*, 2007).

1.3.2 Mass Spectrometry

Mass spectrometry (MS) is an analytical tool that is used to decipher the composition of chemicals and peptides. The technique is often associated with genomic and proteomic mapping, but has applications in structural biology and drug discovery. The principle behind MS involves detecting the mass-to-charge (m/z) ratio of chemical fragments of the molecule of interest. Chemical fragmentation can be in-source or performed during sample preparation. The combination of both can often lead to higher confidence in chemical composition determination. There are several methods used to detect molecular fragments. Native or digested protein samples are typically ionized by electrospray ionization (ESI) or matrix-assisted laser desorption ionization (MALDI). Time-of-flight (TOF) mass detection is achieved by applying a given potential energy from an electric field source to ionized samples. The ions acquire a kinetic energy that causes the ions to drift in a field-free tube with distance D to a detector,

$$zeEs = \frac{1}{2}mv^2 \quad (1)$$

where ze is the charge of multiple electrons, E is the electric field, s is the length of the source region, m is the mass, and v is the velocity of ions. The m/z is calculated by measuring the time t it takes ions to reach the detector

$$\frac{m}{z} = 2eEs \left(\frac{t}{D} \right)^2 \quad (2)$$

with heavier ions reaching the detector later than lighter ions (van Holde *et al.*, 2006).

Quadrupole mass analyzers are used to filter ions based on their m/z by selectively allowing ions to pass through an electric field produced by four parallel electrodes. A static positive potential is applied to two opposing electrodes, while a static negative potential is applied along the other opposing electrodes to concentrate ions towards the central axis of the quadrupole. In addition, an alternating potential is superimposed onto each of these static potentials that will defocus ions based on their inertia (mass), therefore causing these ions to collide with the electrodes and restrict the ions from reaching the detector. Each pair of electrodes will either selectively remove small or large ions based on their respective charges and the potential of the electrodes; electrodes with positive potential will act as a low mass filter to a stream of positive ions, while the electrodes with negative potential will act as a high mass filter. The frequency of alternating current can be scanned to generate a mass spectrum of a mixture of ions to detect a range of m/z values (van Holde *et al.*, 2006).

Additionally, the m/z of ions can be determined by the cyclotron frequency of the ions in a fixed magnetic field. This method is known as Fourier transform ion cyclotron resonance mass spectrometers (FT-ICR-MS) and often further abbreviated as (FTMS). A moving ion with charge q and with velocity v in a uniform magnetic field B will exhibit a force known as the Lorentz force.

$$\vec{F} = m\vec{a} = q\vec{v} \times \vec{B} \quad (3)$$

The magnetic field will cause the ion to move in a circular motion with angular frequency ω_c (in rad/s) known as the ion cyclotron frequency. Ions are then excited by applying an electric field oscillating at or near the cyclotron frequency of ions of a particular m/z value.

$$\omega_c = \frac{qB}{m} \quad (4)$$

Unlike most MS techniques, FTMS does not directly detect m/z , but rather measures the frequency of ion rotation and the m/z is extrapolated by applying a Fourier transform to the current signal produced by the rotating ions. Since frequency can be measured much more accurately than other parameters, m/z measurements by FTMS have higher resolution and mass accuracy than any other type of mass measurement (Marshall *et al.*, 1998). Because of its high resolution and mass accuracy, FTMS has seen a large interest in metabolic profiling and identification (Ohta *et al.*, 2010), hydrogen/deuterium (H/D) exchange (Sperry *et al.*, 2008), top-down proteomics (Ryan *et al.*, 2010) and a number of other MS applications.

More recently, the Orbitrap mass analyzer was introduced to the proteomics field offering similar high resolution and mass accuracy as FTMS but with smaller and less expensive instrumentation (Makarov, 2000; Hardman and Makarov, 2003). The trap consists of a barrel-like geometry with an axial central electrode that creates a unique electric field. This field traps ions and causes them to both rotate around and oscillate along the axial electrode with a harmonic oscillation. Mass-to-charge values are deduced from the current image obtained from the frequency of harmonic oscillations along the axial electrode by applying a Fourier transformation exactly as performed with FTMS (Hu *et al.*, 2005).

1.3.3 Electron Microscopy

Conventional biophysical methods such as nuclear magnetic resonance (NMR) and X-ray crystallography can be instrumental in elucidating the structure and dynamics of proteins to help better understand the function of the given protein. Investigation of large proteins or protein complexes is often hindered, however, due to the size limitations of these techniques. With the advancement of electron microscopy (EM) instrumentation, data collection and processing in the past several decades, EM can be a powerful tool that bridges the size gap of several orders of magnitude between X-ray crystallography and light microscopy. The greater resolution obtained by EM than light microscopy is owed to the significantly small de Broglie wavelengths of the fast electrons used compared to the wavelength of light (Wischnitzer, 1970). EM is particularly useful in structural biology because it allows visualization of large macromolecule structures without the need to crystallize samples and with minimal quantity.

Analogous to basic light microscopy (LM), EM is composed of an illuminating system, an optical system, and a recording system to directly view the object. The illuminating system relies on a beam of electrons produced by thermionic or field electron emission, which is then magnified and focused by magnetic lenses to a single focal point. This highly focused electron beam then transmits through and interacts with an ultra thin sample, scattering some electrons in the process. An image is produced by the diffraction of electrons with the sample viewed on a fluorescent screen, charge-coupled detector (CCD), or film (Wischnitzer, 1970, Frank, 1996). Because scattering of the electron beam is dependent on sample density, heavy metal salt solutions such as uranyl acetate are used as staining solutions to increase the differential scattering of the electron beam, thereby improving image contrast (Watson, 1958).

Similar to X-ray crystallography, which averages the diffraction pattern of many particles organized in the unit cell of a crystal by translational repetition, EM analysis requires averaging thousands of individual images to generate structures with high resolution. The many images are aligned to produce a 2D average of the projected object (Frank, 1996). EM also captures several different conformation classifications during this process and by using the Euler angle of each 2D average of the sample, a three-dimensional reconstruction is generated of the object (Crowther *et al.*, 1970; Mio *et al.*, 2010)

Although negative staining is advantageous for protecting the sample from radiation damage and increasing image contrast, negative staining techniques can also cause distortion to the original structure through sample dehydration and denaturation (Bremer, 1992). By rapidly freezing samples in a vitreous state (cryoEM), samples may be preserved in a more natural state but with lower image contrast (Stahlberg and Walz, 2008). The combination of negative stain and cryo- EM has afforded investigators the opportunity to reach near atomic resolution of large macromolecules and are capable of distinguishing secondary structures such as alpha helices (Conway *et al.*, 1997; Zhang *et al.*, 2008; Cheng and Walz, 2009).

1.3.4 Optical Biosensors

(Taken verbatim from Daghestani, H.N.; Day, B.W. Theory and applications of surface plasmon resonance, resonant mirror, resonant waveguide grating, and dual polarization interferometry biosensors. Sensors, 2010, 10, 9630-9646)

Biosensors are useful tools for research in areas of biophysics and pharmaceutical sciences. The obvious advantage biosensors offer over many other biophysical techniques is that it is label-free, eliminating the need for fluorescent, chemical, or radiolabeled tags. In addition, biosensor technologies are relatively easy to use and offer real-time data collection so that different

biochemical interactions can be monitored. Biosensors have several applications for illuminating explanations to questions arising from the study of macromolecular interactions (Lillis *et al.*, 2006) and the binding of small molecules to surfaces with immobilized biological molecules (Cooper, 2002; Karlsson, 2004; Boozer *et al.*, 2006). The types of biosensor arrangements vary greatly and have been previously reviewed. Examples of biosensor types include electrochemical (Wang, 2008; Ronkainen *et al.*, 2010), carbon nanotube field effect (Allen *et al.*, 2007; Liu *et al.*, 2009), and optical (Fan *et al.*, 2008). Within each of these individual types, there are many variations in the instrument designs.

1.3.4.1 Surface Plasmon Resonance

Surface plasmon resonance (SPR) was first demonstrated by Otto in 1968 (Otto, 1968), but was not made commercially available for biomolecular interaction applications until the fall of 1990 by BiaCore (GE Healthcare) (Owens, 1997). As a starting point, we will consider surface plasmon polaritons (SPP), which are electromagnetic modes or oscillations arising from the interaction of light with mobile surface charges in a metal (typically gold or silver) (Otto, 1968). SPPs are transverse magnetic (TM) waves that propagate along the interface between materials with negative and positive permittivities (e.g., a metal/dielectric layer). According to the Drude model, the dispersion relation (β) of an SPP, which basically correlates the relationship between the wavevector along the interface and the angular frequency ω , can be described by Eq. 5:

$$\beta = \frac{\omega}{c} \sqrt{\frac{\epsilon_m \epsilon_d}{\epsilon_m + \epsilon_d}} \quad (5)$$

where c is the speed of light in a vacuum, while ϵ_m and ϵ_d are the permittivity of a metal and a dielectric material, respectively. The real part of Eq. 5 determines the SPP wavelength, while the

imaginary part determines the propagation length of the SPP along the interface, which is responsible for the evanescent field. Although the electromagnetic field of an SPP decays evanescently into both the metal and dielectric medium, the majority of the field is present in the dielectric medium due to increased damping in the metal (Figure 11) (Novotny and Hecht, 2006). As a result, the real part of the dispersion function is very sensitive and changes proportionally to changes in the refractive index (Homola, 2003). The principle of SPR, however, only occurs when the light's wavevector component parallel to the metal surface matches that of the SPP. This condition is only satisfied at distinct angles of incidence, appearing as a drop in the reflectivity of incident light (Novotny and Hecht, 2006). SPR biosensing relies on the principle that any changes on the dielectric sensing surface will correspond to a shift in the angle of reflectivity, followed by a detector, in order to satisfy the resonance condition (Figure 12).

After Otto demonstrated the ability to excite SPPs with his proposed configuration, a number of other configurations followed suit including prism coupling (Kretschmann configuration; also referred to as attenuated total reflection (ATR)) (Kretschmann, 1971), waveguide coupling (Harris and Wilkinson, 1995), grating coupling (Yu *et al.*, 2004), and fiber optic coupling (Marazuela and Moreno-Bondi, 2002). In the case of the Kretschmann configuration, incident light passes through a prism with a high index of refraction causing the light to internally reflect at the metal/prism boundary. The total internal reflection creates an evanescent wave that penetrates the thin metal layer and propagates along the metal/prism interface. The angle of incident light is varied in order to match the evanescent wave propagation rate with the propagation rate of the SPP (Kretschmann, 1971). Grating coupling may also be used to excite SPPs by stimulating a periodic metal diffraction layer with incident light so that the propagation constant also matches that of the metal/dielectric surface (Homola, 2003; Yu *et*

al., 2004). Waveguide coupling relies on exciting SPPs when the guided light and the SPPs are phase matched (Homola *et al.*, 1997).

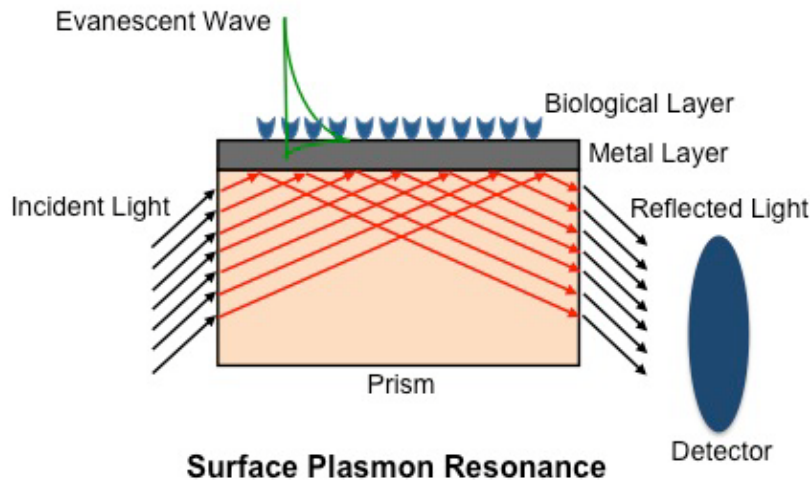


Figure 11. Schematic of a Surface Plasmon Resonance Biosensor

Kretschmann configuration of an SPR biosensor. Light reflected from a prism induces an evanescent field in both the metal and dielectric (biological) layer, with the field being greater in the latter. Light is then reflected out of the prism and a detector records the angle at which resonance is satisfied.

Regardless of the configuration, environmental changes in the dielectric medium cause an alteration to the phase, amplitude, polarization or spectral distribution of the incident light, which can be attributed to changes in the propagation constant and, hence, changes in the refractive index are detected in real time. Piliarik and Homola (2009) recently presented a theoretical analysis evaluating the sensitivity of SPR detection, suggesting that many of the current systems, regardless of their instrumental arrangement, very nearly approach their theoretical limits.

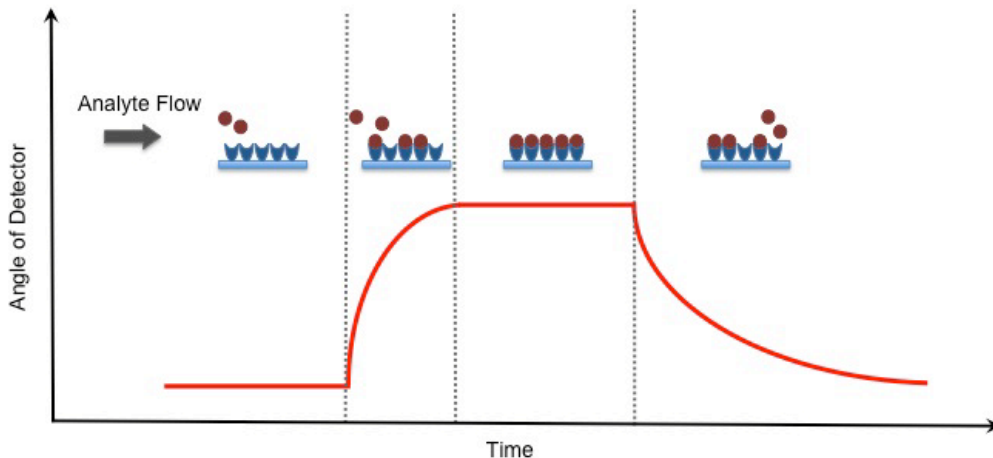


Figure 12. Detection of Binding Events with an SPR Biosensor

As analyte begins to flow over the sensing layer and binds to substrate, the angle of reflectivity that satisfies the resonance condition will change accordingly until it reaches saturation and all the binding sites have been occupied. The dissociation of analyte from the substrate causes the angle of the detector to return back to baseline once all the analyte has been completely removed.

The most common use for SPR sensing is to evaluate protein-ligand (Jung *et al.*, 2000), protein-protein (Karlsson and Falt, 1997), or nucleotide hybridization (Moon *et al.*, 2010) events. Since it is typically not advantageous to directly deposit biological molecules onto surfaces, especially surfaces of inert metals such as silver or gold, surface functionalization can create a more functionally active environment and reduce non-specific binding on the surface. Advancements in surface chemistry have allowed researchers to easily customize a sensing surface to their particular needs. One of the most commonly used surfaces includes those prepared through amine chemistry, such as *N*-hydroxysuccinimide (NHS)-derivatized surfaces (Johnsson *et al.*, 1991; Macbeath and Schreiber, 2000; Rusmini *et al.*, 2007) that nonspecifically bind to the nucleophilic amino groups of peptides and proteins. Similarly, maleimide and other thiol-reactive groups (Lee *et al.*, 2005; Rusmini *et al.*, 2007) are useful for binding proteins containing surface reactive cysteines. Pegylation (polyethyleneglycol) (Lu *et al.*, 2000; Rusmini *et al.*, 2007) is another functionalization method that is often used in biosensor applications.

Additionally, surfaces have also been mimicked to resemble lipid bilayers for studies involving membrane proteins (Fang *et al.*, 2002; Taylor *et al.*, 2009). Protein-carbohydrate interactions can also be monitored by glycan-modified surfaces (Feizi *et al.*, 2003; Wang, 2003). By taking advantage of the extremely strong affinity of biotin for avidin or streptavidin, biotinylated surfaces (Nidumolu *et al.*, 2006) can be particularly useful for capturing labeled proteins, as we have recently demonstrated (Daghestani *et al.*, 2009). Nickel nitrilotriacetic acid (Ni-NTA)-derivatized surfaces (Zhu *et al.*, 2001; Wegner *et al.*, 2003) are also convenient for specific capturing of proteins that have been genetically engineered with an N- or C-terminal polyhistidine tag, a common affinity moiety used during protein expression and purification processes.

High contrast SPR microscopy or imaging was first described by Rothenhausler and Knoll (1988) and was seen as a method to increase the throughput of standard SPR biosensors (Jordan *et al.*, 1997; Bassil *et al.*, 2003; Shumaker-Parry *et al.*, 2004), but suffered from reduced sensitivity compared to conventional SPR. Advances in microfabrication and micromachining techniques have assisted in the development of lab-on-chip sensors with better sensitivity and greater numbers of sample chambers within a single chip. These advancements have played a role in SPR imaging developments for high throughput biosensor screening. Piliarik *et al.* (2005) developed a more sensitive SPR imaging sensor that combines polarization contrast and special SPR multilayer structures capable of screening 108 samples simultaneously at a concentration as low as 500 ng/mL and with minimal crosstalk between chambers. A chip proposed by Ouellet *et al.* (2010) demonstrated the ability to simultaneously monitor multiple ligands against different analytes and at different concentrations by using a parallel 264-microarray chamber with the aid of a high resolution CCD camera. In addition to the increased

number of events detected, the microfluidics was designed for small reaction volumes (as low as 700 pL), reducing unnecessary sample consumption. The authors also demonstrated the ability to recover samples after SPR measurements with minimal cross-contamination.

In recent years, the information obtained from SPR has also been used to complement the information obtained from MS, providing both quantitative and qualitative information (Krone *et al.*, 1997). The combined use of SPR and MS can be used for functional proteomic screening, identifying protein-protein interactions and further characterizing domains involved in the interactions (Buijs and Franklin, 2005; Ohman *et al.*, 2008). This technique can also be used for screening of a number of toxins for their ability to bind a particular ligand, followed by MS analysis to determine the chemical composition of the small molecules (Nedelkov *et al.*, 2000; Nedelkov and Nelson, 2003). Another application involves searching for and characterizing enzyme inhibitors (Borch and Roepstorff, 2004). Some investigators have attempted to elute samples off of and collect samples directly from the sensor and then analyze the eluates by MALDI-TOF-MS (Nelson *et al.*, 1997; Sonksen *et al.*, 1998). Without taking strenuous care, such sample transfer techniques can lead to a great amount of sample loss between steps and can be very time consuming unless more efficient techniques, such as the chip proposed by Ouellet *et al.* (2010), can be put into such practice. Other ways to minimize sample losses include applying MALDI matrix directly onto the sample sensor, which is then physically secured onto a MALDI target to analyze samples directly without an elution step. This technique, however, is destructive to the sample chip and introduces sources of error since not all chips are identical in terms of thickness ($\Delta\text{thickness} = \Delta\text{distance from the MALDI-TOF-MS ion detector}$, and therefore ΔTOF). Natsume *et al.* (2000) showed it possible to collect the samples used in a BiaCore SPR instrument by trapping the sample into a reverse-phase (RP) capillary column

placed in tandem after the sample sensor. In Natsume *et al.*'s configuration, once the desired measurements were obtained from the SPR, the sample flow was started so that buffer eluted the sample from the sensor chamber into the RP capillary column. After the sample was collected on the RP capillary column, the column was transferred to a liquid chromatography system to separate sample constituents followed by ESI-MS analysis (Natsume *et al.*, 2000). It is not feasible to flow samples from an SPR sensor directly to a MS because salts and stabilizers that are present in buffers can often wreak havoc on an ESI-MS system by damaging the ESI needle and decrease the quality of the MS spectra (by, e.g., diluting signals across several adduct species, ion suppression, and increasing the noise-to-signal ratio) (Annesley, 2003). An alternative method is to use an ultra-rapid desalting technique consisting of a microchannel laminar flow device connected online with an ESI-MS (Wilson and Konermann *et al.*, 2005). From these examples, it is evident that combining biosensors with MS offers a promising future at providing immediate structural and behavioral information about potential biologically important agents (therapeutics, toxins, etc.) in a relatively short period with minimal sample loss.

1.3.4.2 Resonant Mirror Biosensor

The resonant mirror (RM) setup is a leaky waveguide structure that first became commercially available as IAsys in 1993 by Fisons Applied Sensor Technologies (Owen, 1997). Although the commercial availability of this instrument was recently discontinued, it is still important to note its application and contribution to the field. The RM configuration is similar to SPR's Kretschmann configuration, but differs in that RM relies on coupling of incident light through a prism with a high-index dielectric layer, rather than a metal surface (Figure 13). This replacement combines the simple structure of SPR systems with the enhanced sensitivity of waveguide structures to produce sharper resonance peaks than SPR (Lukosz, 1991), thereby

increasing the sensitivity of the technique. As light passes through the prism to a low-index medium, it couples with the high-index resonant layer, thereby allowing total internal reflection to occur at the boundary of the sensing layer. Similar to SPR, resonance only occurs when the angle of the incident light and the resonant modes in the high-index layer are phase-matched, resulting in strong reflection at the output. Any change in the refractive index of the biological layer at the surface corresponds to a change in the angle of light that satisfies this resonance condition (Nellen and Lukosz, 1991; Cush *et al.*, 1993). Although the waveguide structure of the RM allows for both TM and transverse electric (TE) resonances (with different angles) to occur, generally only one is physically measured since TM and TE modes diverge when adjusting the thickness of the resonant structure for optimal sensitivity (Cush *et al.*, 1993).

Identical to SPR, RM has been used to monitor many different molecular interactions of macromolecules (Buckle *et al.*, 1993; Duchesne *et al.*, 2006; Benadie *et al.*, 2008; Lemmer *et al.*, 2009) and has parallel capabilities in terms of surface modifications. The cuvette structure of the RM biosensor, however, provides an advantage over flow through microfluidic systems commonly used in SPR when sample conservation is imperative. Use of a stirring bar in the cuvette is also helpful since the constant mixing limits mass transport effects (Owen, 1997).

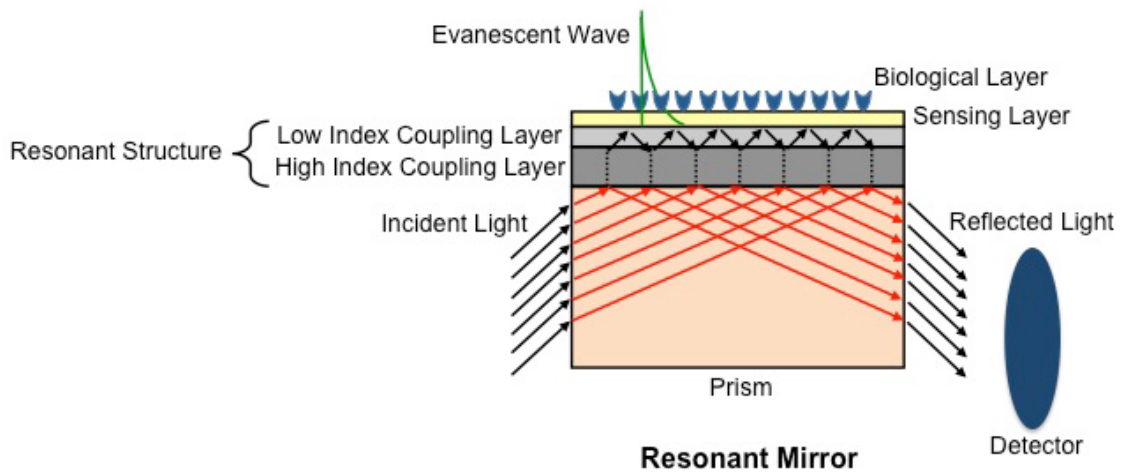


Figure 13. Schematic of a Resonant Mirror Biosensor

Light reflected from a prism is coupled to a resonant structure (low and high index coupling layers) to produce an evanescent wave at the sensing surface. Light is then reflected out of the prism and a detector records the angle at which resonance is satisfied.

1.3.4.3 Resonant Waveguide Grating Biosensor

Although diffraction grating was a phenomenon described over a century ago (Wood, 1902), its application in sensing was not employed until the early 1980's when Tiefenthaler and Lukosz applied grating couplers for gas (1985) and chemical (1989) sensing. In 2002, Cunningham *et al.* (2002) demonstrated the use of a resonant diffractive grating surface to monitor biochemical binding events, which was commercialized as BIND[®] by SRU Biosystems. The resonant waveguide grating (RWG) biosensor is also based on a leaky mode waveguide structure. A subwavelength structured surface is introduced by sandwiching a two-dimensional grating between a substrate and a cover layer that fills the gaps between the gratings, which in turn creates a waveguide when the effective index of refraction of the grating is greater than the substrate or the cover (Cunningham *et al.*, 2002). Incident light, from either side of the grating (Teifenthaler and Lukosz, 1989), propagates through and couples into the waveguide by means of the grating, resulting in a narrowband of reflected or transmitted wavelengths detected as the

output (Figure 14) (Cunningham *et al.*, 2004). Similar to SPR and RM, any change in the biological or sensing layer will cause a change in the reflected or transmitted wavelength (Cunningham *et al.*, 2000; Fang, 2007). Corning Inc., has also introduced its Epic[®] version of the RWG biosensor and both companies have made modifications to their original designs to increase sensitivity and by offering 96-, 384-, and 1536-well plates suitable for high throughput screening (Cunningham *et al.*, 2004; Fang, 2010a). Others have performed theoretical analyses on RWG structures to optimize the design and fabrication of grating structures in an attempt to improve sensitivity (Yih *et al.*, 2006). RWG biosensors are capable of monitoring the binding of small molecules to proteins (Cunningham *et al.*, 2002; Lin *et al.*, 2002; Li *et al.*, 2004) as with SPR and RM, but have most notably been used to monitor mass redistribution of proteins and organelles of live cells upon treatment with test agents (Fang *et al.*, 2006; Fang, 2007; Xi *et al.*, 2008; Fang *et al.*, 2008; Fang *et al.*, 2010b). Changes in cell adhesion and extracellular matrix components play an important role in cell development and migration and it is evident that certain changes in cell adhesion also contribute to a number of diseases (Parsons *et al.*, 2010). The ability of RWG biosensors to monitor changes of cell adhesion of live cells in real time make it an attractive tool in drug discovery. A drawback of evaluating cells with biosensors arises due to the large size of cells (several microns) and the limited penetration depth of an evanescent wave (~100 nm), results can be misleading since observations are only made to a limited portion of the cell (Fang *et al.*, 2006).

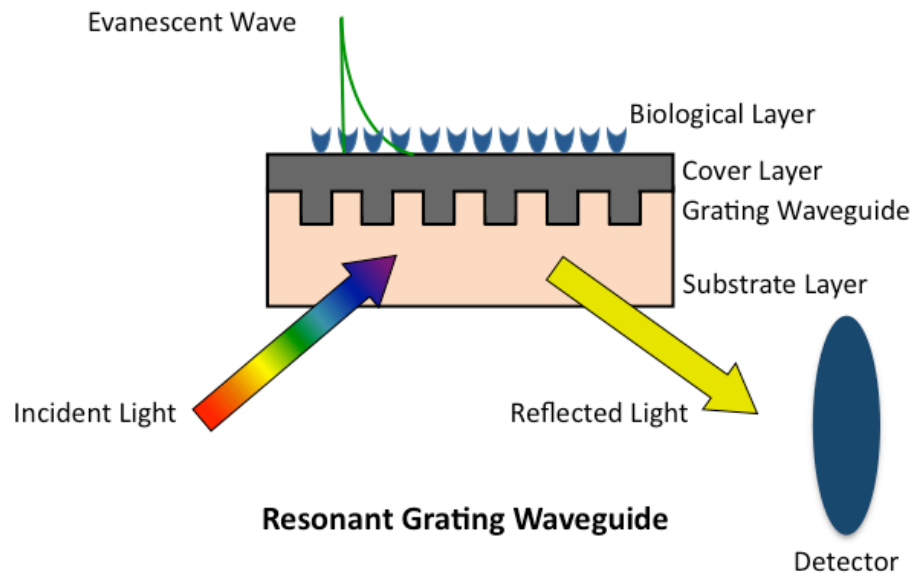


Figure 14. Schematic of a Resonant Grating Waveguide Biosensor

Broadband light is incident from either the substrate or cover layer side of the structure, which then diffracts and couples into the grating waveguide structure. A detector records the wavelength of the narrowband light reflected at which resonance is satisfied.

1.3.4.4 Dual Polarization Interferometry Biosensor

Dual polarization interferometry (DPI) is another evanescent technique that has seen a large increase in interest by the scientific community over the past decade since the technique was first commercialized in 2000 by Farfield Group, Ltd. DPI utilizes a waveguide structure that consists of a stack of dielectric layers with reference and sensing layers separated by a layer of cladding that mimics Young's 2-slit experiment in optics (Cross *et al.*, 2004). A top dielectric layer is etched to reveal the sensing layer so that two separate channels can be present on a single sensor chip (Figure 15). Light from a laser is passed through the sandwiched waveguide structure and an interference pattern is detected on the opposing side by a CCD camera. Any changes in refractive index that take place on the sensing layer alter the phase position of the fringes relative to the reference layer and are detected in real time,

$$\Delta\phi = kL'\Delta n_s \quad (5)$$

where $\Delta\phi$ is the change in the phase position of a fringe, k is the propagation constant, L' is the pathlength and is constant, and Δn_s is the effective change in the refractive index of the sensing waveguide (Cross *et al.*, 2004).

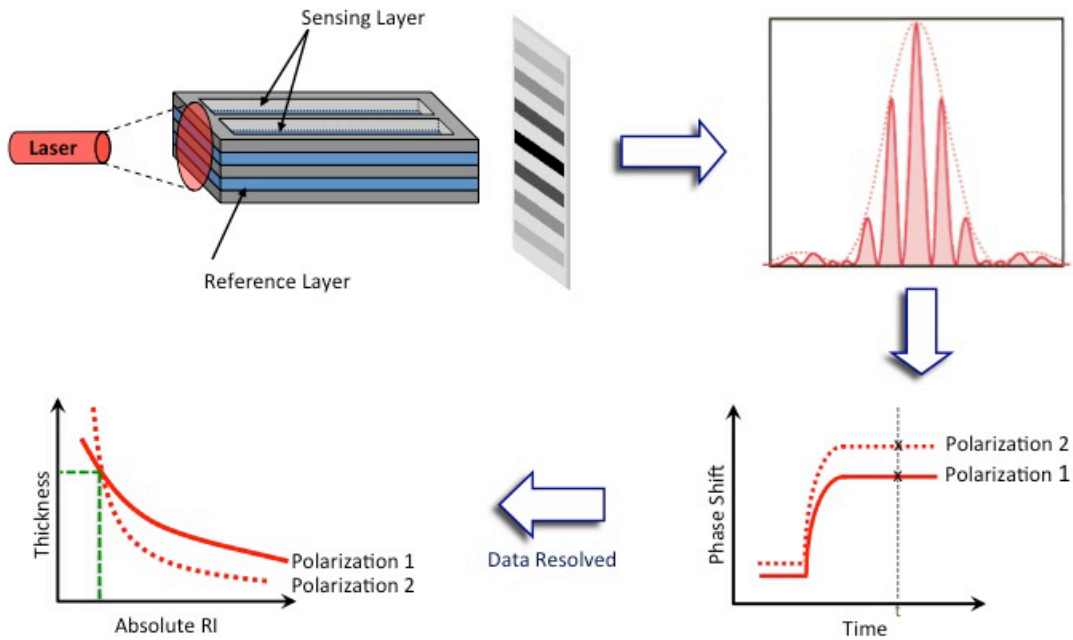


Figure 15. Schematic of a Dual Polarization Interferometer Biosensor

Schematic of a DPI sensor chip and the interference pattern produced when light is applied onto the side of a chip. The phase shift of the fringes (TM and TE) are recorded in real time and data is resolved, where only one value of thickness and absolute refractive index at any given time-point t will satisfy Maxwell's equations of electromagnetism for both TM and TE polarizations.

Unlike SPR, which utilizes only the TM mode, DPI takes advantage of measuring both the TM and TE polarizations (Swann *et al.*, 2003; Swann *et al.*, 2004; Cross *et al.*, 2004). Maxwell's equations of electromagnetism for a system of uniform multiple dielectric layers are employed to provide the absolute effective index for both the TM and TE waveguide modes determined from the refractive index and thickness of each layer from each polarization (Cross *et*

al., 2004). This ultimately gives the relationship between changes in the effective index of refraction Δn_{eff} of the waveguide in each mode and changes of thickness of the adsorbed layer t_{ad} (in nm)

$$\Delta n_{eff} = \left(\frac{\partial n_{eff}}{\partial t_{ad}} \right) \Delta t_{ad} + \left(\frac{\partial n_{eff}}{\partial n_c} \right) \Delta n_c \quad (6)$$

where Δn_c is the change in refractive index of the medium covering the waveguide (i.e., buffer) (Teifenthaler and Lukosz, 1989; Brandenburg *et al.*, 2000). Changes to the adsorbed layer will result in a change to the effective index of each mode that can satisfy a continuous distribution of thickness and refractive index values with only one unique solution that satisfies both the TM and TE modes. In addition, the molar surface coverage Γ (in $\text{nm}^2 \cdot \text{molecule}^{-1}$) can be related to the thickness of the adsorbed layer

$$\Gamma = \frac{n_{ad} - n_c}{dn_{ad}/dC} t_{ad} \quad (7)$$

where n_{ad} is the refractive index of the adsorbed layer and C is the concentration. Consequently, the density ρ (in $\text{g} \cdot \text{cm}^{-3}$) of sample on the surface can be calculated for biological samples with known molecular weight M (Cross *et al.*, 2004) since molar surface coverage can also be written as

$$\Gamma = \frac{\rho}{M} t_{ad} \quad (8)$$

The use of both polarizations to determine effective refractive index and thickness values is clearly a great advantage over SPR, RM, RWG, and other optical biosensor techniques that only report relative changes of refractive index obtained from only one polarization. Swann *et al.* (2003) proposed an elegant matrix that assists interpreting DPI data by correlating the

different parameters (thickness, density, mass coverage) calculated from both the TM and TE responses. This type of detailed information can be extremely helpful for characterizing the conformational changes of macromolecular interactions (Swann *et al.*, 2003; Thompsett and Brown, 2007; Sonesson *et al.*, 2008) and the design of surfaces for optical biosensors (Daghestani *et al.*, 2009; Popplewell *et al.*, 2009).

Before any of the above calculations are performed, each individual chip must be calibrated. Sample injections of degassed 4:1 (w/w) water-ethanol followed by deionized water are typically used to calibrate individual chips because of their known index of refractions (Cross *et al.*, 2004). One disadvantage of DPI is that an experiment must be performed continuously in order to follow the phase shift of the projected interference pattern so that thickness and refractive index values can be computed. This can hinder calibration results if a chip requires *ex situ* modification throughout an experiment. A solution to this issue, however, was recently proposed by modifying the channel so that multiple pathlengths are measured (Coffey *et al.*, 2009). With this adjustment, the number of 2π cycles of the phase shift can be determined if the chip is removed from the instrument, thereby allowing *ex situ* modification of the chip without the loss of any information.

In addition to the same applications of SPR and RM (Berney and Oliver, 2005; Ricard-Blum *et al.*, 2006), DPI has proven to be a powerful technique for characterizing structural dimensions of proteins (Lin *et al.*, 2006) and has recently been shown to be an instrumental tool for characterization of membrane/liposome structure and mimetics (Terry *et al.*, 2006; Popplewell *et al.*, 2007; Mashaghi *et al.*, 2008; Lee *et al.*, 2010). Another unique application to DPI that recently emerged is the ability to monitor early stages of protein crystallization processes by measuring light loss from the waveguide caused by changes in lateral surface

structure (Boudjemline *et al.*, 2008). Not only does this provide insights into the mechanism of protein crystallization, but also has the potential to assist crystallographers in the optimization of conditions and times required for successful protein crystallization. More recently, information from phase measurements has been supplemented by optical extinction measurements due to light absorption to provide additional information of DNA-small molecule interactions (Wang *et al.*, 2010).

It should be noted that any of the above mentioned biosensors can be used to determine the kinetics of biomolecular interactions from the rates of association k_{ass} and dissociation k_{diss} of a substrate-ligand complex by monitoring the change in response of binding as a function of time and concentration

$$\frac{d[SL]}{dt} = k_{ass}[S][L] - k_{diss}[SL] \quad (9)$$

where [S] and [L] are the concentrations of free substrate and ligand, respectively, while [SL] is the concentration of the formed complex (Dmitriev *et al.*, 2003). At equilibrium, the association of ligand to the surface can be followed by the pseudo first order equation

$$R_t = \frac{R_{max} k_{ass} [L]}{k_{ass} [L] + k_{diss}} \left(1 - e^{-(k_{ass} [L] + k_{diss})t} \right) \quad (10)$$

where R_t is the response of the detector at a given time and R_{max} is the maximal response signal upon saturation (Edwards *et al.*, 1998). Typically, experiments are performed by varying the amount of ligand added to the substrate, producing curves with different observed rate constants k_{on} . By plotting the k_{on} against the varying concentration of ligand, Eq. 11, a straight line is typically produced with a slope of k_{ass} and y-axis intercept of k_{diss} (George *et al.*, 1995).

$$k_{on} = k_{ass}[L] + k_{diss} \quad (11)$$

This information can then lead to the association K_a and dissociation K_d equilibrium constants because of the below relationship (Dmitriev *et al.*, 2003)

$$K_a = \frac{1}{K_d} = \frac{k_{ass}}{k_{diss}} \quad (12)$$

With a similar type of analysis as described above, kinetic values from second order reactions may also be calculated as previously described (George *et al.*, 1995; Edwards *et al.*, 1998).

Biosensors offer label free detection of biomolecular interactions with applications in environmental safety, bioterrorism, biomedical research and drug discovery. Several designs are capable of detecting biomolecular interactions. Surface plasmon resonance, resonant mirror, resonant waveguide grating, and dual polarization interferometry biosensors are commonly used techniques with commercial availability. SPR, being the most widely used technique in the field, has provided researchers with a wealth of information ranging from evaluation of many different biomolecular interactions to advances in sensor design. Progress in chip design has allowed for smaller sample volumes, not only to save valuable samples, but also to increase rates of the reactions by reducing diffusion distances. Advances in computer automation and the software to analyze the exquisite data that arise from the discussed methods has also played an important role in greater reproducibility and easier sample handling with all three of the biosensor types capable of employing autosamplers. Although SPR is one of the most commonly used biosensor techniques, the cuvette structure of RM offers an advantage over both SPR and DPI because of its ease of use and ability to reduce sample consumption compared to microfluidic devices. Since the IAsys system has recently been discontinued, RWG structures offered by SRU Biosystems and Corning, Inc. offer an alternative method that takes advantage of the increased sensitivity of a waveguide structure in addition to the high throughput applicability from the

multi-well plates available. On the other hand, DPI offers a unique avenue of monitoring biomolecular interactions and the detailed structural changes that take place during these interactions. Overall, biosensors are immensely useful in many different applications and future research aims at improving the sensitivity and throughput of these devices for greater reproducibility and applicability to larger sets of data acquisition.

2.0 MATERIALS & METHODS

2.1 MATERIALS

ATP, GTP, gentamicin, MES, MSG, and PIPES were from USB, Affymetrix, Inc., USA. Formaldehyde and DTT were from Fisher Scientific, Inc. The 1280-LOPAC Library, CaCl₂, CNBr, dextran blue, DMSO, EGTA, glutathione, glycerol, HEPES, Hoechst 33342, imidazole, iodoacetamide, KCl, 2-mercaptoethanol, MgCl₂, NaN₃, NEM, PBS, Protease Inhibitor Cocktail, TCEP, TRIS-HCl, and tyrosinase were from Sigma-Aldrich. EDTA was from Boehringer Mannheim, Germany. Coomassie blue stain was from BioRad. Thioglo1 (Covalent Associates, Inc.) was generously provided by Dr. Valerian Kagan. Alexa-595, DMEM medium, G418, L-glutamine, High Five™ Cells, Express Five® Serum Free Medium (SFM), Grace's Insect Medium, fetal bovine serum (FBS), Fungizone™, nonessential amino acids, Pen-Strep, NuPAGE® Novex 4-12% Bis-Tris Gels, NuPAGE® Novex 3-8% Tris-Acetate Gels and their respective running buffers, Green Polar Screen™ Glucocorticoid Receptor Competitor Assay Kit, sodium pyruvate, and HiMark™ Pre-stained Protein Standard were from Invitrogen, Inc. Full-Range Rainbow™ Molecular Weight Marker was from GE, Healthcare Life Sciences. BCA™ Protein Assay Kit, EZ-Link NHS-LC-Biotin, and bovine serum albumin (BSA) Standard were from Pierce. P_iColorLock™ Gold was from Innova Biosciences, UK. Kinesin heavy chain motor domain from *H. sapiens* and myosin II from rabbit skeletal muscle were from

Cytoskeleton, Inc. Trypsin Gold, Mass Spectrometry Grade was from Promega Corp. HPLC grade water was from Mallinkckrodt Baker, while HPLC grade CH₃CN was from Honeywell Burdick & Jackson. Drs. Michael Cascio and Tedd Ross generously provided Sf9 cells. Dr. Jeffery Brodsky generously provided Hsc82 and Ssa1p protein along with 17-AAG. The 3617.4 mouse mammary adenocarcinoma cell line stably expressing GR-GFP under the control of a tetracycline regulated promoter was kindly provided by Dr. Gordon Hager from the Laboratory of Receptor Biology and Gene Expression, NCI, Bethesda, MD. Triton X-100 and Tween20 were from BioRad. Mouse monoclonal anti- α -tubulin antibody was obtained from NeoMarkers/Lab Vision Inc., Fremont, CA. Cy3 donkey anti-mouse was obtained from Jackson ImmunoResearch Laboratories, Inc., West Grove, PA. Paclitaxel was obtained from the NIH Drug Synthesis Branch. Dynein translocation test agents used were obtained from the NIH's Molecular Libraries Screening Centers Network (MLSCN).

2.2 METHODS

2.2.1 Protein Purification

2.2.1.1 Tubulin Isolation and Purification from Bovine Brain

Tubulin was isolated from three freshly obtained bovine brains according to a modified procedure of that reported by Hamel and Lin (1984). Bovine brains were homogenized in a blender containing 0.75 mL/g of 0.1 M MES, pH 6.4, containing 1 mM EGTA, 4 M glycerol, 1 mM MgCl₂, 1 mM 2-mercaptoethanol, 0.1 mM EDTA, and 0.1 mM GTP (Solution A). The homogenate was clarified by centrifuging at 6,000 rpm for 15 min at 0 °C and the supernatant

was centrifuged at 28,000 rpm (90,000g) for 44 min at 0 °C using a Ti-45 Beckman-Coulter rotor. ATP and GTP were added to the supernatant to give final concentrations of 1mM and 0.3 mM, respectively and the solution was incubated for 40 min at 37 °C. The solution was centrifuged at 28,000 rpm (90,000g) for 44 min at 37 °C. The supernatant was discarded and the pellet was resuspended in 10 mL/brain of the above-described MES buffer without glycerol (Solution B) and incubated on ice for 30 min. For each 1 mL of solution, 0.553 g of glycerol was added to give a final concentration of 4 M. ATP and GTP were then added to give final concentrations of 1 mM and 0.3 mM, respectively and the mixture was incubated for 1 h at 37 °C. The solution was centrifuged at 28,000 rpm (90,000g) for 44 min at 37 °C and the pellet was resuspended in 6.25 mL/brain of Solution B. The resuspended pellet was incubated on ice for 30 min and centrifuged at 24,000 rpm (67,000g) for 30 min at 0 °C. Lyophilized MES (2M, pH 6.9) was added to the solution to give a final concentration of 1.6 M followed by the addition of 1 mM GTP and 2 mM DTT and the mixture was incubated for 45 min at 37 °C. The mixture was centrifuged at 28,000 rpm (90,000g) for 44 min at 37 °C and the pellet was resuspended in 10 mL cold 1 M MSG, pH 6.6. The mixture was incubated on ice for 2 h and then centrifuged at 28,000 rpm (90,000g) for 30 min at 0 °C. To the supernatant, 1 mM GTP was added and the solution was incubated for 1 h at 37 °C and the mixture was then centrifuged at 28,000 rpm (90,000g) for 90 min at 37 °C. The pellet was resuspended in 10 mL of cold 1 M MSG, pH 6.6 and incubated on ice for 1 h. The solution was centrifuged at 28,000 rpm (90,000g) for 1 h at 0 °C and the supernatant contained soluble tubulin. The electrophoretic homogeneity of the protein was determined with a 4-12% Bis-Tris SDS-PAGE gel electrophoresis run at 150 V for 1 hr and stained with Coomassie Blue Stain. The concentration was determined by a BCA Protein Assay kit using BSA as a standard.

2.2.1.2 Cytoplasmic Dynein Isolation and Purification from Bovine Brain

Cytoplasmic dynein was isolated from two freshly obtained bovine brains. Bovine brains were homogenized in a blender with 0.75 mL/g of an extraction buffer containing of 50 mM HEPES, 50 mM PIPES, pH 7.2, containing 2 mM MgCl₂ and 1 mM EDTA with a protease inhibitor cocktail tablet. The homogenate was clarified by centrifuging at 6,000 rpm for 30 min at 4 °C and the supernatant was centrifuged at 28,000 rpm (90,000g) for 1 h at 4 °C using a Ti-45 Beckman-Coulter rotor. PTX and was added to the supernatant to give a final concentration of 20 μM and the solution was incubated for 20 min at 37 °C. During this time, a prewarmed 6 mL solution of the extraction buffer with 7% sucrose was added to each of the ultracentrifugation tubes. The supernatant solution was slowly added to the tubes, which were then centrifuged in a Ti-45 rotor at 20,000 rpm (46,500g) for 30 min at 30 °C. The supernatant was carefully removed and the pellet was resuspended in 15 mL/brain of the extraction buffer containing 5 μM PTX and 3 mM GTP, then incubated for 15 min at 37 °C. The solution was then centrifuged in a Ti-45 rotor at 28,000 rpm (90,000g) for 30 min at 30 °C. The pellet was then resuspended in 10 mL/brain of the extraction buffer containing 5 μM PTX and 3 mM GTP. The mixture was incubated for 20 min at 37 °C and then centrifuged in a Ti-45 rotor at 28,000 rpm (90,000g) for 30 min at 20 °C. The pellet was resuspended in 10 mL/brain of extraction buffer containing 3 mM GTP and 10 mM ATP. The mixture was incubated for 10 min at 37 °C to release cytoplasmic dynein from MTs and the supernatant was collected after a final centrifugation in a Ti-70.1 rotor at 30,000 rpm (104,600g) for 30 min at 20 °C. The sample was further purified by size exclusion chromatography using a Shodex WS-804F column on a Summit HPLC System (Dionex). The column was pre-equilibrated with 10 mM HEPES, 10 mM PIPES, pH 7.2 with 0.05% (w/v) NaN₃ at a flow rate of 0.75 mL/min at 8 °C. The elution was monitored by the

absorption at 210 and 254 nm and dextran blue (2 MDa), tyrosinase (128 kDa), and BSA (68 kDa) were used as molecular weight standards. Multiple elutions were pooled and concentrated with an Amicon[®] Ultra-15 (100 kDa NMWL) centrifugal filter device at 5000g for approximately 30 min or until a final volume of 50-100 μ L is obtained. The electrophoretic homogeneity of the protein from the retentate was determined from a 3-8% Tris-Acetate SDS-PAGE gel electrophoresis run at 150 V for 1 h and stained using Coomassie blue. Protein concentration was determined by a BCA Protein Assay kit using BSA as a standard.

2.2.1.3 Rat Cytoplasmic Dynein Heavy Chain 1 Expression and Purification

The 380 kDa motor domain fragment was expressed as described by Hook *et al.* (2005). Briefly, the gene encoding rat cytoplasmic dynein motor domain (Gly1286-Glu4644) with a C-terminal in-frame hexahistidine tag was inserted into the baculovirus expression vector pVL1393 (BD biosciences) engineered by the laboratory of Dr. Richard Vallee (Columbia University). Small aliquots of engineered virus were generously provided by Dr. Vallee, which were then amplified by infecting Sf9 cells, generously provided by Drs. Michael Cascio and Ted Ross, and collecting the media after 3-4 days post infection. Hi5 cells (Invitrogen) were infected with the virus for 40 h. The cells were then washed and resuspended in phosphate buffered saline (PBS), and the recombinant motor domain fragments were extracted from the cells by homogenization in the presence of a protease inhibitor cocktail. Extracts were spun at 5,000g for 10 min and then 100,000g for 30 min. The supernatant was applied to a Ni-NTA Superflow (Qiagen, USA) column pre-equilibrated with 50 mM PIPES, 50 mM HEPES, pH 7.2, containing 2 mM MgCl₂ and 2 mM EGTA. The column was washed with 16 volumes of buffer containing 20 mM imidazole before eluting the protein with buffer supplemented with 125 mM imidazole. The imidazole was removed using a PD-10 Desalting Column (GE Healthcare Life Sciences) and

sample was resuspended in 10 mM PIPES, 10 mM HEPES, pH 7.2, containing 0.4 mM MgCl₂ and 0.4 mM EGTA. The electrophoretic homogeneity of the protein was determined from a 3-8% Tris-Acetate SDS-PAGE gel electrophoresis performed at 150 V for 1 h. Protein concentration was then determined by a BCA Protein Assay kit with BSA as a standard.

2.2.2 DEX-induced Glucocorticoid Receptor Translocation HCS Assay

2.2.2.1 Cell Culture

The 3617.4 cell line (Walker *et al.*, 1999) was maintained by Sunita Shinde (University of Pittsburgh Drug Discovery Institute) in complete culture medium containing 10 µg/mL tetracycline (Tet-on) in a humidified incubator at 37°C, 5% CO₂ and 95% humidity to keep the expression of GR-GFP repressed; DMEM medium with 2 mM L-glutamine supplemented with 10 % FBS, 100 µM nonessential amino acids, 100 µM sodium pyruvate, 100 U/mL penicillin and streptomycin, and containing 0.96 mg/mL G418. To induce GR-GFP expression in the 3617.4 cell line, cells were cultured for 48 hrs in the same tissue culture medium without the tetracycline (Tet-off). 3617.4 cells that had been cultured in Tet-containing complete culture medium were detached from tissue culture flasks by trypsinization, cells were centrifuged at 500g for 5 min, re-suspended in 10 mL of Tet-free induction medium and viable cells that excluded trypan blue were counted in a haemocytometer. 3617.4 cells were adjusted to 4.2 x 10⁴ cells/mL in Tet-free induction medium and then 60 µL of cell suspension per well were dispensed into the wells of 384-well black walled clear bottom plates using the Zoom liquid handler (Titertek, Huntsville, AL) to give a final seeding density of 2500 cells/well. Assay plates were incubated under Tet-off conditions for 48 hours at 37 °C, 5 % CO₂ in a humidified incubator and then diluted compounds (20 µL) were added to wells in columns 3 through 22

using an Evolution P3 (Perkin-Elmer, Waltham, MA) outfitted with a 384-well transfer head for a final screening concentration after DEX addition of 20 μM . Compound treated plates were incubated at 37 $^{\circ}\text{C}$, 5 % CO_2 in a humidified incubator for 60 minutes and then 20 μL of 5.0 μM DEX (1.0 μM final in well) was transferred to assay plates using the Evolution P3 liquid handler outfitted with a 384-well transfer head. The plate control wells were located in columns 1, 2, 23 and 24 and the minimum controls (n=24) were treated with 0.5% DMSO and the maximum control wells (n=32) were exposed to 1.0 μM DEX and 0.5% DMSO. Assay plates were incubated for 30 min at 37 $^{\circ}\text{C}$, 5% CO_2 and 95% humidity and then the contents of the wells were aspirated and replaced with 50 μL of 3.7% formaldehyde containing 2 $\mu\text{g}/\text{mL}$ Hoechst 33342 in PBS without Ca^{2+} and Mg^{2+} , pre-warmed to 37 $^{\circ}\text{C}$, using a BioTek ELx405 (BioTek, Winooski, VT) plate washer and cells were fixed for 10-30 min at ambient temperature. The fixative was then aspirated and plates were then washed twice with 50 μL PBS using the BioTek ELx405 (BioTek, Winooski, VT) plate washer and sealed with adhesive aluminum plate seals using the Abgene Seal-IT 100 plate sealer (Abgene, Rochester, NY) with the last 50 μL wash of PBS in place.

2.2.2.2 Image Acquisition

Images of two fluorescent channels (Hoechst and FITC) were sequentially acquired on the ArrayScan V^{TI} (AS-VTI) automated imaging platform (Thermo Fisher Scientific, Waltham, MA) using a 10x 0.3NA objective and the XF100 excitation and emission filter set to obtain images of stained nuclei and GR-GFP. Excitation was provided by an X-CITE^Ò 120 watt high pressure metal halide arc lamp with intelli-lampTM technology (Photonic Solutions Inc. Mississauga, Canada). Typically with the 10x 0.3NA objective, the AS-VTI was set up to acquire 500 selected objects (nuclei) or two fields of view, whichever came first.

2.2.2.3 Image Analysis

The nucleic acid dye Hoechst 33342 was used to stain and identify the nucleus, and this fluorescent signal was used to focus the instrument and to define a nuclear mask for the Molecular Translocation image analysis algorithms. To quantify the DEX-induced translocation of GR-GFP from the cytoplasm to the nucleus, images were analyzed using the Molecular Translocation image analysis algorithm as described previously (Trask *et al.*, 2009). Hoechst stained objects in Ch1 that exhibited the appropriate fluorescent intensities above background and morphological size characteristics (width, length, and area) were identified and classified by the image segmentation as nuclei. The nuclear mask derived from Ch1 was then used to segment the GR-GFP images from Ch2 into nuclear (Circ) and cytoplasmic (Ring) regions. The nuclear mask was eroded by 1 pixel to reduce cytoplasm contamination within the nuclear area, and the reduced mask was used to quantify the amount of target channel GR-GFP fluorescence within the nuclear region. The nuclear mask was then dilated to cover as much of the cytoplasm region as possible without going outside the cell boundary. Removal of the original nuclear region from this dilated mask created a ring mask in the cytoplasm region outside the nuclear envelope. The number of pixels away from the nuclear mask (1 pixel) and the number of pixels (width = 3 pixels) between the inner and outer ring masks were selectable within the TA bio-application software. The ring masks were then used to quantify the amount of target channel GR-GFP fluorescence within the cytoplasm region. The TA image analysis algorithm outputs quantitative data including; the total selected object or cell counts (SCC) from Ch1, the total and average fluorescent intensities of the GR-GFP in the nuclear (Circ) or cytoplasm (Ring) compartments of the cell. To quantify the relative distribution of the GR-GFP within the nucleus and the cytoplasm regions of the 3617.4 cells the TA image analysis algorithm provides a mean average

intensity difference calculated by subtracting the average GR-GFP intensity in the Cytoplasm (Ring) region from the average GR-GFP intensity in the Nuclear (Circ) region of Ch2 to produce a MCRAID-Ch2.

2.2.2.4 Indirect Immuno-fluorescent staining of 3617.4 cell MTs

To visualize the organization of microtubules in images of 3617.4 cells acquired on the AS-VTI we adapted previously described indirect immuno-fluorescence sample preparation methods (Trask *et al.*, 2009). Briefly, fixed Hoechst stained 3617.4 cells prepared as described above for the GR-GFP translocation HCS assay were permeabilized in 0.5% (v/v) Triton X-100 in PBS (without Ca^{2+} and Mg^{2+}) for 5 minutes at ambient temperature, cells were washed once in PBS (without Ca^{2+} and Mg^{2+}) and then incubated for 15 min in 0.1% (v/v) Tween 20 in PBS (without Ca^{2+} and Mg^{2+}) blocking buffer, cells were incubated for 1 hr with a 1:2000 dilution of a mouse monoclonal anti- α -tubulin antibody PBS (without Ca^{2+} and Mg^{2+}). Cells were then washed once in PBS (without Ca^{2+} and Mg^{2+}) and then incubated for 15 min in Tween 20 blocking buffer and then incubated for 45 min with a 1:1000 dilution of goat anti-mouse IgG antibody conjugated to Alexa-595 in PBS (without Ca^{2+} and Mg^{2+}). Cells were then washed twice with 50 μL PBS (without Ca^{2+} and Mg^{2+}) and sealed with the last 50 μL wash of PBS in place. Fluorescent images from three fluorescent channels were then sequentially acquired on the AS-VTI using a 20x 0.4NA objective with the XF53 (Hoechst and FITC) and the XF32 (TRITC) excitation and emission filter sets to obtain images of stained nuclei, GR-GFP and anti- α -tubulin antibody stained MTs.

2.2.3 Glucocorticoid Receptor Competition Binding Assay

The GR competitor assays were performed according to the manufacturer's (Invitrogen, Carlsbad, CA) recommendations with the final sample volume reduced to 40 μL . Human recombinant GR was used at the recommended concentration of 15 nM and Fluormone™ GS1 was used at a concentration of 1 nM. An initial screen was performed with aliquots (20 μL) of the mixture of test compounds in DMSO screening buffer with final concentrations of 12.5 and 50 μM were distributed in 384-well, black flat-bottom plates. 4X Fluormone™ (10 μL) followed by 4X GR (10 μL) was then added to the wells. Each compound was tested in triplicate, and 50 μM dexamethasone was used as a positive control. The DMSO concentration was kept at 1% (v/v) throughout the experiment. After 2 h, the fluorescence polarization (485 nm excitation and 530 nm emission) was measured using a SpectraMax® M5 Microplate Reader. Data was then fit to a one-site competition curve using KaleidaGraph Software V.4.03. The fit was constrained by the high polarization control, which was the GR/GS1 complex with no competition, and the low polarization control, which was the GR/GS1 complex with 50 μM dexamethasone for 100% competition.

2.2.4 ATPase Activity Inhibition Assays

2.2.4.1 Cytoplasmic Dynein

Test agents at 10 and 50 μM or DMSO were added to buffer consisting of 20 mM Tris-HCl, pH 7.6, containing 50 mM KCl, 5 mM MgCl_2 and 28 nM dynein was incubated for 15 min on ice. A positive control was performed using 100 μM sodium orthovanadate. Separately,

microtubules were preformed by incubating 10 μ M bovine tubulin with 10 μ M PTX in 1 M MSG, pH 6.6, at 37 $^{\circ}$ C for 30 min. The preformed MTs were then centrifuged at 17,000g for 30 min at 37 $^{\circ}$ C. The pellet was resuspended in the same buffer used for cytoplasmic dynein with 10 μ M paclitaxel and incubated for an additional 20 min while maintaining samples at 37 $^{\circ}$ C. Then, 1 mM ATP was added to the sample mixtures and were incubated at 37 $^{\circ}$ C for 30 min with or without preformed microtubules for a final volume of 50 μ L per well of a 384-well clear, flat-bottom plate. The amount of free phosphate was detected using a modified malachite kit (P_iColorlock™ Gold Assay) according to the manufacturer's protocol. Samples were then read with a SpectraMax® M5 Microplate Reader at 630 nm. The absorbance of an ATP blank was subtracted from all sample readings. Amount of activity inhibition was calculated by the amount of absorbance normalized to DMSO control: *Percent inhibition = (1-(absorbance of sample with test agent/absorbance of sample with DMSO))*100.*

2.2.4.2 Hsp70

Ssa1p (1300 nM) was incubated on ice with test agents at 10 and 50 μ M or DMSO for 15 min in buffer consisting of 50 mM HEPES, pH 7.2, containing 2 mM MgCl₂. Sodium orthovanadate (100 μ M) was used as the positive control. Then 1 mM ATP was added to the sample mixtures and were incubated at 32 $^{\circ}$ C for 1 h for a final volume of 30 μ L per well of a 384-well clear, flat-bottom plate. The amount of free phosphate was detected and activity inhibition was performed as described above (2.2.4.1).

2.2.4.3 Hsp90

Hsc82p (1300 nM) was incubated on ice with test agents at 10 and 50 μ M or DMSO for 15 min in buffer consisting of 20 mM Tris-HCl, pH 7.4, containing 2 mM $MgCl_2$. 17-AAG (50 μ M) was used as the positive control. Then, 1 mM ATP was added to the sample mixtures and were incubated at 32 °C for 1 h for a final volume of 30 μ L per well of a 384-well clear, flat-bottom plate. The amount of free phosphate was detected and activity inhibition was performed as described above (2.2.4.1).

2.2.4.4 Myosin

Rabbit skeletal muscle myosin II (125 nM) and the test agents at 10 and 50 μ M were premixed in 50 mM Tris-HCl, pH 7.9, containing 0.23 M KCl and 2.5 mM $CaCl_2$, then incubated on ice for 15 min. Then, 1 mM ATP was added to give a final volume of 50 μ L per well of a 384-well clear, flat-bottom plate. *N*-Ethylmaleimide (100 μ M) was used as the positive control. The reaction mixture was incubated at room temperature for 30 min. The amount of free phosphate was detected and activity inhibition was performed as described above (2.2.4.1).

2.2.5 Microtubule Polymerization Assay

Microtubule polymerization was measured by the change in absorbance of the solution at 340 nm with a SpectraMax[®] M5 Microplate Reader. Tubulin (or biotinylated-tubulin) at a final concentration of 1 mg/mL in 1 M monosodium glutamate (MSG), pH 6.6, with 400 μ M GTP, at 37 °C was used, and positive and negative controls included 10 μ M PTX and colchicine (CHC), respectively. The relative MT stabilization or destabilization was measured from the absolute

change in absorbance after 20 min normalized to the PTX or CHC absorbance, respectively, also at the 20 min time point.

2.2.6 Optical Biosensors

2.2.6.1 Tubulin Biotinylation

Purified tubulin was biotinylated with 20-fold molar excess (50 mM) EZ-Link NHS-LC-Biotin diluted in DMSO following the manufacturer's procedures in 0.1 M MES, pH 6.9. Samples were then incubated on ice in a cold room for 2 h. Unreacted biotin was removed by membrane-based size exclusion filtration via centrifugation in a 30 kDa Nanosep (PALL Corp., Portsmouth, Hants, UK) microcentrifuge tube four times for 4 min at 5000g and 4 °C (Jouan BR4i AB-2.14 rotor), washing the sample with 0.1 M MES buffer after each spin. The concentration of the biotinylated protein was determined with a BCA Protein Assay kit and the activity was tested as described above (2.2.4).

2.2.6.2 Biosensor Surface Functionalization

Dual Polarization Interferometry Chip

NHS-LC-biotin (Pierce, Chester, UK) (200 mM in DMSO) was dropped onto the channels of an Amine AnaChipTM (Farfield Group Ltd, Crewe, UK) *ex situ* for 10 min. The channels were then rinsed with deionized water before inserting into the chip manifold of an AnaLight[®] DPI instrument (Farfield Group Ltd, Crewe, UK). The chips were pre-equilibrated with 0.1 M MES, pH 6.9 running buffer. Streptavidin was injected at 35 μ L/min for 4 min followed by an injection of biotinylated tubulin at the same rate and time period. After each injection, the flow

was returned to running buffer for a given time period so that unbound molecules were washed from the chip and the baseline was stabilized.

Resonant Mirror Cuvette

A biotin cuvette (NeoSensors, Ltd., UK) was used as the base for the biotin-tubulin surface for experiments monitored by the IAsys RM instrument (NeoSensors, Ltd., UK). The volume of sample used during all steps of the experiment was 30 μL . Streptavidin (50 μg) was added to a cuvette containing 10 mM phosphate buffer, pH 7.7 and incubated for approximately 20 min or until a response of ~ 2000 arcseconds was obtained (1 arcsecond = $1/3600^\circ$; 600 arcseconds corresponds to 1 ng/mm^2 protein on the sensor surface). The phosphate buffer was removed from the cuvette, which was then washed and filled with 1 M MSG, pH 6.6 buffer. Approximately 50-60 μg of biotinylated tubulin was added to the cuvette for 10-15 min and the bound tubulin was washed with MSG buffer. For re-use, cuvettes were stripped with 12.5 M KOH for 20 s, which removes all the bound streptavidin, and rinsed with water before a new layer of streptavidin was formed.

2.2.6.3 Microtubule Polymerization on Biosensor Surfaces

Dual Polarization Interferometry Biosensor

An injection of 1 M MSG, pH 6.6 with 400 μM GTP was performed at 35 $\mu\text{L}/\text{min}$ for 2 min to subtract the relative bulk shift due to MSG when the sample was injected. Tubulin (1 mg/mL) in the MSG buffer was then injected continuously at 35 $\mu\text{L}/\text{min}$ for 45 min by replacing the standard sample loop with a 5 mL sample loop. Data was resolved with the *AnaLight Resolver*[®]

Software using the MSG, water, and 4:1 ethanol-water (w/w) injections with the instrument set at 37 °C for calibration as described by Swann *et al.* (2003).

Resonant Mirror Biosensor

After the addition of biotinylated tubulin, the cuvette was washed with 1 M MSG, pH 6.6 with 400 μ M GTP. Approximately 70 μ g of tubulin was then added to the cuvette and the change in response was monitored. When testing temperature dependence and the effect of compounds on initial rates of assembly, a mixture of sample buffer \pm 10 μ M of various MT stabilizers and destabilizers was added before the addition of tubulin. In one instance, tubulin was pre-incubated on ice with CHC for 15 min before addition to the cuvette. The stirrer setting on the instrument was maintained at 70%, while the temperature was set at 37 °C.

2.2.7 Computational Modeling

2.2.7.1 Secondary Structure Prediction

The sequence of rat cytoplasmic dynein heavy chain 1 from Gly1286-Glu4644 was submitted to NetSurfP ver. 1.1 (Petersen *et al.*, 2009) for secondary structure (alpha helix, beta sheet, random coil) prediction and to Real-SPINE 3.0 (Faraggi *et al.*, 2008) for dihedral angle (Φ , Ψ) prediction. The sequence was also submitted to DISULFIND (Ceroni *et al.*, 2006) for prediction of disulfide connectivity.

2.2.7.2 Three-Dimensional Comparative/Homology Modeling

The sequence of rat cytoplasmic dynein heavy chain 1 from Gly1286-Glu4644 was aligned with the sequence of the previously reported models of cytoplasmic dynein's motor domain with the PDB files 2GF8 (Serohijos *et al.*, 2006) and 1HN5 (Mocz and Gibbons, 2001) using the ClustalW2 program (EMBL-EBI). This sequence alignment was then used to generate 3D models using MODELLER 9v8 (Eswar *et al.*, 2006). Based on the sequence alignment produced, the rat cytoplasmic dynein heavy chain 1 sequence was shortened to Tyr1866-Pro3121, Ala3450-Ala3461, and Leu3551-Glu4644 in order to facilitate the best match between the rat cytoplasmic dynein heavy chain 1 bases and the ATOM records from the PDB files 2GF8 and 1HN5. 3D models based on the truncated sequence were generated using MODELLER using PDB files 2GF8 and 1HN5 as a reference individually and then combined. For each of the aforementioned procedures MODELLER created five PDB files each and the best model of each procedure was selected based on the lowest Discrete Optimized Protein Energy (DOPE) score.

2.2.8 Cysteine Labeling

Labeling of cysteine residues of dynein and BSA samples was monitored using the maleimide-based fluorescent dye methyl-10-(2,5-dioxo-2,5-dihydro-1*H*-pyrrol-1-yl)-9-methoxy-3-oxo-3*H*-benzo[*f*]chromene-2-carboxylate (ThioGlo1[®]), referred to hereon as TG1. A 2-fold increment concentration range of 0.18-0.72 μ M of protein in 10 mM PBS, pH 7.4, was incubated with TG1 at a final concentration of 10 μ M and in the presence and absence of 2% (w/v) SDS for 1 h in the dark at room temperature. Fluorescence emission of cysteine-TG1 protein adducts was recorded of 80 μ L samples in a black, flat-bottom Costar[®] 384-well plate (Corning, Inc.) using excitation and emission wavelengths of 379 and 513 nm, respectively, using a Spectramax[®] M5 Microplate

Reader. The slope of a concentration curve of glutathione incubated with excess TG1 was used to calibrate the absolute amount of thiols in dynein and BSA samples.

For sequence identification of labeled peptides, protein samples were labeled with 10 μM TG1 for 1 h at room temperature in the dark before a 3 kDa NMWL Microcon[®] filter-based centrifugation device was used to remove excess TG1. Protein sample added to the reservoir and the centrifugal device was spun at 14,000g for 8 min. The retentate was diluted with 300 μL 50 mM Tris-HCl, pH 7.2 buffer and sample was centrifuged for 12 min at 14,000g. The device was inverted into a clean vial and centrifuged for 2 min at 1,000g to collect sample for MS analysis.

2.2.9 Protein Digestion

2.2.9.1 In-gel Trypsin Digestion

Individual protein bands were excised from gels and placed in microcentrifuge Eppendorf tubes containing 1:1 acetonitrile (CH_3CN) in 25 mM ammonium bicarbonate (NH_4HCO_3), pH 7.8, solution and were gently agitated overnight to remove Coomassie stain. The supernatant was removed and replaced with fresh solution for another 2 h to remove any remaining Coomassie stain. Where indicated, gel pieces were reduced by adding a solution of 10 mM *tris*(2-carboxyethyl)phosphine (TCEP) for 30 min at 37 °C. Reducing solution was then replaced with 50 mM iodoacetamide (IAC) for 45 min at 56 °C for alkylation. Alkylating solution was then removed and the gel pieces were washed with 25 mM NH_4HCO_3 , pH 7.8, while vortexing for 10 min. Regardless of whether reduction and alkylation steps were performed, gel pieces were then washed with 100% CH_3CN until plugs were completely white. The CH_3CN was removed and gel pieces were air dried for 10 min. Gel pieces were then rehydrated with 10 μL (20 ng/ μL)

trypsin solution or enough to cover gel pieces for 15 min on ice. Excess trypsin was removed and 30 μL of 25 mM NH_4HCO_3 to keep gel pieces immersed throughout digestion. Gel pieces were incubated for 12 h at 37 $^\circ\text{C}$. The digestion was quenched by adding 5 μL of 5% aqueous formic acid (HCO_2H). The supernatant was removed and placed in a new tube. Peptides were extracted from the gel pieces by adding a 70% CH_3CN , 25 mM NH_4HCO_3 , 5% HCO_2H solution and sonicating for 10 min. Extraction was repeated three times and the supernatants were pooled together with the original supernatant. The extract was dried to completeness using a centrifugal evaporator (SpeedVac). The pellet was resuspended in 25 mM NH_4HCO_3 with 1% HCO_2H for MS and MS/MS analyses.

2.2.9.2 In-solution CNBr Digestion

Protein samples were dried with a SpeedVac and then resuspended in 200 μL of 70% HCO_2H in glass vials for in-solution digestion with cyanogen bromide (CNBr). Samples were handled with extra care in the fume hood for safety purposes. Approximately 2-3 CNBr crystals were dissolved into the solution and N_2 gas was gently blown for 15 s into the vials before they were capped and placed in the dark overnight at room temperature. The reaction was quenched by adding 1 mL of H_2O and drying the sample with a SpeedVac. Samples were resuspended in 25 mM NH_4HCO_3 and then desalted with a C_{18} ZipTip[®] (Millipore).

2.2.10 Mass Spectrometry

2.2.10.1 MALDI-TOF-MS and -MS/MS

For MS analysis, 0.5 μL of extract was spotted onto a stainless steel target and allowed to air dry. A 0.5 μL aliquot of a 10 mg/ml solution of γ -cyano-4-hydroxycinnamic acid (CHCA) dissolved in

CH₃CN was then applied atop of the peptide spot and then allowed to air dry. MALDI-TOF and MALDI-TOF/TOF mass spectra were recorded with an Applied Biosystems 4800 Proteomics Analyzer (ABI, Foster City, CA) in the reflectron positive ion detection mode. MS spectra were acquired from *m/z* 800 to 4000 with a focus mass of *m/z* 2000. MS processing was done using the angiotensin II internal standard by matching 6 individual peaks. Up to 20 precursor peaks per spot were selected for MS/MS analysis starting from the strongest precursor with a 20 S/N cutoff. Peptide CID (air) was performed at 2 kV and with a laser intensity setting of 4400. Peaks were submitted through the ProteinPilot™ Software 3.0 to the MSDB protein database using the MASCOT method, searching the mammalian taxonomy with six maximum missed trypsin cleavages and variable modifications including cysteine carbamidomethylation and methionine oxidation.

2.2.10.2 LC-ESI-MS

Samples were injected onto a C₁₈ PepMap100 column (I.D. 300 μm, length 15 cm, 3 μm particles, 100 Å pore size) (LC Packings, Dionex), which was pre-equilibrated with a solution of 2.5% CH₃CN and 0.1 % HCO₂H on an UltiMate® 3000 Rapid Separation LC System (LC Packings, Dionex) at a flow rate of 3.5 μL/min. Elution of sample was first directed to waste for the first 2 min to desalt samples. After 2 min, the valve was changed so that eluates were directed to the ESI needle of a micrOTOF (Bruker Daltonics) MS. An organic solvent gradient was applied to the LC column beginning with an increase from 2 to 5% of an 80% CH₃CN, 0.1% HCO₂H solution over 2 min followed by a rapid increase to 45% of the solution over another 2 min. The gradient was then slowly increased to 100% of the 80% CH₃CN, 0.1% HCO₂H solution over 80 min followed by a decrease to 20% for a final 10 min. The mass detection

range was set between m/z 500-3000 in positive ion detection mode. Selected mass spectra were then deconvoluted using the SUM PEAK algorithm selected for large peptides/proteins with a S/N cutoff of 10 and a minimum of 3 peaks to be considered a component and can be extracted from the original spectrum.

2.2.10.3 LC-ESI-FTMS

Samples were injected onto a C₁₈ Acclaim PepMap100 column (I.D. 75 μ m, length 15 cm, 3 μ m particles, 100 Å pore size) (LC Packings, Dionex), which was pre-equilibrated with a solution of 2% CH₃CN and 0.1 % HCO₂H on an UltiMate[®] 3000 Rapid Separation LC System (LC Packings, Dionex) at a flow rate of 200 nL/min. Elution of sample was first directed to waste for the first 4 min to desalt samples. After 4 min, the valve was changed so that eluates were directed to the nano-ESI needle of a 12T FT-ICR (Bruker Daltonics) MS. An organic solvent gradient was applied to the LC column beginning with 4% of a 100% CH₃CN, 0.1% HCO₂H solution over 5 min followed by an increase to 50% of the solution over 25 min. The gradient was then increased to 80% of the 100% CH₃CN, 0.1% HCO₂H solution over 0.1 min and maintained for 5 min. The gradient was then returned to 4% of the 100% CH₃CN, 0.1% HCO₂H solution for a final 10 min. The mass detection range was set between m/z 184.26-3000. Selected mass spectra were then deconvoluted using the SNAP 2.0 algorithm selected for large peptides/proteins with a S/N cutoff of 10 and a minimum of 3 peaks to be considered a component and can be extracted from the original spectrum.

2.2.10.4 LC-ESI-MS/MS

Tryptic digests were analyzed by reversed-phase liquid chromatography (LC)-MS/MS using a nanoflow LC (Dionex Ultimate 3000, Dionex Corporation, Sunnyvale, CA) coupled online to an

LTQ-Orbitrap MS (ThermoFisher). Separations were performed using 75 μm i.d. x 360 o.d. x 20 cm long fused silica capillary columns (Polymicro Technologies, Phoenix, AZ) slurry packed in house with 5 μm , 300 \AA pore size C-18 silica-bonded stationary phase (Jupiter, Phenomenex, Torrance, CA). Following sample injection onto a C-18 trap column (Dionex), the column was washed for 3 min with mobile phase A (2% CH_3CN , 0.1% HCO_2H) at a flow rate of 30 $\mu\text{L}/\text{min}$. Peptides were eluted using a linear gradient of 0.33% mobile phase B (0.1% HCO_2H in CH_3CN)/minute for 130 min, then to 95% B in an additional 15 min, all at a constant flow rate of 200 nL/min. Column washing was performed at 95% B for 15 min after which the column was re-equilibrated in mobile phase A prior to subsequent injections.

The MS was operated using a high resolution ($R=60,000$ at m/z 400) full MS scan conducted in the Orbitrap followed by tandem MS of the top thirteen most abundant peptide molecular ions by collision-induced dissociation (CID) using a normalized collision energy of 35%. Data were collected over a broad precursor ion selection scan range of m/z 375-1800 with the lock mass feature enabled using a polydimethylcyclosiloxane (PCM) ion generated in the electrospray process (m/z 445.120025) (Olsen *et al.*, 2005) and an applied voltage of 1.8 kV. Dynamic exclusion was enabled to minimize redundant selection of peptides previously selected for CID (repeat count of 2, sixty second exclusion duration).

Tandem mass spectra were searched against the rat dynein UniProt sequence (P38650; version 87, 06-15-2010; <http://www.uniprot.org>), using SEQUEST (ThermoFisher Scientific). Peptides were searched for methionine oxidation with a mass addition of 15.9949 Da and cysteine modification by the ThiGlo1 reagent with the following potential masses: 365.0473, 379.0692, 383.0641 and 397.0798 Da. Peptides were considered legitimately identified if they met specific charge state and proteolytic cleavage-dependent cross correlation scores of 1.9 for

$[M+H]^+$, 2.2 for $[M+2H]^{2+}$ and 3.5 for $[M+3H]^{3+}$ with no delta correlation constraint given the single protein database search. All labeled peptide spectra were manually inspected to verify the matched ions and confirm the identification.

2.2.11 Electron Microscopy

Carbon-coated copper electron microscopy grids were first glow-discharged for 15 s. Protein samples of approximately 1 mg/mL were diluted between 1/100 - 1/20 fold with 10 mM PIPES, 10 mM HEPES, pH 7.2, and approximately 2 μ L was spotted onto copper grids for 30 s. Excess sample was blotted off using a filter paper. Grids were then floated for 30 s atop a drop of either 1% (w/v) uranyl acetate ($UO_2Ac_2 \cdot 2H_2O$, UAc), 2% (w/v) ammonium molybdate ($(NH_4)_6Mo_7O_{24} \cdot 4H_2O$), or 2% (w/v) phosphotungstic acid ($H_3PW_{12}O_{40} \cdot 24HO$, PTA). Excess stain was blotted with filter paper from the grids. Samples were then observed with an FEI Tecnai T12 electron microscope with a lanthanum hexaboride (LaB_6) cathode operating at 120 kV and equipped with a Gatan UltraScan 1000 CCD camera (2048x2048 pixels in area, each pixel 14 μ m x 14 μ m).

3.0 IDENTIFICATION OF SMALL MOLECULES THAT TARGET RETROGRADE TRANSPORT

3.1 INTRODUCTION

The motor protein cytoplasmic dynein transports many important cargos along microtubules in a retrograde manner; the minus end of most microtubules is the microtubule organizing center (aka centrosome), near the nuclear pore. The nucleus, where many of these cargos are often imported, is the site where some cargo signal for a cascade of events, including transcription and subsequent translation of proteins involved in a number of different cellular roles (Galigniana *et al.*, 2004). Retrograde transport is often also hijacked by microbes and viruses in their host cell infection process (Dohner *et al.*, 2002; McDonald *et al.*, 2002). Additionally, cytoplasmic dynein plays important roles in crucial cellular events including mitosis (Vaisberg *et al.*, 1993), chromosome segregation (Sharp *et al.*, 2000), and cytokinesis (Yeh *et al.*, 1995). Because cytoplasmic dynein contributes to so many important cellular processes, small molecules that perturb dynein function would provide useful chemical and cell biology tools to further investigate the critical roles of cytoplasmic dynein in the cell. To date, there are only a handful of small molecules that perturb cytoplasmic dynein's functions, most of which are either ATP/transition state mimics (*e.g.*, erythro-9-(2-hydroxy-3-nonyl)adenine (EHNA), AMP, orthovanadate) (Bouchard *et al.*, 1981; Vallee and Shpetner, 1990) or sulfhydryl-reactive agents

(e.g., thiourea, *N*-ethylmaleimide (NEM)) (Blum *et al.*, 1979; Vallee and Shpetner, 1990). The Day lab has previously examined purealin, a natural product derived from the sea sponge *Psammaphysilla purea*, known to enhance the ATPase activity of myosin (Takito *et al.*, 1986) while also inhibiting the ATPase activity of axonemal dynein (Fang *et al.*, 1997). The Day lab found that racemic purealin and some synthetic analogues inhibited the ATPase activity of rat cytoplasmic dynein heavy chain 1 (Zhu *et al.*, 2006); although purealin itself is a potent inhibitor of cytoplasmic dynein heavy chain *in vitro*, the compound does not exhibit such action in cells.

The Day lab therefore decided that the screening approach should be altered so that only cell-active hits would be identified in the initial screen. The glucocorticoid receptor (GR) is a cargo of cytoplasmic dynein and is, upon agonist activation, transported along MTs to the nucleus. GR is linked to cytoplasmic dynein through interactions with dynactin and immunophilin-heat shock protein complexes (Pratt *et al.*, 2004). Once agonist-bound GR reaches the nucleus, it then acts as a transcription factor for genes responsible for both upregulating and downregulating the expression of proteins involved in inflammatory and immune responses (Glass and Saijo, 2010). Because GR translocation to the nucleus is agonist-dependent, GR translocation is a recognized model for retrograde transport studies (Pratt *et al.*, 2004). By using a cell-based high-information content screening (HCS) assay to quantify the agonist-induced translocation of GR from the cytoplasm to the nucleus as a cellular model of dynein-mediated cargo transport, the Day lab in collaboration with Dr. Paul Johnston (University of Pittsburgh Drug Discovery Institute) recently identified several concentration-dependent inhibitors in a library screen of small molecules. First, the distribution of glucocorticoid receptor-green fluorescent protein (GR-GFP) present in the cytoplasm and nuclei of cells was examined and compared to determine the compounds that inhibited agonist-induced GR

translocation. From these same images, the cellular toxicity of compounds was evaluated, defined by a loss of cells, as were compound-induced changes in the morphology of α -tubulin antibody staining, along with the intensity and the overall MT organization of treated cells.

I then developed and optimized secondary biochemical assays to characterize the cell-based assay hits and to investigate the potential mechanisms of action of these inhibitors of cytoplasmic dynein-mediated cargo transport. GR competitive binding and MT polymerization assays *in vitro* were performed to identify potential GR binding antagonists and MT perturbing agents, respectively. Compounds were then tested against the ATPase activity of Hsp90 and Hsp70 molecular chaperones, which are both important components of the GR cargo transport process. The ability of the GR translocation inhibitors to inhibit both the basal and the MT-stimulated ATPase activity of recombinant cytoplasmic dynein heavy chain 1 motor domain was then tested. Finally, to evaluate the ATPase selectivity of the hits, compounds were screened against the ATPase activity of the myosin molecular motor, since the only known inhibitor of dynein (puralin; *vide supra*) has also been shown to specifically alter myosin's ATPase activity. Once each of the described assays were validated and optimized using a number of compounds from the Sigma LOPAC collection, the assays were performed on a larger subset of compounds from the MLSCN collection.

3.2 RESULTS & DISCUSSION

3.2.1 High Information Content Cell-Based Screen

Multi-parameter immunofluorescence microscopy was first utilized to provide high-content information on the cellular effects of the compounds on cells expressing GR-GFP. Such an analysis provides information on the location of GR-GFP within the cell, as well as effects on MT mass, nuclear morphology, and cytotoxicity by surveying different components of the cell with specific labels: in this case GR-GFP, tubulin antibodies, and Hoechst (Figure 16). This was performed in a concentration-dependent manner to determine an ideal concentration to test compounds for inhibition of GR-GFP translocation before results were attributed to cytotoxic effects (Figure 16). The difference in the GR-GFP signal between the nuclei and the cytoplasm, or mean circ-ring average intensity difference (MCRAID), indicated the inhibition of dexamethasone-induced GR-GFP translocation with all of the compounds tested. The number of cells was determined from the number of circular Hoechst-stained objects, while MT mass was determined from the intensity of antitubulin antibody fluorescence in the ring (cytoplasmic) surrounding the circles (nuclei). Inhibition of GR-GFP translocation in cells appeared to be concentration-dependent and this analysis also revealed maximally tolerated concentrations of compounds before significant cytotoxicity was observed. Upon analysis of the hits from the 1280 LOPAC screen, Bay 11-7085 exhibited the most significant cell toxicity at higher concentrations than did any of the other compounds, but still inhibited GR translocation at lower, non-cytotoxic concentrations (around 12.5 μ M). Unlike Bay 11-7085, calcimycin and GR(127935) HCl hydrate were toxic at even low concentrations and were deemed undesirable for further HCS studies but were still evaluated in the biochemical assays.

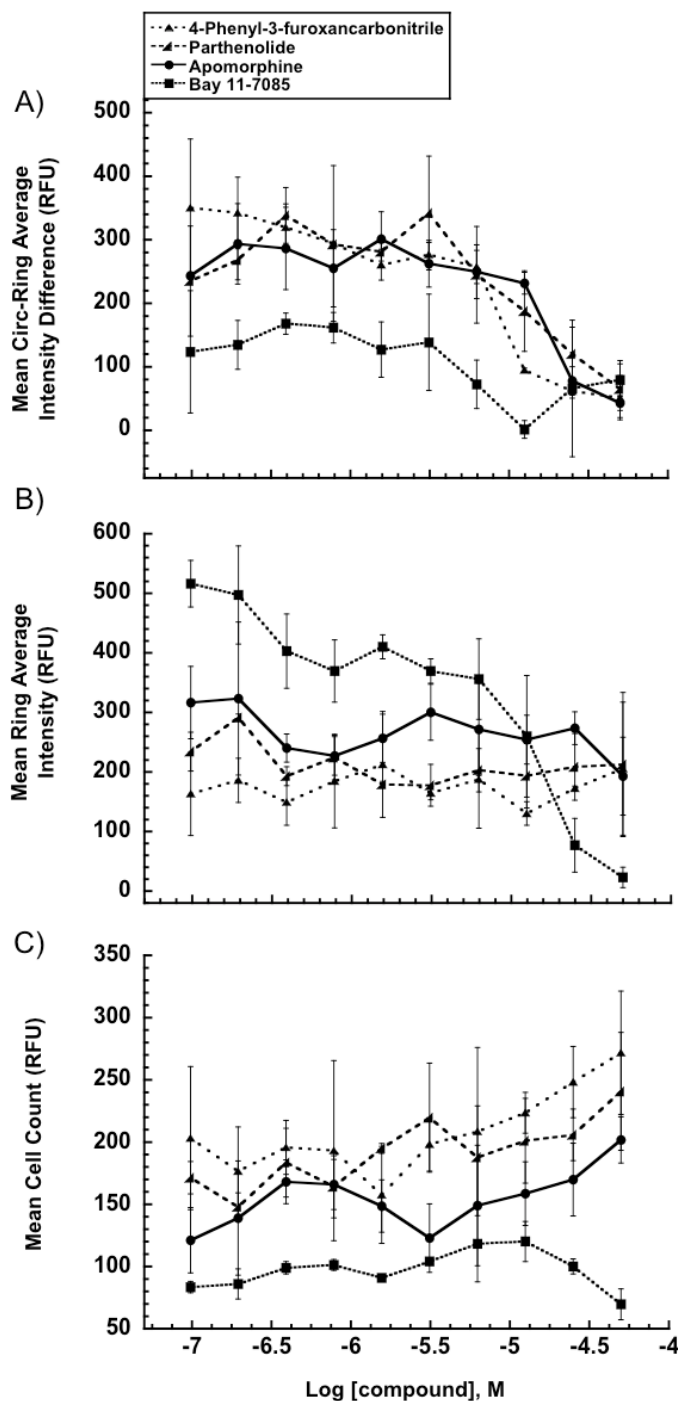


Figure 16. Cell-Based Concentration Dependence of LOPAC Collection on GR-GFP Translocation

A) Mean circ-ring average intensity difference indicates the amount of GR-GFP in the nucleus compared to the cytoplasm as a function of concentration with less GR-GFP present in the nuclei at higher concentrations of compound. B) Mean ring average intensity indicates the amount MTs present surrounding nuclei with Bay 11-7085 being the only compound demonstrating fewer MT masses at higher concentrations of compound. C) Mean cells counts indicate the cytotoxic effects of compounds with Bay 11-7085 being cytotoxic at concentrations greater than 12.5 μ M. Graphs provided by Sunita Shinde and Dr. Paul Johnston.

Upon evaluation of the images of treated cells, the cellular phenotype of the DMSO control demonstrated well-organized cells with a few cells undergoing mitosis and diffuse GR-GFP located predominantly in the cytoplasm (Figure 17). The cells were also uniformly rounded with numerous sizeable cellular projections. Upon the addition of the GR agonist dexamethasone (DEX), the cell morphology appeared very similar to the DMSO control with the exception that all of the GR-GFP had translocated into the nuclei, as expected. A total of 7 compounds from the 1280 Sigma LOPAC screen that were incubated 60 min prior to DEX treatment noticeably decreased the GR-GFP content within nuclei relative to the DEX control. These compounds did not show any significant differences in cell counts and MT masses compared to the DMSO control, but still caused considerable inhibition of GR-GFP translocation. Parthenolide, along with apomorphine, Bay 11-7085, and 4-phenyl-3-furoxanarbonitrile, all appeared to alter cell morphology and MT organization, indicating they interfered with dynein-mediated translocation. Most noticeably, there was excess accumulation of GR-GFP in the cytoplasm along with fewer and shorter cellular projections protruding from the nuclei.

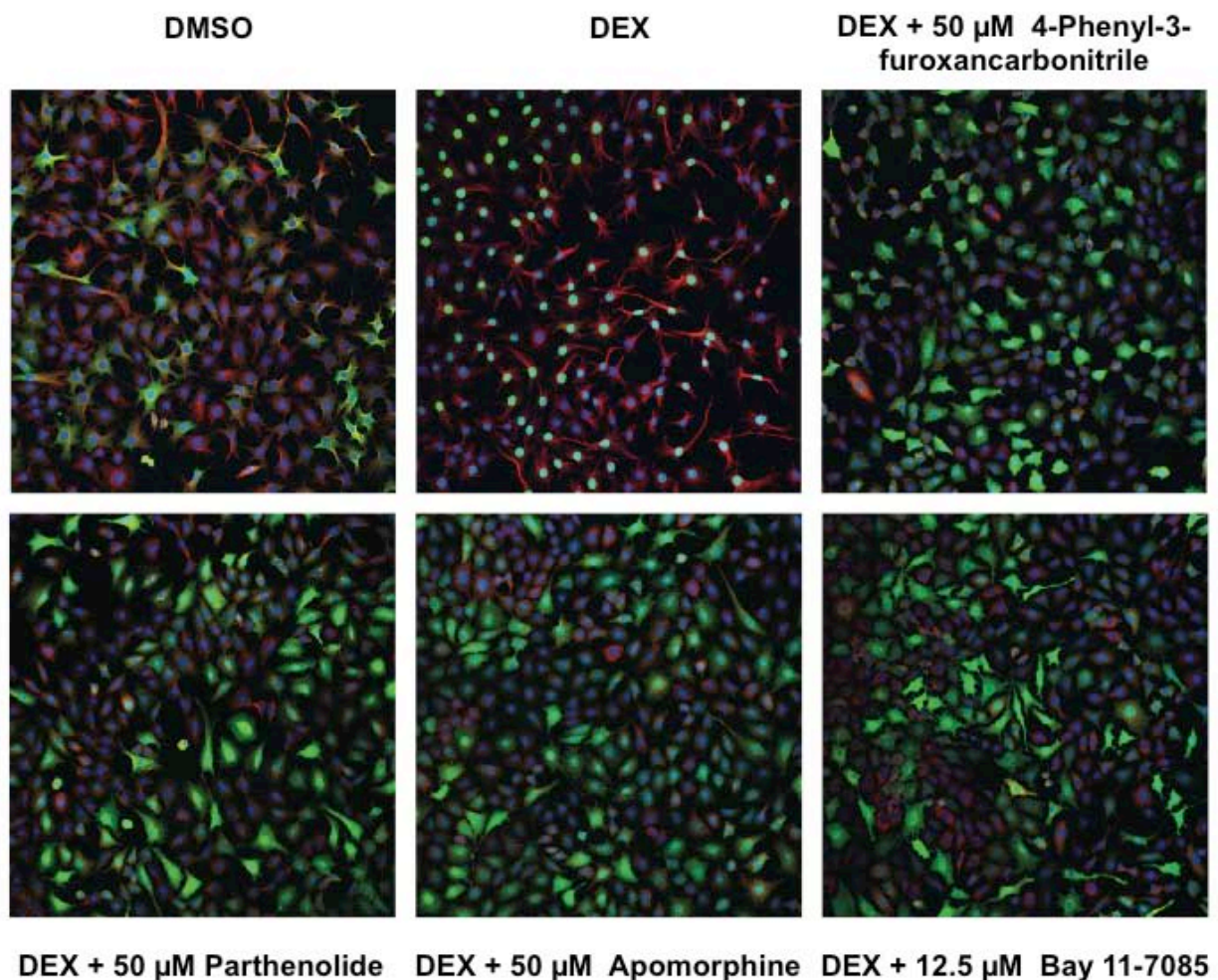


Figure 17. Multi-Parameter Immunofluorescence Visualization of Treated Cells

GR-GFP (green) was used to track cytoplasmic dynein translocation, a fluorescent tubulin antibody (red) to label MTs, and Hoechst 33342 was used to label DNA (blue) to visualize the nuclei. Images provided by Sunita Shinde and Dr. Paul Johnston.

The immunofluorescence of the individual components from the images was also quantified (Figure 18). The difference in the GR-GFP signal between the nuclei and the cytoplasm (MCRAID) indicated the inhibition of DEX-induced GR-GFP translocation with all of the compounds tested compared to the DEX control. MT mass and cell counts were also quantified and demonstrated comparable values to the DMSO and DEX controls, with the exception of Bay 11-7085.

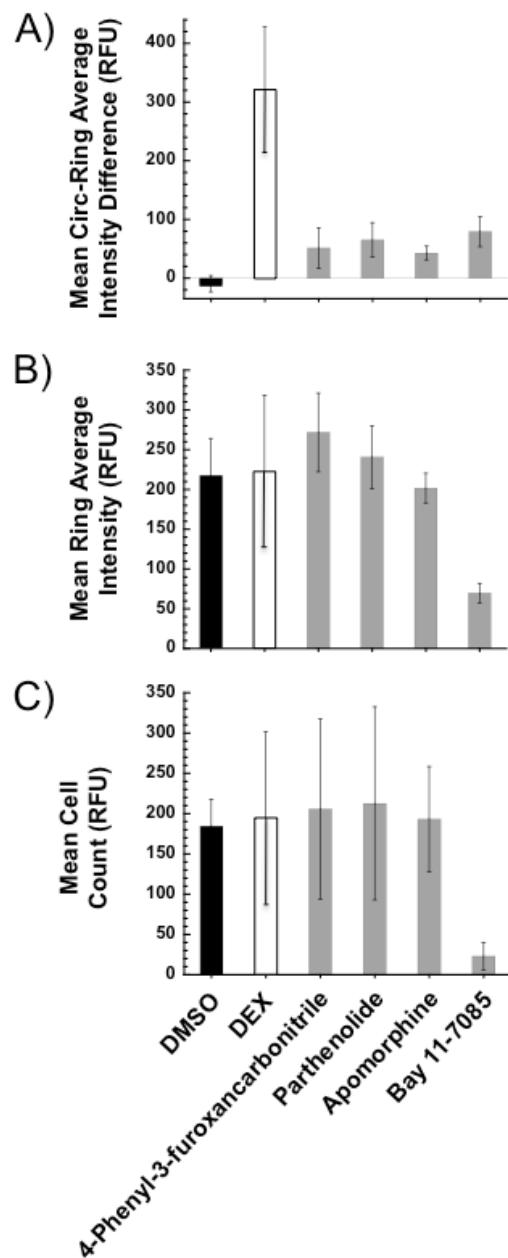


Figure 18. Quantitation of Multi-Parameter Immunofluorescence in Cells Treated with LOPAC 1280 Hits

A) Mean circ-ring average intensity difference indicates the amount of GR-GFP in the nucleus compared to the cytoplasm with all compounds demonstrating decreased GR-GFP in nuclei relative to the DEX control. B) Mean ring average intensity indicates the amount of MTs present surrounding nuclei with Bay 11-7085 being the only compound demonstrating fewer MT masses. C) Mean cells counts indicate the cytotoxic effects of compounds being negligible compared to the DMSO control with the exception of Bay 11-7085. Quantitation of images performed by Sunita Shinde and Dr. Paul Johnston.

Since GR translocation is dependent on agonist binding (Galigniana *et al.*, 1998), association with Hsp chaperones, an intact cytoskeleton (Harrell *et al.*, 2004), and manifestly cytoplasmic dynein activity, a number of biochemical assays were performed to evaluate the target(s) of these small molecules that caused inhibition of GR-GFP accumulation in the nuclei of cells (Figure 19).

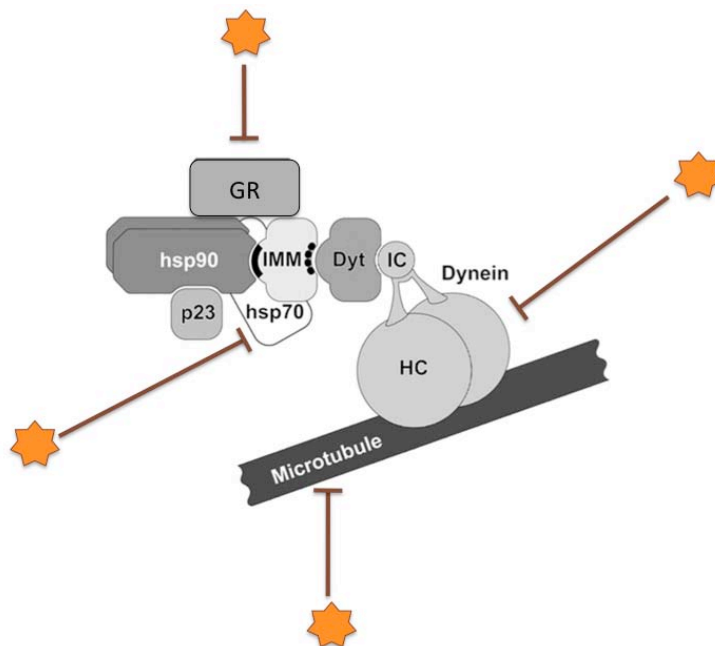


Figure 19. Four of the Potential Target(s) of Retrograde Transport Inhibitors

Small molecules can inhibit the transport of GR to the nucleus by either preventing direct binding of agonist to GR, inhibition of either Hsp 70 or 90 necessary for dynein-cargo complex formation, perturbation of MT dynamics necessary for dynein translocation, and direct inhibition of cytoplasmic dynein ATPase activity. Cytoplasmic dynein translocation can also be inhibited by disruption of other proteins or protein-protein interactions necessary for complex formation including dynactin and immunophilins [adapted from Pratt *et al.* (2004) with permission from publisher].

3.2.2 Biochemical Characterization of GR-GFP Translocation Inhibitors

3.2.2.1 Glucocorticoid Receptor Competitive Binding

The ability of GR-translocation inhibitors to compete with and disrupt the binding of a fluorescent-labeled ligand to the GR was investigated using a fluorescence polarization (FP)

binding assay. In the FP assay, dexamethasone inhibited ligand binding in a concentration-dependent manner (Figure 20A) and exhibited an IC_{50} value of 10.1 ± 1.5 nM, which compares well to previously published values (Reynolds *et al.*, 1997). At the two concentrations tested against the LOPAC collection, 12.5 μ M and 50 μ M, neither parthenolide nor 4-phenyl-3-furoxanarbonitrile disrupted the binding of the agonist to GR in the FP binding assay (Figure 20B). At 50 μ M, all of the remaining GR-translocation inhibitors appeared to disrupt GR binding by an average of > 60%. At 12.5 μ M (Figure 20B), however, the percent inhibition of GR-binding for most of these compounds was considerably lower. Given the large standard errors in the compound binding data it is unclear whether the apparent disruption of GR binding at high concentrations contributes to the inhibition of DEX-induced GR translocation observed at compound concentrations lower than 12.5 μ M.

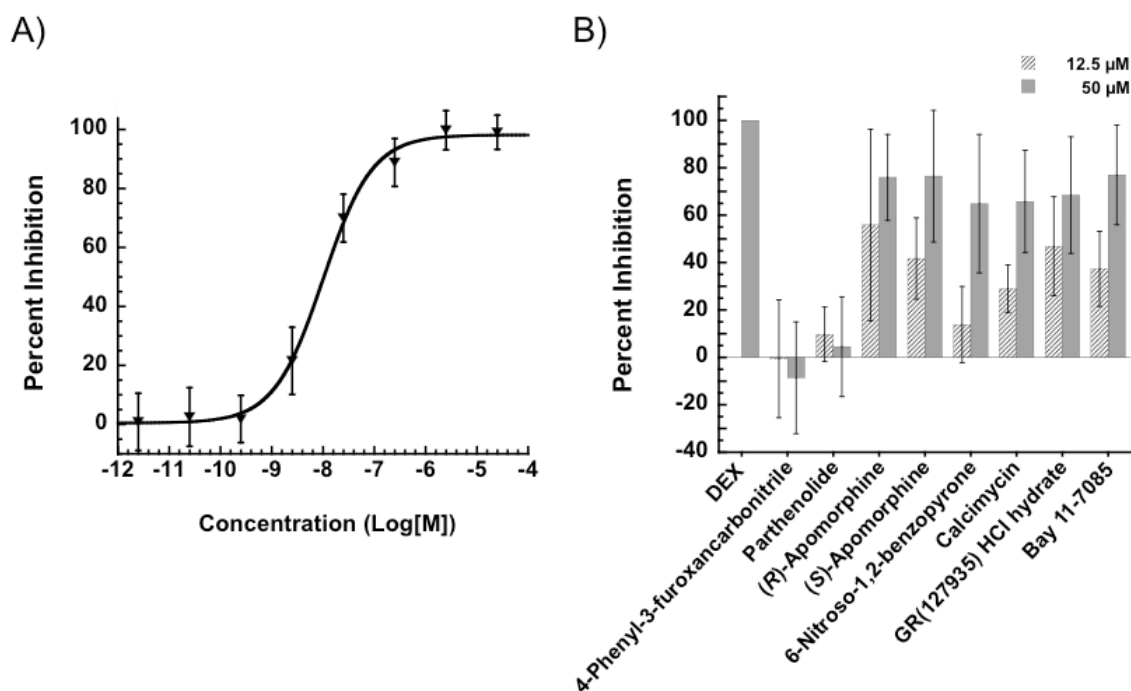


Figure 20. Fluorescence Polarization GR Competitive Binding Assay

A) Concentration dependent evaluation of the competitive binding of the GR agonist DEX fitted by a one-site competition curve with an IC_{50} value of 10.1 nM. B) Percent competition of test compounds against binding to GR normalized to DEX control. Data represented as mean values with SD from six independent measurements.

Once methods were established with the LOPAC collection, a large subset (69) of compounds from the MLSCN that inhibited GR-GFP translocation was also tested for competitive binding to GR at an intermediary concentration of 20 μM . Other hits from the MLSCN screen were disregarded from secondary screening due to their poor pharmacological properties. At this concentration, only six out of the 69 compounds tested exhibited competition greater than 50% (Figure 21). This was an indication that perhaps the remaining 63 compounds had other targets within the cell responsible for inhibiting GR translocation. A small number of compounds also appeared to have negative percent competition values, most notably compound #23. Given that this assay relies on the anisotropy a fluorescent molecule that binds to the GR ligand binding domain, it is unlikely that these results are indicative of enhanced binding, but rather due to protein precipitation or aggregation in the presence of that particular compound.

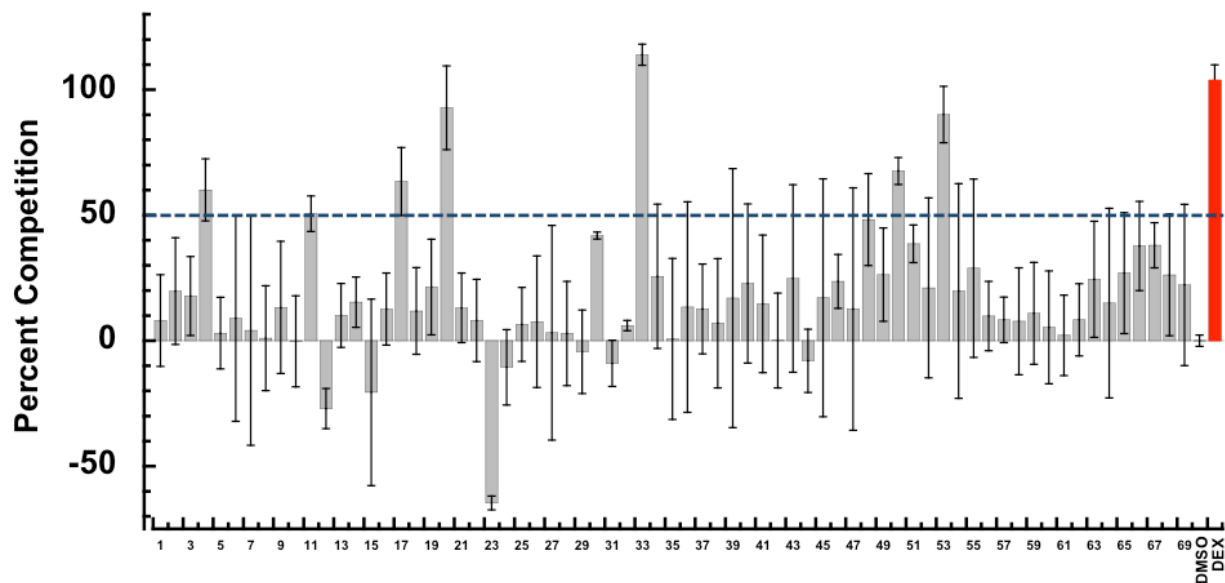


Figure 21. GR Competitive Binding Assay with MLSCN Collection

Percent competition of test compounds against binding to GR normalized to DEX control. Six out of a total of 69 compounds exhibited competition >50% (chemical structures shown in Appendix A). Data represented as mean values with SD from three independent measurements.

3.2.2.2 Targeting the Cellular Tracks

Since retrograde transport requires the existence of functionally structured MTs (Galigniana *et al.*, 1998) alterations in MTs can stall GR translocation by cytoplasmic dynein. Many compounds have been previously demonstrated to alter MT dynamics by either acting as MT stabilizers (PTX (Schiff *et al.*, 1979) and DCD (Ter Haar *et al.*, 1996)), or destabilizers (CHC (Bhattacharyya *et al.*, 2008) and VCN (Jordan *et al.*, 1985)). MT perturbing agents have been shown to inhibit transport of p53 via cytoplasmic dynein to the nucleus (Giannakakou *et al.*, 2000). Compounds identified as MT perturbing agents may also serve as cytoplasmic dynein enhancers when used at low concentrations (Giannakakou *et al.*, 2002). Therefore, we also tested the ability of the selected compounds to perturb MT dynamics relative to the MT stabilizer PTX and the MT destabilizer CHC (Table 1), which disrupt the ability of dynein to transport its cargo. Of the eight LOPAC compounds that were tested, 4-phenyl-3-furoxanarbonitrile and Bay 11-7085 both exhibited MT destabilization characteristics. 4-Phenyl-3-furoxanarbonitrile is a nitric oxide donor (Medana *et al.*, 1994), while Bay 11-7085 is an NF- κ B inhibitor (Pierce *et al.*, 1997) that induces apoptosis with no other evidence of altering MT dynamics. Additionally, calcimycin showed only minor MT destabilization *in vitro* but has been demonstrated to cause blood platelet microtubules to depolymerize (Kenny and Chao, 1980). Incidentally, parthenolide, a previously recognized MT stabilizer (Miglietta *et al.*, 2004), was the only compound tested to induce MT polymerization *in vitro*. MT perturbation measurements by turbidity were effective for a small number of samples, but were not robust enough for high throughput assays using 384-well plates as evident by the large standard deviations. Attempts to resolve this issue will be discussed in the following chapter.

Table 1. Inhibition of GTP-induced assembly and hypernucleation/polymer stabilization of bovine brain tubulin by hits from the HCS analysis of the LOPAC1280 collection.

Compound (10 μM)	Percent Destabilization Relative to 10 μM CHC	Percent Stabilization Relative to 10 μM PTX
4-Phenyl-3-furoxancarboxitrile	50.71 \pm 10.7	NP
Parthenolide	-26.41 \pm 11.7	80.6 \pm 7.9
(<i>R</i>)-Apomorphine HCl hydrate	-2.51 \pm 54.8	NP
(<i>S</i>)-Apomorphine HCl hydrate	23.81 \pm 6.8	NP
6-Nitroso-1,2-benzopyrone	42.21 \pm 44.8	NP
Calcimycin	20 \pm 8.9	NP
GR(127935) HCl hydrate	0.4 \pm 19.5	NP
Bay 11-7085	64.5 \pm 27.4	NP

Data are mean values \pm SD (n=3). NP: No Polymerization.

3.2.2.3 Targeting Hsp Chaperones

Other factors such as the stability of the dynein-cargo complex play an important role in the transport of cytoplasmic dynein. In the case of the GR, complex formation begins with the ATP-dependent binding of Hsp70 to the GR along with the nonessential co-chaperone Hsp40 creating a ‘primed’ GR/Hsp70 complex (Murphy *et al.*, 2003). The GR/Hsp70 complex then binds to Hsp90 followed by the binding of p23 to stabilize this newly formed complex (Dittmar *et al.*, 1997). GR translocation is dependent on its association with Hsp90 and it has been suggested that the dynamics of this complex is dependent on ligand binding to the receptor (Pratt *et al.*, 2004). A number of Hsp-binding immunophilins then link the cargo complex to the light and intermediate chains of cytoplasmic dynein (Harrell *et al.*, 2004). Inhibition of Hsp90 with geldanamycin has been demonstrated to halt GR translocation (Czar *et al.*, 1997). Given the importance of the Hsps in stabilizing the cargo complex with cytoplasmic dynein, we investigated whether or not the targeting of these proteins inhibited GR translocation. Ssa1p and Hsc82p, the yeast versions of Hsp 70 and 90, respectively were used in this study because of the shared homology with mammalian versions (Schlesinger, 1986) along with the fact that the

formation of the cargo complex is conserved among different species (Harrell *et al.*, 2002). Therefore, screening for compounds that alter the ATPase activity of Hsps can indicate potential targets of compounds inhibiting GR translocation. In addition, the identification of Hsp inhibitors/activators could prove to be useful since Hsps are a therapeutic target in oncology (Calderwood *et al.*, 2006) and against neurodegenerative diseases because of their involvement in protein folding (Luo *et al.*, 2010).

Through the use of a colorimetric assay, the percent inhibition of ATPase activity was calculated by comparing the amount of inorganic phosphate released in the presence of the compounds relative to a DMSO control. Initial ATPase experiments resulted in immediate protein precipitation upon addition of malachite reagents used to detect free phosphate in solution. Precipitation occurred even at low divalent cation (Mg^{2+}) concentrations that could have interfered with the malachite reagents and free phosphate, forming water insoluble salts (Shih *et al.*, 2004). In order to overcome issues with precipitation, a modified malachite reagent was used further on. A variation in DMSO concentration demonstrated that assays tolerated up to 2% DMSO without any significant change in absorbance (Figure 22).

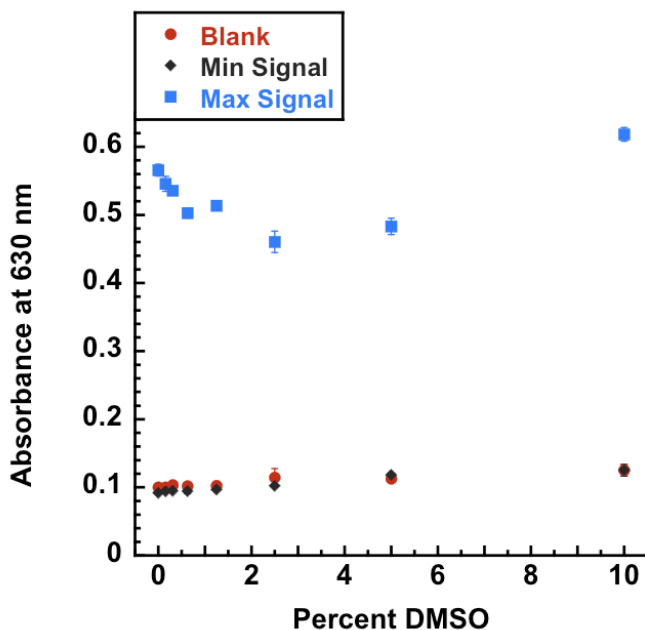


Figure 22. DMSO Tolerance of Hsp70 ATPase Activity

The ATPase activity of Ssa1p (Hsp70) was evaluated at different DMSO concentrations. The maximum (max) signal represented the amount of free inorganic phosphate detected with modified malachite reagents upon hydrolysis of ATP by Ssa1p as a function of absorbance at 630 nm. The minimum (min) signal represented the amount of free phosphate detected with modified malachite reagents in the absence of ATP. The blank signal represents the absorbance change of buffer and modified malachite reagents due to DMSO alone. Data represented as mean values with SD from three independent measurements.

Ssa1p in the presence of compound concentrations greater than 10 μ M caused protein precipitation once modified malachite reagents were added to the mixture, hindering measurement of ATPase activity. Protein precipitation was also observed in the absence of malachite reagents by evaluating by gel electrophoresis the supernatants and pellets of protein incubated with compounds (Figure 23).

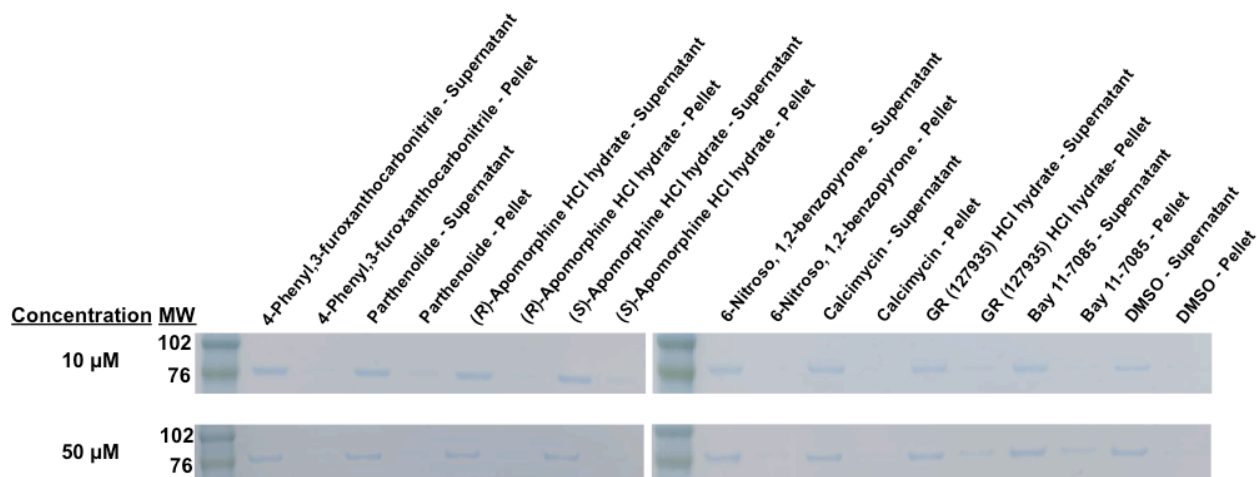


Figure 23. Evidence of Precipitation of Ssa1p Samples in the Presence of LOPAC Collection

Compared to Ssa1p samples treated with the LOPAC collection at 10 μM, greater amount of protein sample was present in the pellet when samples were treated with 50 μM suggesting the presence of a precipitate even in the absence of added modified malachite reagents.

At the highest concentration tested, 50 μM, none of the compounds had any significant effect on Hsc82p (the yeast homolog of Hsp90) (Figure 24). Hsp90 has a unique ATP binding pocket near its N-terminus, where only specific inhibitors such as geldanamycin can bind (Grenert *et al.*, 1997). The use of 17-AAG, which is an ansamycin antibiotic that binds Hsp90 (Neckers, 2002), as a control (Figure 3) exhibited expected inhibition of Hsp90 activity (Rowlands *et al.*, 2004). It is also apparent that GR(127935) HCl hydrate may be an Hsp90 activator rather than an inhibitor.

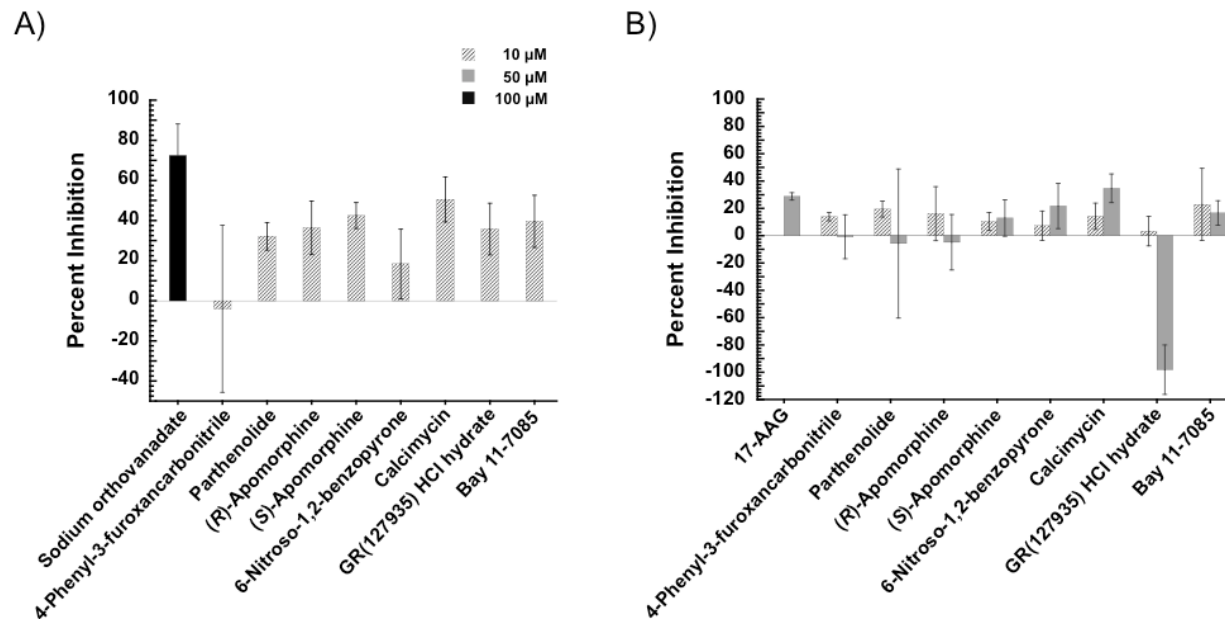


Figure 24. Hsp ATPase Inhibition Assays with LOPAC Collection

A) Percent inhibition of ATPase activity of Ssa1p with test compounds compared to DMSO control and sodium orthovanadate as a control. B) Percent inhibition of ATPase activity Hsc82p with test compounds compared to DMSO control and 17-AAG as a control. Data represented as mean values with SD from six independent measurements.

Although testing the ATPase activity inhibition of Ssa1p with compounds from the MLSCN revealed 29 potential inhibitors that inhibited activity >50%, many of these results had extraordinarily large standard deviation values and additional replicates are required to eliminate any false positive results (Figure 25). These results are due to the relatively low ATPase activity of hsp leading to a smaller window between maximum and minimum absorbance signals. In addition, several compounds, particularly compound #23, appeared to inhibit the ATPase activity >100% (i.e., sample absorbance was lower than the ATP only control). Given that percent inhibition >100% is not physically possible, the most likely explanation of these results is due to protein precipitation as experienced in earlier experiments with compounds from the LOPAC screen.

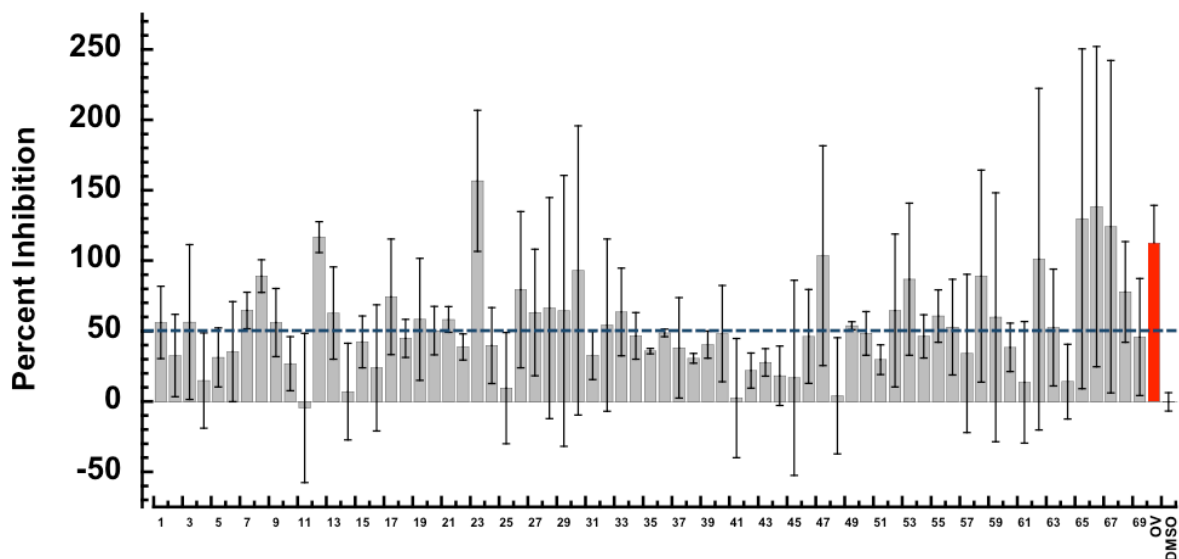


Figure 25. Hsp70 ATPase Inhibition Assay with MLSCN Collection

Percent ATPase activity inhibition of test compounds against Ssa1p compared to an orthovanadate (OV) control. Twenty-nine out of a total of 69 compounds exhibited competition >50%. Data represented as mean values with SD from three independent measurements.

3.2.2.4 Targeting Cytoplasmic Dynein

The ability of the compounds to selectively inhibit cytoplasmic dynein's ATP-driven motor activity was then investigated. An initial DMSO tolerance assay indicated that dynein assays tolerated up to 5% DMSO without any significant change in absorbance (Figure 26).

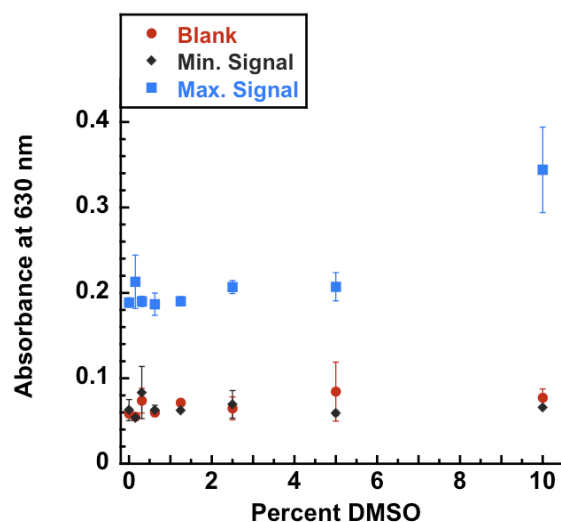


Figure 26. DMSO Tolerance of Cytoplasmic Dynein ATPase Activity

The ATPase activity of cytoplasmic dynein was evaluated at different DMSO concentrations. The maximum (max) signal represented the amount of free inorganic phosphate detected with modified malachite reagents upon hydrolysis of ATP by cytoplasmic dynein as a function of absorbance at 630 nm. The minimum (min) signal represented the amount of free phosphate detected with modified malachite reagents in the absence of ATP. The blank signal represents the absorbance change of buffer and modified malachite reagents due to DMSO alone. Data represented as mean values with SD from three independent measurements.

ATPase inhibition assays were then performed on the 1280 Sigma LOPAC library with a baculovirus/insect cell system-expressed, 380 kDa version of cytoplasmic dynein lacking the stalk in both basal and MT-stimulated environments. It is evident from Figure 27 that the addition of MTs increases the ATPase activity of the expressed construct of cytoplasmic dynein as expected. Since cytoplasmic dynein interacts with MTs via a unique MTBD, compounds that bind to the MTBD could potentially interfere with cytoplasmic dynein latching onto MTs and being transported in the GR-GFP translocation assay.

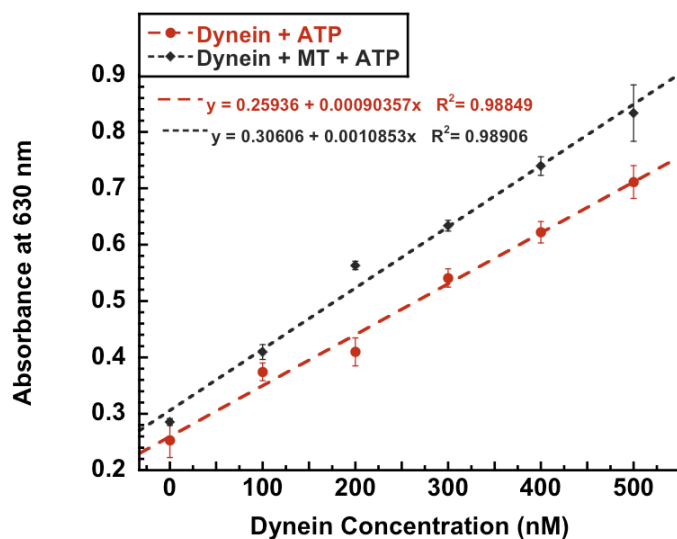


Figure 27. Comparison of Basal and MT-Stimulated ATPase Activity of Cytoplasmic Dynein

Red circles represented the amount of free inorganic phosphate detected with modified malachite reagents upon hydrolysis of ATP by basal cytoplasmic dynein as a function of absorbance at 630 nm. Black diamonds represented the amount of free inorganic phosphate detected with modified malachite reagents upon hydrolysis of ATP by MT-stimulated cytoplasmic dynein as a function of absorbance at 630 nm. Data represented as mean values with SD from three independent measurements and fit to a linear curve.

Results from the ATPase activity assays showed that only four of the compounds exhibited any significant concentration dependent effect on the ATPase activity of both basal and MT-stimulated activity of cytoplasmic dynein (Figure 28A,C). Both enantiomers of apomorphine inhibited cytoplasmic dynein at similar IC_{50} values, whether in the basal or MT-stimulated state (Table 2). 6-Nitroso-1,2-benzopyrone and Bay 11-7085 also inhibited cytoplasmic dynein but there was a more significant change in IC_{50} values between basal and MT-stimulated states. Although there was no indication that any of the compounds significantly altered the interaction of cytoplasmic dynein's MT-binding domain with the MTs, this type of comparison can be important in identifying compounds that interfere with the dynein-MT interaction in future screens. The decreased IC_{50} value of 6-nitroso-1,2-benzopyrone in the MT-stimulated state could indicate the targeting of nitric oxide or one of its oxidizing offspring on the sulfhydryls on tubulin heterodimers (Ikeda and Steiner, 1978) and subsequently destabilizing

the MTs as suggested by the decreased MT polymerization in Table 1, rather than binding to a defined active site. The double sigmoidal behavior of 6-nitroso-1,2-benzopyrone also suggested its non specific binding to cytoplasmic dynein (Figure 28B,D).

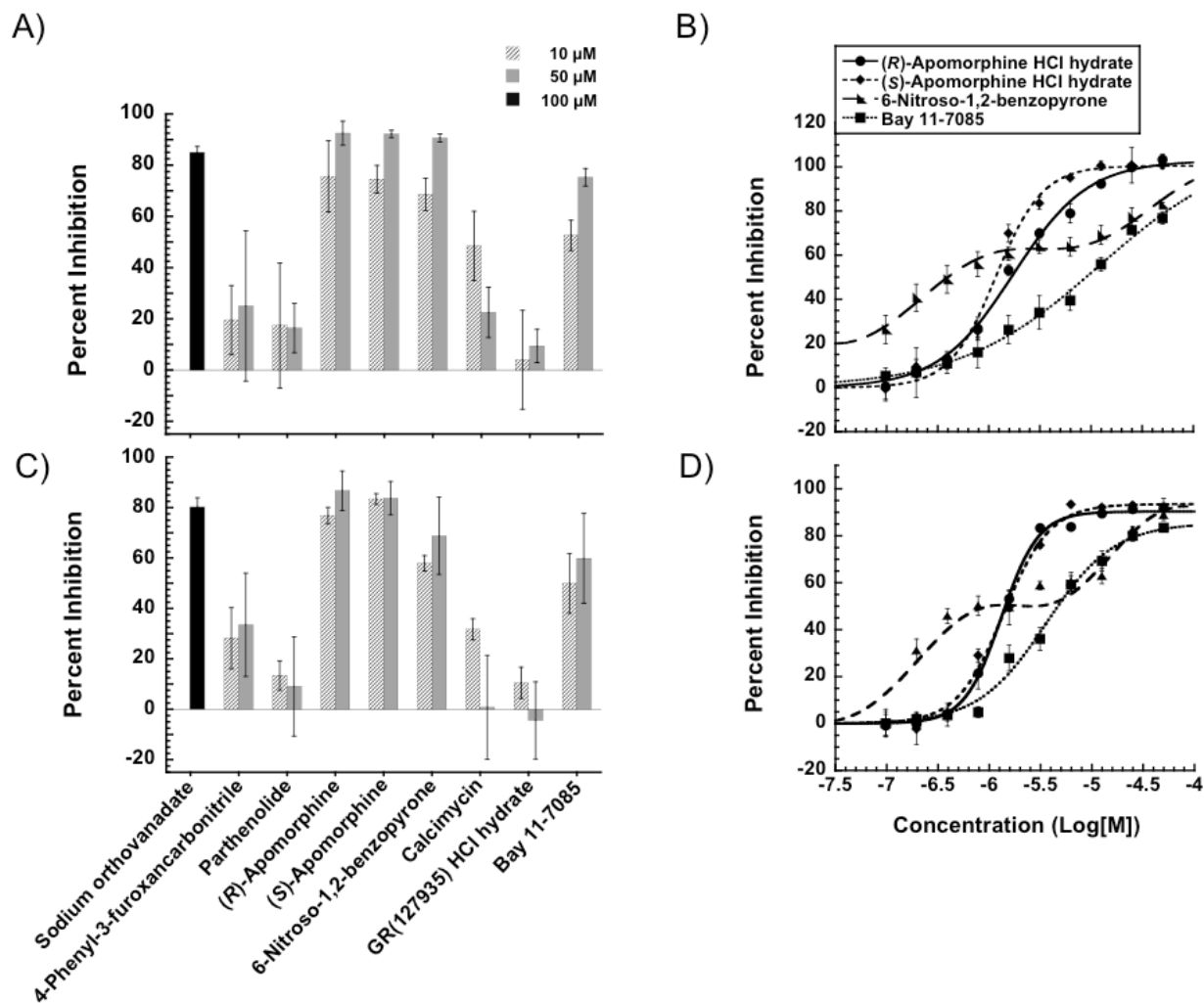


Figure 28. Cytoplasmic Dynein ATPase Inhibition Assay with LOPAC Collection

A) Percent inhibition of ATPase activity of basal dynein with test compounds compared to DMSO control and sodium orthovanadate as a control. B) Concentration-dependent inhibition of basal cytoplasmic dynein ATPase activities of 6-nitroso-1,2-benzopyrone, Bay 11-7805, and the enantiomers of apomorphine. C) Percent inhibition of ATPase activity of MT-stimulated dynein with test compounds compared to DMSO control and sodium orthovanadate as a control. D) Concentration-dependent inhibition of MT-stimulated cytoplasmic dynein ATPase activities of 6-nitroso-1,2-benzopyrone, Bay 11-7805, and the enantiomers of apomorphine. Data represented as mean values with SD from eight independent measurements.

Table 2. Biochemical IC₅₀ values of test agents against both basal and MT-stimulated cytoplasmic dynein.

Compound	IC ₅₀ (μM)	
	Basal	MT-Stimulated
(<i>R</i>)-Apomorphine HCl hydrate	1.5	1.7
(<i>S</i>)-Apomorphine HCl hydrate	1.5	1.3
6-Nitroso-1,2-benzopyrone	1.8	0.7
Bay 11-7085	4.6	8.9

The MLSCN compounds at a concentration of 20 μM were then tested for effects on the ATPase activity of basal cytoplasmic dynein. From the 69 compounds tested, it was encouraging to observe that 17 compounds exhibited a mean inhibition of ATPase activity by >50%.

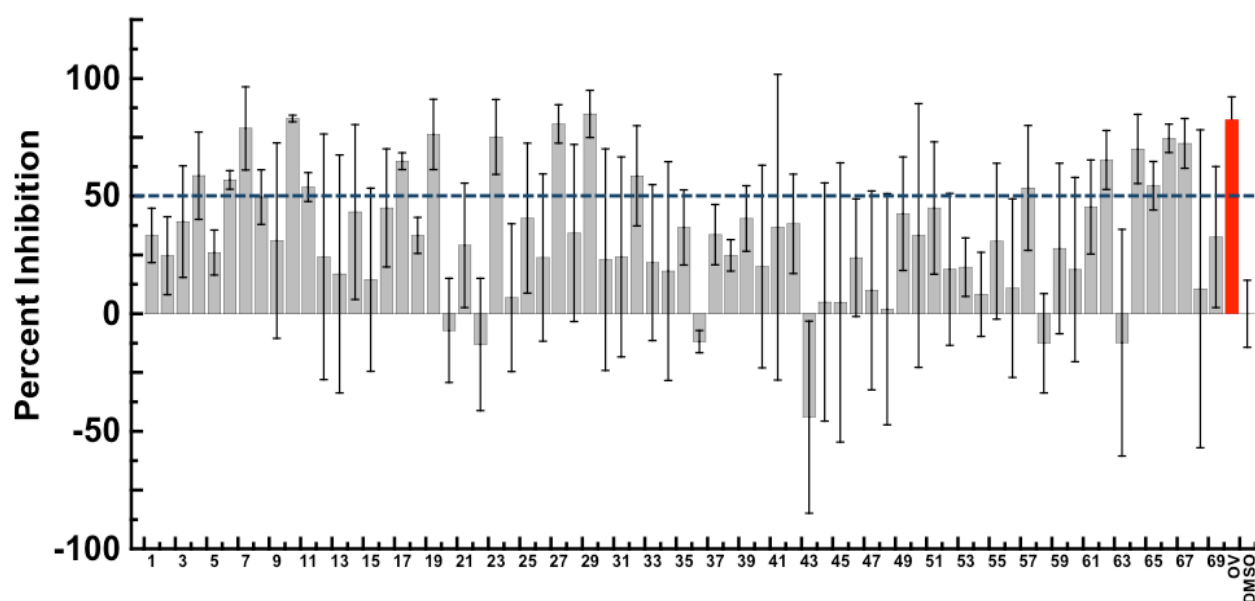


Figure 29. Cytoplasmic Dynein ATPase Inhibition Assay with MLSCN Collection

Percent ATPase activity inhibition of test compounds against basal cytoplasmic dynein compared to an orthovanadate (OV) control. Seventeen out of a total of 69 compounds exhibited competition >50% (chemical structures shown in Appendix A). Data represented as mean values with SD from three independent measurements.

3.2.2.5 Eliminating Non-Specific Motor Protein Inhibitors

Finally, in order to rule out any compounds that might be general ATPase motor protein inhibitors, the compounds' abilities to inhibit the ATPase activities of both kinesin and myosin

were tested, especially since the only known specific inhibitor of cytoplasmic dynein, purealin, is also a myosin activator. As with previous results, vehicle tolerance experiments indicated that DMSO could be used in myosin ATPase assays at a content of up to 5% before any decrease in absorbance signal was observed (Figure 30). Unfortunately, even after several exhaustive attempts to optimize buffers and reagents, measurement of kinesin ATPase activity was hindered by formation of a precipitate immediately after the addition of modified malachite reagents with any sample containing DMSO. Detection of the ATPase activity of kinesin was conducted using the buffer and protein concentrations described in Funk *et al.* (2004), but also displayed precipitate formation immediately after addition of modified malachite reagents and therefore future assays may require the use reagents obtained from Cytoskeleton, Inc for this assay to be successful.

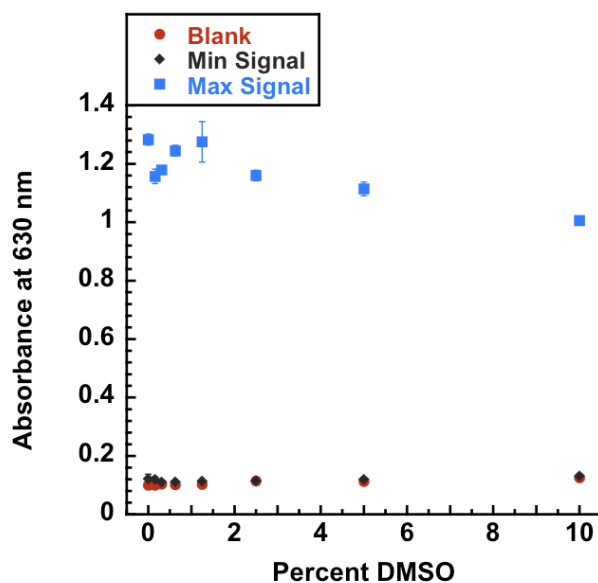


Figure 30. DMSO Tolerance of Myosin ATPase Activity

The ATPase activity of myosin was evaluated at different DMSO concentrations. The maximum (max) signal represented the amount of free inorganic phosphate detected with modified malachite reagents upon hydrolysis of ATP by myosin as a function of absorbance at 630 nm. The minimum (min) signal represented the amount of free phosphate detected with modified malachite reagents in the absence of ATP. The blank signal represents the absorbance change of buffer and modified malachite reagents due to DMSO alone. Data represented as mean values with SD from three independent measurements.

At the two concentrations the Sigma LOPAC members were examined, 10 μM and 50 μM , only the apomorphines exhibited any significant inhibition of the ATPase activity of myosin (Figure 31A) with concentration-dependent behavior and IC_{50} values of 1.4 and 3.2 μM for the *R* and *S* enantiomers, respectively (Figure 31B). The broad spectrum of targets apomorphine exhibited in our assays suggests that apomorphine would not be an attractive cytoplasmic dynein inhibitor despite being the most potent in our assays; i.e., these enantiomers were promiscuous compounds.

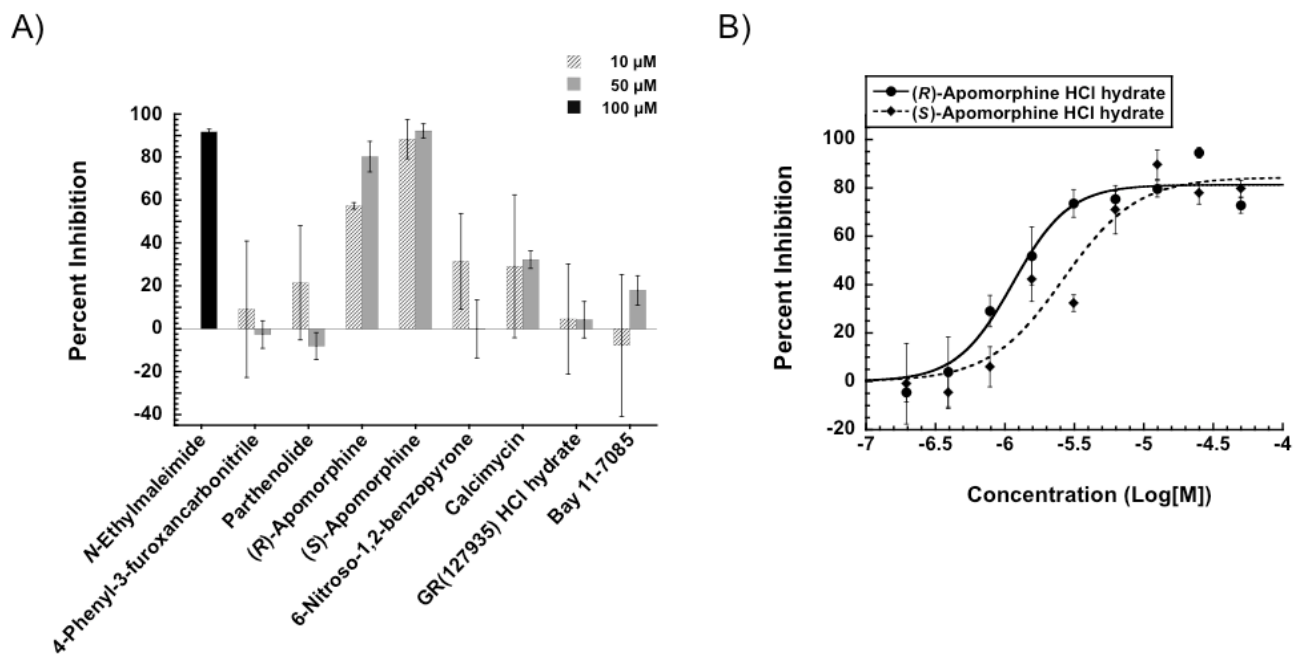


Figure 31. Myosin ATPase Inhibition Assay with LOPAC Collection

A) Percent inhibition of ATPase activity of myosin with test compounds compared to DMSO control and NEM as a control. B) Concentration-dependent inhibition of myosin ATPase activity by the enantiomers of apomorphine. Data represented as mean values with SD from six independent measurements.

Upon evaluation of the MLSCN collection against the ATPase activity of myosin, it was revealed that only two compounds out of 69 inhibited the ATPase activity of myosin >50%.

This was an encouraging observation suggesting that indeed compounds were specifically targeting the cytoplasmic dynein complex to inhibit GR-GFP translocation.

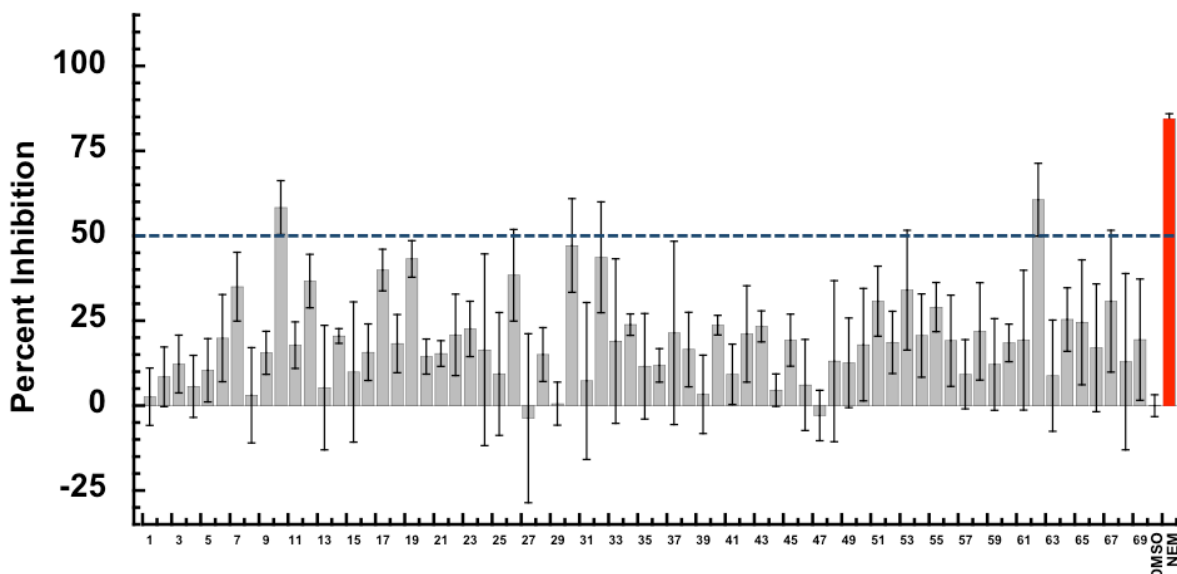


Figure 32. Myosin ATPase Inhibition Assay with MLSCN Collection

Percent ATPase activity inhibition of test compounds against myosin compared to an *N*-ethylmaleimide (NEM) control. Only two out of a total of 69 compounds exhibited competition >50% (chemical structures shown in Appendix A). Data represented as mean values with SD from three independent measurements.

3.3 CONCLUSIONS

Cell-based screening reliably revealed a number of small molecules from LOPAC and MLSCN collections that stalled the agonist-induced transport of GR from the cytoplasm to the nucleus. Since there are a number of potential reasons for interruption of this dynein-mediated transport, I sought to identify the target(s) of these molecules through a number of biochemical assays applicable to the translocation process. The potential target(s) of these molecules were summarized in Table 3.

Table 3. Summary of the potential target(s) of molecules that inhibited GR translocation.

Compound	Dynein	Microtubules	Hsp70	Hsp90	GR	Myosin
4-Phenyl-3-furoxanarbonitrile	×	×	×	×	×	×
Parthenolide	×	✓	×	×	×	×
(R)-Apomorphine HCl Hydrate	✓	×	×	×	×	✓
(S)-Apomorphine HCl Hydrate	✓	×	×	×	×	✓
6-Nitroso-1,2-benzopyrone	✓	×	×	×	×	×
Calcimycin	×	×	✓	×	×	×
GR-127935	×	×	×	×	×	×
Bay 11-7085	✓	✓	×	×	×	×
MLSCN#4	✓	NA	NA	NA	✓	×
MLSCN#6	✓	NA	NA	NA	×	×
MLSCN#7	✓	NA	NA	NA	×	×
MLSCN#10	✓	NA	NA	NA	×	✓
MLSCN#11	✓	NA	NA	NA	✓	×
MLSCN#17	✓	NA	NA	NA	✓	×
MLSCN#19	✓	NA	NA	NA	×	×
MLSCN#23	✓	NA	NA	NA	×	×
MLSCN#27	✓	NA	NA	NA	×	×
MLSCN#29	✓	NA	NA	NA	×	×
MLSCN#32	✓	NA	NA	NA	×	×
MLSCN#57	✓	NA	NA	NA	×	×
MLSCN#62	✓	NA	NA	NA	×	✓
MLSCN#64	✓	NA	NA	NA	×	×
MLSCN#65	✓	NA	NA	NA	×	×
MLSCN#66	✓	NA	NA	NA	×	×
MLSCN#67	✓	NA	NA	NA	×	×

A (✓) indicated that compounds targeted $\geq 50\%$ a particular component of the cytoplasmic dynein-cargo complex, while a (×) indicated that there was little ($< 50\%$) or no interaction of compound with target(s).

From the seven LOPAC compounds tested, the apomorphine enantiomers exhibited the most potency towards the ATPase activities of cytoplasmic dynein and myosin, but also appeared to inhibit GR binding. The pleiotropic property of these mirror image molecules, however, makes them unattractive for further study in this quest. Parthenolide is a previously recognized MT stabilizer that most likely altered the tracks needed for dynein to transport GR-GFP to the nuclei. Based on the chemical structures of the remaining cell-based screening hits

from the LOPAC collection, it is likely that the compounds targeted reactive sulfhydryls of dynein and MTs, both contributing to inhibition of dynein-mediated transport. The reliability of the LOPAC hits from the cell-based screen was further supplemented by the concentration dependent inhibition of activity determined from the biochemical assays with R^2 values >0.9 for the fitted curves. A number of compounds from the MLSCN collection were then tested using 384-well plates. Seventeen compounds were shown to have a mean ATPase activity inhibition $>50\%$ against cytoplasmic dynein. Several of these compounds also targeted either GR or myosin. Given the large standard deviation of the Hsp70 assay, further replicates are needed to reach any final conclusions regarding inhibition of ATPase activity. Ideally, specific dynein-mediated transport inhibitors would target dynein itself rather than one of the other important proteins associated with the transport process. Although the hits from the cell-based screen of the 1280 LOPAC collection did not exhibit this desired profile, a number of compounds from the MLSCN screen appear to have greater specificity towards dynein. Future experiments involving the ATPase activity inhibition assay of Hsp90 and the MT perturbation screen will help categorize how compounds inhibit GR translocation. Concentration-dependent assays with the compounds will also determine their binding strength and specificity. Regardless of identification of dynein modulators from the tested libraries, these assays demonstrated the ability to examine cell permeable inhibitors of GR translocation followed by an attempt to identify the target(s) of these molecules through biochemical screening. We envision that further screening of additional compound libraries for inhibition of cell-based cytoplasmic dynein transport will reveal specific cytoplasmic dynein and/or Hsp inhibitors. We also believe this route of identifying inhibitors via a cell based assay followed by target validation is an

improvement over conventional biochemical screening that suffers when “hits” eventually are cell impermeable and/or severely cytotoxic.

4.0 DEVELOPMENT OF BIOSENSOR APPLICATIONS TO EVALUATE MICROTUBULE PERTURBING AGENTS

4.1 INTRODUCTION

Results published in Daghestani, H.N.; Fernig, D.G.; Day, B.W. Evaluation of biosensor surfaces for the detection of microtubule perturbation. *Biosens. Bioelectron.*, **2009**, 25, 136-141.

Biosensors have many applications, providing data to help explain biological questions ranging from macromolecular interactions (Lillis *et al.*, 2006) to the binding of small molecules to surfaces and immobilized large molecules (Karlsson, 2004; Boozer *et al.*, 2006). There are several types of instruments available that use different detection methods, each possessing their own advantages and disadvantages. Although DPI provides more detailed information of samples on the sensing surface, its current flow-through configuration consumes a much larger amount of sample in comparison with RM's small volume (microliter) cuvette. The RM cuvettes are also re-usable for multiple experiments. The ability to grow MTs on surfaces is also an important step in the development of more robust high throughput (e.g., microtiter plate-based or microarray) assays to monitor MT polymerization in the presence of various de-/stabilizing agents as discussed in the previous chapter. Here, a novel method is discussed to polymerize MTs on biosensor surfaces and demonstrate the ability to distinguish the interaction of stabilizers from destabilizers on MTs using a combination of RM and DPI, a major advance on previous

work where only the binding of MT inhibitors to tubulin immobilized onto SPR surfaces has been reported (Aoyama *et al.*, 2007).

4.2 RESULTS & DISCUSSION

4.2.1 Microtubule Polymerization on Biosensor Surfaces

Initial attempts to immobilize tubulin directly onto non-functionalized surfaces were unsuccessful, with changes in thickness of the layer determined by DPI measurements rarely exceeding 2 nm, rather than the expected 4 nm width or 8 nm height of a tubulin heterodimer, most likely due to denaturation of the protein upon contact with the somewhat hydrophobic biosensor surfaces (Andrade and Hlady, 1986). After trials with various functionalized surfaces, biotinylated surfaces appeared to provide the best environment for a streptavidin layer followed by subsequent biotinylated tubulin and MT layers.

A key feature of tubulin polymerization is its temperature dependence (Hamel, 2003), with the ordered assembly of mammalian tubulin occurring optimally at 37 °C, while cold temperatures tend to destabilize MTs. Turbidimetry experiments, most commonly used to measure MT polymerization and the influence of test agents on tubulin/MT dynamics (Hamel, 2003; Hall and Minton, 2005), are typically started at 0 °C to 4 °C and the change in absorbance is recorded while increasing the temperature to 30 °C (typically 30 °C or 37 °C) and subsequently dropping the temperature back to 4 °C to determine the stability of the MTs. The ability of biotinylated tubulin to successfully polymerize was assessed by performing a standard turbidity assay. Tubulin conjugated with a maleimide-based biotin was inactive, most likely

because microtubule polymerization is very sensitive to blocking of the many free sulfhydryl groups on α and β tubulin (Ikeda and Steiner, 1978). Although biotin conjugation to tubulin via amine-reactive agents renders far more labels on tubulin than thiol-reactive groups, biotinylated tubulin was still active. Polymer formation required more time to occur when only biotinylated tubulin was used compared to a 1:1 mixture of tubulin:biotinylated-tubulin and even more so than tubulin alone (Figure 33).

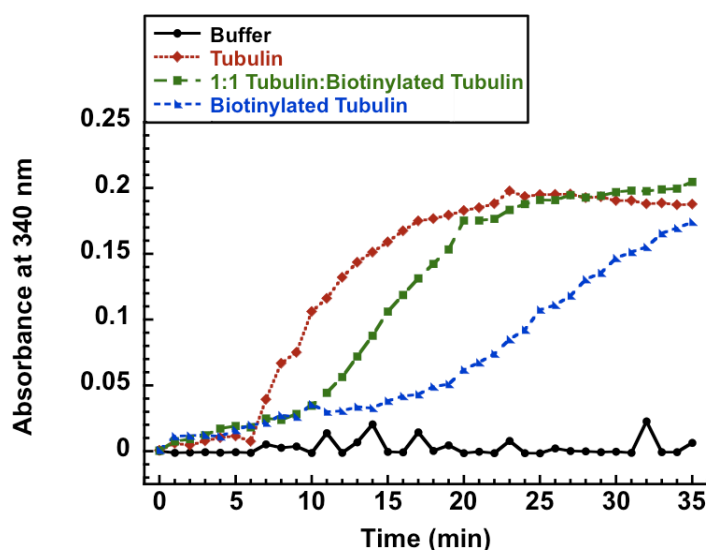


Figure 33. Functionality of Biotinylated Tubulin

Microtubule polymerization was monitored by the change in turbidity at 340 nm when 10 μ M tubulin supplemented with GTP was warmed from 4 $^{\circ}$ C to 37 $^{\circ}$ C. The absorbance of 1 M MSG buffer did not change due to the change in temperature, while the bovine brain tubulin-containing sample increased in absorbance within 5 min of warming. A 1:1 mixture of tubulin:biotinylated tubulin formed the same amount of polymer as the tubulin sample but required a longer time to fully polymerize. Biotinylated tubulin was also capable of forming polymer but at a much slower rate than the former samples, suggesting that biotinylated tubulin was active for further studies.

Streptavidin was deposited on a biotinylated DPI Amine *AnaChip*TM to form a layer with a mass of 3.34 ng/mm^2 , thickness of 5.94 nm and a density of 0.56 g/cm^3 , consistent with previously obtained values and the dimensions of streptavidin derived from X-ray crystallography (Swann *et al.*, 2003). The addition of biotinylated tubulin caused mass and

thickness to increase to 4.12 ng/mm² and 7.18 nm, respectively, accompanied by an increase in density to 0.57(5) g/cm³, which indicates binding of biotinylated tubulin to the streptavidin surface (Figure 34).

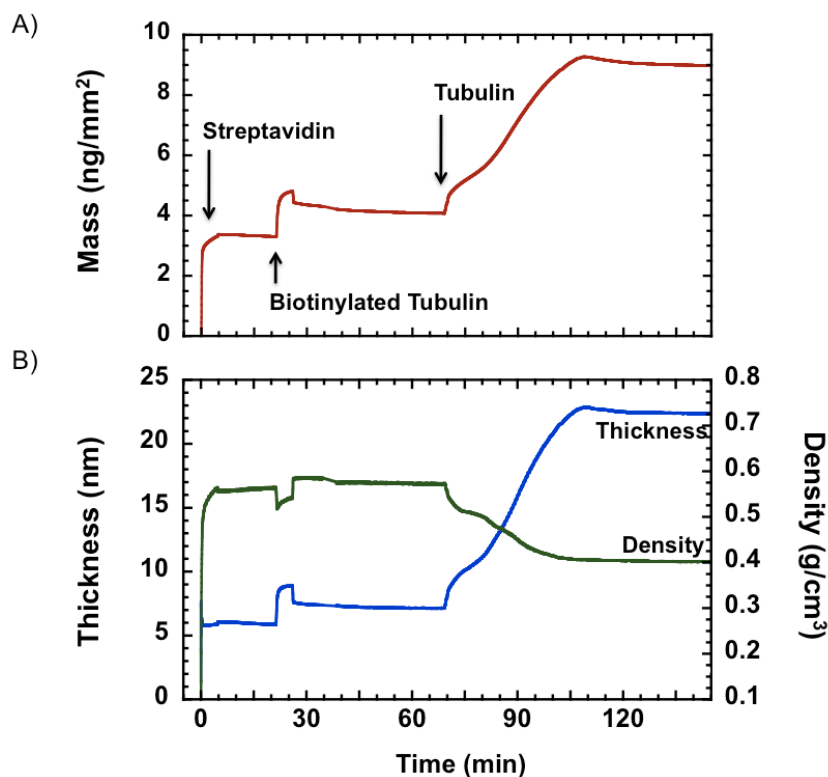


Figure 34. Resolved Mass, Thickness, and Density of Tubulin Assembly as Assessed with DPI

(A) The increase in mass when streptavidin, biotinylated-tubulin, and tubulin were added indicated specific binding to each of the underlying layers. (B) The increase in thickness with decreasing density after the addition of tubulin to biotinylated tubulin suggested the formation of MTs on the biosensor surface [adapted from Daghestani *et al.*, 2009 with permission from publisher].

The increase in thickness above the streptavidin layer was only 1.24 nm, rather than the size of a tubulin heterodimer (~8 nm), accompanied by a slight increase of 0.01 g/cm³ in the density. The small increase in mass (molar ratio of biotinylated tubulin to streptavidin of 1:7) suggested that the layer of tubulin formed might not be optically homogeneous, since it corresponds to a surface coverage by biotinylated tubulin of the order of 12%, compared to 35% coverage for streptavidin (Swann *et al.*, 2004). The initial binding of biotinylated-tubulin to the

streptavidin was rapid, however, which suggested the association of biotinylated-tubulin to streptavidin to be specific, while the increase in density indicated that other processes occurred simultaneously. Thus, an alternative but not mutually exclusive explanation is that, since tubulin has many exposed lysine residues, biotin may occupy multiple positions on the heterodimer and at various locations throughout, resulting in a number of different orientations of biotinylated-tubulin bound to streptavidin. For example, heterodimers that lie on their sides might fill any gaps between streptavidin molecules, accounting for the small thickness and density increase. Other orientations are likely to either promote or block subsequent binding of heterodimers to the surface depending on its surrounding environment. Nonetheless, the immobilized biotinylated-tubulin was sufficient to provide a starting point for MT growth. Any unbound biotinylated-tubulin was then washed away when the injection was complete and flow returned to running buffer. The subsequent introduction of tubulin in sample buffer caused a significant increase in mass and thickness reaching up to 22.85 nm with a continuous decrease in density to 0.40 g/cm^3 . The increase in thickness provided evidence that MTs were growing vertically on the surface, while the decrease in density is in accord with the formation of hollow MTs that are quite sparse, rather than continuous layering of tubulin dimers onto the surface. The first 10 min of the process may represent the initial nucleation and elongation process of protofilaments at a rate of 0.236 nm/min before an inflection point, where the extended protofilaments is believed to join together laterally to form the microtubule and the growth process accelerated to 0.436 nm/min (Figure 35).

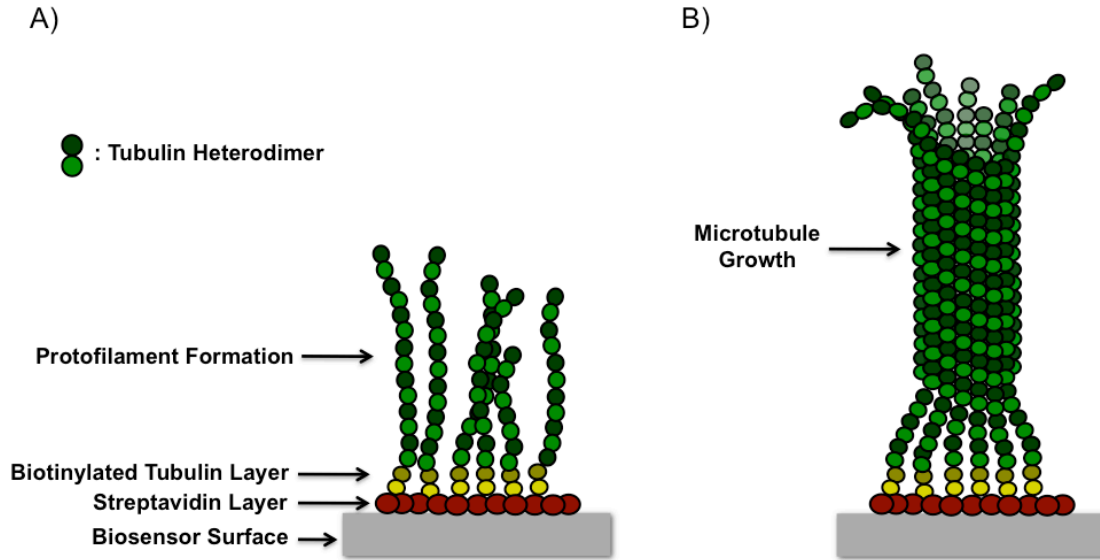


Figure 35. Schematic Representation of the Microtubule Polymerization Process on Biosensor Surfaces

(A) Schematic representation of the formation of a uniform streptavidin layer on a biotin chip followed by the growth of tubulin protofilaments on biotinylated tubulin. (B) As protofilaments continue to grow in length, they join laterally to form MTs [adapted from Daghestani *et al.*, 2009 with permission from publisher].

Microtubule growth was halted in instances where the tubulin flow was decreased or stopped for an incubation, which reflects the need for mixing to take place near the surface. In a flow system, which is limited by the properties of laminar flow, mixing can only occur by flowing the sample relatively rapidly. The DPI chips were cleaned for re-use with various surfactant cleaners, sodium dodecyl sulfate, ethanol/acetone, etc., all while sonicating the chips followed by rinsing with deionized water. When chips were placed back into the instrument, however, the fringes had very low contrast and baseline signal was not stable enough to perform an experiment. Other harsher methods that etch the surface could be used, but will likely require the reintroduction of amine functional groups onto the chip surface before use.

Once MT polymerization was established on such surfaces using data from DPI, the assembly of MTs was evaluated using the RM cuvette system in an effort to establish a technique that conserves sample, is more user-friendly and applicable to larger sampling sets. The addition of streptavidin in 10 mM phosphate buffer, pH 7.7, at 37 °C to a biotinylated RM cuvette caused

a typical increase in response to ~2000 arcseconds over approximately 15 min and excess streptavidin was removed by a phosphate buffer wash (Figure 36). The phosphate buffer was then replaced by 1 M MSG buffer, which caused a large bulk shift, followed by the addition of biotinylated tubulin until the response reached a plateau. The addition of soluble tubulin to the biotinylated-tubulin-streptavidin RM surface caused a bulk shift over the first 5 s, followed by a continuous increase in response, corresponding to an increase in mass at the surface. In other attempts to assemble MTs on the surface, the addition of GTP after tubulin caused the increase in response to halt, possibly due to the polymerization of tubulin in solution rather than on the surface. It is thought that the presence of a high concentration of GTP near the surface of the cuvette and the biotinylated tubulin allows for the tubulin to diffuse towards and bind to the surface.

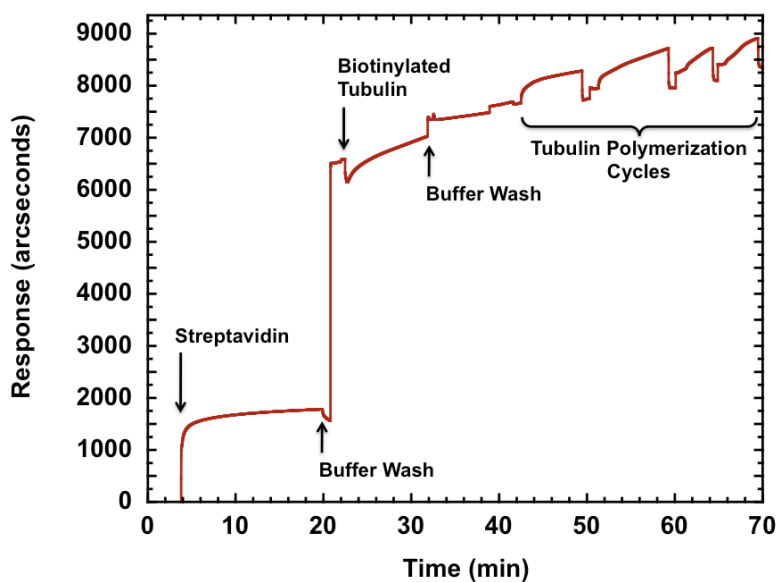


Figure 36. Microtubule Assembly Process as Assessed with RM

The increase in response due to the addition of streptavidin and subsequently biotinylated tubulin without the decrease in signal upon buffer washes indicated their specific binding events. The addition of tubulin to the biotinylated tubulin layer containing GTP demonstrated continuous growth periods and was repeatable over several buffer wash cycles without any significant loss of underlying biotinylated tubulin layer [adapted from Daghestani *et al.*, 2009 with permission from publisher].

The non-linear behavior of signal increase and occasional “bursts” of sudden increase in response in Figure 37 suggested periods of MT rescue and catastrophe events. The return of response back to baseline after a buffer wash indicated the removal of the polymerized tubulin layer rather than the underlying biotinylated tubulin layer. Tubulin polymerization on such surfaces was reproducible over several (~20) cycles, but activity was lost once the surface was left at room temperature or at 4 °C overnight.

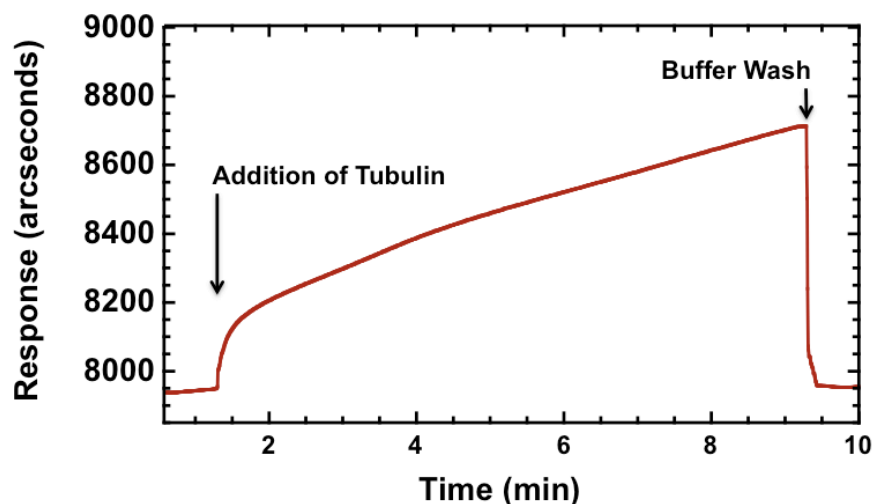


Figure 37. Microtubule Polymerization on a RM Biosensor

Binding profile of tubulin to a biotinylated tubulin surface in 1 M MSG buffer, pH 6.6, with GTP at 37 °C using the RM biosensor. The response continuously increased until a buffer wash was performed and the process repeated. The increase in response was non-linear and exhibited “bursts” that suggest rescue and catastrophe events [adapted from Daghestani *et al.*, 2009 with permission from publisher].

The ability of preformed MTs to bind to a biotinylated tubulin surface was also assessed. The binding of preformed MTs, however, was non-specific as indicated by the step response upon sample addition and subsequent wash. The large change in response was primarily due to a bulk shift of the MTs and further response increase was not observed in instances where preformed MTs were added (Figure 38), suggesting that MTs simply lay horizontally on the surface rather than the suggested model in Figure 35B. The buffer wash following preformed MT deposition also appeared to remove some of the biotinylated tubulin layer.

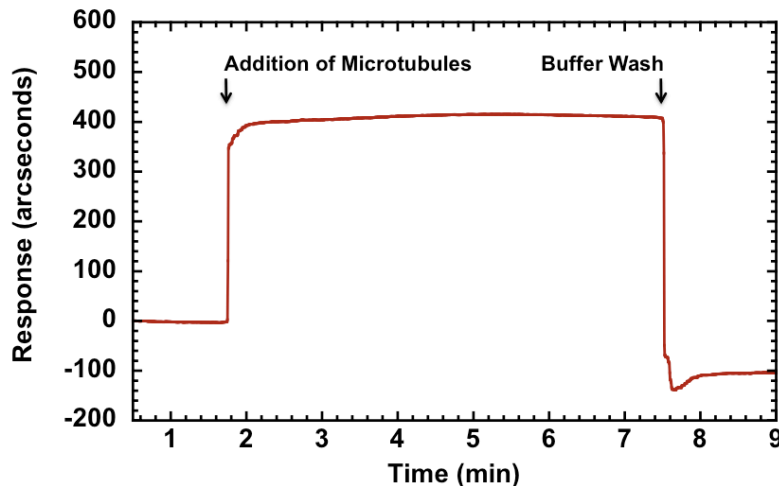


Figure 38. Binding of Preformed Microtubules to a Biotinylated Tubulin Surface as Assessed with RM

The addition of preformed microtubules to a biotinylated tubulin surface and subsequent buffer wash caused a step-like response suggesting non-specific binding to the surface. The buffer wash also caused a loss in biotinylated tubulin layer.

4.2.2 Temperature Dependent Microtubule Polymerization using Biosensors

The temperature dependence of tubulin polymerization was evaluated on the RM surface to further demonstrate the functionality of tubulin on biosensor surfaces. Due to fogging of the optical system, the lowest temperature achievable on the system was 15 °C, which is still an acceptable starting point for soluble (unpolymerized) tubulin, since normal polymerization does not take place at temperatures below 15 °C (Olmsted and Borisy, 1973). Since refractive index is also temperature-dependent (Grassi and Georgiadis, 1999), the response from a separate channel (reference channel) containing only sample buffer was subtracted from the sample channel to obtain the absolute change in response upon temperature change. The binding of tubulin to the surface at 15 °C was a slow process (Figure 39) and reached a plateau with a lower response rather than exhibiting the continuously increasing response observed at 37 °C in Figure 37. The lower response of tubulin binding at 15 °C was most likely due to the lower affinity of

heterodimer association at such temperatures. Once the temperature was increased to 37 °C, the absolute change in response increased, suggesting increased binding to the surface. It is worth mentioning that the change in response in Figure 39 does not correspond to the observations from Figure 37, most likely due to the preference and shift in dynamics of tubulin to polymerize in solution rather than on the surface with such conditions. This is also suggested by the observation that addition of GTP after the addition of tubulin did not show a large increase in response as in Figure 37. MT polymerization in solution most likely occurs in both situations due to the constant collisions of tubulin heterodimers and protofilaments with each other. The difference in the amount of solution polymerization is speculated to be a result of Fick's law of diffusion; at lower temperatures, mass transfer of the macromolecules to the surface is decreased due to the increased viscosity of the solution (Seeton, 2006). As a result, there is less protofilament seeding occurring near the surface at 15 °C and polymerization in solution becomes more favorable once temperature is increased. When tubulin is introduced at 37 °C, mass transfer of the tubulin to the surface is greater and the current temperature allows for binding to biotinylated tubulin and further MT polymerization onto the surface. Previous SPR studies have also indicated that binding association constants of antigen-antibody interactions are greater when temperature is increased (Zeder-Lutz *et al.*, 1997), supporting the argument that increased mass transfer at higher temperatures affects the rate of interactions at a surface.

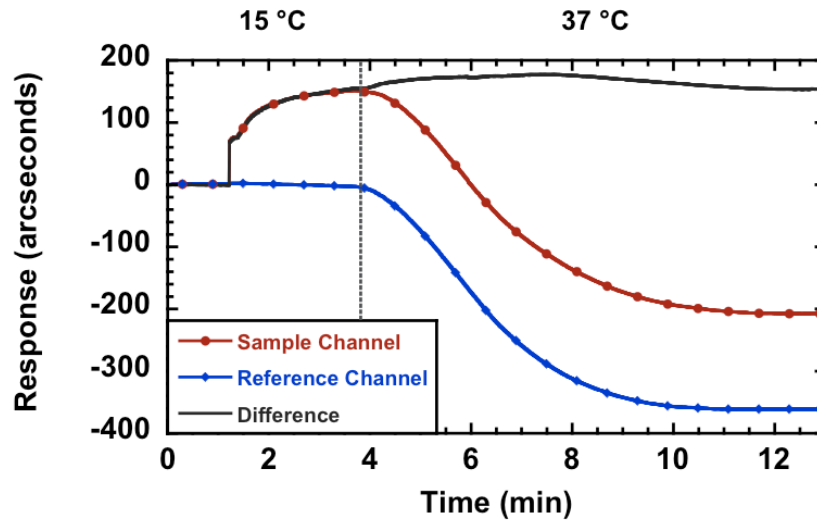


Figure 39. Temperature Dependent Microtubule Polymerization assessed with RM

Temperature dependence of tubulin binding to biotinylated tubulin using the RM biosensor. “Sample Channel” represents the observed response of the instrument upon the addition of tubulin to a biotinylated tubulin surface at 15 °C followed by an increase in temperature to 37 °C, where the dotted line indicates the start of temperature change. “Reference Channel” represents the change in response due to the change in temperature. “Difference” represents the subtraction of “Reference Channel” from the “Sample Channel” to give the absolute change in response due to the change in temperature [adapted from Daghestani *et al.*, 2009 with permission from publisher].

In an effort to evaluate the effect of stabilizers and destabilizers on the binding of tubulin to biotinylated-tubulin surfaces, either paclitaxel or colchicine, respectively, were introduced to the mixture. When paclitaxel was added to the cuvette before the addition of tubulin, a similar binding profile was observed, even after the temperature change (Figure 40). The binding response was also generally more stable to subsequent decreases in absolute response observed after a few minutes with tubulin alone, which most likely represent events of MT disassembly. Colchicine had a delayed inhibition effect when added before tubulin, in all likelihood due to its known slow association rate with tubulin (Banerjee *et al.*, 1997), especially since it completely inhibited binding when pre-incubated with tubulin on ice for 15 min prior to the addition of the tubulin to the cuvette. This provided further evidence that microtubules bound to the surface were functional and exhibited similar characteristics as those in solution.

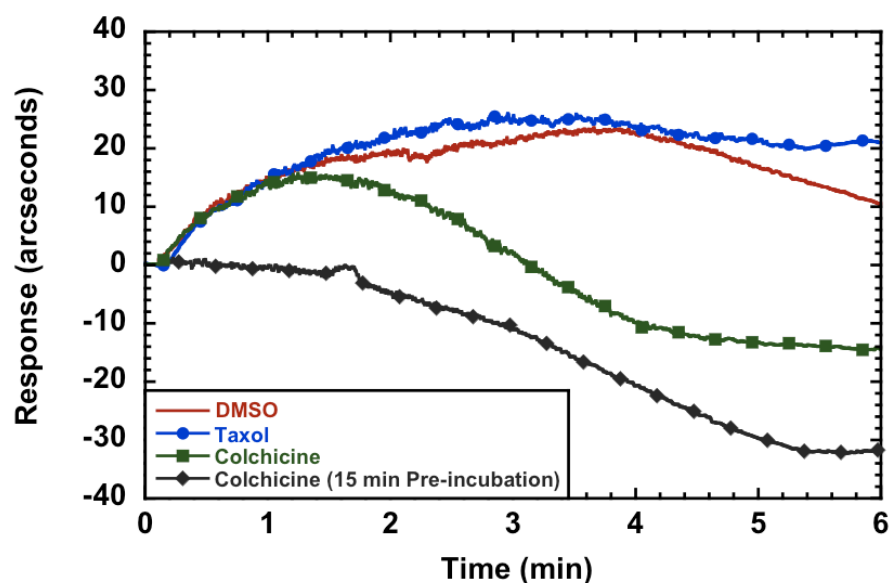


Figure 40. Effect of Microtubule Perturbing Agents on the Temperature-Dependent Polymerization as Assessed with RM

The absolute change in response starting from the time of temperature change from 15 to 37 °C is shown. Paclitaxel addition gave a similar response to tubulin with GTP, but the MTs formed remained more stable from disassembly afterwards. Colchicine caused a decrease in the response after an initial increase in response, but completely inhibited binding when it was pre-incubated with tubulin [adapted from Daghestani *et al.*, 2009 with permission from publisher].

4.2.3 Comparison of Microtubule-Perturbing Agents Using RM Biosensors

The binding profile of microtubule polymerization generally did not fit well to mono- or bi-phasic binding profiles upon analysis with FASTfit Software (NeoSensors, Ltd., UK). This is not necessarily surprising given the complexity of MT polymerization (Hall and Minton, 2005), which involves many processes, such as GTP binding and hydrolysis, as well as constant assembly and disassembly events (Jordan and Wilson, 2004). The most consistent parameter, however, that described interactions of tubulin with various agents from biosensor experiments appeared to be the slopes of initial rates of assembly: the change in response during the first 15 s after tubulin is added to a cuvette pre-warmed to 37 °C with buffer containing GTP (allowing for

a 5 s mixing time during the bulk shift). These values appear to provide a means to evaluate the polymerization process in the presence of various de-/stabilizer agents. When paclitaxel and epothilone B, both MT stabilizers, were introduced to the system, the slopes of initial rates (mean \pm SD, n=3) were significantly higher at 1.50 ± 0.27 arcseconds/s and 1.04 ± 0.13 arcseconds/s, respectively, compared to 0.37 ± 0.11 arcseconds/s for tubulin containing GTP only (Figure 41). This is expected given that tubulin in the presence of paclitaxel polymerizes at a faster rate than in the presence of epothilone B (Gertsch *et al.*, 2009). In the presence of MT destabilizers such as colchicine and dolastatin 10, the slopes of initial rates were lower than in their absence at 0.05 ± 0.01 arcseconds/s and 0.27 ± 0.08 arcseconds/s, respectively. Thus, the present approach provides a means for screening, differentiating compounds acting as stabilizers from those that are destabilizers based on the slopes of initial rates.

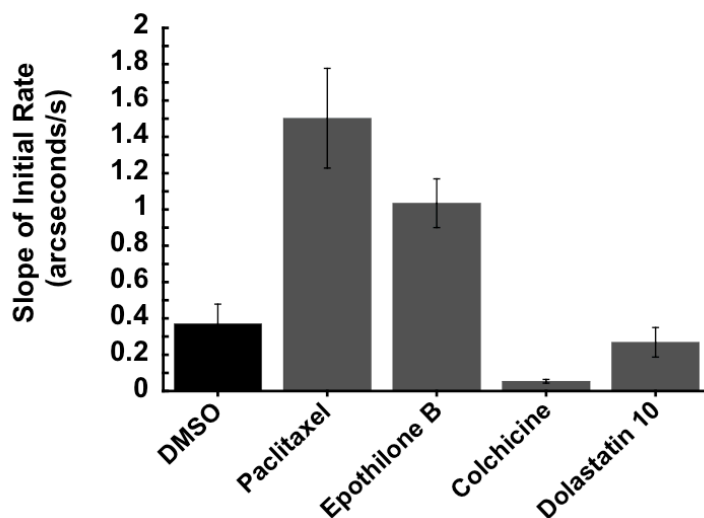


Figure 41. Comparison of the Slopes of Initial Rates of Microtubule Assembly with Various Microtubule-Perturbing Agents

Paclitaxel and epothilone B, both MT stabilizers, exhibited greater slopes of initial rates in comparison with the DMSO control. MT destabilizers, colchicine and dolastatin, gave lower values than the control. Values are reported as a mean with n=3 and the error bars representing the standard deviation. The pair-wise P values in comparison with the tubulin control were 0.035, 0.005, 0.033, and 0.838 for paclitaxel, epothilone B, colchicine, and dolastatin 10, respectively [adapted from Daghestani *et al.*, 2009 with permission from publisher].

4.3 CONCLUSIONS

The ability to grow MTs vertically on surfaces is a novel approach and vast improvement over other techniques that directly deposit soluble tubulin onto SPR surfaces to evaluate agent binding. This is because the functionality and dynamics of MT polymerization can be assessed in the presence of compounds rather than merely agent binding. In addition, the deposition of tubulin directly onto a surface may likely block agent binding access to a large surface area of the protein. Resolved mass, thickness, and density measurements from DPI indicated the growth of protofilaments on a biotinylated-tubulin/streptavidin surface, followed by the polymerization of microtubules. MT polymerization on surfaces was then evaluated on RM biosensors in order to increase throughput and decrease sample consumption. The temperature and perturbing agent –dependence of MT polymerization evaluated by RM behaved similarly to turbidity experiments. MT stabilizing agents were clearly distinguishable from MT destabilizing agents compared to a DMSO control using the slopes of initial rates. These results are encouraging for future screening of MT perturbing compounds. Although RM biosensors can only accommodate two simultaneous channels, RWG biosensors offer a very similar detection capability and sensitivity but are capable of implementation into 96-, 384-, and 1536-well plates for higher throughput and even less sample consumption.

5.0 BIOPHYSICAL CHARACTERIZATION OF CYTOPLASMIC DYNEIN

5.1 INTRODUCTION

The large size of cytoplasmic dynein renders structural characterization immensely difficult by conventional NMR and X-ray crystallography. A number of researchers have attempted to characterize the structure of cytoplasmic dynein by negative stain and cryo- electron microscopy, but have not been able to break the 25Å resolution barrier (Samso and Koonce, 2004). Many of these structures have provided an immense amount of information regarding the structural changes that take place upon ATP binding and hydrolysis followed by the release of ADP (Burgess *et al.*, 2003). The crystal structure of the MTBD of cytoplasmic dynein explains the binding mechanism to MTs (Carter *et al.*, 2008). Biophysical studies have also provided insights into the stepping size and forces as cytoplasmic dynein translocates in a retrograde manner along MTs (Mallik *et al.*, 2004). Computational models have also been proposed to simulate the atomic structure of cytoplasmic dynein's motor domain (Mocz and Gibbons, 2001; Serihojis *et al.*, 2006), but have not been correlated with experimental methods. Here, a computational model of mammalian cytoplasmic dynein was generated and results were compared with experimental data obtained from several biophysical techniques as a method to discern details of the cytoplasmic dynein motor domain and provide a stepping-stone to propose a more accurate representation of the protein.

5.2 RESULTS & DISCUSSION

5.2.1 Computational Modeling of Cytoplasmic Dynein Heavy Chain 1 Motor Domain

5.2.1.1 Secondary Structure Prediction

There are many computational programs available that can provide insight into the secondary and tertiary structures of proteins based on the amino acid sequence by comparison with known crystallographic and NMR structures deposited in the protein data bank (PDB). Unfortunately, the present form of the PDB does not contain structural data for proteins of similar large size and sequence homology to cytoplasmic dynein heavy chain 1. Computational programs are also often restricted by the input size of amino acid sequences, as was the case when searching for programs that could be used for secondary structure and disulfide bond prediction of cytoplasmic dynein. NetSurfP ver. 1.1 (Petersen *et al.*, 2009) was the one of very few available programs found to be capable of handling the long sequence of cytoplasmic dynein heavy chain 1 for secondary structure prediction. This program employs a neural network algorithm to predict the secondary structure of a protein from an input amino acid sequence. The output is a probability score, ranging from 0 to 1, given for each residue to be in an alpha-helical, beta sheet, or random coil conformation. Typically probability values are plotted as a function of residue number, but as observed in Figure 42, the plot for cytoplasmic dynein heavy chain 1 was quite complex and difficult to discern. The data was simplified by plotting the probabilities of the secondary structures in a histogram (Figure 43), where it became more evident that the predicted secondary structure of cytoplasmic dynein heavy chain 1 motor domain was heavily alpha-helical, in accordance with previous models proposed by Mocz and Gibbons (2001) and Serihojis *et al.* (2006). Partitioning the sequence into smaller, more manageable, sequences with overlapping

portions proved to be unfruitful since secondary structure prediction of several of the overlapping regions did not match with each other.

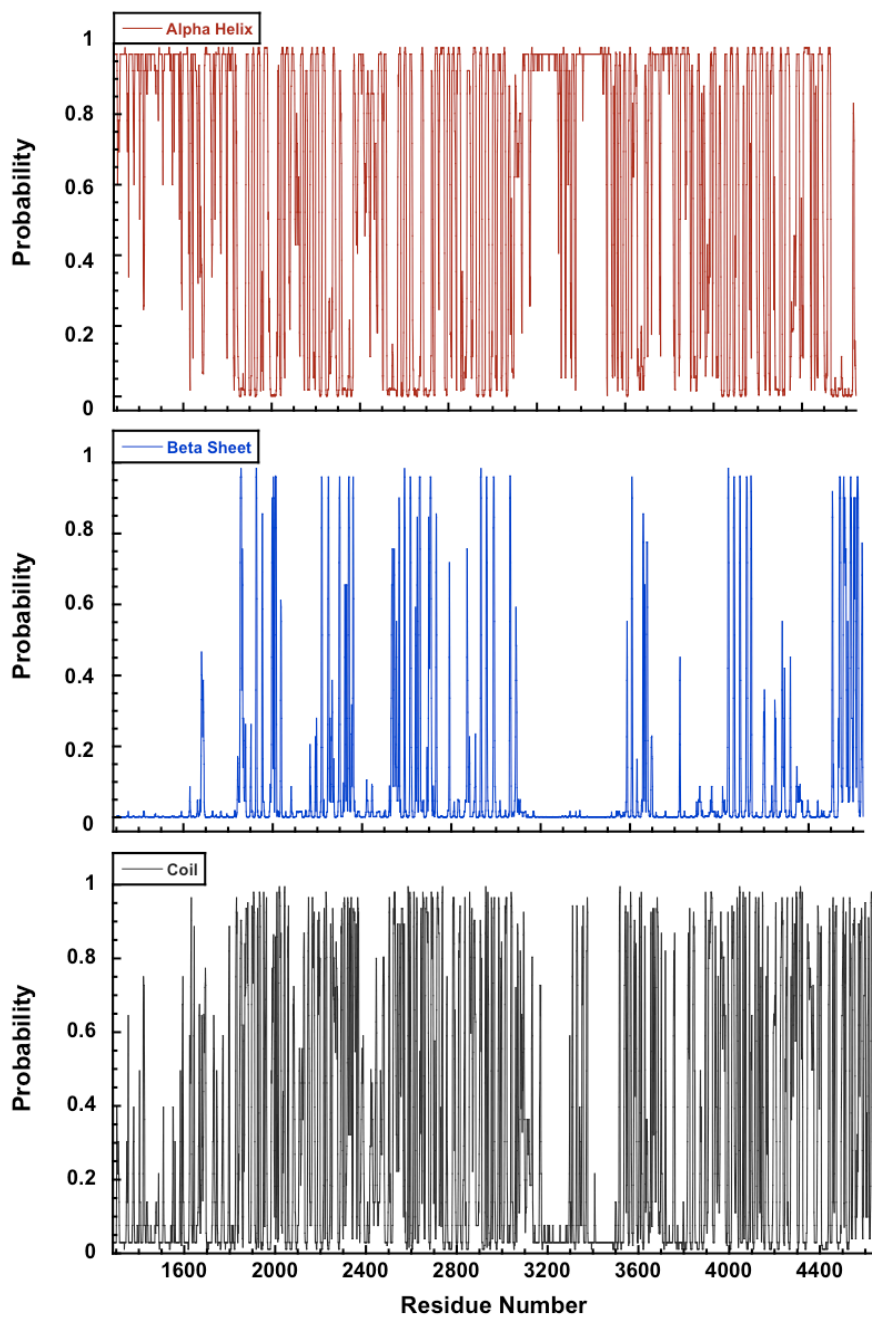


Figure 42. Secondary Structure Prediction of Cytoplasmic Dynein Motor Domain

Probabilities for formation of secondary structures: alpha helix (red), beta sheet (blue), or random coil (grey) as a function of residue number of rat cytoplasmic dynein heavy chain 1.

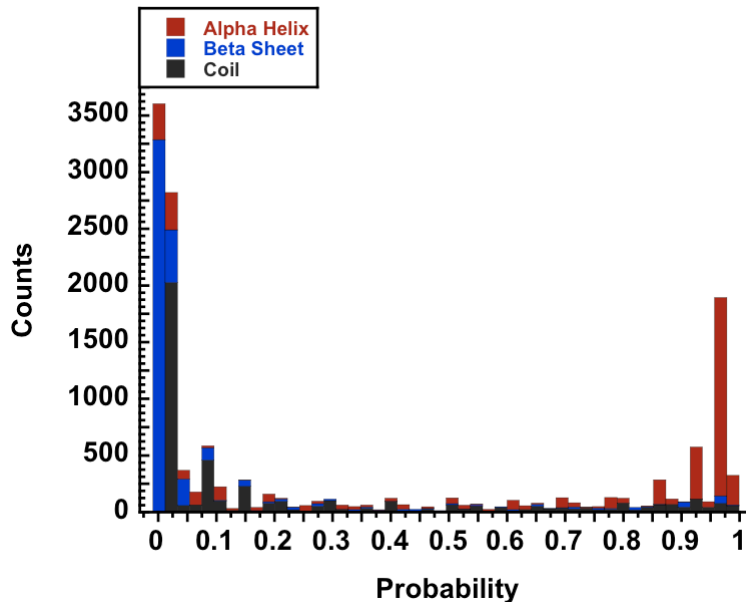


Figure 43. Histogram of Secondary Structure Probabilities for Cytoplasmic Dynein Motor Domain

Range of probabilities for formation of secondary structures: alpha helix (red), beta sheet (blue), or random coil (grey) of rat cytoplasmic dynein heavy chain 1.

Additionally, a prediction of dihedral (Φ, Ψ) angles from the protein sequence by guided-learning (Faraggi *et al.*, 2008) provided an alternative means to predict secondary structure through the use of a Ramachandran plot. The sequence of rat cytoplasmic dynein was submitted to Real-SPINE 3.0 (Faraggi *et al.*, 2008) and the program output was in the form of predicted dihedral angles for each residue. As evident from Figure 44, there was a large cluster of residues predicted to lie in the lower left quadrant of the Ramachandran plot, an indication of right-handed alpha-helices (Oldfield and Hubbard, 2004). Unexpectedly, a large number of residues resided in the upper left quadrant, a prediction of beta sheet structure, while very few residues were in the upper right quadrant that provides a prediction of random coils (Oldfield and Hubbard, 2004). The large size of the sequence hinders the ability to evaluate it with multiple programs. making it difficult to reach any conclusive results without comparison with other

programs. Yet, these results hint at the predominant alpha-helical nature of cytoplasmic dynein heavy chain 1.

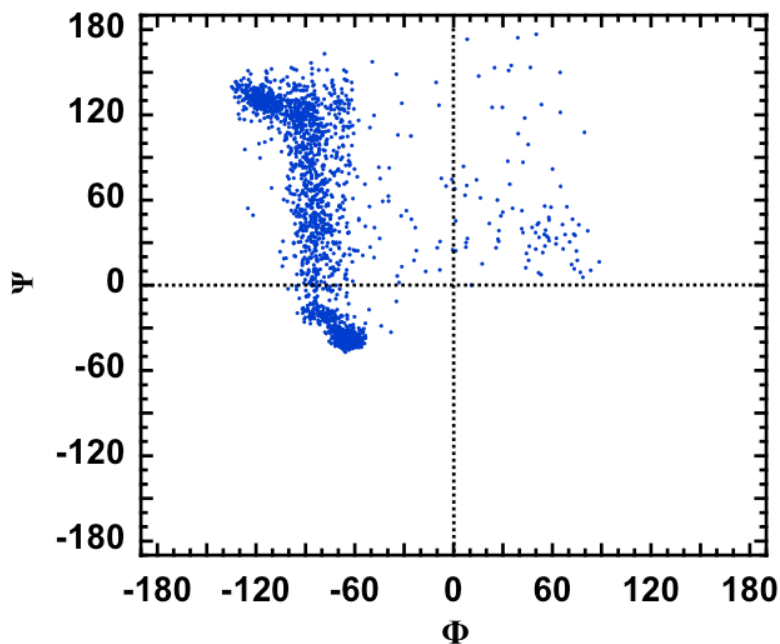


Figure 44. Ramachandran Plot of Predicted Dihedral Angles of Cytoplasmic Dynein Motor Domain

Predicted dihedral angles are plotted to show the steric conformation of residues. Conformations in the lower left quadrant represent alpha helices. Conformations in the upper left quadrant represent beta sheets, while conformations in the upper right quadrant represent random coils.

In addition to secondary structure prediction, disulfide connectivity prediction can be instrumental in assisting with modeling and characterization of the structure of a given protein. Similar to most computational programs, many of the programs available for disulfide bond prediction are incompatible with the large size of cytoplasmic dynein. The program DISULFIND (Ceroni *et al.*, 2006), which relies on predicting disulfide connectivity from a sequence using a trained neural network, was found to be capable of analyzing the 380 kDa sequence of rat cytoplasmic dynein heavy chain 1. The results from DISULFIND analysis indicated, however and with high statistical scoring, that disulfide bonds do not exist in the structure. It is unclear at this point if these results are reliable given the large number (41) of

cysteines present in the sequence. It is, however, possible that disulfide bonds do not exist in the structure given the fact that cytoplasmic dynein's environment in the cytoplasm is reducing and is therefore not conducive to disulfide bond formation (Fahey *et al.*, 1977). This is also supported by the fact that MTs, which are also in the cytoplasm, are inhibited in the presence of oxidizing agents (Huber *et al.*, 2008).

5.2.1.2 Three Dimensional Modeling of Cytoplasmic Dynein Motor Domain

Another avenue explored was 3D structural prediction of the motor domain of cytoplasmic dynein using comparative/homology modeling. Since cytoplasmic dynein motor domain is a hexameric AAA protein, previous models of the structure have been proposed based on the shared homology of known AAA protein structures (Mocz and Gibbons, 2001; Serihojis *et al.*, 2006). There is, however, very little correlation of these results with experimental data -- the previously reported structures were primarily fit into the electron density maps obtained by negative stain electron microscopy (Samsó and Koonce, 2004). Here, a computational model of rat cytoplasmic dynein heavy chain 1 motor domain was generated using MODELLER v9.8 (Eswar *et al.*, 2006). Initial attempts to generate a model were unsuccessful (Figure 45) with many residues lacking coordinate specification due to the mismatch in number of amino acids between the input sequence and the PDB files of the previously proposed models.

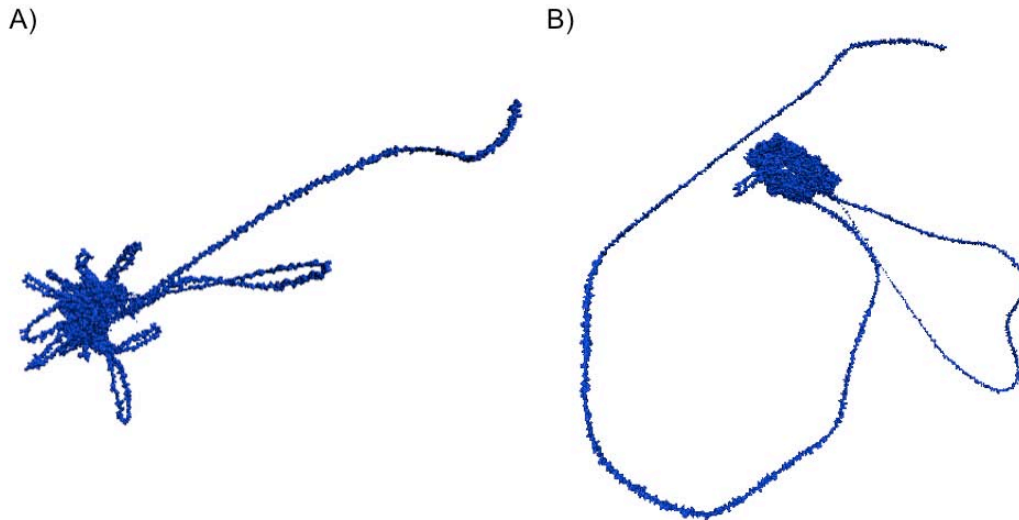


Figure 45. Surface Representation of Comparative/Homology Structural Models of Cytoplasmic Dynein Motor Domain

Residues Gly1286-Glu4644 of rat cytoplasmic dynein heavy chain 1 were applied to MODELLER v.9.8 to generate models of the motor domain based on comparative homology modeling using A) PDB 1HN5 (Mocz and Gibbons, 2001) and B) 2GF8 (Serohijos *et al.*, 2006) as a templates.

A sequence homology alignment was conducted using Clustal W (Larkin *et al.*, 2007) to identify and remove the mismatched amino acids from the input sequence. Another model was generated using the truncated sequence with the PDB files 2GF8 (Serohijos *et al.*, 2006) and 1HN5 (Mocz and Gibbons, 2001) as the templates and the model with the lowest DOPE score was selected after five reiterated models were generated (Figure 46). Surface volume rendering of this model indicated the presence of 15 surface-exposed cysteines.

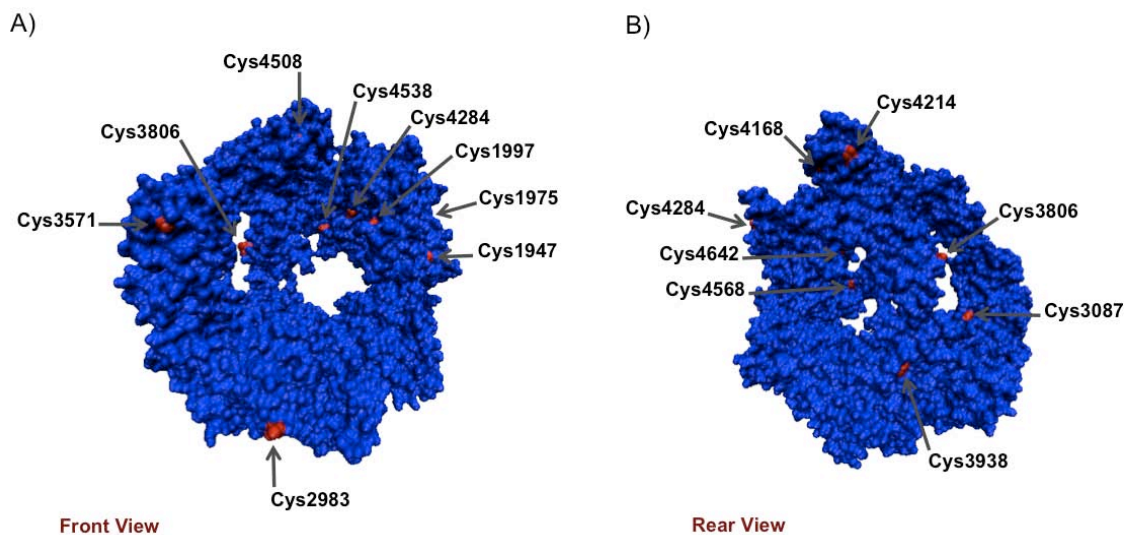


Figure 46. Surface Representation of a Modified Comparative Homology Structural Model of Cytoplasmic Dynein Motor Domain

Residues from rat cytoplasmic dynein heavy chain 1 that did not align with residues from PDB coordinates in 1HN5 and 2GF8 were deleted and the modified sequence was applied to MODELLER v.9.8 to produce a modified structural model of the motor domain. Surface-accessible cysteine residues were highlighted in red.

5.2.2 Cysteine Mapping

In order to evaluate the computational model of cytoplasmic dynein motor domain produced (*vide supra*) and to validate the prediction of surface accessible cysteine residues, the number of reactive cysteines was investigated experimentally. The motor domain of cytoplasmic dynein was labeled with a maleimide-based fluorescent dye under both native and denaturing conditions. The fluorescence was measured as a function of protein concentration under both native and denaturing conditions (Figure 47). By calibrating thiol concentration using glutathione, the number of reactive cysteines was initially determined for BSA to validate the method. From the slope, it was determined that the ratio of cysteines compared to glutathione was 0.32. Even though there is one surface-accessible cysteine in BSA, its reactivity has been reported to be relatively weak at neutral pH values, and in fact titrates with Ellman's reagent

[5,5'-dithiobis-(2-nitrobenzoic acid) or DTNB] at ~0.3-times the level of low molecular weight thiol-containing compounds (Svenson and Carlsson, 1975), suggesting that the reactivity of TG1 was similar to the commonly used Ellman's reagent. The number of surface-accessible reactive cysteines of the 380 kDa cytoplasmic dynein heavy chain 1 protein in bulk solution was calculated to be 6, while under denaturing conditions (SDS) 15 additional reactive cysteines were revealed.

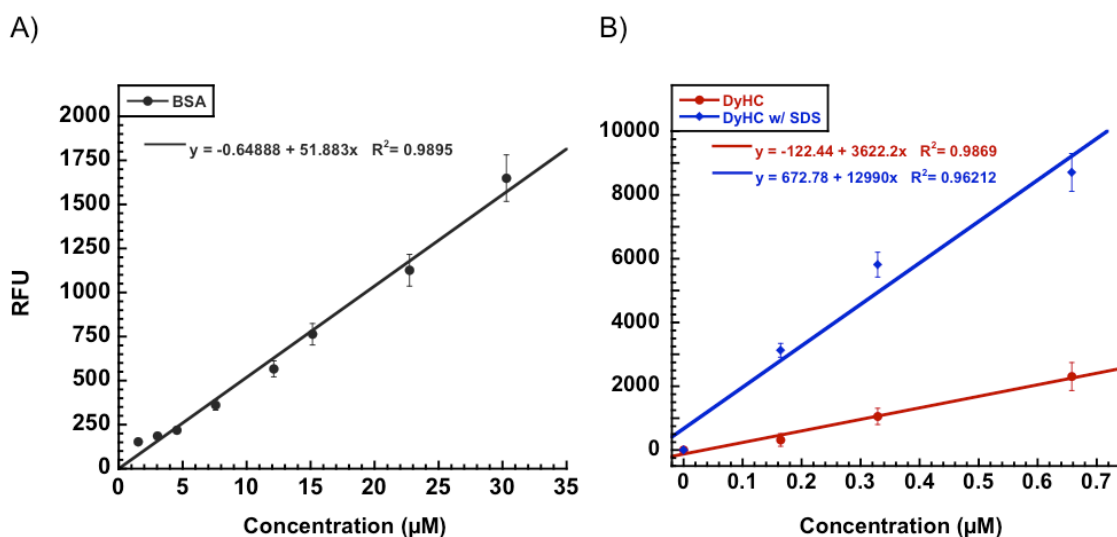


Figure 47. Quantitation of Reactive Cysteines by Fluorescence Spectroscopy

The amount of cysteines is determined from the slopes of concentration-dependent fluorescence of protein-TG1 adducts for A) BSA and B) cytoplasmic dynein heavy chain 1 under both native and denaturing conditions. Error bars represent SD from three independent experiments.

Although cytoplasmic dynein is not expected to possess disulfide bonds due to the inherent reducing environment of the cytoplasm (Fahey *et al.*, 1977), bulk fluorescence results suggested the presence of 10 disulfide bonds (i.e., $\frac{41-21}{2} = 10$). Reduction of protein disulfides before fluorescent labeling would have vindicated these findings, but TG1 interacted with all of the various reductants used (DTT, 2-mercaptoethanol, TCEP) as expected (Tyagarajan *et al.*, 2003), producing high fluorescence values independent of concentration (Figure 48). Given that

sufficient amounts of protein concentration needed for experiments was difficult to express and purify, samples treated with reductants were not dialyzed in order to maintain enough sample for fluorescence analysis. Alternatively, excess reductant may be dialyzed in a denaturing and deoxygenated buffer before labeling cysteines as described by Hedin *et al.* (2002).

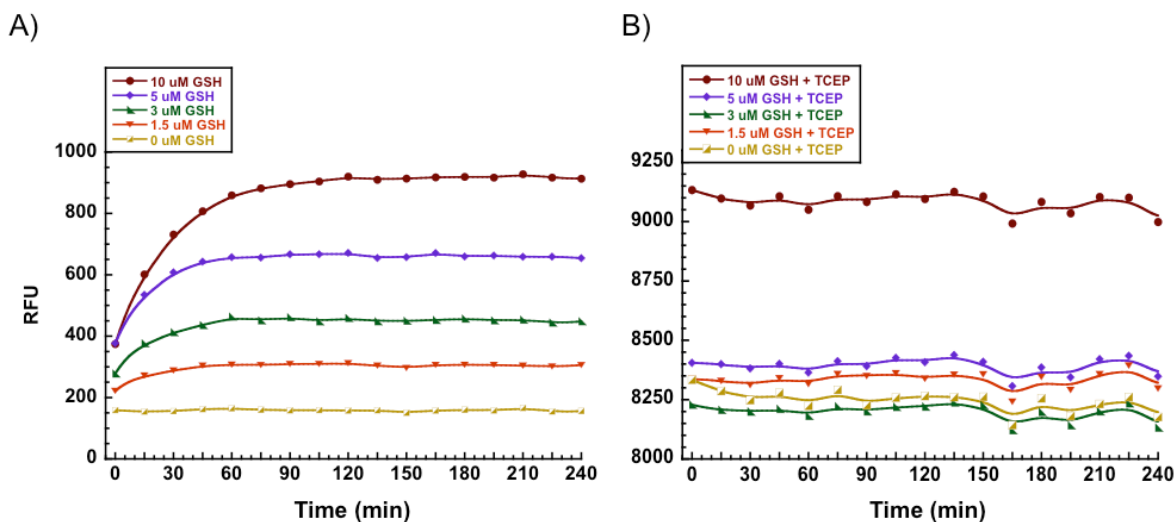


Figure 48. Time Dependence of GSH-TG1 Fluorescence Signal

A) Variation of GSH concentration was used to calibrate reactive cysteines while time dependence indicated optimal time of 60 min incubation for fluorescence readings. B) The addition of TCEP, independent of time or concentration, hindered fluorescence measurements.

In order to verify the fluorescence spectroscopy results and to identify labeled cysteines, MS analysis of labeled proteins was performed. Because of the large size of the protein and the complexity of the generated peptides generated, CNBr was initially selected as the method to digest cytoplasmic dynein, cleaving peptides only at methionine residues (Gross and Witkop, 1962). Upon analysis of the base peak chromatogram of the eluted peptides (Figure 49) a large number of ions were detected for a given time point (Figure 50) even when a long elution gradient was applied.

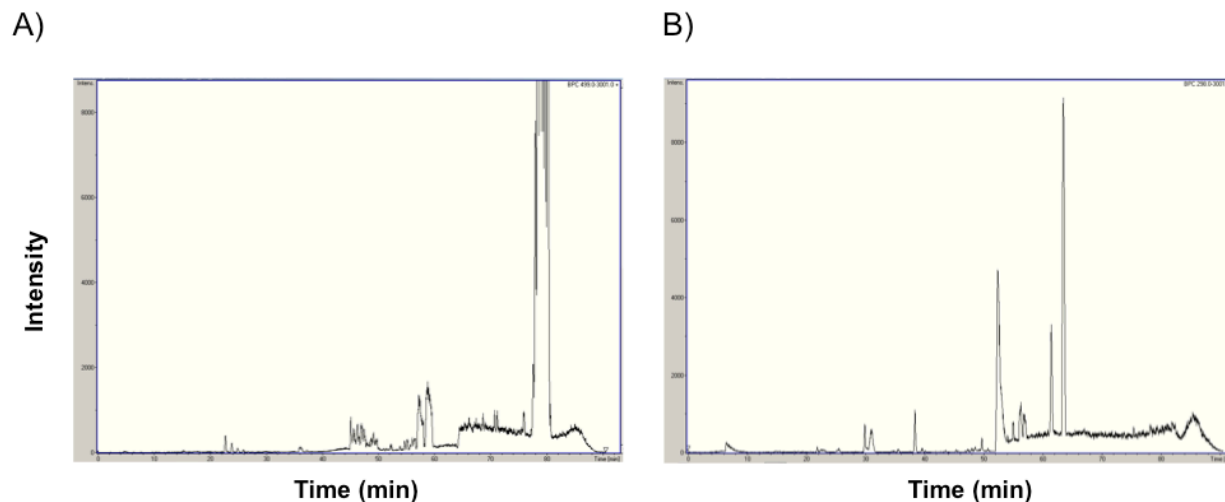


Figure 49. Base Peak Chromatogram of CNBr Digests of Cytoplasmic Dynein from LC-ESI-TOF-MS with Positive Ion Detection

A) CNBr digests of cytoplasmic dynein control. B) CNBr digests of cytoplasmic dynein reacted with TG1.

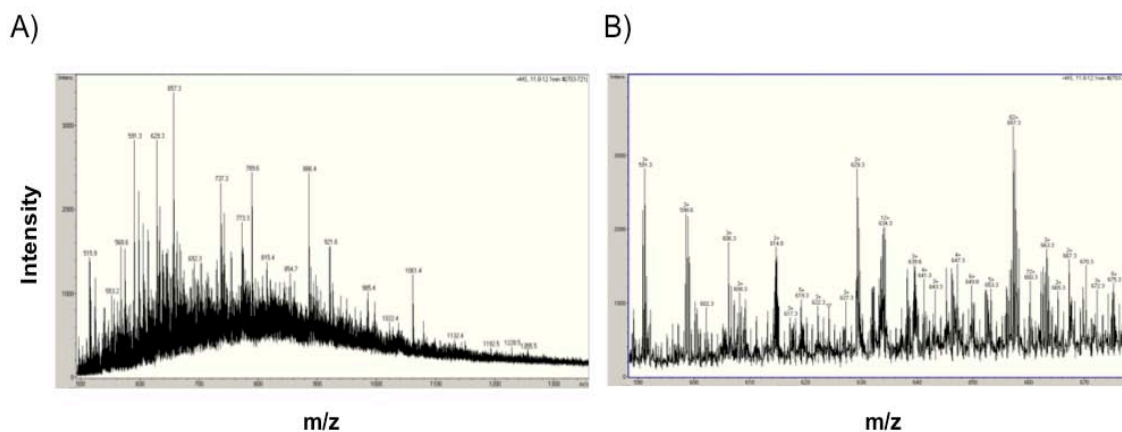


Figure 50. Positive Ion Mass Spectra of Cytoplasmic Dynein CNBr Digests from LC-ESI-TOF-MS Analysis

A) Raw MS spectrum from the 11.8-12.1 min region of the base peak chromatogram showing the many ions detected. B) The reconstructed spectrum shows many multiply charged ions detected.

Upon reconstruction (a.k.a. deconvolution) of the spectrum (Figure 51), a monoisotopic mass list was generated using the SUM PEAK algorithm with multiply charged peptides ranging from 1182.5 – 63,431 Da in size. The resolution of the TOF-MS instrument used did not, however, allow for clear correlation of detected peptide masses with those with *in situ* peptide

mass values, as many of the detected masses differed from potential values by several tens or even hundreds of Daltons.

Although there was somewhat improved peptide separation when a nano-LC system was used (Figure 51), the complexity of samples still provided a very high number of ions detected by 12 Tesla FTMS after ESI, and many of the reconstructed spectra were overlapping (Figure 52). In addition to the complexity of the sample itself and the uncertainty of formation of serine or homoserine lactone with CNBr digestion (Gross and Witkop, 1961), the CNBr/formic acid mixture used for digestion can also introduce several types of variable modifications to peptides, including amide formylation and esterification of carboxyl groups (Goodlett *et al.*, 1990), in addition to the potential missed cleavages that can take place (Lubec and Afjehi-Sadat, 2007).

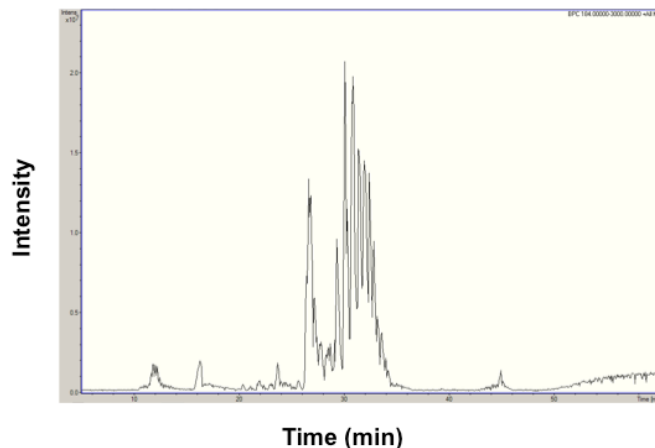


Figure 51. Base Peak Chromatogram of CNBr Digests of Cytoplasmic Dynein from nanoLC-ESI-FTMS with Positive Ion Detection

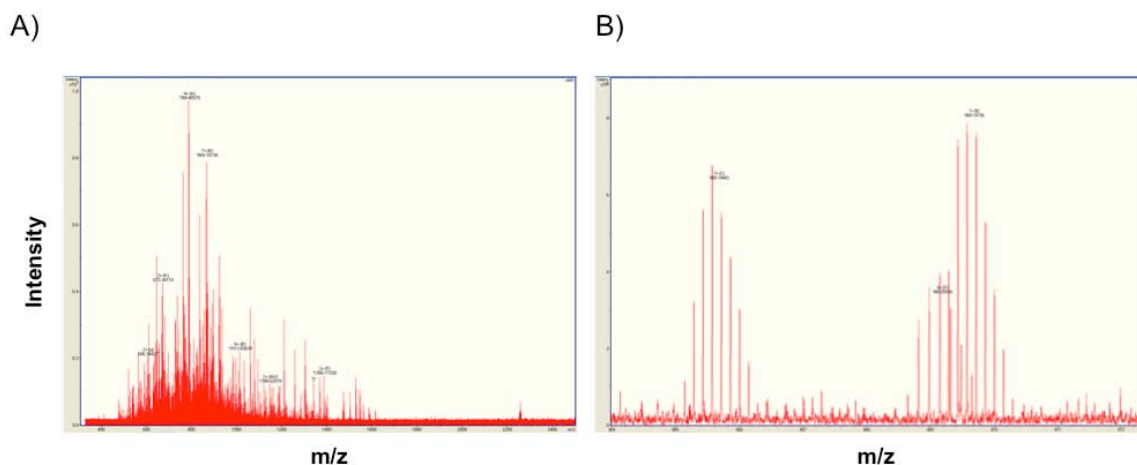


Figure 52. Mass Spectra of Cytoplasmic Dynein CNBr Digests from ESI-FTMS

A) Raw positive ion MS spectrum from the base peak chromatogram showing the many ions detected. B) The reconstructed spectrum shows overlapping multiply charged ions.

These results all hinted at the necessity for more detailed sequence information by tandem MS and perhaps peptide cleavage with reagents that cause less modifications and chemical interference as compared to CNBr. TG1-labeled rat dynein heavy chain 1 motor domain was therefore electrophoresed in an SDS-PAGE system and the purified protein was digested in-gel with trypsin. The peptides extracted from the gel plug were analyzed by nanoLC-ESI-LIT-Orbitrap-MS and -MS/MS with positive ion detection. Base peak chromatograms indicated a large amount of ions for both labeled and unlabeled samples (Figure 53). The combined MS and MS/MS analyses identified a large amount of sequence information (shown in Appendix B) of both unlabeled and labeled protein with sequence coverages of 56.53% and 61.59%, respectively, compared to the sequence coverage of ~4% with the FTMS.

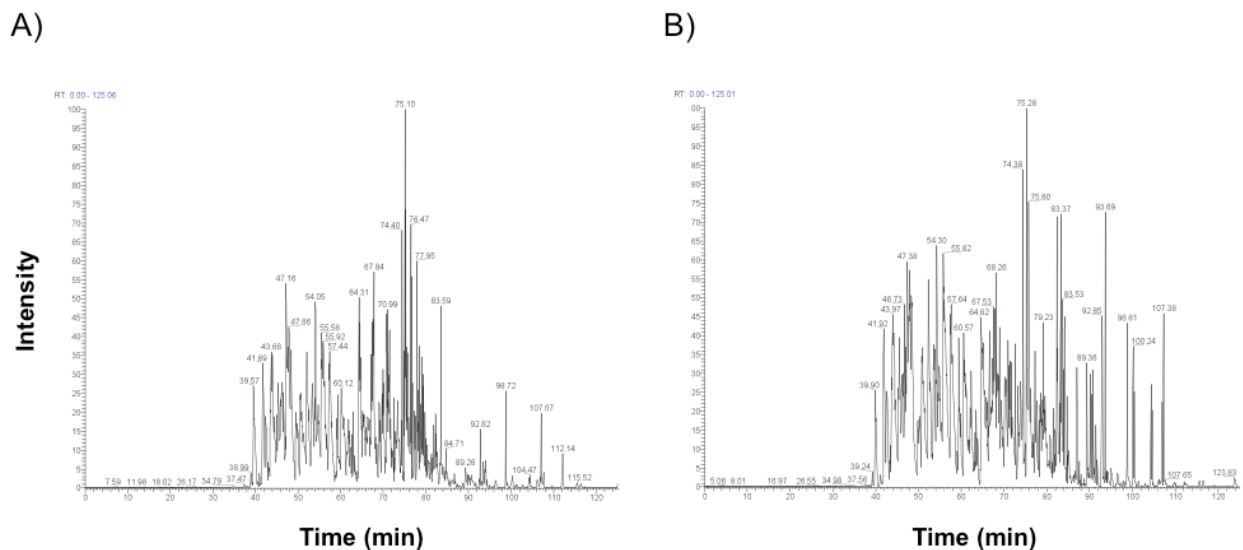


Figure 53. Base Peak Chromatogram of CNBr Digests of Cytoplasmic Dynein from nanoLC-ESI-LIT-Orbitrap with Positive Ion Detection

A) In-gel trypsin digests of cytoplasmic dynein control. B) In-gel trypsin digests of cytoplasmic dynein reacted with TG1.

Upon further analysis of the identified peptides, seventeen total cysteines were detected on peptides, thirteen of which were detected with increased masses. Initial modification searches using the Δ mass of the expected TG1 adduct (379.1 Da) (Figure 54) resulted in identification of only a few labeled peptides, even though several other cysteines appeared to be modified. Many of the modified peptides had $\Delta m/z$ values of 365, 383, or 397 Da rather than the parent adduct (shown in Appendix C) attributed to the modifications depicted in Figure 55 (Sharov *et al.*, 2006). Although the size and fragmentation patterns of the TG1 adduct may encumber MS analysis, TG1 was selected for its common use to compare the results obtained by fluorescence measurements with MS analysis. The labeled cysteines identified were compared with the predicted surface accessible residues in Table 4. There were five cysteines that matched experimental and computational results. The remaining eight cysteines identified experimentally may have been inadvertently labeled if excess TG1 was present during the denaturation step

before loading onto the electrophoresis gel, even though care was taken to remove label with centrifugal filtration units. Since sequence coverage was not complete, there may be more labeled peptides detected, which could be in agreement with computational predictions. Additionally, given that the computational model of cytoplasmic dynein motor domain was generated from an incomplete sequence in comparison with other computational models, rather than experimentally determined structures with similar size and sequence homology, mismatch in surface-accessible cysteines may be due to errors in the model itself.

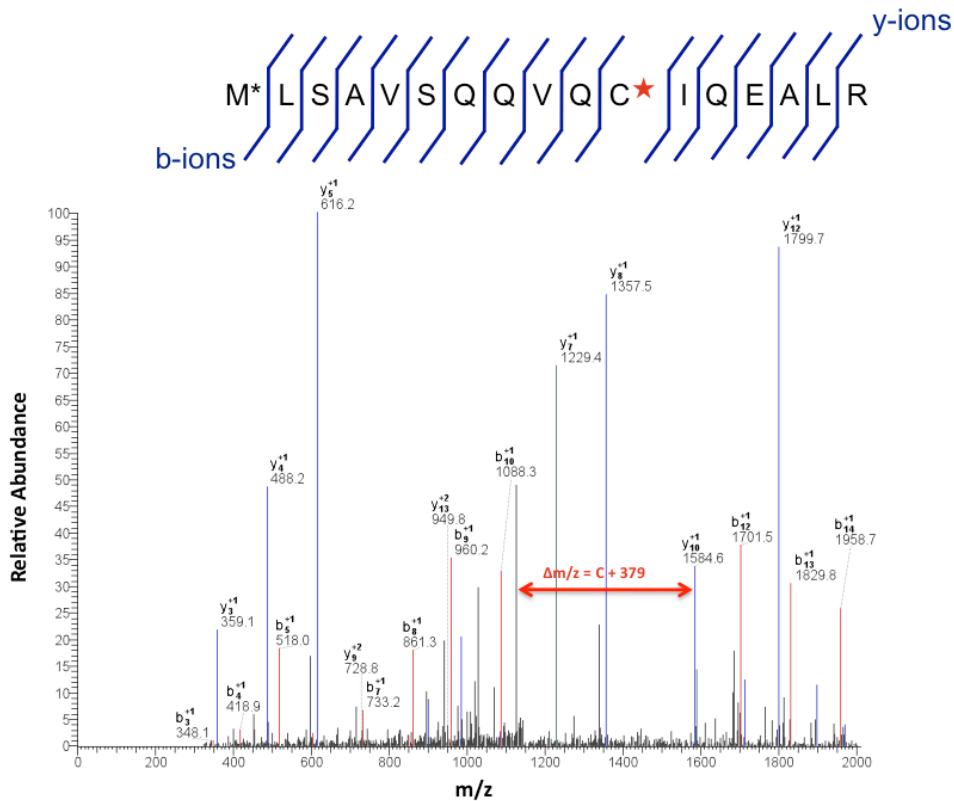


Figure 54. LIT-Orbitrap-MS/MS Spectrum of a Dynein-Derived Peptide Found to be Labeled with TG1

One of the several MS/MS spectra demonstrating a derived peptide sequence from the difference in m/z from the b and y ions. Methionine is detected with a monooxygenation (*), while a cysteine is detected with an increase of 379 Da, indicating the mass of TG1.

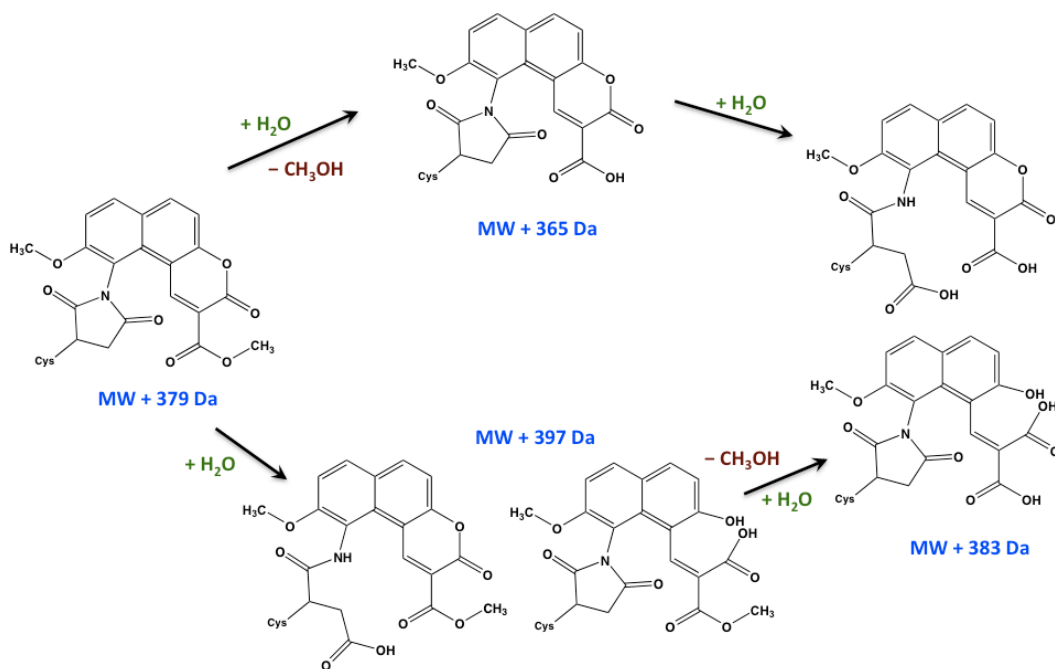


Figure 55. ThioGlo1 Adducts Detected by MS/MS

Potential modifications of the Cys-TG1 adduct detected by MS/MS due to several combinations of gaining H_2O and losing CH_3OH .

Table 4. Comparison of Surface-Accessible Cysteines Detected by Mass Spectrometry and Computational Prediction

Comparison of Surface Accessible Cysteines by	
Computation	Mass Spectrometry
—	Cys1886
—	Cys1930
Cys1947	Cys1947
Cys1975	—
Cys1997	—
—	Cys2637
—	Cys2710
Cys2983	—
Cys3087	Cys3087
—	*Cys3145
—	*Cys3323
Cys3571	—
—	Cys3691
—	Cys3710
Cys3806	—
Cys3938	Cys3938
Cys4168	—
Cys4214	Cys4214
Cys4284	—
Cys4508	—
Cys4538	—
Cys4568	Cys4568
Cys4642	—

* Residues deleted from sequence during modeling

5.2.3 Electron Microscopy

Finally, electron microscopy can be used to provide detailed electron density maps that can be used in conjunction with the computational models predicted to generate a more accurate structural representation of the cytoplasmic dynein heavy chain 1 motor domain. The 380 kDa purified construct of cytoplasmic dynein heavy chain 1 motor domain was initially evaluated by

negative stain electron microscopy. After several attempts to purify the protein from a baculovirus/insect cell system (Figure 56) it was evident from the SDS-PAGE gels that other proteins were still associated with the desired cytoplasmic dynein protein after nickel affinity chromatography, but that purity improved through the use of size exclusion chromatography, although not thoroughly, to a degree that the cytoplasmic dynein band was the most dominant.

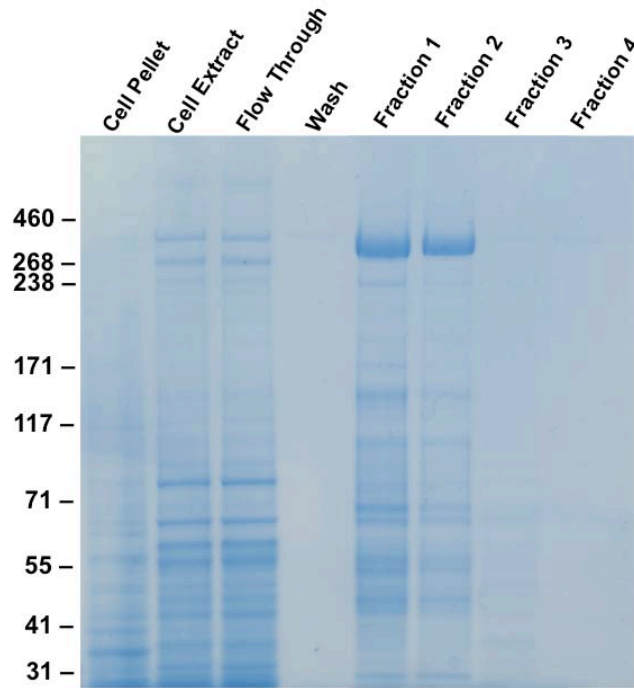


Figure 56. SDS-PAGE Gel Electrophoresis of Hi5/Baculovirus Expression of 380 kDa Cytoplasmic Dynein

Purity of cytoplasmic dynein fractions purified by nickel affinity column chromatography indicated the presence of many contaminants.

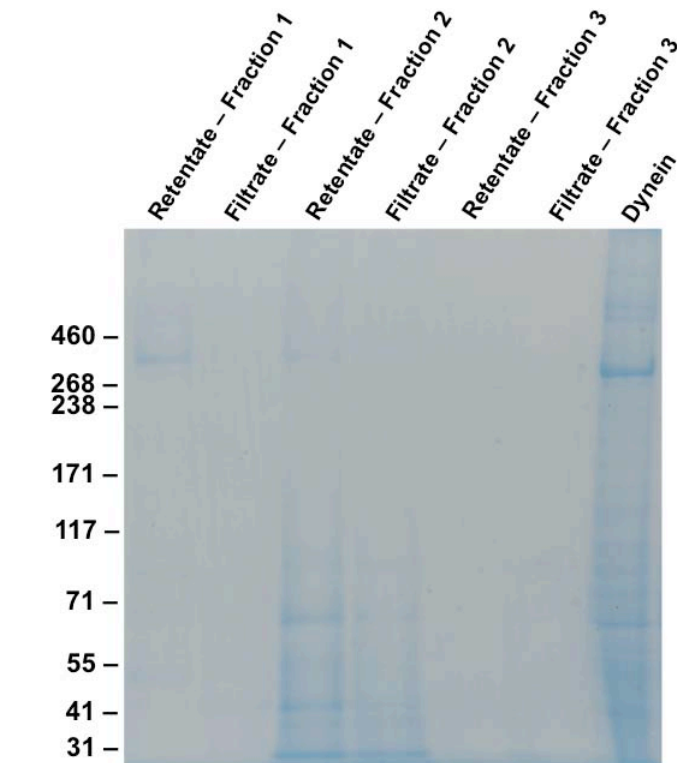


Figure 57. SDS-PAGE Gel of Cytoplasmic Dynein After Additional Purification

Purity of cytoplasmic dynein fractions purified by size exclusion chromatography followed by centrifugal filtration indicated the removal of most of the contaminants from cytoplasmic dynein.

Nonetheless, the protein fraction obtained from size exclusion chromatography that alluded to the purest sample (“Retentate - Fraction 1” Figure 57) was evaluated by negative stain electron microscopy in an effort to reach an improved structural model of cytoplasmic dynein’s motor domain than previously reported in the literature (Samsó and Koonce, 2004). Several different negative stains were tested to evaluate which would provide the highest image contrast (Figure 58). In these images, several ring-like structures were seen using uranyl acetate, ammonium molybdate, and phosphotungstic acid. Although uranyl acetate appeared to highlight more cytoplasmic dynein particles, the stain also made other smaller protein contaminants or buffer staining artifacts more apparent. There were also what appeared to be potential side orientations of cytoplasmic dynein present, but this was difficult to assess given the large amount

of background signal. The latter two negative stains appeared to highlight cytoplasmic dynein more clearly, but yielded much fewer particles on the copper grids. These issues rendered it difficult to obtain the large amounts of particles ($\sim 10^3$ – 10^6) necessary for averaging and image reconstruction purposes (Frank, 2009).

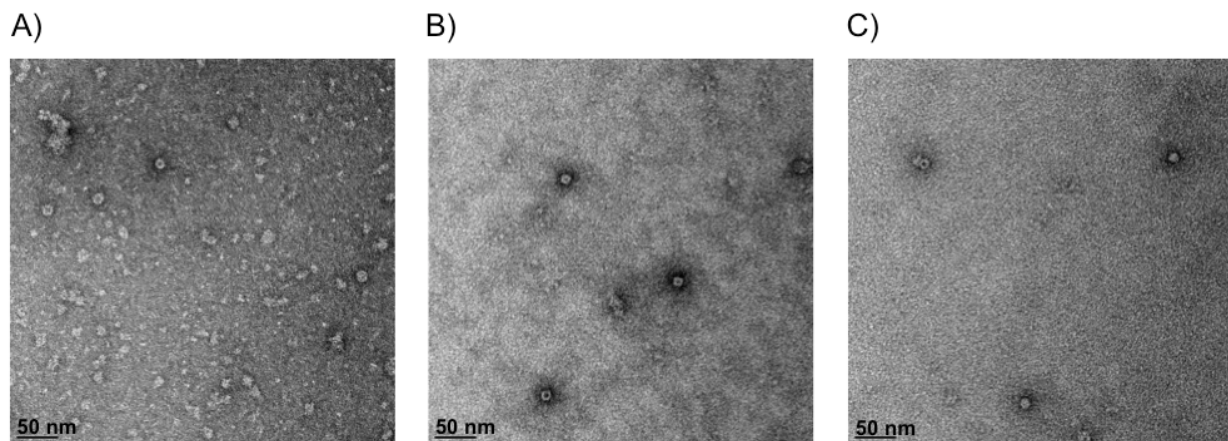


Figure 58. Negative Stain Electron Micrographs of 380 kDa Rat Cytoplasmic Dynein Fragment

Cytoplasmic dynein on copper grids stained with A) uranyl acetate, B) phosphotungstic acid, and C) ammonium molybdate. Images were then acquired with an FEI Tecnai T12 electron microscope.

Since negative stain EM images of cytoplasmic dynein expressed from a *Dictyostelium discoideum* (slime mold) construct have been recently reported in the literature (Roberts *et al.*, 2009), we were interested in isolating native protein from a mammalian source that was perhaps less contaminated than the previous purification attempts and/or perhaps be in complex with its accessory proteins (dynactin, immunophilins, Hsps, etc.) (Pratt *et al.*, 2004). The tubulin purification protocol (Hamel and Lin, 1984) routinely employed in the Day lab was an ideal starting point to isolate cytoplasmic dynein. Since the isolation protocol relies on consecutive MT polymerization and depolymerization steps to remove the various MAPs, each of the steps performed during the isolation protocol were analyzed by gel electrophoresis (Figure 59) in order to determine the fraction(s) in which cytoplasmic dynein was most abundantly present. A

number of gel bands were then excised, digested with trypsin, and then analyzed by MALDI-TOF-MS and -MS/MS to identify the proteins.

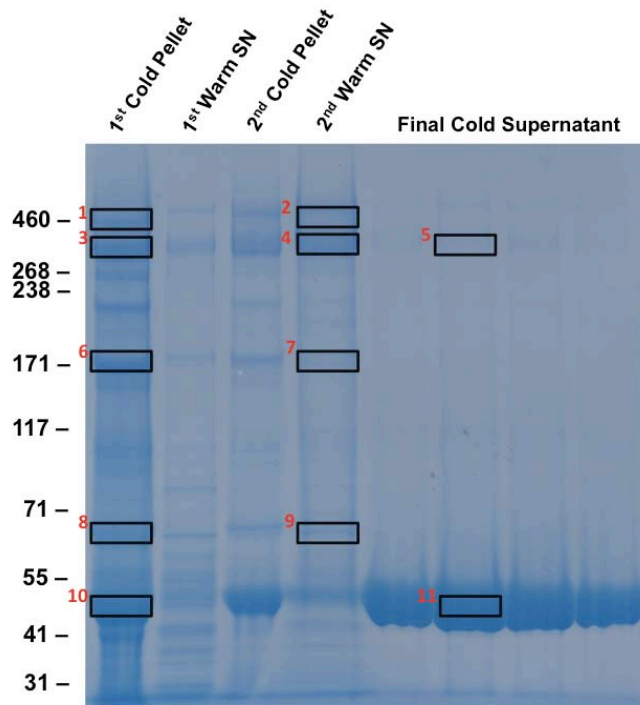


Figure 59. SDS-PAGE Gel from Tubulin Isolation Protocol

Individual steps from bovine brain tubulin isolation procedure were used to identify where cytoplasmic dynein would be most abundant. Boxed gel bands were excised and digested with trypsin and peptide extracts were identified by MS/MS.

As expected, cytoplasmic dynein heavy chain 1 was identified as the high molecular weight bands (Table 5). In addition, heat shock cognate 70 (hsc70), a homolog of hsp70 from a gel band near 70 kDa was identified, which is often a companion of cytoplasmic dynein (Giannakakou *et al.*, 2000). Moreover, the microtubule-associated protein MAP2 (200 kDa), medium neurofilaments (100 kDa), light chain neurofilaments (62 kDa), and tubulin (50 kDa) co-purified with cytoplasmic dynein heavy chain were also identified. These results were consistent with proteins expected to be isolated from bovine brain. In particular, MAP2 has been

previously reported to stabilize MT formation and has been shown to link MTs to IFs or other MTs in mammalian brains (Bloom and Vallee, 1983).

Table 5. Protein Identification of Gel Bands by MALDI-TOF-MS and -MS/MS

Gel Band	Name	Protein Mass (Da)	Protein Pilot Score	Percent Coverage
1	Cytoplasmic Dynein Heavy Chain 1	532072	75	13
2	Cytoplasmic Dynein Heavy Chain 1	531916	69	13
3	Microtubule Associated Protein 2	199404	361	35
4	Microtubule Associated Protein 2	199404	285	27
5	Microtubule Associated Protein 2	199404	165	15
6	Neurofilament Medium Peptide	103148	939	43
7	Neurofilament Medium Peptide	103148	50	17
8	Neurofilament Light Peptide	62608	635	62
9	Heat Shock Cognate 71 kDa Protein	70761	440	43
10	Tubulin Beta 2A	49875	702	57
11	Tubulin Beta 2A	49875	743	51

Based on the intensity of the cytoplasmic dynein gel bands from the different stages of tubulin isolation and purification, it was determined that the “second warm supernatant” stage would provide a significant amount of cytoplasmic dynein with less tubulin present compared to any of the other protein isolation steps. Because the proteins identified in Table 5 were present in the sample, it was necessary to further isolate cytoplasmic dynein from the protein mixture. In an effort to remove MAP2, which is comparable in size to cytoplasmic dynein, the protein mixture was taken through two additional rounds of MT polymerization and depolymerization in the presence of GTP and PTX. The MT mixture was allowed to polymerize once more and ATP was added to release cytoplasmic dynein from the MTs (Burgess *et al.*, 2003) in order to separate the two by ultracentrifugation. When aliquots from each of the individual steps were evaluated by gel electrophoresis, it was evident that cytoplasmic dynein was more concentrated, but there was still a large amount of the lower molecular weight proteins (Figure 59). The ATP-released fraction of cytoplasmic dynein was then further subjected to size exclusion chromatography.

Even though the majority of the protein contaminants were removed as evident by the gel electrophoresis of collected size exclusion chromatography fractions (Figure 60), a protein band similar in size to cytoplasmic dynein was still present and was not separable even by applying a slow elution gradient during chromatography. A faint band around 55 kDa also persisted, suggesting that tubulin heterodimers were still bound to the MTBD of cytoplasmic dynein.

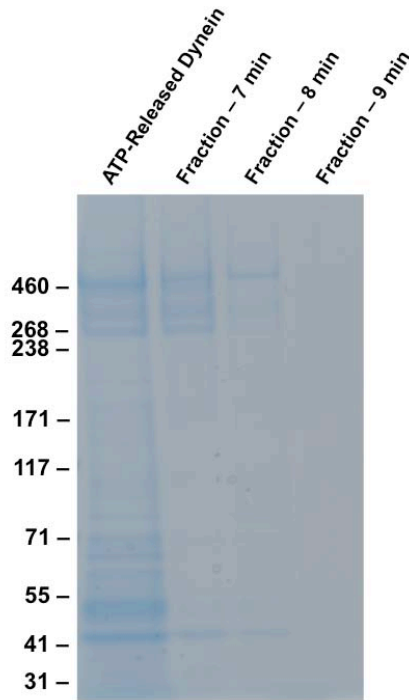


Figure 60. SDS-PAGE Gel of ATP-Released Cytoplasmic Dynein Fraction Purified by Size Exclusion Chromatography

Fractions collected every 1 min from size exclusion chromatography show a relatively purified fraction of cytoplasmic dynein extracted from bovine brain compared to ATP-released cytoplasmic dynein.

Regardless, the fractions with the most abundant amount of cytoplasmic dynein were concentrated and applied to EM grids for analysis. As evident in Figure 61, there were several ring-like structures representing the motor domain of cytoplasmic dynein. In addition, there were several large helical polymers, which resemble structures previously reported to be formed by MAP2 (DeTure *et al.*, 1996). Preliminary results from the EM images of isolated cytoplasmic

dynein were not conclusive as to whether or not dynein was in the dimeric form, but a few motor domains appeared to be paired with minor electron densities connecting the two structures.

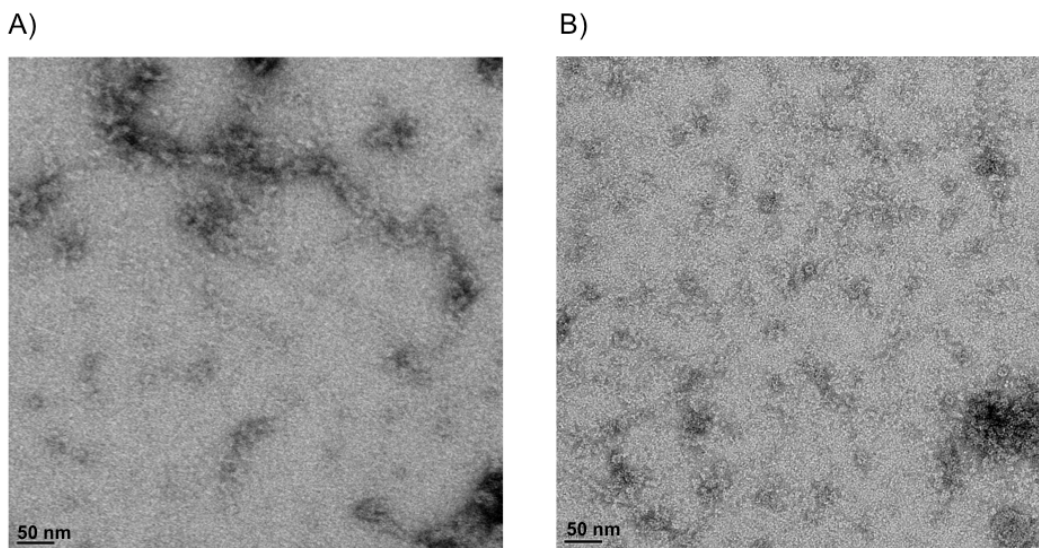


Figure 61. Negative Stain Electron Micrographs of Bovine Cytoplasmic Dynein

Bovine cytoplasmic dynein on copper grids stained with uranyl acetate. A) Several aggregates were present on the grids including the potential helical polymerization of MAP2. B) Individual cytoplasmic dynein particles were more present after size exclusion chromatography of samples. Images were then acquired with an FEI Tecnai T12 electron microscope.

5.3 CONCLUSIONS

Given the large size of cytoplasmic dynein, conventional biophysical tools such as X-ray crystallography and NMR cannot be applied to identify the large structure of cytoplasmic dynein. Therefore, a number of other methods including computational prediction and cysteine mapping were employed to evaluate the structure of cytoplasmic dynein heavy chain 1 motor domain. Based on the sequence alone, secondary structure and dihedral angle prediction suggested a predominantly α -helical structure, which was in agreement with previously proposed models. Ideally, prediction of secondary structure and dihedral angles should be performed using more

than one computational approach or algorithm for comparison purposes, but many of the programs were incapable of handling the long input sequence of the protein. Disulfide bond connectivity prediction indicated the absence of disulfide bonds in the structure, which is possible given the reducing environment of the cytoplasm. Comparative homology modeling of the cytoplasmic dynein heavy chain motor domain was generated using the Serihojis *et al.* (2006) model because it most resembled the electron density map of cytoplasmic dynein generated by cryo-electron microscopy (Mizuno *et al.*, 2007). Since the template was generated from crystal structures of proteins with high sequence homology to the domains of cytoplasmic dynein, several portions of the coordinates were missing and 999 residues from the input sequence were removed in order for a structural model to be generated. Regardless, a structural model suggested the presence of 15 surface accessible cysteine residues. Fluorescence spectroscopy measurements using the fluorescent tag TG1 indicated the presence of 6 surface accessible cysteine residues in the native state, while 15 additional residues were labeled in the presence of SDS. Mass spectrometry was then applied to identify the TG1-labeled peptides, revealing 13 cysteines. A comparison between the computationally predicted and experimentally determined surface accessible cysteine residues revealed 5 cysteines in agreement. The remaining unmatched cysteines most likely suggests some inadequacy of the proposed structural model given the large number of residues removed from the sequence along with the lack of other AAA proteins with similar size to be used as additional templates. Additional analysis of the mass spectral data in order to identify cysteines with other TG1 modifications than those suggested is necessary to evaluate if other cysteines correspond to those predicted from the computational model.

6.0 OVERALL CONCLUSIONS & FUTURE DIRECTIONS

In summary, efforts were made to identify compounds that modulate the activity and characterize the structure of cytoplasmic dynein heavy chain 1. An HCS cell-based nuclear translocation assay, previously employed in the Day and Johnston labs, were employed to identify cell-permeable compounds that inhibited GR translocation mediated by cytoplasmic dynein. Hits were further evaluated biochemically to identify the most likely target(s) of the compound resulting in inhibition of GR translocation. High throughput assays were developed to screen for GR ligand competition and the ATPase activities of Hsp 70 and 90, cytoplasmic dynein heavy chain 1, and myosin. Although a number of compounds were identified from the screening of the 1280 LOPAC library that inhibited cytoplasmic dynein, the non-specific characteristics of the apomorphines were unattractive for further studies. Additional screening of the MLSCN collection appeared to highlight a number of compounds that specifically inhibited the ATPase activity of cytoplasmic dynein with little or no interaction with other proteins involved in cargo complex formation such as MLSCN compounds # 7, 19, 29, 64, 66, and 67. Future work is necessary to perform concentration-dependent ATPase inhibition assays on these secondary hits to determine binding affinity and specificity. Several of these compounds are already believed to have poor pharmacological or druggable characteristics such as the presence of nitric oxide and other sulfhydryl reactive moieties. Therefore, synthetic chemistry approaches in conjunction with quantitative structure-activity relationship (QSAR) studies (Andrade *et al.*, 2010) will assist

with the development of compounds with similar backbone structures and better pharmacological properties.

A novel approach to screen for MT perturbing agents was also designed and implemented using biosensors. Results from DPI followed the polymerization process of MTs on biotinylated-tubulin surfaces. The process of MT polymerization was then implemented onto a similar RM biosensor surface using a cuvette-based setup in order to reduce sample consumption and increase throughput. The initial rates of the polymerization process in the presence of MT perturbing agents was successfully used to distinguish MT stabilizers from destabilizers. With current limited access to DPI and RM instruments, efforts were made to apply the same methodologies using an RWG biosensor. With the availability of 96-, 384-, or 1536-well plates, more robust and rapid screening of MT perturbing agents compared to conventional turbidity assays may be conducted.

The structure of the cytoplasmic dynein motor domain was then evaluated by a combination of computational and experimental methods. Secondary structure and dihedral angle prediction both suggested that the structure of the motor domain was predominantly alpha-helical, though the use of additional computational algorithms are needed to compare the validity of the proposed results. Circular dichroism experiments, although complex with a protein of this size, could verify these results experimentally by approximating the ratio of secondary structure conformations of the protein (Provencher and Gloeckner, 1981). Comparative homology structural modeling has allowed for prediction of surface accessible residues, specifically cysteine residues, which were correlated experimentally by MS. Five cysteines were matched computationally and experimentally to be surface-accessible. The remaining eight experimentally-detected reactive cysteines could also correlate with many of the other surface-

accessible cysteines predicted computationally by additional experiments with smaller alkylating reagents. Detection of the entire amino acid sequence is also necessary for a thorough correlation between computational and experimental results. The current low correlation between computational and experimental results suggests that the proposed computational model has some inadequacies since only 1/3 (5 out of 15) of proposed cysteines matched between the two techniques. Chemical crosslinking with certain affinity tags of cysteines may also provide another avenue for determining surface accessible cysteine residues while also providing Cys-Cys distances within the structure (Sinz, 2003). Pairwise cysteine mutagenesis along with EPR spectroscopy of attached spin labels will also allow for distance measurements within the structure (Schiemann and Prisner, 2007).

Finally, negative stain EM was used to evaluate the structure of cytoplasmic dynein. Several ring-like structures were visible indicating the motor domain of cytoplasmic dynein. Most notably, the asymmetric electron density distribution of the motor domain resembled that of the proposed model. Protein samples isolated from bovine brains appeared to have several paired rings that were in complex. Attempts to construct a model of cytoplasmic dynein from electron microscopy images were hindered by the difficulties encountered in protein purification of both Hi5/baculovirus-expressed rat cytoplasmic dynein heavy chain 1 and protein isolated from bovine brain, although the latter appeared to provide better quality samples. Ion exchange chromatography was of interest as a method to separate non-specific proteins during the protein purification, but was limited at the time by the availability of a column suitable for the molecular weight of cytoplasmic dynein. Modifications in the protein purification of isolated protein, including perhaps expressing a protein with two distinct affinity moieties to reduce non-specific association of contaminants, should also be explored. Once a purer sample is produced, many

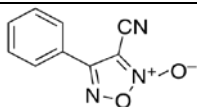
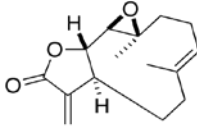
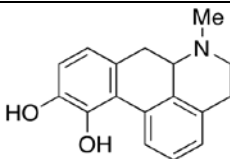
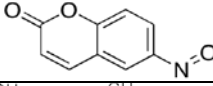
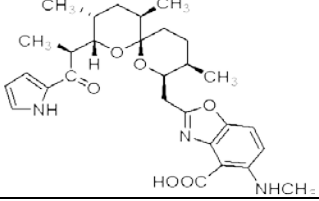
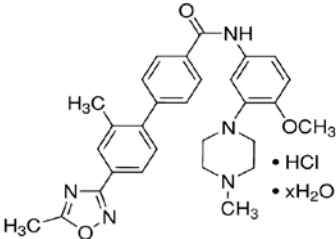
dynein particles should be selected by negative stain EM followed by cryo-EM for structure reconstruction. Once an electron density map of the protein is produced, the computational model along with information from the surface accessible cysteines determined experimentally will assist with the refinement of a structural model into the electron density map as suggested by Alexander *et al.* (2008).

Ultimately, the structural characterization of cytoplasmic dynein plays an important role in the discovery of compounds that specifically bind to and modulate cytoplasmic dynein activity. Similarly, compounds that “lock” dynamic cytoplasmic dynein into a rigid structure may assist with structural characterization of the protein, especially with electron microscopy. Here, several biophysical and pharmacological approaches have been attempted to identify the structure of and compounds that modulate the activity of cytoplasmic dynein heavy chain 1. This process is clearly in the preliminary stages, but builds a strong foundation for future experiments to follow.

APPENDIX A

A.1 LIST OF COMPOUNDS FROM LOPAC SCREEN

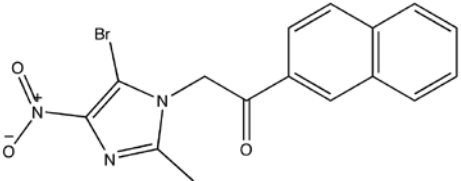
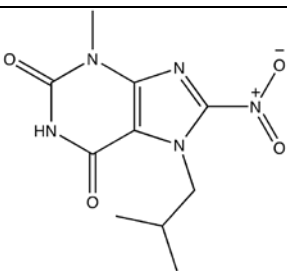
Chemical structures of compounds from the LOPAC screen identified as GR translocation inhibitors

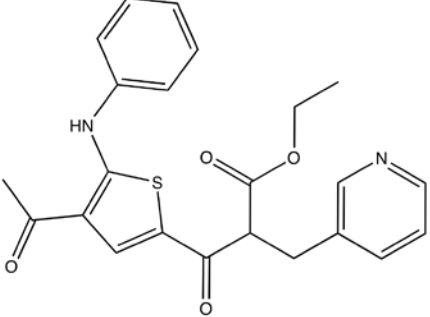
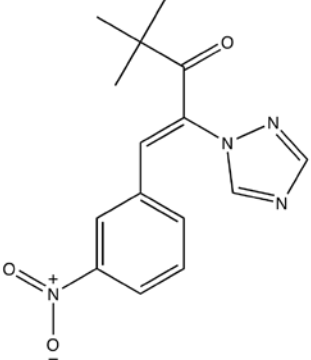
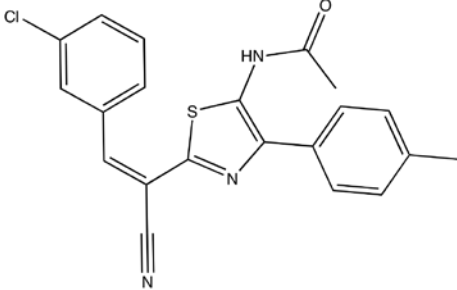
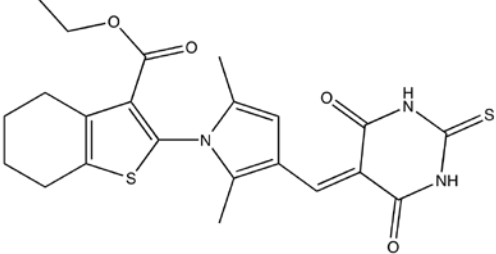
Compound	Chemical Structure
4-Phenyl-3-furoxan carbonitrile	
Parthenolide	
Apomorphine	
6-Nitroso-1,2-benzopyrone	
Calcimycin	
GR-127935	

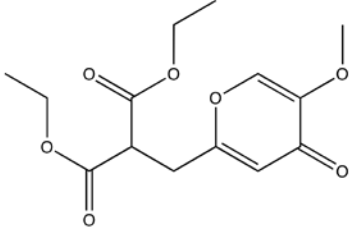
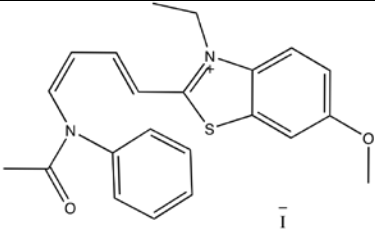
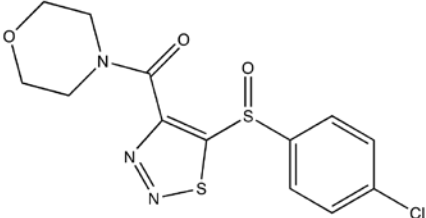
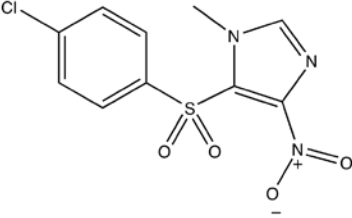
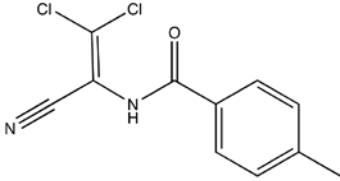
Bay 11-7085	
-------------	--

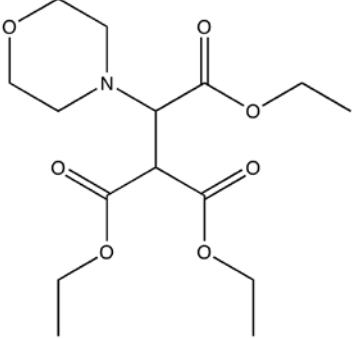
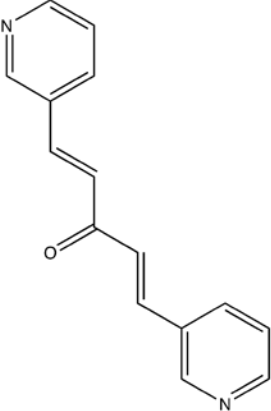
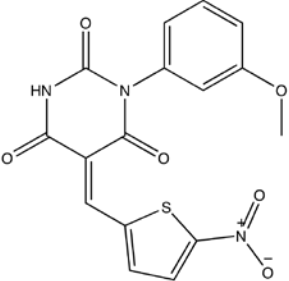
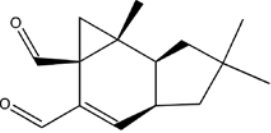
A.2 LIST OF COMPOUNDS FROM MLSCN SCREEN

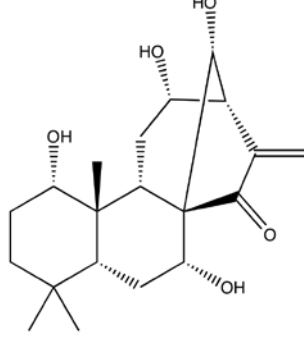
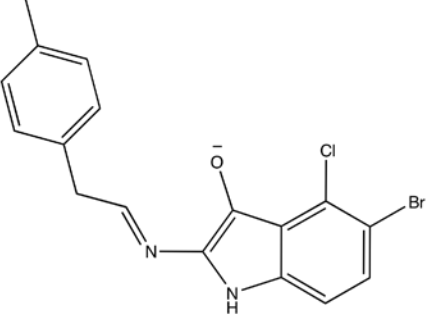
Compounds identified from biochemical assays as an inhibitor >50% (highlighted in red) at 20 μ M for at least one of the potential targets associated with cytoplasmic dynein translocation or other non-specific motor proteins.

Number	PubChem SID	Chemical Structure	Percent Inhibition		
			Dynein	GR	Myosin
4	14737082	 2-(5-bromo-2-methyl-4-nitro-1H-imidazol-1-yl)-1-(naphthalen-2-yl)ethanone	58.7 \pm 18.5	60.1 \pm 12.3	5.7 \pm 9.9
6	26725810	 7-isobutyl-3-methyl-8-nitro-1H-purine-2,6(3H,7H)-dione	56.9 \pm 4.0	8.9 \pm 41.0	19.9 \pm 12.8

7	14739323	 <p data-bbox="557 531 1049 575">ethyl 3-(4-ethanoyl-5-(phenylamino)thiophen-2-yl)-3-oxo-2-(pyridin-3-ylmethyl)propanoate</p>	78.8 ± 17.7	4.1 ± 45.8	35.0 ± 10.1
10	14731075	 <p data-bbox="609 997 1000 1041">(Z)-4,4-dimethyl-1-(3-nitrophenyl)-2-(1H-1,2,4-triazol-1-yl)pent-1-en-3-one</p>	83.0 ± 1.4	-0.2 ± 18.1	58.3 ± 7.9
11	17513591	 <p data-bbox="505 1381 1105 1407">(Z)-N-(2-(2-(3-chlorophenyl)-1-cyanovinyl)-4-p-tolylthiazol-5-yl)ethanamide</p>	53.8 ± 6.1	50.6 ± 7.0	17.8 ± 6.9
17	17412566	 <p data-bbox="505 1722 1105 1766">ethyl 2-(3-((4,6-dioxo-2-thioxotetrahydropyrimidin-5(6H)-ylidene)methyl)-2,5-dimethyl-1H-pyrrol-1-yl)-4,5,6,7-tetrahydrobenzo[b]thiophene-3-carboxylate</p>	64.8 ± 3.6	63.4 ± 13.5	39.0 ± 6.1

19	22414253	 <p>diethyl 2-((5-methoxy-4-oxo-4H-pyran-2-yl)methyl)propanedioate</p>	76.2 ± 14.9	21.4 ± 19.0	43.2 ± 5.4
23	17507787	 <p>3-ethyl-6-methoxy-2-((1E,3Z)-4-(N-phenylethanamido)buta-1,3-dienyl)benzo[d]thiazol-3-ium iodide</p>	75.1 ± 15.9	-64.6 ± 2.8	22.6 ± 8.1
27	24817175	 <p>(5-(4-chlorophenylsulfinyl)-1,2,3-thiadiazol-4-yl)(morpholino)methanone</p>	80.7 ± 8.2	3.1 ± 42.8	-3.7 ± 24.9
29	22404816	 <p>5-(4-chlorophenylsulfonyl)-1-methyl-4-nitro-1H-imidazole</p>	84.9 ± 10.0	-4.4 ± 16.6	0.6 ± 6.3
32	24805460	 <p>N-(2,2-dichloro-1-cyanovinyl)-4-methylbenzamide</p>	58.6 ± 21.3	6.0 ± 2.0	43.7 ± 16.3

57	14739918	 <p>triethyl 2-morpholinoethane-1,1,2-tricarboxylate</p>	53.4 ± 26.5	8.3 ± 9.1	9.2 ± 10.2
62	26664802	 <p>(1E,4E)-1,5-di(pyridin-3-yl)penta-1,4-dien-3-one</p>	65.3 ± 12.5	8.3 ± 14.4	60.6 ± 10.7
64	26725671	 <p>(Z)-1-(3-methoxyphenyl)-5-((5-nitrothiophen-2-yl)methylene)pyrimidine-2,4,6(1H,3H,5H)-trione</p>	70.0 ± 14.7	14.9 ± 37.8	25.3 ± 9.3
65	14719329		54.4 ± 10.3	26.9 ± 24.1	24.5 ± 18.4

66	17504722		74.6 ± 6.0	37.7 ± 17.7	17.0 ± 18.8
67	14732770	 <p data-bbox="568 903 1039 955"><i>(E)</i>-5-bromo-4-chloro-2-(2-<i>p</i>-tolylethylideneamino)-1<i>H</i>-indol-3-olate</p>	72.4 ± 10.6	38.0 ± 9.0	3.7 ± 20.9

APPENDIX B

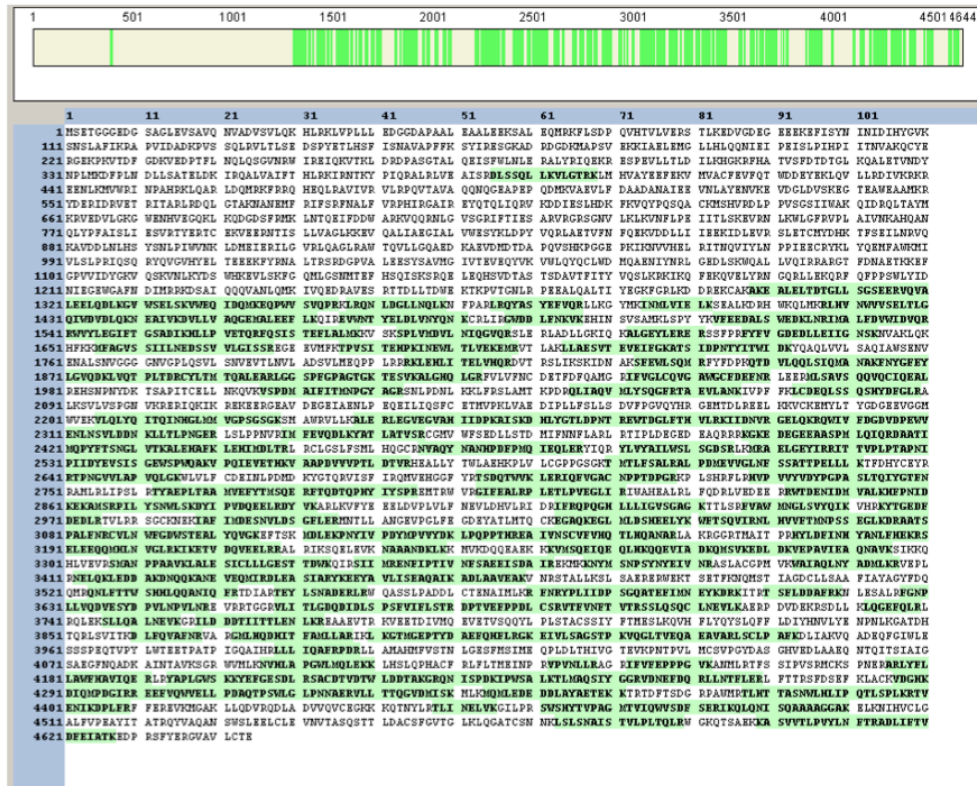
SEQUENCE COVERAGE OF CYTOPLASMIC DYNEIN BY MS AND MS/MS

B.1 SEQUENCE COVERAGE FROM LC-MS/MS OF TRYPSIN DIGEST OF CYTOPLASMIC DYNEIN

Sequence of rat cytoplasmic dynein heavy chain 1 with identified peptides highlighted in green with 56.53% sequence coverage.

B.2 SEQUENCE COVERAGE FROM LC-MS/MS OF TRYPSIN DIGEST OF CYTOPLASMIC DYNEIN HEAVY CHAIN 1 WITH TG1

Sequence of rat cytoplasmic dynein heavy chain 1 with identified peptides highlighted in green with 56.53% sequence coverage.

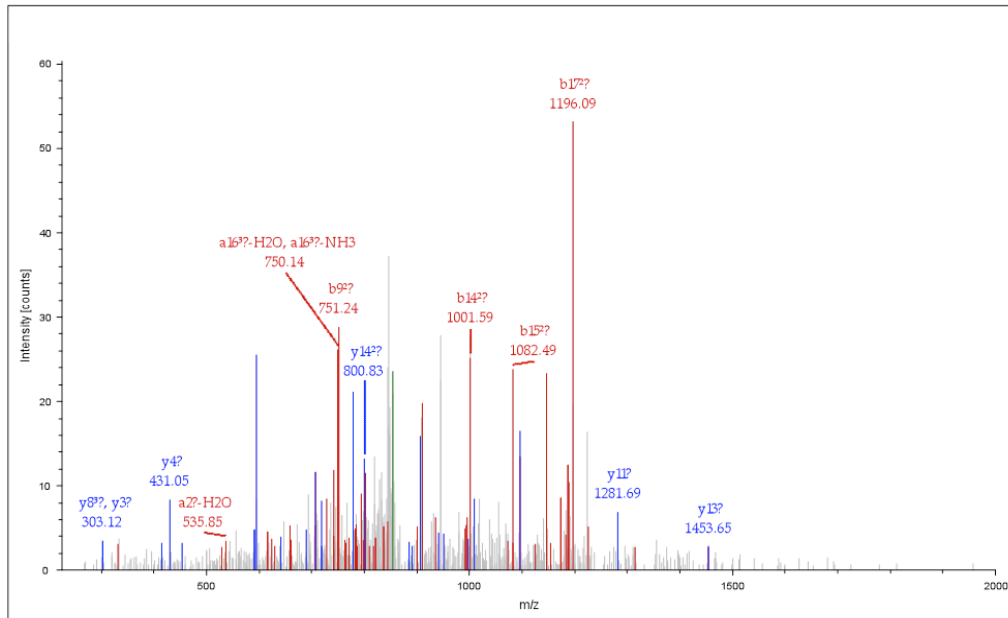


APPENDIX C

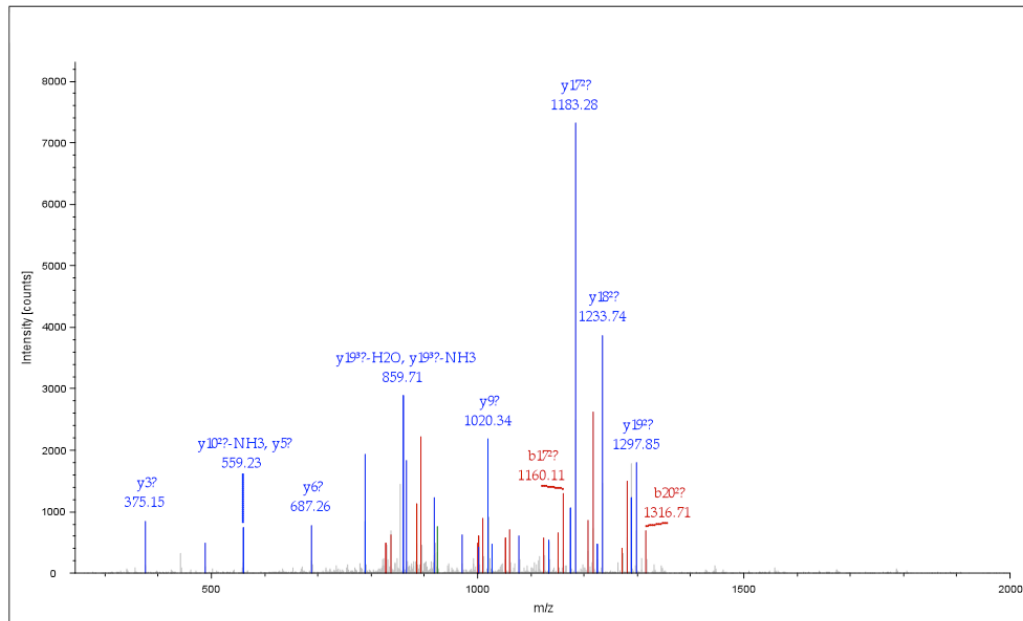
MS/MS SPECTRA OF TG1-LABELED PEPTIDES

Below are the MS/MS b (red) and y (blue) ions of peptides containing TG1-labeled cysteines. Shown above each spectrum is the sequence identity followed by the mass of the detected label (365, 379, 383, 397 Da). Also included is the charge of the parent monoisotopic ion and the calculated mass of the peptide. Retention time (RT) of eluted peptide and statistical information (cross correlation score (XCORR), probability, and number of ions matched) are also provided. (“?” = + charge)

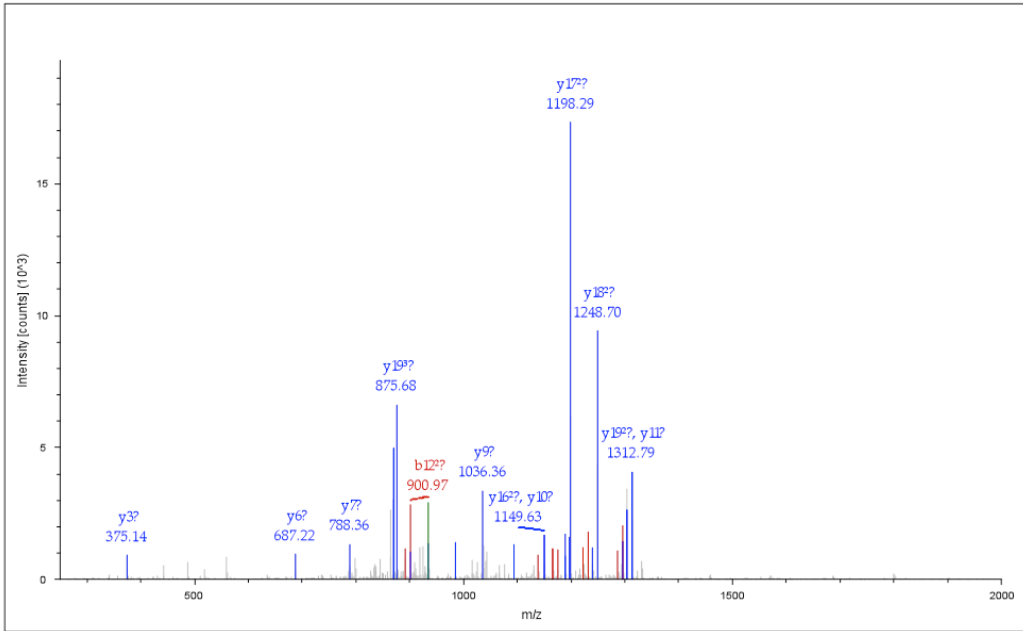
Sequence: CVLNWFGDWSTEALYQVGK, C1-TG1-1 (379.06920 Da)
 Charge: +3, Monoisotopic m/z: 865.40735 Da (-303.54 mmu/-350.74 ppm), MH+: 2594.20749 Da, RT: 96.16 min,
 Identified with: SEQUEST (v1.13); XCorr:4.32, Probability:63.76, Ions matched by search engine: 21/72
 Fragment match tolerance used for search: 0.5 Da



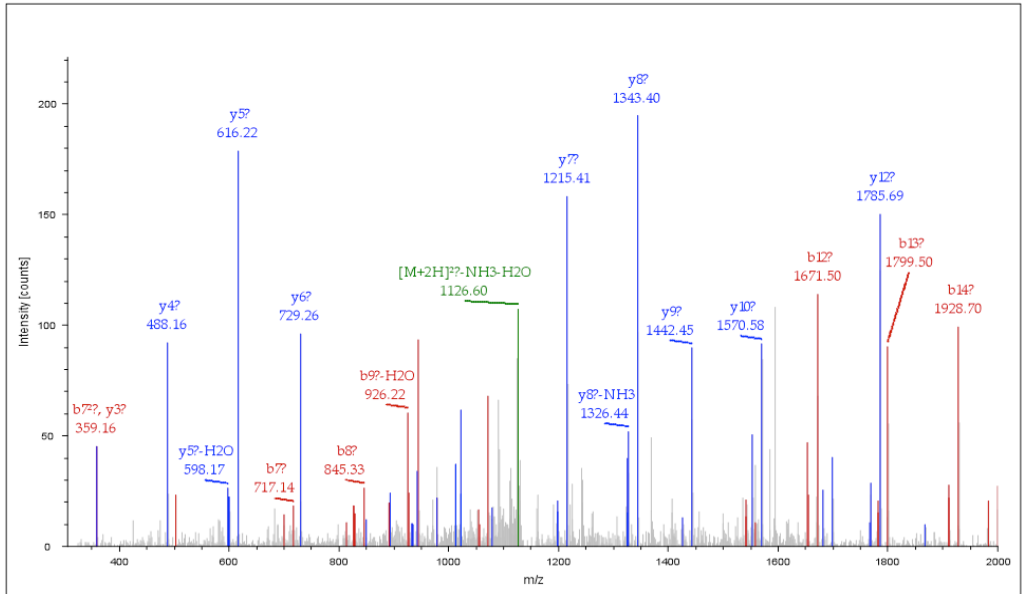
Sequence: LVQTPLTDRCYLTMTQALEAR, C10-TG1-3 (383.06412 Da)
 Charge: +3, Monoisotopic m/z: 936.11133 Da (+4.36 mmu/+4.66 ppm), MH+: 2806.31943 Da, RT: 92.67 min,
 Identified with: SEQUEST (v1.13); XCorr:5.67, Probability:124.47, Ions matched by search engine: 26/80
 Fragment match tolerance used for search: 0.5 Da



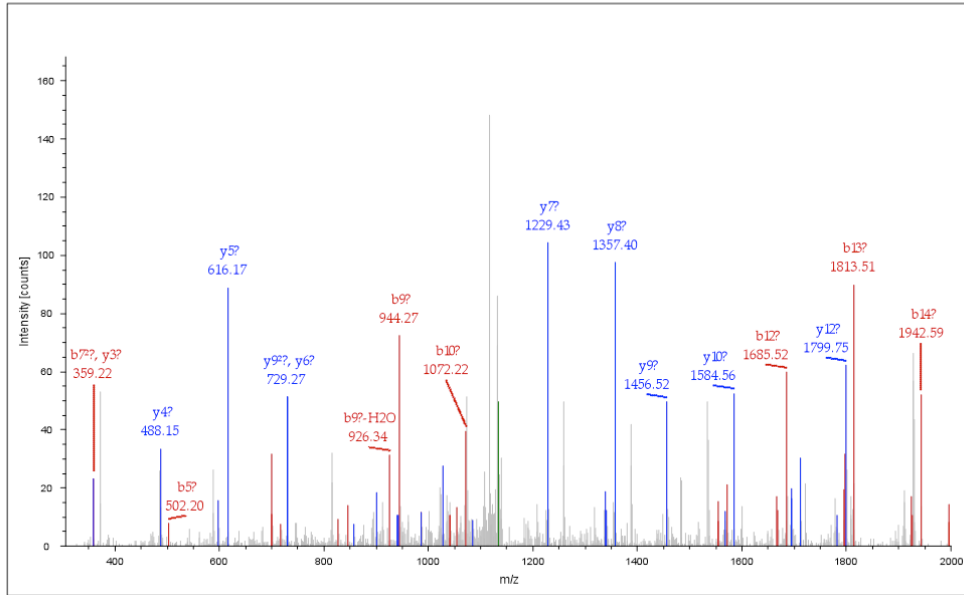
Sequence: LVQTPLTDRCYLTMTQALEAR, C10-TG1-4 (397.07977 Da), M14-Oxidation (15.99492 Da)
 Charge: +3, Monoisotopic m/z: 946.11481 Da (+4.32 mmu/+4.57 ppm), MH+: 2836.32987 Da, RT: 81.07 min,
 Identified with: SEQUEST (v1.13); XCorr:5.56, Probability:132.36, Ions matched by search engine: 29/80
 Fragment match tolerance used for search: 0.5 Da



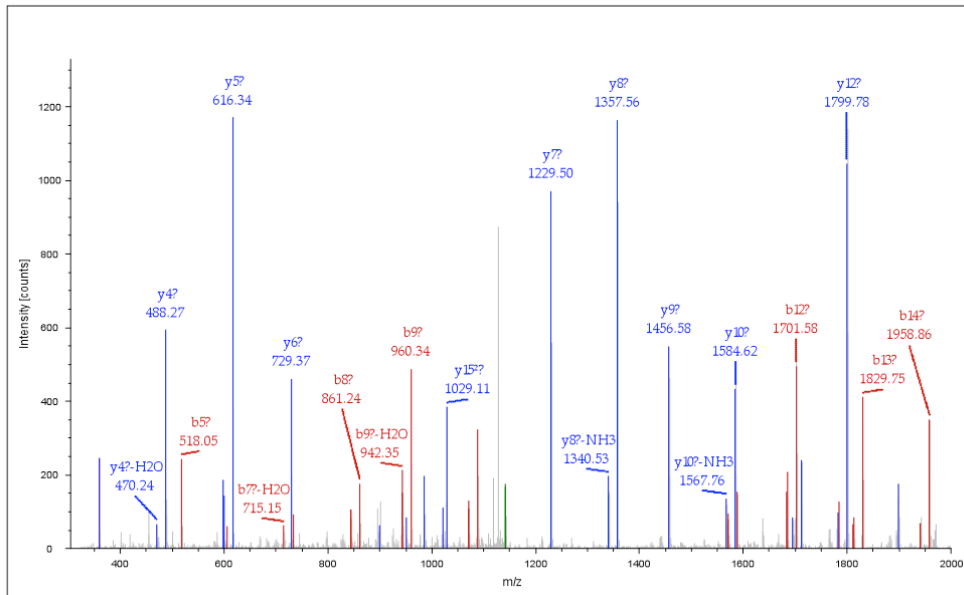
Sequence: MLSAVSQVQCIQEAR, C11-TG1-3 (383.06412 Da)
 Charge: +2, Monoisotopic m/z: 1144.02930 Da (+7.14 mmu/+6.24 ppm), MH+: 2287.05132 Da, RT: 97.15 min,
 Identified with: SEQUEST (v1.13); XCorr:3.06, Probability:70.77, Ions matched by search engine: 18/32
 Fragment match tolerance used for search: 0.5 Da



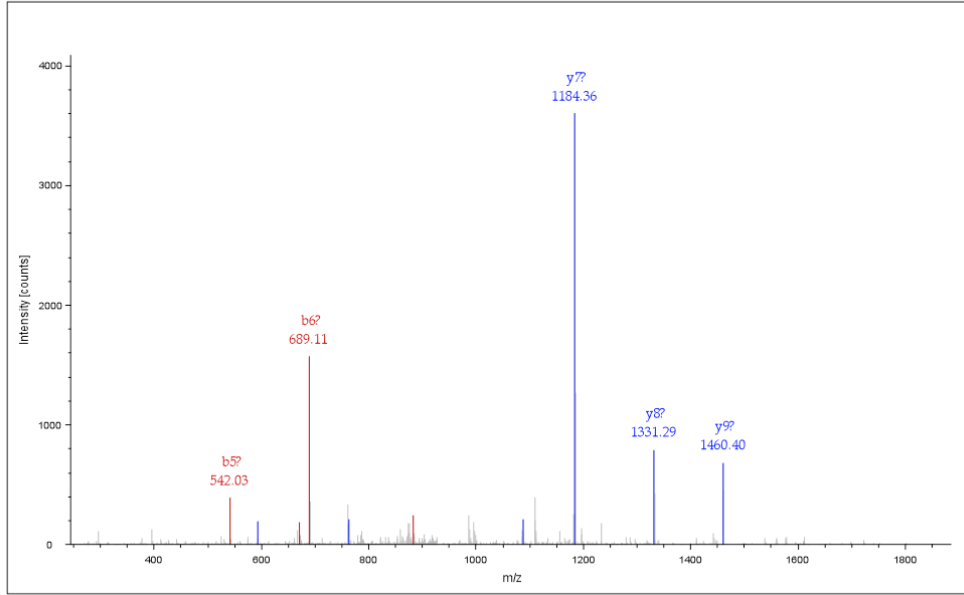
Sequence: MLSAVSQVQCIEALR, C11-TG1-4 (397.07977 Da)
 Charge: +2, Monoisotopic m/z: 1151.03491 Da (+4.93 mmu/+4.29 ppm), MH+: 2301.06255 Da, RT: 100.53 min,
 Identified with: SEQUEST (v1.13); XCorr:3.11, Probability:60.22, Ions matched by search engine: 16/32
 Fragment match tolerance used for search: 0.5 Da



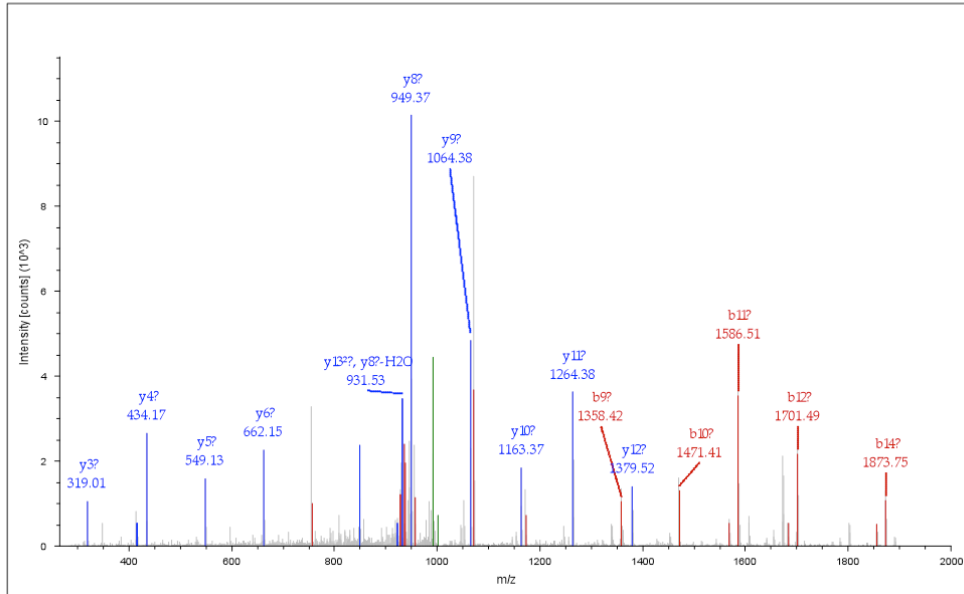
Sequence: MLSAVSQVQCIEALR, M1-Oxidation (15.99492 Da), C11-TG1-4 (397.07977 Da)
 Charge: +2, Monoisotopic m/z: 1159.03516 Da (+7.72 mmu/+6.66 ppm), MH+: 2317.06304 Da, RT: 95.72 min,
 Identified with: SEQUEST (v1.13); XCorr:4.96, Probability:119.43, Ions matched by search engine: 20/32
 Fragment match tolerance used for search: 0.5 Da



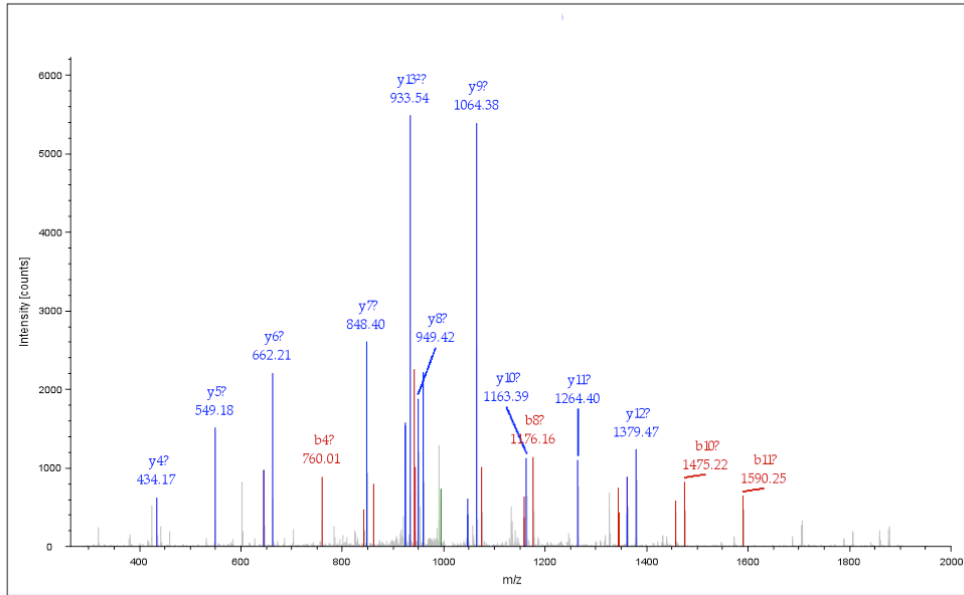
Sequence: DPTVEFPPDLCSR, C11-TG1-4 (397.07977 Da)
Charge: +2, Monoisotopic m/z: 936.89044 Da (+5.13 mmu/+5.48 ppm), MH+: 1872.77361 Da, RT: 85.85 min,
Identified with: SEQUEST (v1.13); XCorr:2.33, Probability:96.78, Ions matched by search engine: 16/24
Fragment match tolerance used for search: 0.5 Da



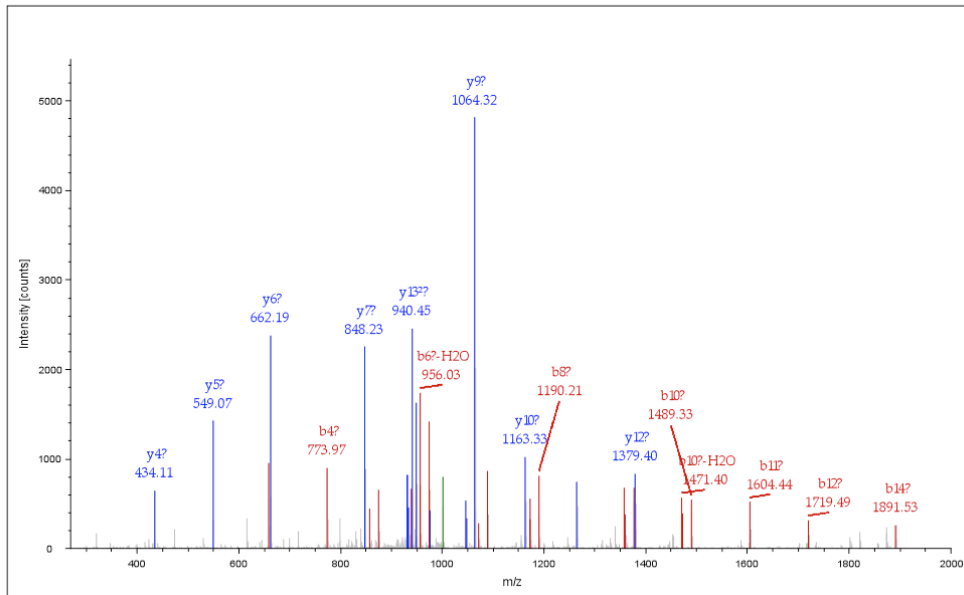
Sequence: SACDTVDTWLDDTA, C3-TG1-1 (379.06920 Da)
Charge: +2, Monoisotopic m/z: 1009.93304 Da (-460.89 mmu/-456.35 ppm), MH+: 2018.85881 Da, RT: 63.28 min,
Identified with: SEQUEST (v1.13); XCorr:3.68, Probability:104.24, Ions matched by search engine: 19/28
Fragment match tolerance used for search: 0.5 Da



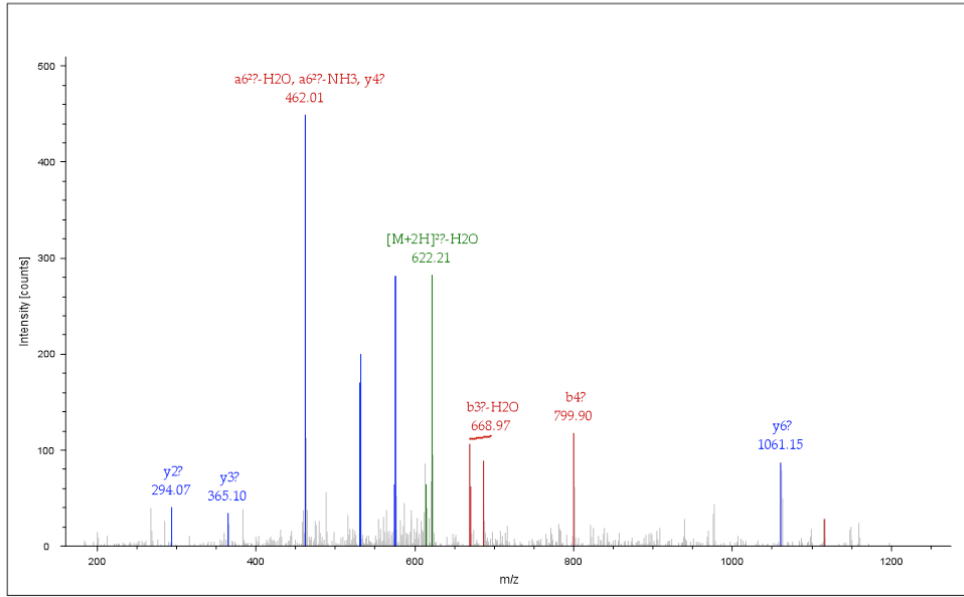
Sequence: SACDTVDTWLDDTAK, C3-TG1-3 (383.06412 Da)
 Charge: +2, Monoisotopic m/z: 1012.39600 Da (+4.84 mmu/+4.78 ppm), MH+: 2023.78472 Da, RT: 86.49 min,
 Identified with: SEQUEST (v1.13); XCorr:3.86, Probability:118.73, Ions matched by search engine: 22/28
 Fragment match tolerance used for search: 0.5 Da



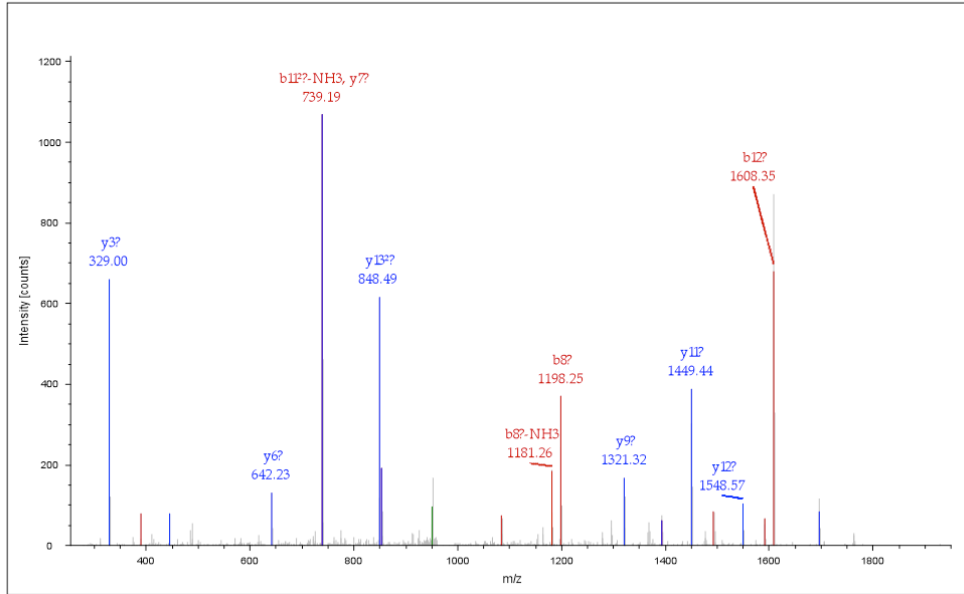
Sequence: SACDTVDTWLDDTAK, C3-TG1-4 (397.07977 Da)
 Charge: +2, Monoisotopic m/z: 1019.40533 Da (+6.36 mmu/+6.23 ppm), MH+: 2037.80339 Da, RT: 89.23 min,
 Identified with: SEQUEST (v1.13); XCorr:3.36, Probability:137.64, Ions matched by search engine: 20/28
 Fragment match tolerance used for search: 0.5 Da



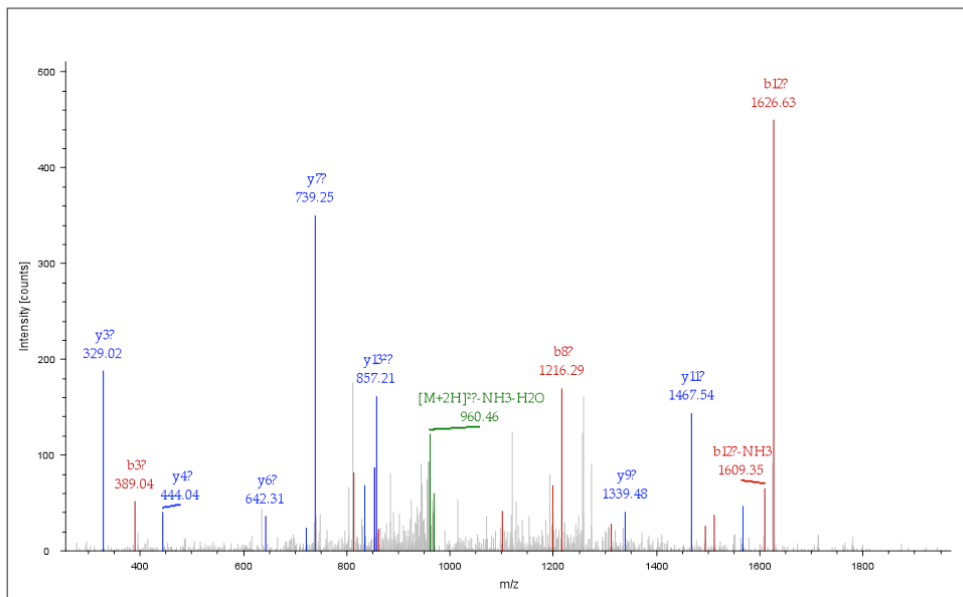
Sequence: LSCLPAFK, C3-TG1-3 (383.06412 Da)
Charge: +2, Monoisotopic m/z: 631.27966 Da (+3.73 mmu/+5.91 ppm), MH+: 1261.55205 Da, RT: 85.36 min,
Identified with: SEQUEST (v1.13); XCorr:2.37, Probability:55.80, Ions matched by search engine: 12/14
Fragment match tolerance used for search: 0.5 Da



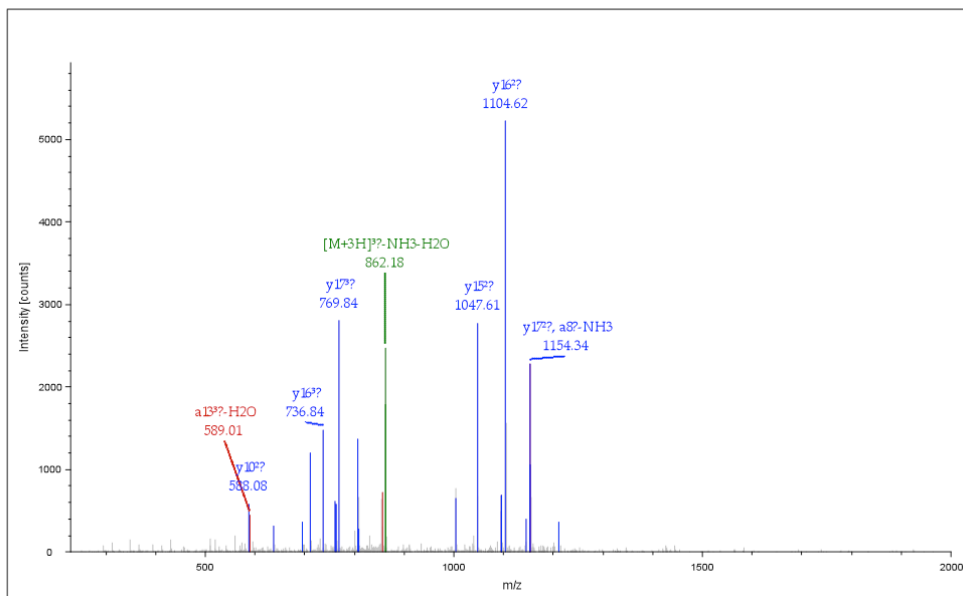
Sequence: IQFVGACNPPTDGR, C7-TG1-2 (365.04727 Da)
Charge: +2, Monoisotopic m/z: 968.91650 Da (+7.45 mmu/+7.69 ppm), MH+: 1936.82573 Da, RT: 79.98 min,
Identified with: SEQUEST (v1.13); XCorr:2.23, Probability:99.53, Ions matched by search engine: 20/28
Fragment match tolerance used for search: 0.5 Da



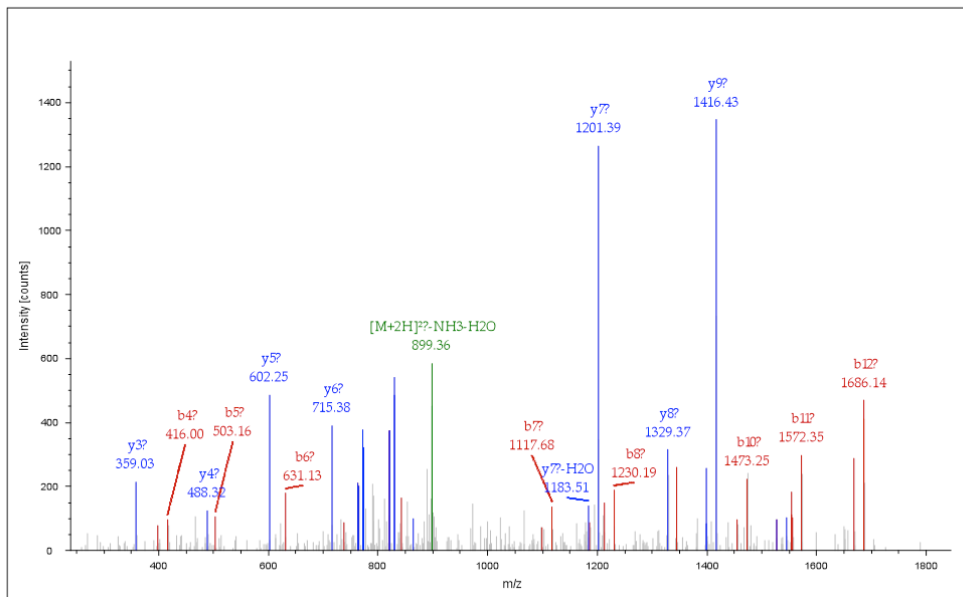
Sequence: IQFVGACNPPTDPGR, C7-TG1-3 (383.06412 Da)
Charge: +2, Monoisotopic m/z: 977.92175 Da (+4.27 mmu/+4.37 ppm), MH+: 1954.83623 Da, RT: 74.85 min,
Identified with: SEQUEST (v1.13); XCorr:2.50, Probability:40.30, Ions matched by search engine: 14/28
Fragment match tolerance used for search: 0.5 Da



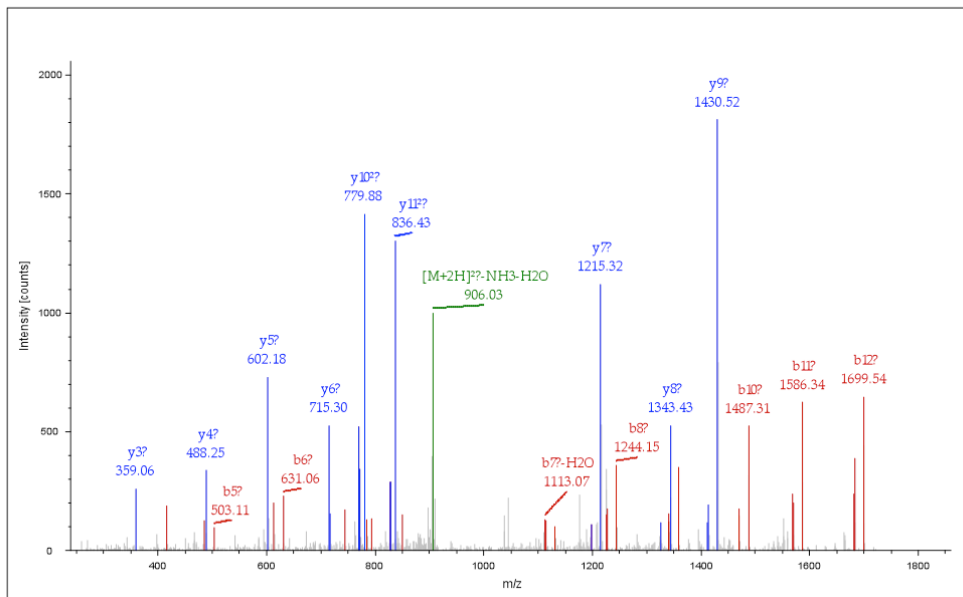
Sequence: EAIVNSCVFVHQTLLQANAR, C7-TG1-3 (383.06412 Da)
Charge: +3, Monoisotopic m/z: 874.07123 Da (+3.51 mmu/+4.02 ppm), MH+: 2620.19913 Da, RT: 75.08 min,
Identified with: SEQUEST (v1.13); XCorr:3.57, Probability:129.45, Ions matched by search engine: 26/76
Fragment match tolerance used for search: 0.5 Da



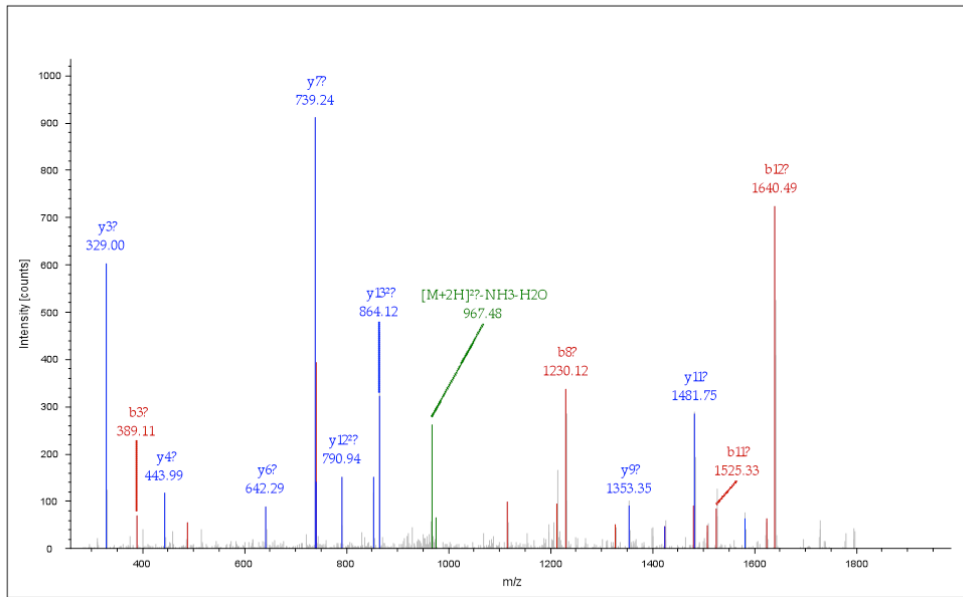
Sequence: SSLQSQCLNEVLK, C7-TG1-3 (383.06412 Da)
 Charge: +2, Monoisotopic m/z: 916.41187 Da (+5.47 mmu/+5.96 ppm), MH+: 1831.81645 Da, RT: 77.80 min,
 Identified with: SEQUEST (v1.13); XCorr:2.21, Probability:92.91, Ions matched by search engine: 17/24
 Fragment match tolerance used for search: 0.5 Da



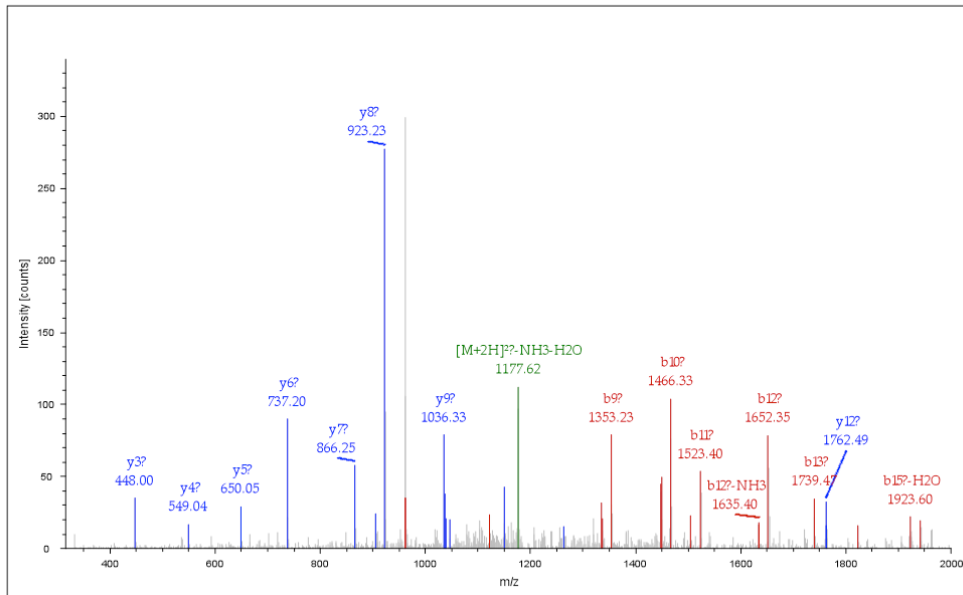
Sequence: SSLQSQCLNEVLK, C7-TG1-4 (397.07977 Da)
 Charge: +2, Monoisotopic m/z: 923.41827 Da (+4.05 mmu/+4.38 ppm), MH+: 1845.82927 Da, RT: 80.49 min,
 Identified with: SEQUEST (v1.13); XCorr:2.25, Probability:73.10, Ions matched by search engine: 16/24
 Fragment match tolerance used for search: 0.5 Da



Sequence: IQFVGACNPPTDPGR, C7-TG1-4 (397.07977 Da)
 Charge: +2, Monoisotopic m/z: 984.92828 Da (+2.98 mmu/+3.02 ppm), MH+: 1968.84929 Da, RT: 75.51 min,
 Identified with: SEQUEST (v1.13); XCorr:2.29, Probability:115.93, Ions matched by search engine: 18/28
 Fragment match tolerance used for search: 0.5 Da



Sequence: LALESICLLLGESTTDWK, C7-TG1-4 (397.07977 Da)
 Charge: +2, Monoisotopic m/z: 1195.07043 Da (+8.97 mmu/+7.5 ppm), MH+: 2389.13359 Da, RT: 115.64 min,
 Identified with: SEQUEST (v1.13); XCorr:2.31, Probability:123.03, Ions matched by search engine: 17/34
 Fragment match tolerance used for search: 0.5 Da



BIBLIOGRAPHY

- Alberts, B.; Johnson, A.; Lewis, J.; Raff, M.; Roberts, K.; Walter, P. *Molecular Biology of the Cell*, 5th Ed; Garland Science, Taylor & Francis Group, LLC: NY, USA, 2008; pp 974-984.
- Alexander, N.; Bortolus, M.; Al-Mestarihi, A.; Mchaourab, H.; Meiler, J. De novo high-resolution protein structure determination from sparse spin-labeling EPR data. *Structure*, **2008**, *16*, 181-195.
- Allen, B.L.; Kichambare, P.D.; Star, A. Carbon nanotube field-effect-transistor-based biosensors. *Adv. Mater.*, **2007**, *19*, 1439-1451.
- Ambrose, J.C.; Li, W.; Marcus, A.; Ma, H.; Cyr, R. A minus-end-directed kinesin with plus-end tracking protein activity is involved in spindle morphogenesis. *Mol. Biol. Cell*, **2005**, *16*, 1584-1592.
- Andrade, C.H.; Pasqualoto, K.F.M.; Ferreira, E.I.; Hopfinger, A.J. 4D-QSAR: Perspectives in drug design. *Molecules*, **2010**, *15*, 3281-3294.
- Andrade, J.D.; Hlady, V. Protein adsorption and materials biocompatibility: A tutorial review and suggested hypotheses. *Adv. Polym. Sci.*, **1986**, *79*, 1-63.
- Angelides, K.J.; Smith, K.E.; Takeda, M. Assembly and exchange of intermediate filament proteins of neurons: neurofilaments are dynamic structures. *J. Cell Biol.*, **1989**, *108*, 1495-1506.
- Annesley, T.M. Ion suppression in mass spectrometry. *Clin. Chem.*, **2003**, *49*, 1041-1044.
- Aoyama, H.; Noguchi, T.; Misawa, T.; Nakamura, T.; Miyachi, H.; Hashimoto, Y.; Kobayashi, H. Development of tubulin-polymerization inhibitors based on the thalidomide skeleton. *Chem. Pharm. Bull.*, **2007**, *55*, 944-949.
- Asai, D.J.; Koonce, M.P. The dynein heavy chain: structure, mechanics, and evolution. *Trends Cell Biol.*, **2001**, *11*, 196-202.
- Ateh, D.D.; Hussain, I.K.; Mustafa, A.H.; Price, K.M.; Gulati, R.; Nickols, C.D.; Bird, M.M.; Greensmith, L.; Hafezparast, M.; Fisher, E.M.C.; Baker, C.S.; Martin, J.E. Dynein-dynactin complex subunits are differentially localized in brain and spinal cord, with

- selective involvement in pathological features of neurodegenerative disease. *Neuropathol. Appl. Neurobiol.*, **2008**, *34*, 88-94.
- Banerjee, S.; Chakrabarti, G.; Bhattacharyya, B. Colchicine binding to tubulin monomers: A mechanistic study. *Biochemistry*, **1997**, *36*, 5600-5606.
- Banks, G.T.; Fisher, E.M.C. Cytoplasmic dynein could be key to understanding neurodegeneration. *Genome Biol.*, **2008**, *9*, 214.
- Bartlett, S.E.; Reynolds, A.J.; Hendry, I.A. Retrograde axonal transport of neurotrophins: Differences between neuronal populations and implications for motor neuron disease. *Immunol. Cell Biol.*, **1998**, *76*, 419-423.
- Barton, N.R.; Goldstein, L.S. Going mobile: microtubule motors and chromosome segregation. *PNAS*, **1996**, *93*, 1735-1742.
- Bassil, N.; Maillart, E.; Canva, M.; Levy, Y.; Millot, M.C.; Pissard, S.; Narwa, R.; Goossens, M. One hundred spots parallel monitoring of DNA interactions by SPR imaging of polymer-functionalized surfaces applied to the detection of cystic fibrosis mutations. *Sens. Actuators, B*, **2003**, *94*, 313-323.
- Benadie, Y.; Deysel, M.; Siko, D.G.R.; Roberts, V.V.; Wyngaardt, S.V.; Thanyani, S.T.; Sekanka, G.; ten Bokum, A.M.C.; Collett, L.A.; Grooten, J.; Baird, M.S.; Verschoor, J.A. Cholesteroid nature of free mycolic acids from *M. tuberculosis*. *Chem. Phys. Lipids*, **2008**, *152*, 95-103.
- Berney, H.; Oliver, K. Dual polarization interferometry size and density characterization of DNA immobilisation and hybridisation. *Biosens. Bioelectron.*, **2005**, *21*, 618-626.
- Bhattacharyya, B.; Panda, D.; Gupta, S.; Banerjee, M. Anti-mitotic activity of colchicine and the structural basis for its interaction with tubulin. *Med. Res. Rev.*, **2008**, *28*, 155-183.
- Bloom, G.S.; Vallee, R.B. Association of microtubule-associated protein 2 (MAP 2) with microtubules and intermediate filaments in cultured brain cells. *J. Cell Biol.*, **1983**, *96*, 1523-1531.
- Blum, J.J.; Hayes, A. Effect of thiourea and substituted thioureas on dynein ATPase and on the turbidity response of *Tetrahymena cilia*. *J. Supramol. Struct.*, **1979**, *12*, 23-34.
- Blundell, T.L.; Sibanda, B.L.; Sternberg, M.J.; Thornton, J.M. Knowledge-based prediction of protein structures and the design of novel molecules. *Nature*, **1987**, *326*, 347-352.
- Boozer, C.; Kim, G.; Cong, S.; Guan, H.; Londergan, T. Looking towards label-free biomolecular interaction analysis in a high-throughput format: a review of new surface plasmon resonance technologies. *Curr. Opin. Biotechnol.*, **2006**, *17*, 400-405.
- Borch, J.; Roepstorff, P. Screening for enzyme inhibitors by surface plasmon resonance combined with mass spectrometry. *Anal. Chem.*, **2004**, *76*, 5243-5248.

- Bouchard, P.; Penningroth, S.M.; Cheung, A.; Gagnon, C.; Bardin, C.W. *erythro-9-[3-(2-Hydroxynonyl)]adenine* is an inhibitor of sperm motility that blocks dynein ATPase and protein carboxylmethylase activities. *PNAS*, **1981**, 78, 1033-1036.
- Boudjemline, A.; Clarke, D.T.; Freeman, N.J.; Nicholson, J.M.; Jones, G.R. Early stages of protein crystallization as revealed by emerging optical waveguide technology. *J. Appl. Crystallogr.*, **2008**, 41, 523-530.
- Brandenburg, A.; Krauter, R.; Kunzel, C.; Stefan, M.; Schulte, H. Interferometric sensor for detection of surface-bound bioreactions. *Appl. Opt.*, **2000**, 39, 6396-6405.
- Bremer, A.; Henn, C.; Engel, A.; Baumeister, W.; Ueli, A. Has negative staining still a place in biomacromolecular electron microscopy? *Ultramicroscopy*, **1992**, 46, 85-111.
- Bremner, K.H.; Scherer, J.; Yi, J.; Vershinin, M.; Gross, S.P.; Vallee, R.B. Adenovirus transport via direct interaction of cytoplasmic dynein with viral capsid hexon subunit. *Cell Host Microbe.*, **2009**, 6, 523-535.
- Buckle, P.E.; Davies, R.J.; Kinning, T.; Yeung, D.; Edwards, P.R.; Pollard-Knight, D.; Lowe, C.R. The resonant mirror: a novel optical sensor for direct sensing of biomolecular interactions Part II: Applications. *Biosens. Bioelectron.*, **1993**, 8, 355-363.
- Buijs, J.; Franklin, G.C. SPR-MS in functional proteomics. *Brief. Funct. Genomics Proteomics*, **2005**, 4, 39-47.
- Burgess, S.A.; Walker, M.L.; Sakakibara, H.; Knight, P.J.; Oiwa, K. Dynein structure and power stroke. *Nature*, **2003**, 421, 715-718.
- Burns, R.G. α -, β -, γ -tubulins: Sequence comparisons and structural constraints. *Cell Motil. Cytoskeleton*, **1991**, 20, 181-189.
- Calderwood, D.A.; Huttenlocher, A.; Kiosses, W.B.; Rose, D.M.; Woodside, D.G.; Schwartz, M.A.; Ginsberg, M.H. Increased filamin binding to β -integrin cytoplasmic domains inhibits cell migration. *Nat. Cell Biol.*, **2001**, 3, 1060-1068.
- Calderwood, S.K.; Khaleque, M.A.; Sawyer, D.B.; Ciocca, D.R. Heat shock proteins in cancer: chaperones of tumorigenesis. *Trends Biochem. Sci.*, **2006**, 31, 164-172.
- Carter, A.P.; Garbarino, J.E.; Wilson-Kubalek, E.M.; Shipley, W.E.; Cho, C.; Milligan, R.A.; Vale, R.D.; Gibbons, I.R. Structure and functional role of dynein's microtubule-binding domain. *Science*, **2008**, 322, 1691-1695.
- Cassimeris, L. The oncoprotein 18/stathmin family of microtubule destabilizers. *Curr. Opin. Cell Biol.*, **2002**, 14, 18-24.
- Ceroni, A.; Passerini, A.; Vullo, A.; Frasconi, P. DISULFIND: a disulfide bonding state and cysteine connectivity prediction server. *Nucleic Acids Res.*, **2006**, 34(Web Server issue):W177-W181.

- Cheng, Y.; Walz, T. The advent of near-atomic resolution in single-particle electron microscopy. *Annu. Rev. Biochem.*, **2009**, *78*, 723-742.
- Chibalina, M.V.; Puri, C.; Kendrick-Jones, J.; Buss, F. Potential roles of myosin VI in cell motility. *Biochem. Soc. Trans.*, **2009**, *37*, 966-970.
- Cho, C.; Reck-Peterson, S.L.; Vale, R.D. Regulatory ATPase sites of cytoplasmic dynein affect processivity and force generation. *J. Biol. Chem.*, **2008**, *283*, 25839-25845.
- Chretien, D.; Fuller, S.D. Microtubules switch occasionally into unfavorable configurations during elongation. *J. Mol. Biol.*, **2000**, *298*, 663-676.
- Coffey, P.D.; Swann, M.J.; Waigh, T.A.; Schedin, F.; Lu, J.R. Multiple path length dual polarization interferometry. *Opt. Express*, **2009**, *17*, 10959-10969.
- Conde, C.; Caceres, A. Microtubule assembly, organization and dynamics in axons and dendrites. *Nat. Rev. Neurosci.*, **2009**, *10*, 319-332.
- Conway, J.F.; Cheng, N.; Zlotnick, A.; Wingfield, P.T.; Stahl, S.J.; Steven, A.C. Visualization of a 4-helix bundle in the hepatitis B virus capsid by cryo-electron microscopy. *Nature*, **1997**, *386*, 91-94.
- Cooper, M.A. Optical biosensors in drug discovery. *Nat. Rev. Drug Discovery*, **2002**, *1*, 515-528.
- Corthesy-Theulaz, I.; Pauloin, A.; Pfeffer, S.R. Cytoplasmic dynein participates in the centrosomal localization of the golgi complex. *J. Cell Biol.*, **1992**, *118*, 1333-1345.
- Cross, G.H.; Reeves, A.; Brand, S.; Swann, M.J.; Peel, L.L.; Freeman, N.J.; and Lu, J.R. The metrics of surface adsorbed small molecules on the Young's fringe dual-slab waveguide interferometer. *J. Phys. D: Appl. Phys.*, **2004**, *37*, 74-80.
- Crowther, R.A.; DeRosier, D.J.; Klug, A. The reconstruction of a three-dimensional structure from projections and its application to electron. *Proc. R. Soc. Lond. A.*, **1970**, *317*, 319-340.
- Cunningham, B.; Li, P.; Lin, B.; Pepper, J. Colorimetric resonant reflection as a direct biochemical assay technique. *Sens. Actuators, B*, **2002**, *81*, 316-328.
- Cunningham, B.T.; Li, P.; Schultz, S.; Lin, B.; Baird, C.; Gerstenmaier, J.; Genick, C.; Wang, F.; Fine, E.; Laing, L. Label-free Assays on the BIND system. *J. Biomol. Screen*, **2004**, *9*, 481-490.
- Cush, R.; Cronin, J.M.; Stewart, W.J.; Maule, C.H.; Molloy, J.; Goddard, N.J. The resonant mirror: a novel optical biosensor for direct sensing of biomolecular interactions. Part I: Principle of operation and associated instrumentation. *Biosens. Bioelectron.*, **1993**, *8*, 347-353.

- Czar, M.J.; Galigniana, M.D.; Silverstein, A.M.; Pratt, W.B. Geldanamycin, a heat shock protein 90-binding benzoquinone ansamycin, inhibits steroid-dependent translocation of the glucocorticoid receptor from the cytoplasm to the nucleus. *Biochemistry*, **1997**, *36*, 7776-7785.
- Daghestani, H.N.; Day, B.W. Theory and applications of surface plasmon resonance, resonant mirror, resonant waveguide grating, and dual polarization interferometry biosensors. *Sensors*, **2010**, *10*, 9630-9646.
- Daghestani, H.N.; Fernig, D.G.; Day, B.W. Evaluation of biosensor surfaces for the detection of microtubule perturbation. *Biosens. Bioelectron.*, **2009**, *25*, 136-141.
- Den Hollander, P.; Kumar, R. Dynein light chain 1 contributes to cell cycle progression by increasing cyclin-dependent kinase 2 activity in estrogen-stimulated cells. *Cancer Res.*, **2006**, *66*, 5941-5949.
- DeTure, M.A.; Zhang, E.Y.; Bubb, M.R.; Purich, D.L. *In vitro* polymerization of embryonic MAP-2c and fragments of the MAP-2 microtubule binding region in structures resembling paired helical filaments. *J. Biol. Chem.*, **1996**, *271*, 32702-32706.
- Dittmar, K.D.; Demady, D.R.; Stancato, L.F.; Krishna, P.; Pratt, W.B. Folding of the glucocorticoid receptor by the heat shock protein (hsp) 90-based chaperone machinery – the role of p23 is to stabilize receptor•hsp90 heterocomplexes formed by hsp90•p60•hsp70. *J. Biol. Chem.*, **1997**, *272*, 21213-21220.
- Dmitriev, D.A.; Massino, Y.S.; Segal, O.L. Kinetic analysis of interactions between biospecific monoclonal antibodies and immobilized antigens using a resonant mirror biosensor. *J. Immunol Methods*, **2003**, *280*, 183-202.
- Dohner, K.; Wolfstein, A.; Prank, U.; Echeverri, C.; Dujardin, D.; Vallee, R.; Sodeik, B. Function of dynein and dynactin in herpes simplex virus capsid transport. *Mol. Biol. Cell*, **2002**, *13*, 2795-2809.
- Dos Remedios, C.G.; Chhabra, D.; Kekic, M.; Dedova, I.V.; Tsubakihara, M.; Berry, D.A.; Nosworthy, N.J. Actin binding proteins: regulation of cytoskeletal microfilaments. *Physiol. Rev.*, **2003**, *83*, 433-473.
- Downing, K.H.; Nogales, E. Tubulin structure: insights into microtubule properties and functions. *Curr. Opin. Struct. Biol.* **1998**, *8*, 785-791.
- Drukman, S.; Kavallaris, M. Microtubule alterations and resistance to tubulin-binding agents. *Int. J. Oncol.*, **2002**, *21*, 621-628.
- Duchesne, L.; Tissot, B.; Rudd, T.R.; Dell, A.; Fernig, D.G. N-Glycosylation of fibroblast growth factor receptor 1 regulates ligand and heparan sulfate co-receptor binding. *J. Biol. Chem.*, **2006**, *281*, 27178-27189.

- Edwards, P.R.; Maule, C.H.; Leatherbarrow, R.J.; Winzor, D.J. Second-order kinetic analysis of IAsys biosensor data: its use and applicability. *Anal Biochem.*, **1998**, *263*, 1-12.
- Eswar, N.; Marti-Renom, M.A.; Webb, B.; Madhusudhan, M.S.; Eramian, D.; Shen, M.; Pieper, U.; Sali, A. Comparative protein structure modeling with MODELLER. *Curr. Protoc. Bioinformatics*, **2006**, *15*, 1-30.
- Eswar, N.; Webb, B.; Marti-Renom, M.A.; Madhusudhan, M.S.; Eramian, D.; Shen, M.; Pieper, U.; Sali, A. Comparative protein structure modeling using MODELLER. *Curr. Protoc. Protein Sci.*, **2007**, *2*, 1-31.
- Fahey, R.C.; Hunt, J.S.; Windham, G.C. On the cysteine and cystine content of proteins: Differences between intracellular and extracellular proteins. *J. Mol. Evol.*, **1977**, *10*, 155-160.
- Fan, X.; White, I.M.; Shopova, S.I.; Zhu, H.; Suter, J.; Sun, Y. Sensitive optical biosensors for unlabeled targets: a review. *Anal. Chim. Acta*, **2008**, *620*, 8-26.
- Fang, Y. Label-free and non-invasive biosensor cellular assays for cell adhesion. *J. Adhes. Sci. Technol.*, **2010b**, *24*, 1011-1021.
- Fang, Y. Non-invasive optical biosensor for probing cell signaling. *Sensors*, **2007**, *7*, 2316-2329.
- Fang, Y. Resonant waveguide grating biosensor for microarrays. In *Optical Guided-wave Chemical and Biosensors II*, Springer Series on Chemical Sensors and Biosensors; Zourob, M. and Lakhtakia, A., Eds.; Springer: Verlag Berlin Beidelberg, **2010a**; Vol. 8, Part 1, 27-42.
- Fang, Y.; Ferrie, A.M. Label-free optical biosensor for ligand-directed functional selectivity acting on β_2 adrenoceptor in living cells. *FEBS Lett.*, **2008**, *582*, 558-564.
- Fang, Y.; Ferrie, A.M.; Fontaine, N.H.; Mauro, J.; Balakrishnan, J. Resonant waveguide grating biosensor for living cell sensing. *Biophys. J.*, **2006**, *91*, 1925-1940.
- Fang, Y.; Frutos, A.G.; Lahiri, J. Membrane protein microarrays. *J. Am. Chem. Soc.*, **2002**, *124*, 2394-2395.
- Fang, Y.; Yokota, E.; Mabuchi, I.; Nakamura, H.; Ohizumi, Y. Puralin blocks the sliding movement of sea urchin flagellar axonemes by selective inhibition of half the ATPase activity of axonemal dyneins. *Biochemistry*, **1997**, *36*, 15561-15567.
- Faraggi, E.; Xue, B.; Zhou, Y. Improving the prediction accuracy of residue solvent accessibility and real-value backbone torsion angles of protein by guided-learning through a two-layer neural network. *Proteins: Struct., Funct., Bioinf.*, **2008**, *74*, 847-856.
- Feizi, T.; Fazio, F.; Chai, W.; Wong, C.H. Carbohydrate microarrays – a new set of technologies at the frontiers of glycomics. *Curr. Opin. Struct. Biol.*, **2003**, *13*, 637-645.

- Frank, J. Single-particle reconstruction of biological macromolecules in electron microscopy – 30 years. *Q. Rev. Biophys.*, **2009**, *42*, 139-158.
- Frank, J. *Three-Dimensional Electron Microscopy of Macromolecular Assemblies*; Academic Press, Inc.: San Diego, CA, 1996; pp 1-25.
- Fuchs, E.; Weber, K. Intermediate filaments: structure, dynamics, function, and disease. *Annu. Rev. Biochem.*, **1994**, *63*, 345-382.
- Funk, C.J.; Davis, A.S.; Hopkins, J.A.; Middleton, K.M. Development of high-throughput screens for discovery of kinesin adenosine triphosphate modulators. *Anal. Biochem.*, **2004**, *329*, 68-76.
- Galigniana, M.D.; Harrell, J.M.; O'Hagen, H.M.; Ljungman, M.; Pratt, W.B. Hsp90-binding immunophilins link p53 to dynein during p53 transport to the nucleus. *J. Biol. Chem.*, **2004**, *279*, 22483-22489.
- Galigniana, M.D.; Scruggs, J.L.; Herrington, J.; Welsh, M.J.; Carter-Su, C.; Housley, P.R.; Pratt, W.B. Heat shock protein 90-dependent (geldanamycin-inhibited) movement of glucocorticoid receptor through the cytoplasm to the nucleus requires intact cytoskeleton. *Mol. Endocrinol.*, **1998**, *12*, 1903-1913.
- Gamblin, C.T.; Nachmanoff, K.; Halpain, S.; Williams, R.C. Recombinant MAP2c reduces the dynamic instability of individual microtubules. *Biochemistry*, **1996**, *35*, 12576–12586
- Gennerich, A.; Vale, R.D. Walking the walk: how kinesin and dynein coordinate their steps. *Curr. Opin. Cell Biol.*, **2009**, *21*, 59-67.
- George, A.J.T.; French, R.R.; Glennie, M.J. Measurement of kinetic binding constants of a panel of anti-saporin antibodies using a resonant mirror biosensor. *J. Immunol Methods*, **1995**, *183*: 51-63.
- Gertsch, J.; Meier, S.; Müller, M.; Altmann, K.H. Differential effects of natural product microtubule stabilizers on microtubule assembly: single agent and combination studies with taxol, epothilone B, and discodermolide. *ChemBioChem*, **2009**, *10*, 166-175.
- Giannakakou, P.; Nakano, M.; Nicolaou, K.C.; O'Brate, A.; Yu, J.; Blagosklonny, M.V.; Greber, U.F.; Fojo, T. Enhanced microtubule-dependent trafficking and p53 nuclear accumulation by suppression of microtubule dynamics. *PNAS*, **2002**, *99*, 10855-10860.
- Giannakakou, P.; Sackett, D.L.; Ward, Y.; Webster, K.R.; Blagosklonny, M.V.; Fojo, T. p53 is associated with cellular microtubules and is transported to the nucleus by dynein. *Nat. Cell Biol.*, **2000**, *2*, 709-717.
- Gill, S.R.; Schroer, T.A.; Szilak, I.; Steuer, E.R.; Sheetz, M.P.; Cleveland, D.W. Dynactin, a conserved, ubiquitously expressed component of an activator of vesicle motility mediated by cytoplasmic dynein. *J. Cell Biol.*, **1991**, *115*, 1639-1650.

- Glass, C.K.; Saijo, K. Nuclear receptor transrepression pathways that regulate inflammation in macrophages and T cells. *Nat. Rev. Immunol.*, **2010**, *10*, 365-376.
- Goldman, R.D.; Grin, B.; Mendez, M.G.; Kuczumski, E.R. Intermediate filaments: versatile building blocks of cell structure. *Curr. Opin. Cell Biol.*, **2008**, *20*, 28-34.
- Goldmann, W.H.; Tempel, M.; Sprenger, I.; Isenberg, G.; Ezzell, R.M. Viscoelasticity of actin-gelsolin networks in the presence of filamin. *Eur. J. Biochem.*, **1997**, *246*, 373-379.
- Goodlett, D.R.; Armstrong, F.B.; Creech, R.J.; van Breemen, R.B. Formylated peptides from cyanogen bromide digests identified by fast atom bombardment mass spectrometry. *Anal. Biochem.*, **1990**, *186*, 166-120.
- Grassi, J.H.; Georgiadis, R.M. Temperature-dependent refractive index determination from critical angle measurements: Implications for quantitative SPR sensing. *Anal. Chem.*, **1999**, *71*, 4392-4396.
- Grenert, J.P.; Sullivan, W.P.; Fadden, P.; Haystead, T.A.; Clark, J.; Mimnaugh, E.; Krutzsch, H.; Ochel, H.J.; Schulte, T.W.; Sausville, E.; Neckers, L.M.; Toft, D.O. The amino-terminal domain of heat shock protein 90 (hsp90) that binds geldanamycin is an ATP/ADP switch domain that regulates hsp90 conformation. *J. Biol. Chem.*, **1997**, *272*, 23843-23850.
- Gross, E.; Witkop, B. Nonenzymatic cleavage of peptide bonds: The methionine residues in bovine pancreatic ribonuclease. *J. Biol. Chem.*, **1962**, *237*, 1856-1860.
- Gross, E.; Witkop, B. Selective cleavage of the methionyl peptide bonds in ribonuclease with cyanogen bromide. *J. Am. Chem. Soc.*, **1961**, *83*, 1510-1511.
- Hall, D.; Minton, A.P. Turbidity as a probe of tubulin polymerization kinetics: A theoretical and experimental re-examination. *Anal. Biochem.*, **2005**, *345*, 198-213.
- Hamel, E. Evaluation of antimetabolic agents by quantitative comparisons of their effects on the polymerization of purified tubulin. *Cell Biochem. Biophys.*, **2003**, *38*, 1-21.
- Hamel, E. Natural products which interact with tubulin in the vinca domain: Maytansine, rhizoxin, phomopsin a, dolastatins 10 and 15 and halichondrin B. *Pharmacol. Ther.*, **1992**, *55*, 31-51.
- Hamel, E.; Lin, C.M. Separation of active tubulin and microtubule-associated proteins by ultracentrifugation and isolation of a component causing the formation of microtubule bundles. *Biochemistry*, **1984**, *23*, 4173-4184.
- Hardman, M.; Makarov, A.A. Interfacing the orbitrap mass analyzer to an electrospray ion source. *Anal. Chem.*, **2003**, *75*, 1699-1705.
- Harrell, J.M.; Kurek, I.; Breiman, A.; Radanyi, C.; Renoir, J.M.; Pratt, W.B.; Galigniana, M.D. All of the protein interactions that link steroid receptor•hsp90•immunophilin

- heterocomplexes to cytoplasmic dynein are common to plant and animal cells. *Biochemistry*, **2002**, *41*, 5581-5587.
- Harrell, J.M.; Murphy, P.J.M.; Morishima, Y.; Chen, H.; Mansfield, J.F.; Galigniana, M.D.; Pratt, W.B. Evidence for glucocorticoid receptor transport on microtubules by dynein. *J. Biol. Chem.*, **2004**, *279*, 54647-54654.
- Harris, R.D.; Wilkinson, J.S. Waveguide surface plasmon resonance sensors. *Sens. Actuators, B*, **1995**, *29*, 261-267.
- Hedin, E.M.K.; Patkar, S.A.; Vind, J.; Svendsen, A.; Hult, K.; Berglund, P. Selective reduction and chemical modification of oxidized lipase cysteine mutants. *Can. J. Chem.*, **2002**, *80*, 529-539.
- Herrmann, H.; Bar, H.; Kreplak, L.; Strelkov, S.V.; Aebi, U. Intermediate filaments: from cell architecture to nanomechanics. *Nat. Rev. Mol. Cell Biol.*, **2007**, *8*, 562-573.
- Hirokawa, N. Kinesin and dynein superfamily proteins and the mechanism of organelle transport. *Science*, **1998**, *279*, 519-526.
- Hirokawa, N.; Noda, Y.; Okada, Y. Kinesin and dynein superfamily proteins in organelle transport and cell division. *Curr. Opin. Cell Biol.*, **1998**, *10*, 60-73.
- Hirokawa, N.; Sato-Yoshitake, R.; Kobayashi, N.; Pfister, K.K.; Bloom, G.S.; Brady, S.T. Kinesin associates with anterogradely transported membranous organelles *in vivo*. *J. Cell Biol.*, **1991**, *114*, 295-302.
- Hollenbeck, P.J.; Saxton, W.M. The axonal transport of mitochondria. *J. Cell Sci.*, **2005**, *118*, 5411-5419.
- Holleran, E.A.; Karki, S.; Holzbaur, E.L.F. The role of the dynactin complex in intracellular motility. *Int. Rev. Cytol.*, **1998**, *182*, 69-109.
- Homola, J. Present and future of surface plasmon resonance biosensors. *Anal. Bioanal. Chem.*, **2003**, *377*, 528-539.
- Homola, J.; Ctyroky, J.; Skalsky, M.; Hradilova, J.; Kolarav. P. A surface plasmon resonance based integrated optical sensor. *Sens. Actuators, B*, **1997**, *38-39*, 286-290.
- Hook, P.; Mikami, A.; Shafer, B.; Chait, B.T.; Rosenfeld, S.S.; Vallee, R.B. Long range allosteric control of cytoplasmic dynein ATPase activity by the stalk and C-terminal domains. *J. Biol. Chem.*, **2005**, *280*, 33045-33054.
- Howard, W.D.; Timasheff, S.N. Linkages between the effects of taxol, colchicine, and GTP on tubulin polymerization. *J. Biol. Chem.*, **1988**, *263*, 1342-1346.
- Hu, Q.; Noll, R.J.; Li, H.; Makarov, A.; Hardman, M.; Cooks, R.G. The orbitrap: a new mass spectrometer. *J. Mass Spectrom.*, **2005**, *40*, 430-443.

- Hubber, K.; Patel, P.; Zhang, L.; Evans, H.; Westwell, A.D.; Fischer, P.M.; Chan, S.; Martin, S. 2-[(1Methylpropyl)dithio]-1*H*-imidazole inhibits tubulin polymerization through cysteine oxidation. *Mol. Cancer Ther.*, **2008**, *7*, 143-151.
- Ikeda, Y.; Steiner, M. Sulfhydryls of platelet tubulin: their role in polymerization and colchicine binding. *Biochemistry*, **1978**, *17*, 3454-3459.
- Ikonen, E.; de Almeida, J.B.; Fath, K.R.; Burgess, D.R.; Ashman, K.; Simons, K.; Stow, J.L. Myosin II is associated with golgi membranes: identification of p200 as nonmuscle myosin II on golgi-derived vesicles. *J. Cell Sci.*, **1997**, *110*, 2155-2164.
- Johnsson, B.; Lofas, S.; Lindquist, G. Immobilization of proteins to a carboxymethyl-dextran-modified gold surface for biospecific interaction analysis in surface plasmon resonance sensors. *Anal. Biochem.*, **1991**, *198*, 268-277.
- Jordan, C.E.; Frutos, A.G.; Thiel, A.J.; Corn, R.M. Surface plasmon resonance imaging measurements of DNA hybridization adsorption and streptavidin/DNA multilayer formation at chemically modified gold surfaces. *Anal. Chem.*, **1997**, *69*, 4939-4947.
- Jordan, M.A.; Himes, R.H.; Wilson, L. Comparison of the effects of vinblastine, vincristine, vindesine, and vinepidine on microtubule dynamics and cell proliferation *in vitro*. *Cancer Res.*, **1985**, *45*, 2741-2747.
- Jordan, M.A.; Wilson, L. Microtubules and actin filaments: dynamic targets for cancer chemotherapy. *Curr. Opin. Cell Biol.*, **1998**, *10*, 123-130.
- Jordan, M.A.; Wilson, L. Microtubules as a target for anticancer drugs. *Nat. Rev. Cancer*, **2004**, *4*, 253-265.
- Jung, L.S.; Nelson, K.E.; Stayton, P.S.; Campbell, C.T. Binding and dissociation kinetics of wild-type and mutant streptavidins on mixed biotin-containing alkylthiolate monolayers. *Langmuir*, **2000**, *16*, 9421-9432.
- Kamal, A.; Stokin, G.B.; Yang, Z.; Xia, C.; Goldstein, L.S.B. Axonal transport of amyloid precursor protein is mediated by direct binding to the kinesin light chain subunit of kinesin-1. *Neuron*, **2000**, *28*, 449-459.
- Karlsson, R. SPR for molecular interaction analysis: a review of emerging application areas. *J. Mol. Recognit.*, **2004**, *17*, 151-161.
- Karlsson, R.; Falt, A. Experimental design for kinetic analysis of protein-protein interactions with surface plasmon resonance biosensors. *J. Immunol. Methods*, **1997**, *200*, 121-133.
- Kavallaris, M. Microtubules and resistance to tubulin-binding agents. *Nat. Rev. Cancer*, **2010**, *10*, 1-11.
- Kenney, D.M.; Chao, F.C. Ionophore-induced disassembly of blood platelet microtubules: effect of cyclic AMP and indomethacin. *J. Cell Physiol.*, **1980**, *103*, 289-298.

- King, S.M. AAA domains and organization of the dynein motor unit. *J. Cell Sci.*, **2000**, *113*, 2521-2526.
- Kirschner, M.W. Implications of treadmilling for the stability and polarity of actin and tubulin polymers *in vivo*. *J. Cell Biol.*, **1980**, *86*, 330-334.
- Korn, E.D.; Carlier, M.F.; Pantaloni, D. Actin polymerization and ATP hydrolysis. *Science*, **1987**, *238*, 638-644.
- Kretschmann, E. The determination of the optical constants of metals by excitation of surface plasmons. *Z. Phys.*, **1971**, *241*, 313-324.
- Krone, J.R.; Nelson, R.W.; Dogruel, D.; Williams, P.; Granzow, R. BIA/MS: interfacing biomolecular interaction analysis with mass spectrometry. *Anal. Biochem.*, **1997**, *244*, 124-132.
- Kull, F.J.; Sablin, E.P.; Lau, R.; Fletterick, R.J.; Vale, R.D. Crystal structure of the kinesin motor domain reveals a structural similarity to myosin. *Nature*, **1996**, *380*, 550-555.
- Kumar, N. Taxol-induced polymerization of purified tubulin. *J. Biol. Chem.*, **1998**, *256*, 10435-10441.
- LaMonte, B.H.; Wallace, K.E.; Holloway, B.A.; Shelly, S.S.; Ascaño, J.; Tokito, M.; Winkle, T.V.; Howland, D.S.; Holzbaur, E.L.F. Disruption of dynein/dynactin inhibits axonal transport in motor neurons causing late-onset progressive degeneration. *Neuron*, **2002**, *34*, 715-727.
- Larkin, M.A.; Blackshields, G.; Brown, N.P.; Chenna, R.; McGettigan, P.A.; McWilliam, H.; Valentin, F.; Wallace, I.M.; Wilm A.; Lopez, R.; Thompson, J.D.; Gibson, T.J.; Higgins, D.G. Clustal W and Clustal X version 2.0. *Bioinformatics*, **2007**, *23*, 2947-2948.
- Lee, J.W.; Sim, S.J.; Cho, S.M.; Lee, J. Characterization of a self-assembled monolayer of thiol on a gold surface and the fabrication of a biosensor chip based on surface plasmon resonance for detecting anti-GAD antibody. *Biosens. Bioelectron.*, **2005**, *20*, 1422-1427.
- Lee, T.H.; Hall, K.N.; Swann, M.J.; Popplewell, J.F.; Unabia, S.; Park, Y.; Hahm, K.S.; Aguilar, M.I. The membrane insertion of helical antimicrobial peptides from the N-terminus of *Helicobacter pylori* ribosomal protein L1. *Biochim Biophys Acta, Biomembr*, **2010**, *1798*, 544-557.
- Lemmer, Y.; Thanyani, S.T.; Vrey, P.J.; Driver, C.H.S.; Venter, L.; van Wyngaardt, S.; ten Bokum, A.M.C.; Ozoemena, K.I.; Pilcher, L.A.; Fernig, D.G.; Stoltz, A.C.; Swai, H.S.; Verschoor, J.A. Detection of antimycotic acid antibodies by liposomal biosensors. *Methods Enzymol*, **2009**, *464*, 79-104.
- Li, P.Y.; Lin, B.; Gerstenmaier, J.; Cunningham, B.T. A new method for label-free imaging of biomolecular interactions. *Sens. Actuators, B*, **2004**, *99*, 6-13.

- Lillis, B.; Manning, M.; Berney, H.; Hurley, E.; Mathewson, A.; Sheehan, M.M. Dual polarisation interferometry characterisation of DNA immobilisation and hybridisation detection on a silanised support. *Biosens. Bioelectron.*, **2006**, *21*, 1459-1467.
- Lin, B.; Qiu, J.; Gerstenmeier, J.; Li, P.; Pien, H.; Pepper, J.; Cunningham, B. A label-free optical technique for detecting small molecule interactions. *Biosens. Bioelectron.*, **2002**, *17*, 827-834.
- Lin, S.; Lee, C.K.; Wang, Y.M.; Huang, L.S.; Lin, Y.H.; Lee, S.Y.; Sheu, B.C.; Hsu, S.M. Measurement of dimensions of pentagonal doughnut-shaped C-reactive protein using an atomic force microscope and a dual polarisation interferometric biosensor. *Biosens. Bioelectron.*, **2006**, *22*, 323-327.
- Liu, Y.; Kulesz-Martin, M. P53 protein at the hub of cellular DNA damage response pathways through sequence-specific and non-sequence-specific DNA binding. *Carcinogenesis*, **2001**, *22*, 851-860.
- Liu, Z.; Tabakman, S.; Welsher, K.; Dai, H. Carbon nanotubes in biology and medicine: *In vitro* and *in vivo* detection, imaging and drug delivery. *Nano Res.*, **2009**, *2*: 85-120.
- Lu, H.B.; Campbell C.T., and David G. Castner. Attachment of functionalized poly(ethylene glycol) films to gold surfaces. *Langmuir*, **2000**, *16*, 1711-1718.
- Lubec, G.; Afjehi-Sadat, L. Limitations and pitfalls in protein identification by mass spectrometry. *Chem. Rev.*, **2007**, *107*, 3568-3584.
- Lukosz, W. Principles and sensitivities of integrated optical and surface plasmon sensors for direct affinity sensing and immunosensing. *Biosens. Bioelectron.*, **1991**, *6*, 215-225.
- Luo, W.; Sun, W.; Taldone, T.; Rodina, A.; Chiosis, G. Heat shock protein 90 in neurodegenerative diseases. *Mol. Neurodegener.* **2010**, *5*, 24-31.
- MacBeath, G.; Schreiber, S.L. Printing proteins as microarrays for high-throughput function determination. *Science*, **2000**, *289*, 1760-1763.
- MacNeal, R.K.; Purich, D.L. Stoichiometry and role of GTP hydrolysis in bovine neurotubule assembly. *J. Biol. Chem.*, **1978**, *253*, 4683-4687.
- Makarov, A. Electrostatic axially harmonic orbital trapping: A high-performance technique of mass analysis. *Anal., Chem.*, **2000**, *72*, 1156-1162.
- Mallik, R.; Carter, B.C.; Lex, S.A.; King, S.J.; Gross, S.P. Cytoplasmic dynein functions as a gear in response to load. *Nature*, **2004**, *427*, 649-652.
- Marazuela, M.D.; Moreno-Bondi, M.C. Fiber-optic biosensors – an overview. *Anal. Bioanal. Chem.*, **2002**, *372*, 664-682.

- Marshall, A.G.; Hendrickson, C.L.; Jackson, G.S. Fourier transform ion cyclotron resonance mass spectrometer: a primer. *Mass Spectrom. Rev.*, **1998**, *17*, 1-35.
- Marti-Renom, M.A.; Stuart, A.C.; Fiser, A.; Sanchez, R.; Melo, F.; Sali, A. Comparative protein structure modeling of genes and genomes. *Annu. Rev. Biophys. Biomol. Struct.*, **2000**, *29*, 291-325.
- Mashaghi, A.; Swann, M.; Popplewell, J.; Textor, M.; Reimhult, E. Optical anisotropy of supported lipid structures probed by waveguide spectroscopy and its application to study supported lipid bilayer formation kinetics. *Anal. Chem.*, **2008**, *80*, 3666-3676.
- Matsumura, F. Regulation of myosin II during cytokinesis in higher eukaryotes. *Trends Cell Biol.*, **2005**, *15*, 371-377.
- McDonald, D.; Vodicka, M.A.; Lucero, G.; Svitkina, T.M.; Borisy, G.G.; Emerman, M.; Hope, T.J. Visualization of the intracellular behavior of HIV in living cells. *J. Cell Biol.*, **2002**, *159*, 441-452.
- McGough, A.M.; Staiger, C.J.; Min, J.K.; Simonetti, K.D. The gelsolin family of actin regulatory proteins: modular structures, versatile functions. *FEBS Lett.*, **2003**, *552*, 75-81.
- Medana, C.; Ermondi, G.; Fruttero, R.; Di Stilo, A.; Ferretti, C.; Gasco, A. Furoxans as nitric oxide donors. 4-Phenyl-3-furoxancarboxitrile: thiol-mediated nitric oxide release and biological evaluation. *J. Med. Chem.*, **1994**, *37*, 4412-4416.
- Mermall, V.; Post, P.L.; Mooseker, M.S. Unconventional myosins in cell movement, membrane traffic, and signal transduction. *Science*, **1998**, *279*, 527-533.
- Mesngon, M.T.; Tarricone, C.; Hebbar, S.; Guillotte, A.M.; Schmitt, E.W.; Lanier, L.; Musacchio, A.; King, S.J.; Smith, D.S. Regulation of cytoplasmic dynein ATPase by Lis1. *J. Neurosci.*, **2009**, *26*, 2132-2139.
- Miglietta, A.; Bozzo, F.; Gabriel, L.; Bocca, C. Microtubule-interfering activity of parthenolide. *Chem. Biol. Interact.*, **2004**, *149*, 165-173.
- Mio, K.; Maruyama, Y.; Ogura, T.; Kawata, M.; Moriya, T.; Mio, M.; Sato, C. Single particle reconstruction of membrane proteins: a tool for understanding the 3D structure of disease-related macromolecules. *Prog. Biophys. Mol. Biol.*, **2010**, *103*, 122-130.
- Misamore, M.J.; Lynn, J.W. Role of the cytoskeleton in sperm entry during fertilization in the freshwater bivalve *Dreissena polymorpha*. *Biol. Bull.*, **2000**, *199*, 144-156.
- Mizuno, N.; Narita, A.; Kon, T.; Sutoh, K.; Kikkawa, M. Three-dimensional structure of cytoplasmic dynein bound to microtubules. *PNAS*, **2007**, *104*, 20832-20837.
- Mocz, G.; Gibbons, I.R. Model for the motor component of dynein heavy chain based on homology to the AAA family of oligomeric ATPases. *Structure*, **2001**, *9*, 93-103.

- Moon, S.; Kim, D.J.; Kim, K.; Kim, D.; Lee, H.; Lee, K.; Haam, S. Surface-enhanced plasmon resonance detection of nanoparticle-conjugated DNA hybridization. *Appl. Opt.*, **2010**, *49*, 484-491.
- Murphy, P.J.M.; Morishima, Y.; Chen, H.; Galigniana, M.D.; Mansfield, J.F.; Simons, S.S.; Pratt, W.B. Visualization and mechanism of assembly of a glucocorticoid receptor•hsp70 complex that is primed for subsequent hsp90-dependent opening of the steroid binding cleft. *J. Biol. Chem.*, **2003**, *278*, 34764-34773.
- Natsume, T.; Nakayama, H.; Jansson, O.; Isobe, T.; Takio, K.; Mikoshiba, K. Combination of biomolecular interaction analysis and mass spectrometric amino acid sequencing. *Anal. Chem.*, **2000**, *72*, 4193-4198.
- Neckers, L. Hsp90 inhibitors as novel cancer chemotherapeutic agents. *Trends Mol. Med.*, **2002**, *8*, S55-S61.
- Nedelkov, D.; Nelson, R.W. Detection of staphylococcal enterotoxin B via biomolecular interaction analysis mass spectrometry. *Appl. Environ. Microbiol.*, **2003**, *69*, 5212-5215.
- Nedelkov, D.; Rasooly, A.; Nelson, R.W. Multitoxin biosensor-mass spectrometry analysis: a new approach for rapid, real-time, sensitive analysis of staphylococcal toxins in food. *Int. J. Food Microbiol.*, **2000**, *60*, 1-13.
- Nellen, P.M.; Lukosz, W., Model experiments with integrated optical input grating couplers as direct immunosensors. *Biosens. Bioelectron.*, **1991**, *6*, 517-525.
- Nelson, D.L.; Cox, M.M. *Lehninger Principles of Biochemistry*, 4th Ed; W. H. Freeman and Company: New York, USA, 2005; pp 211.
- Nelson, R.W.; Krone, J.R.; Jansson, O. Surface plasmon resonance biomolecular interaction analysis mass spectrometry. 1. Chip-based analysis. *Anal. Chem.*, **1997**, *69*, 4363-4368.
- Nidumolu, B.G.; Urbina, M.C.; Hormes, J.; Kumar, C.S.S.R.; Monroe, W.T. Functionalization of gold and glass surfaces with magnetic nanoparticles using biomolecular interactions. *Biotechnol. Prog.*, **2006**, *22*, 91-95.
- Novotny, L. and Hecht, B. *Principles of Nano-Optics*; Cambridge University Press: Cambridge, UK, 2006; pp 378-393.
- Ohman, E.; Nilsson, A.; Maderia, A.; Sjogren, B.; Andren, P.E.; Svenningsson, P. Use of surface plasmon resonance coupled with mass spectrometry reveals an interaction between the voltage-gated sodium channel type X α -subunit and caveolin-1. *J. Proteome Res.*, **2008**, *7*, 5333-5338.
- Ohta, D.; Kanaya, S.; Suzuki, H. Application of Fourier-transform ion cyclotron resonance mass spectrometry to metabolic profiling and metabolite identification. *Curr. Opin. Biotechnol.*, **2010**, *21*, 35-44.

- Oldfield, T.J.; Hubbard, R.E. Analysis of the C α geometry in protein structures. *Proteins: Struct., Funct., Bioinf.*, **1994**, *18*, 324-337.
- Olmsted, J.B.; Borisy, G.G. Characterization of microtubule assembly in porcine brain extracts by viscometry. *Biochemistry*, **1973**, *12*, 4282-4289.
- Olsen, J.V.; de Godoy, L.M.F.; Li, G.; Macek, B.; Mortensen, P.; Pesch, R.; Makarov, A.; Lange, O.; Horning S.; Mann, M. Parts per million mass accuracy on an Orbitrap mass spectrometer via lock mass injection into a C-trap. *Mol. Cell Prot.*, **2005**, *4*, 2010-2021.
- Otto, A. Excitation of nonradiative surface plasma waves in silver by the method of frustrated total reflection. *Z. Phys. A: Hadrons Nucl.*, **1968**, *216*, 398-410.
- Ouellet, E.; Lausted, C.; Lin, T.; Yang, C.W.T.; Hood, L.; Lagally, E.T. Parallel microfluidic surface plasmon resonance imaging arrays. *Lab Chip*, **2010**, *10*, 581-588.
- Owen, V. Real-time optical immunosensors – a commercial reality. *Biosens. Bioelectron.*, **1997**, *12*, i-ii.
- Parsons, J.T.; Horwitz, A.R.; Schwartz, M.A. Cell adhesion: integrating cytoskeletal dynamics and cellular tension. *Nat. Rev. Mol. Cell Biol.*, **2010**, *11*, 633-643.
- Paschal, B.M.; Shpetner, H.S.; Vallee, R.B. MAP 1C is a microtubule-activated ATPase which translocates microtubules *in vitro* and has dynein-like properties. *J. Cell Biol.*, **1987**, *105*, 1273-1282.
- Pavlov, D.; Muhrad, A.; Cooper, J.; Wear, M.; Reisler, E. Actin filament severing by cofilin. *J. Mol. Biol.*, **2007**, *365*, 1350-1358.
- Petersen, P.; Petersen, T.N.; Andersen, P.; Nielsen, M.; Lundegaard, C. A generic method for assignment of reliability scores applied to solvent accessibility predictions. *BMC Struct. Biol.*, **2009**, *9*, 51-60.
- Pierce, J.W.; Schoenleber, R.; Jesmok, G.; Best, J.; Moore, S.A.; Collins, T.; Gerritsen, M.E. Novel inhibitors of cytokine-induced I κ B α phosphorylation and endothelial cell adhesion molecule expression show anti-inflammatory effects *in vivo*. *J. Biol. Chem.*, **1997**, *272*, 21096-21103.
- Piliarik M.; Homola, J. Surface plasmon resonance (SPR) sensors: approaching their limits? *Opt. Express*, **2009**, *17*, 16505-16517.
- Piliarik, M.; Vaisocherova, H.; Homola, J. A new surface plasmon resonance sensor for high-throughput screening applications. *Biosens. Bioelectron.*, **2005**, *20*, 2104-2110.
- Pollard, T.D.; Borisy, G.G. Cellular motility driven by assembly and disassembly of actin filaments. *Cell*, **2003**, *112*, 453-465.

- Popplewell, J.F.; Swann, M.J.; Ahmed, Y.; Turnbull, J.E.; Fernig, D.G. Fabrication of carbohydrate surfaces by using nonderivatised oligosaccharides, and their application to measuring the assembly of sugar-protein complexes. *ChemBioChem*, **2009**, *10*, 1218-1226.
- Popplewell, J.F.; Swann, M.J.; Freeman, N.J.; McDonnell, C.; Ford, R.C. Quantifying the effects of melittin on liposomes. *Biochim Biophys Acta, Biomembr*, **2007**, *1768*, 13-20.
- Pratt, W.B.; Galigniana, M.D.; Harrell, J.M.; DeFranco, D.B. Role of hsp90 and the hsp90-binding immunophilins in signaling protein movement. *Cell Signal*, **2004**, *16*, 857-872.
- Provencher, S.W.; Gloeckner, J. Estimation of globular protein secondary structure from circular dichroism. *Biochemistry*, **1981**, *20*, 33-37.
- Rayala SK, der Hollander P, Balasenthil S, Yang Z, Broaddus RR, and Kumar R. (2005). Function regulation of oestrogen receptor pathway by the dynein light chain 1. *EMBO reports*, **6(6)**: 538-545.
- Reck-Peterson, S.L.; Vale, R.D. Molecular dissection of the roles of nucleotide binding and hydrolysis in dynein's AAA domains in *Saccharomyces cerevisiae*. *PNAS*, **2004**, *101*, 1491-1495.
- Reynolds, P.D., Pittler, S.J.; Scammell, J.G. Cloning and expression of the glucocorticoid receptor from the squirrel monkey (*Saimiri boliviensis boliviensis*), a glucocorticoid resistant primate. *J. Clin. Endocrinol. Metab.*, **1997**, *82*, 465-472.
- Ricard-Blum, S.; Peel, L.L.; Ruggiero, F.; Freeman, N.J. Dual polarization interferometry characterization of carbohydrate-protein interactions. *Anal. Biochem.*, **2006**, *352*, 252-259.
- Roberts, A.J.; Numata, N.; Walker, M.L.; Kato, Y.S.; Malkova, B.; Kon, T.; Ohkura, R.; Ariska, F.; Knight, P.J.; Sutoh, K.; Burgess, S.A. AAA+ ring and linker swing mechanisms in the dynein motor. *Cell*, **2009**, *136*, 485-495.
- Rodriguez, O.C.; Cheney, R.E. A new direction for myosin. *Trends Cell Biol.*, **2000**, *10*, 307-311.
- Ronkainen, N.J.; Halsall, H.B.; Heineman, W.R. Electrochemical biosensors. *Chem. Soc. Rev.*, **2010**, *39*, 1747-1763.
- Rothenhausler, B.; Knoll, W. Surface-plasmon microscopy. *Nature*, **1988**, *332*, 615-617.
- Rowinsky, E.K.; Donehower, R.C. Paclitaxel (Taxol). *N. Engl. J. Med.*, **1995**, *332*, 1004-1014.
- Rowlands, M.G.; Newbatt, Y.M.; Prodromou, C.; Pearl, L.H.; Workman, P.; Aherne, W. High-throughput screening assay for inhibitors of heat-shock protein 90 ATPase activity. *Anal. Biochem.*, **2004**, *327*, 176-183.

- Rusmini, F.; Zhong, Z.; Feijen, J. Protein immobilization strategies for protein biochips. *Biomacromolecules*, **2007**, *8*, 1775-1789.
- Ryan, C.M.; Souda, P.; Halgand, F.; Wong, D.T.; Loo, J.A.; Faull, K.F.; Whitelegge, J.P. Confident assignment of intact mass tags to human salivary cystatins using top-down Fourier-transform ion cyclotron resonance mass spectrometry. *J. Am. Soc. Mass Spectrom.*, **2010**, *21*, 908-917.
- Sackett, D.L. Vinca site agents induce structural changes in tubulin different from and antagonistic to changes induced by colchicine site agents. *Biochemistry*, **1995**, *34*, 7010-7019.
- Sali, A.; Overington, J.P. Derivation of rules for comparative protein modeling from a database of protein structure alignments. *Protein Sci.*, **1994**, *3*, 1582-1596.
- Salina, D.; Bodoor, K.; Eckley, D.M.; Schroer, T.A.; Rattner, J.B.; Burke, B. Cytoplasmic dynein as a facilitator of nuclear envelope breakdown. *Cell*, **2002**, *108*, 97-107.
- Samsó, M.; Koonce, M.P. 25 Å resolution structure of a cytoplasmic dynein motor reveals a seven-member planar ring. *J. Mol. Biol.*, **2004**, *340*, 1059-1072.
- Saxton, W.M.; Stemple, D.L.; Leslie, R.J.; Salmon, E.D.; Zavortink, M.; McIntosh, J.R. Tubulin dynamics in cultured mammalian cells. *J. Cell Biol.*, **1984**, *99*, 2175-2186.
- Schaferling, M.; Riepl, M.; Pavlickova, P.; Paul, H.; Kambhampati, D.; Liedberg, B. Functionalized self-assembled monolayers on gold as binding matrices for the screening of antibody-antigen interactions. *Microchim. Acta*, **2003**, *142*, 193-203.
- Schiemann, O.; Prisner, T.F. Long-range distance determinations in biomacromolecules by EPR spectroscopy. *Q. Rev. Biophys.*, **2007**, *40*, 1-53.
- Schiff, P.B.; Fant, J.; Horwitz, S.B. Promotion of microtubule assembly *in vitro* by taxol. *Nature*, **1979**, *277*, 665-667.
- Seeton, C.J. Viscosity-temperature correlation for liquids. *Tribol. Lett.*, **2006**, *22*, 67-78.
- Serohijos, A.W.; Chen, Y.; Ding, F.; Elston, T.C.; Dokholyan, N.V. *PNAS*, **2006**, *103*, 18540-18545.
- Sharov, V.S.; Dremina, E.S.; Galeva, N.A.; Williams, T.D.; Schoneich, C. Quantitative mapping of oxidation-sensitive cysteine residues in SERCA *in vivo* and *in vitro* by HPLC-electrospray-tandem MS: selective protein oxidation during biological aging. *Biochem. J.*, **2006**, *394*, 605-615.
- Sharp, D.J.; Rogers, G.C.; Scholey, J.M. Cytoplasmic dynein is required for poleward chromosome movement during mitosis in *Drosophila* embryos. *Nat. Cell Biol.*, **2000**, *2*, 922-930.

- Shih, Y.; Prausnitz, J.M.; Blanch, H.W. Some characteristics of protein precipitation salts. *Biotechnol. Bioeng.*, **2004**, *40*, 1155-1164.
- Shumaker-Parry, J.S.; Aebersold, R.; Campbell, C.T. Parallel, quantitative measurement of protein binding to a 120-element double-stranded DNA array in real time using surface plasmon resonance microscopy. *Anal. Chem.*, **2004**, *76*, 2071-2082.
- Sinz, A. Chemical cross-linking and mass spectrometry for mapping three-dimensional structures of proteins and protein complexes. *J. Mass Spectrom.*, **2003**, *38*, 1225-1237.
- Sippl, M.J. Calculation of conformational ensembles from potentials of mean force. An approach to the knowledge-based prediction of local structures in globular proteins. *J. Mol. Biol.*, **1990**, *213*, 859-883.
- Smith, D.S.; Niethammer, M.; Ayala, R.; Zhou, Y.; Gambello, M.J.; Wynshaw-Boris, A.; Tsai, L. Regulation of cytoplasmic dynein behavior and microtubule organization by mammalian Lis1. *Nat. Cell Biol.*, **2000**, *2*, 767-775.
- Sonesson, A.W.; Callisen, T.H.; Brismar, H.; Elofsson, U.M. Adsorption and activity of *Thermomyces lanuginosus* lipase on hydrophobic and hydrophilic surfaces measured with dual polarization interferometry (DPI) and confocal microscopy. *Colloids Surf., B*, **2008**, *61*, 208-215.
- Sonksen, C.P.; Nordhoff, E.; Jansson, O.; Malmqvist, M.; Roepstorff, P. Combining MALDI mass spectrometry and biomolecular interaction analysis using a biomolecular interaction analysis instrument. *Anal. Chem.*, **1998**, *70*, 2731-2736.
- Sperry, J.B.; Wilcox, J.M.; Gross, M.L. Strong anion exchange for studying protein-DNA interactions by H/D exchange mass spectrometry. *J. Am. Soc. Mass Spectrom.*, **2008**, *19*, 887-890.
- Stahlberg, H.; Walz, T. Molecular electron microscopy: state of the art and current challenges. *ACS Chem. Biol.*, **2008**, *3*, 268-281.
- Straube, A.; Hause, G.; Fink, G.; Steinberg, G. Conventional kinesin mediates microtubule-microtubule interactions in vivo. *Mol. Biol. Cell*, **2006**, *17*, 907-916.
- Sutcliffe, M.J.; Hayes, F.R.; Blundell, T.L. Knowledge-based modeling of homologous proteins, part II: rules for the conformations of substituted side chains. *Protein Eng.*, **1987**, *1*, 385-392.
- Svenson, A.; Carlsson, J. The thiol group of bovine serum albumin. High reactivity at acid pH as measured by the reaction with 2,2'-dipyridyl disulphide. *Biochim. Biophys. Acta*, **1975**, *400*, 433-438.
- Swann, M.; Freeman, N.; Carrington, S.; Ronan, G.; Barrett, P. Quantifying structural changes and stoichiometry of protein interactions using size and density profiling. *Lett. Pept. Sci.*, **2003**, *10*, 487-494.

- Swann, M.J.; Peel, L.L.; Carrington, S.; Freeman, N.J. Dual-polarization interferometry: an analytical technique to measure changes in protein structure in real time, to determine the stoichiometry of binding events, and to differentiate between specific and nonspecific interactions. *Anal. Biochem.*, **2004**, *329*, 190-198.
- Takito, J.; Nakamura, H.; Kobayashi, J.; Ohizumi, Y.; Ebisawa, K.; Nonomura, Y. Puralin, a novel stabilizer of smooth muscle myosin filaments that modulates ATPase activity of dephosphorylated myosin. *J. Biol. Chem.*, **1986**, *261*, 13861-13865.
- Taylor, J.D.; Linman, M.J.; Wilkop, T.; Cheng, Q. Regenerable tethered bilayer lipid membrane arrays for multiplexed label-free analysis of lipid-protein interactions on poly(dimethylsiloxane) microchips using SPR imaging. *Anal. Chem.*, **2009**, *81*, 1146-1153.
- Ter Haar, E.; Kowalski, R.J.; Hamel, E.; Lin, C.M.; Longley, R.E.; Gunasekera, S.P.; Rosenkranz, H.S.; Day, B.W. Discodermolide, a cytotoxic marine agent that stabilizes microtubules more potently than taxol. *Biochemistry*, **1996**, *35*, 243-250.
- Terry, C.J.; Popplewell, J.F.; Swann, M.J.; Freeman, N.J.; Fernig, D.G. Characterisation of membrane mimetics on a dual polarisation interferometer. *Biosens. Bioelectron.*, **2006**, *22*, 627-632.
- Theriot, J.A.; Mitchison, T.J. Actin microfilament dynamics in locomoting cells. *Nature*, **1991**, *352*, 126-131.
- Thompsett, A.R.; Brown, D.R. Dual polarisation interferometry analysis of copper binding to the prion protein: Evidence for two folding states. *Biochim. Biophys. Acta*, **2007**, *1774*, 920-927.
- Tiefenthaler, K.; Lukosz, W. Grating couplers as integrated optical humidity and gas sensors. *Thin Solid Films*, **1985**, *126*, 205-211.
- Tiefenthaler, K.; Lukosz, W. Sensitivity of grating couplers as integrated-optical chemical sensors. *J. Opt. Soc. Am. B*, **1989**, *6*, 209-220.
- Tolic-Norrelykke, I.M. Push-me-pull-you: how microtubules organize the cell interior. *Eur. Biophys. J.*, **2008**, *37*, 1271-1278.
- Topham, C.M.; McLeod, A.; Eisenmenger, F.; Overington, J.P.; Johnson, M.S.; Blundell, T.L. Fragment ranking in modeling of protein structure. Conformationally constrained environmental amino acid substitution tables. *J. Mol. Biol.*, **1993**, *229*, 194-220.
- Trask, O.J.; Nickischer, D.; Burton, A.; Williams, R.G.; Kandasamy, R.A.; Johnston, P.A.; Johnston, P.A. High-throughput automated confocal microscopy imaging screen of a kinase-focused library to identify p38 mitogen-activated protein kinase inhibitors using the GE InCell 3000 Analyzer. *Methods Mol. Biol.*, **2009**, *565*, 159-186.

- Tyagarajan, K.; Pretzer, E.; Wiktorowicz, J.E. Thiol-reactive dyes for fluorescence labeling of proteomic samples. *Electrophoresis*, **2003**, *24*, 2348-2358.
- Vadlamudi RK, Bagheri-Yarmand R, Yang Z, Balasenthil S, Nguyen D, Sahin AA, der Hollander P, and Kumar R. (2004). Dynein light chain 1, a p21-activated kinase 1-interacting substrate, promotes cancerous phenotypes. *Cancer Cell*, **5**: 575-585.
- Vaisberg, E.A.; Koonce, M.P.; McIntosh, J.R. Cytoplasmic dynein plays a role in mammalian mitotic spindle formation. *J. Cell Biol.*, **1993**, *123*, 849-858.
- Vale, R.D. The molecular motor toolbox for intracellular transport. *Cell*, **2003**, *112*, 467-480.
- Vallee, R.B.; Shpetner, H.S. Motor proteins of cytoplasmic microtubules. *Annu. Rev. Biochem.*, **1990**, *59*, 909-932.
- Vallee, R.B.; Williams, J.C.; Varma, D.; Barnhart, L.E. Dynein: an ancient motor protein involved in multiple modes of transport. *J. Neurobiol.*, **2004**, *58*, 189-200.
- Van Holde, K.E.; Johnson, W.C.; Ho, P.S. *Principles of Physical Biochemistry*, 2nd Ed; Pearson Education, Inc.: USA, 2006; pp 660-670.
- Verhey, K.J.; Deehan, R.; Blenis, J.; Schnapp, B.J.; Rapoport, T.A.; Margolis, B. Cargo of kinesin identified as Jip scaffolding proteins and associated signaling molecules. *J. Cell Biol.*, **2001**, *152*, 959-970.
- Voter, W.A.; Erickson, H.P. The kinetics of microtubule assembly. Evidence for a two-stage nucleation mechanism. *J. Biol. Chem.*, **1984**, *259*, 10430-10438.
- Wacker, S.A.; Kapoor, T.M. Targeting a kinetochore-associated motor protein to kill cancer cells. *PNAS*, **2010**, *107*, 5699-5700.
- Wade, R.H.; Chretien, D. Cryoelectron microscopy of microtubules. *J. Struct. Biol.*, **1993**, *110*, 1-27.
- Wagner, M. C.; Pfister, K. K.; Brady, S. T.; Bloom, G. S. Purification of kinesin from bovine brain and assay of microtubule-stimulated ATPase activity. *Methods Enzymol.*, **1991**, *196*, 157-175.
- Walker, D.; Htun, H.; Hager, G.L. Using inducible vectors to study intracellular trafficking of GFP-tagged steroid/nuclear receptors in living cells. *Methods*, **1999**, *19*, 386-393.
- Wang, D. Carbohydrate microarrays. *Proteomics*, **2003**, *3*, 2167-2175.
- Wang, J. Electrochemical glucose biosensors. *Chem. Rev.*, **2008**, *108*, 814-825.
- Wang, J.; Coffey, P.D.; Swann, M.J.; Yang, F.; Lu, J.R.; Yang, X. Optical extinction combined with phase measurements for probing DNA-small molecule interactions using an evanescent waveguide biosensor. *Anal. Chem.*, **2010**, *82*, 5455-5462.

- Watson, M.L. Staining of tissue sections for electron microscopy with heavy metals. *J. Cell Biol.*, **1958**, *4*, 475-478.
- Wegner, G.J.; Lee, H.J.; Marriott, G.; Corn, R.M. Fabrication of histidine-tagged fusion protein arrays for surface plasmon resonance imaging studies of protein-protein and protein-DNA interactions. *Anal. Chem.*, **2003**, *75*, 4740-4746.
- Wilson, D.J.; Konermann, L. Ultrarapid desalting of protein solutions for electrospray mass spectrometry in a microchannel laminar flow device. *Anal. Chem.*, **2005**, *77*, 6887-6894.
- Wischnitzer, S. *Introduction to Electron Microscopy*, 2nd Ed; Pergamon Press Inc.: Elmsford, N.Y., 1970; pp 6-108.
- Wood, R.W. Remarkable spectrum from a diffraction grating. *Philos. Mag.*, **1902**, *4*, 396-402.
- Wynshaw-Boris, A.; Gambello, M.J. LIS1 and dynein motor function in neuronal migration and development. *Genes Dev.*, **2001**, *15*, 639-651.
- Xi, B.; Yu, N.; Wang, X.; Xu, X.; Abassi, Y.A. The application of cell-based label-free technology in drug discovery. *Biotechnol. J.*, **2008**, *3*, 484-495.
- Yeh, E.; Skibbens, R.V.; Cheng, J.W.; Salmon, E.D.; Bloom, K. Spindle dynamics and cell cycle regulation of dynein in the budding yeast, *Saccharomyces cerevisiae*. *J. Cell Biol.*, **1995**, *130*, 687-700.
- Yih, J.; Chu, Y.; Mao, Y.; Wang, W.; Chien, F.; Lin, C.; Lee, K.; Wei, P.; Chen, S. Optical waveguide biosensors constructed with subwavelength gratings. *Appl. Opt.*, **2006**, *45*, 1938-1942.
- Yu, F.; Tian, S.; Yao, D.; Knoll, W. Surface plasmon enhanced diffraction for label-free biosensing. *Anal. Chem.*, **2004**, *76*, 3530-3535.
- Zeder-Lutz, G.; Zuber, E.; Witz, J.; Van Regenmortel, M.H.V. Thermodynamic analysis of antigen-antibody binding using biosensor measurements at different temperatures. *Anal. Biochem.*, **1997**, *246*, 123-132.
- Zhang, X.; Settembre, E.; Xu, C.; Dormitzer, P.R.; Bellamy, R.; Harrison, S.C.; Grigorieff. Near-atomic resolution using electron cryomicroscopy and single particle reconstruction. *PNAS*, **2008**, *105*, 1867-1872.
- Zhu, G.; Yang, F.; Balachandran, R.; Höök, P.; Vallee, R.B.; Curran, D.P.; Day, B.W. Synthesis and biological evaluation of purealin and analogues as cytoplasmic dynein heavy chain inhibitors. *J. Med. Chem.*, **2006**, *49*, 2063-2076.
- Zhu, H.; Bilgin, M.; Hangham, R.; Hall, D.; Casamayor, A.; Bertone, P.; Lan, N.; Jansen, R.; Bidlingmaier, S.; Houfek, T.; Mitchell, T.; Miller, P.; Dean, R.A.; Gerstein, M.; Snyder, M. Global analysis of protein activities using proteome chips. *Science*, **2001**, *293*, 2101-2105.